Excited State Intramolecular Proton Transfer in 2-(2'-Hydroxyphenyl)benzimidazole and its Nitrogen Substituted Analogues and 2-(2'-Hydroxyphenyl)-3*H*-oxazo[4,5-*b*]pyridine

A dissertation
as partial fulfillment of requirement
for the degree of Doctor of Philosophy in Chemistry

by

Francis A. S. Chipem
07612201

Department of Chemistry
Indian Institute of Technology Guwahati
Guwahati 781 039
Assam, India

Statement

The work contained in this thesis entitled "**Excited State Intramolecular Proton Transfer in 2-(2'-Hydroxyphenyl)benzimidazole and its Nitrogen Substituted Analogues and 2-(2'-Hydroxyphenyl)-3*H*-oxazo[4,5-*b*]pyridine**" is the outcome of the research work carried out by me under the supervision of Dr. G. Krishnamoorthy, Department of Chemistry, Indian Institute of Technology Guwahati, India.

In keeping with the general practice of reporting scientific observations, due acknowledgements have been made whenever work described here has been based on the findings of other investigators. This work has not been submitted elsewhere for the award of any degree.

Francis A. S. Chipem

Department of Chemistry,
Indian Institute of Technology Guwahati,
Guwahati – 781 039, India

31st December, 2012

Certificate

It is certified that the work contained in the thesis entitled "**Excited State Intramolecular Proton Transfer in 2-(2'-Hydroxyphenyl)benzimidazole and its Nitrogen Substituted Analogues and 2-(2'-Hydroxyphenyl)-3*H*-oxazo[4,5-*b*]pyridine**" by Francis A. S. Chipem is an authentic record of the results obtained from the research work carried out under my supervision in the Department of Chemistry, Indian Institute of Technology Guwahati, India.

Dr. G. Krishnamoorthy

Department of Chemistry,
Indian Institute of Technology Guwahati,
Guwahati – 781 039, India.

31st December, 2012

Dedicated to

Late Rev. Fr. John Med sdb

Acknowledgements

At this stage of ending my PhD programme, I would like to appreciate the people around me all throughout my academic journey without whom this thesis would not have been a reality.

First of all, I would like to express my sincere gratitude to my supervisor Dr. G. Krishnamoothy who has been an excellent supervisor and taught me how to carry out research problems. His meticulous analysis on the problems and results is one that I need to learn. He has been very patient waiting for my results. I got all the freedom to pursue my own interests under his supervision. Besides he has been with me throughout during my good and bad times and I find myself privileged to have worked under his guidance.

I would like to acknowledge my doctoral committee members Prof. Anil K. Saikia (Chairman), Dr. Aditya N. Panda, and Dr. Mihir K. Purkait who have been constantly guiding me with their valuable suggestions, encouragements and constructive criticism which helped to improve my thesis.

I take this opportunity to thank Prof. A. Chattopadhyay, Prof. T. Punniyamurthy, Prof. M. Ray, and Dr. A. K. Gupta for teaching me during my course works. I also thank Dr. M. Sarma for teaching me Fortran.

I really thank my former and present labmates Dr. N. Dash, Soumyada, Anu, Ashim, Santosh, Saugata, Dr. M. D. Saikia, Mrinmoy, Dr. A. Thangamani, Debpratim, Rameshwar, Sourav, Manoj, Arvind, Aswini and Suman for creating a good environment in the lab. They are always there providing their help whenever I need. I thank specially Santosh for helping me carry out my research works.

I acknowledge Dr. R. Boomishankar, Dr. S. C. Sahoo, Dr. M. Singh, Babulalda, and Himanshu for their help in solving single crystal structures of my compounds. I took the help of Mr. K. Singh from Central Instruments Facility (CIF), and Chaitanya for measuring the molecular mass of my samples. Somasekhar helped me in compound purification. I am thankful to Anu and Mohan for teaching me how to carry out Docking experiments. Thanks to AC/AP Lab and its members for providing help whenever/whatever needed from stationary items to measuring mass of the samples.

I take this opportunity to thank IIT Guwahati and CSIR for providing me Fellowship for my PhD programme. I thank the Department of Chemistry for providing instrumental and computational facilities, and CIF for instrumental facilities. I remain thankful to Dr. M. Qureshi

for allowing me to use his fluorimeter. I really appreciate Mr. Chandanda and Mr. K. Singh from CIF for being there whenever I need. I am thankful to all the faculties and scientific staff specially Mr. N. Kalita, Mrs. L. Nath, Mrs. A. M. Baruah, Mr. P. Gogoi, Mr. A. Gogoi, Mr. D. Hira, Mr. S. K. Mondol, Mr. I. Islam, Mr. N. Deka, Mr. S. Deka, and Mr. Subal who are associated with me at the Department of Chemistry and are always helpful.

I remain thankful to friends from other universities/institutes namely Dr. J. Joly, Dr. A. Murugadoss, Animesh, Anukul, Arvind, Ashish, Baidya, Biswajit, Hari, Jagannath, Mrinmoy, Rasomoy, Shyam, Suman, Supriya, and Yu-Chi for sending materials whenever I need. My stay in the campus becomes more colorful because of the company of Dr. K. Darunkumar and his family, Dr. L. Boeing, Mr. and Mrs. Haokip and their family, Mr. and Mrs. Joy and their family,Mr. R. Khangembam, Dr. S. Nongmaithem, Dr. G. Haobijam, Dr. A. Potsangbam, Dr. M. Singh, Dr. J. Deka, Shilpa, Raihana, Subhojit, Sandeep, Bharati, Ashish, Chandrasekhar, James, and my PhD batchmates - Atul, Devendra, Faizi, Fulwa, Mohan, Partha, Rezzak, Sadhu, Sayak, and Somasekhar.

My parents, brothers, and sister have been the source of inspiration throughout my life. I am so grateful that Late Rev. Fr. John Med sdb, Rev. Fr. John Larrea sdb, and Late Uncle Fabian came into my life and family. They have been with my family protecting us both in good and bad times. Late Fr. Med and Fr. Larrea are just like my grand fathers.

Sincerely,
Chipem Francis

~ SYNOPSIS ~

The PhD work is focused on the study of photophysical properties of excited state intramolecular proton transfer (ESIPT) exhibiting organic molecules. The thesis is divided into six chapters.

Chapter 1: Introduction

Chapter 1 gives a brief account of ESIPT process with literature survey. ESIPT is a phototautomerization of enol to keto form in the excited state in a cyclic intramolecular hydrogen bonded ring system. Factors affecting the process are also reviewed in this chapter. The scope of the present work is presented in the end of the chapter.

Chapter 2: Materials, Methods and Instrumentation

Chapter 2 provides the details of the materials used in the present work and the synthetic procedures followed in the syntheses of the fluorophores. Methods used for the analysis, calculations and preparation of the samples are also elaborated in this chapter. The chapter also describes the methods used for the quantum chemical calculations. In addition, brief descriptions of UV-Visible absorption spectrophotometer, and steady-state and time-resolved fluorimeters are provided.

Chapter 3: Excited State Intramolecular Proton Transfer and Rotamerism in 2-(2'-Hydroxyphenyl)benzimidazole and its Nitrogen Substituted Analogues

Chapter 3 consists of three sections. The first two sections discuss the role of nitrogen substitution in 2-(2'-hydroxyphenyl)benzimidazole (HPBI, **Chart 1**) on ESIPT and rotamerism based on the theoretical results obtained from *ab initio* and density functional theory calculations performed on HPBI and its nitrogen substituted analogues. Theoretical study on the effect of azo substitution in benzene ring of HPBI is carried out in the first section. In the second section the theoretical study is extended to study the effect of nitrogen substitution on the phenolic ring. These groups of molecules can exist in different rotameric and isomeric forms as shown in **Chart 2**. *cis*-Enol which forms an intramolecularly hydrogen bonded ring is the most stable form of these compounds except in 2-(2'-hydroxy-3'-pyridyl)benzimidazole (2',3'-HPyBI) where K-2 keto (**Chart 3**) is the most stable form. *cis*-Enol undergoes ESIPT through the hydrogen bond to give the keto isomer. The proton

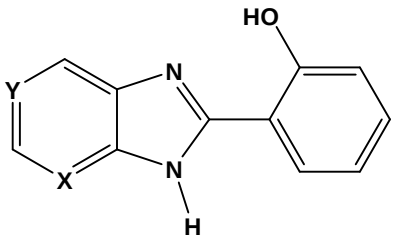

A

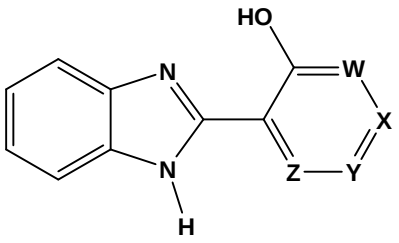

B

X = Y = CH	**HPBI**
X = N, Y = CH	**HPIP-b**
X = CH, Y = N	**HPIP-c**
X = Y = N	**HPP**

W = N, X = Y = Z = CH, 2',3'-HPyBI

X = N, W = Y = Z = CH, 3',4'-HPyBI

Y = N, W = X = Z = CH, 4',3'-HPyBI

Z = N, W = X = Y = CH, 3',2'-HPyBI

X = Z = N, W = Y = CH, 5',4'-HPymBI

Chart 1. HPBI and its nitrogen substituted analogues.

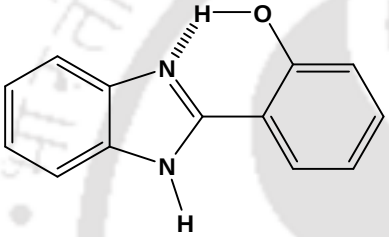

***cis*-Enol**

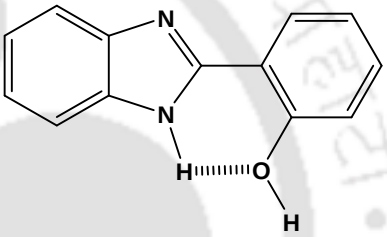

***trans*-Enol**

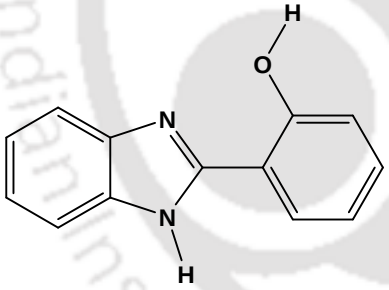

Open Enol

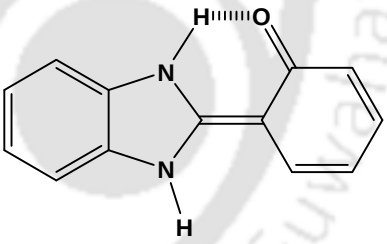

Keto

Chart 2. Different conformeric and isomeric forms of HPBI.

transfer is unfavorable in the S_0 state but becomes feasible in the S_1 state except in 2-(5'-hydroxy-4'-pyrimidinyl)benzimidazole. Upon excitation, ultrafast proton transfer occurs in *cis*-enol form to give the phototautomer keto form. The *trans*-enol is responsible for the normal band while the highly Stokes' shifted band is due to emission from the keto form. After ESIPT, the keto form undergoes torsion rotation through the carbon-carbon double bond linking the two aromatic rings to form a twisted keto structure at 90°. The twisted keto structure is characterized by intramolecular charge transfer

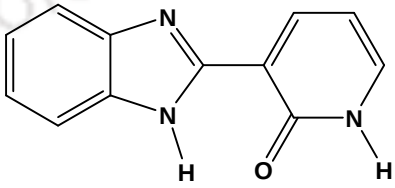

Chart 3. Structure of K-2 form

(ICT) and its energy is lower than the planar keto. This can act as a nonradiative channel from the keto tautomer. This may be the possible cause of smaller quantum yield of the phototautomer of 2-(2'-hydroxyphenyl)-3*H*-imidazo[4,5-*b*]pyridine (HPIP-b) and 2-(2'-hydroxyphenyl)-3*H*-imidazo[4,5-*c*]pyridine (HPIP-c) compared to that of HPBI.

However, when more electronegative nitrogen is substituted in the phenolic ring of HPBI, the charge donating capacity of the dissociated pyridinol or pyrimidinol moiety is less than the dissociated phenol. This reduces the ICT and thus destabilizing the twisted keto tautomer. This is consistent with the experimental fact that the quantum yield of 2-(3'-hydroxy-2'-pyridyl)benzimidazole (3',2'-HPyBI) is higher than that of HPBI.

The third section of chapter 3 is an experimental study on the effect of temperature on ESIPT of HPBI and its nitrogen substituted analogues HPIP-b and HPIP-c in solvents of different polarity and hydrogen bonding capacity. With increase in temperature, the fluorescence of both normal and tautomer emissions decrease. The rate of decrease of tautomer emission is more than that of normal emission. The decrease in fluorescence of tautomer is governed by two factors: (i) decrease in relative population of *cis*-enol, and (ii) increase in nonradiative decay from the excited state. The changes in the fluorescence emission are also reflected in the lifetime of the normal and the tautomer fluorescence. In general, decrease in lifetime values is observed with rise in temperature indicating the increase in the rate of nonradiative decay.

Chapter 4: Study of Fluorescence Sensing Ability of 2-(2'-Hydroxyphenyl) benzimidazole and its Nitrogen Substituted Analogues Toward Metal Ions

In **Chapter 4**, the interactions of HPBI, HPIP-b and HPIP-c with different metal ions are elaborated. In this study the potential implications of the fluorophores as probes and sensors are also explored based on ratiometric fluorescence emission.

Alkali and alkaline metal ions Na^{+}, Mg^{2+}, Ca^{2+} and Ba^{2+} have little or no effects on the absorption and fluorescence properties of the fluorophores in the concentration range of the metal ions (0 to 500 μM) studied. However, changes in fluorescence are observed upon binding with transition metal ions Ni^{2+}, Cu^{2+} and Zn^{2+}. Transition metal ions form complexes with the fluorophores by coordination between the metal ion and the fluorophores through the phenolic oxygen and imidazole nitrogen. This is confirmed by the single crystal structure obtained for Ni^{2+}:HPIP-b of 1:2 complex which shows that the fluorophore acts as bidentate ligand by coordinating with the metal centre through its phenolic oxygen and imidazole nitrogen.

The ratio of normal to tautomer emissions of HPBI increases by 143 folds in presence of Cu^{2+} ions and 10.4 folds in presence of Zn^{2+} ion at 1:5 concentration ratio of the fluorophore to that of metal ion. While the fluorescence ratio of HPIP-b at 1:5 concentration ratio increases by 2.1 and 2.8 folds in presence of Ni^{2+} and Cu^{2+}, respectively. Cu^{2+} ion enhances the fluorescence ratio of HPIP-c by 1.9 folds at 1:5 concentration ratio. The increase in the ratio is attributed to the disruption of ESIPT process due to the binding of the fluorophores with metal ions by coordinating through imidazole nitrogen and phenolic oxygen.

However, the normal to tautomer fluorescence ratio decreases for HPIP-b in presence of Zn^{2+} ion and for HPIP-c in presence of Mg^{2+} and Zn^{2+} ions. This indicates that these metal ions bind with the fluorophores through the pyridine nitrogen.

Chapter 5: Photophysical Properties of 2-(2'-Hydroxyphenyl)benzimidazole and its Nitrogen Substituted Analogues in Microheterogeneous Media

Chapter 5 reports the effect of the presence and position of N-heteroatom in benzene ring of HPBI on the photophysical properties in different microheterogeneous environments. The chapter is divided into three sections. The study of photophysical properties of HPBI, HPIP-b and HPIP-c in presence of β-cyclodextrin (β-CD) is presented in the first section. The fluorophores form 1:1 inclusion complexes with β-CD in water as well as dimethylsulphoxide (DMSO). Both pK_a and ^{1}H-NMR experiments indicate that the fluorophores enter the β-CD cavity through benzimidazole/imidazopyridine moiety. The effects of encapsulation by β-CD are much significant in HPIP-b and HPIP-c compared to HPBI. The encapsulation enhances the ESIPT reaction which is reflected by remarkable enhancement in fluorescence of tautomer emission of HPIP-b and HPIP-c though the effect is much less in HPBI. In DMSO, HPBI is present in neutral form, but the nitrogen substituted analogues are present both in neutral and monoanionic forms. However, upon encapsulation by β-CD all three molecules are present in both neutral and monoanionic forms in the nanocavity. The monoanion is stabilized more inside the β-CD cavity. The studies revealed that the ESIPT of nitrogen substituted analogues is more susceptible to environment than HPBI and therefore are more promising probes.

The second section discusses the ESIPT behavior of all three fluorophores in AOT reverse micelle. The tautomer to normal band ratio of these fluorophores decrease with increasing value of $w_o = [H_2O]/[AOT]$. The decrease in the ratio is 5 times in HPBI from w_o =

0 to 30. In addition a blue shift is observed in the tautomer band of HPBI with increasing volume of water quantity in reverse micelle. However, there are no shift in the tautomer bands of HPIP-b and HPIP-c and the decrease in ratio is ~2.4 and 3.2 times, respectively. The results show that initially these molecules preferentially reside in the interfacial region between the oil and water surface. Upon increase in w_0, the molecules drift away toward the bulk of the nanopool and the formation of solvated open enol conformer is favored. The decrease in tautomer to normal emission ratio is due to (i) nonradiative de-excitation of the tautomer by torsion rotation, (ii) shifting of *cis*-enol to *trans*-enol equilibrium toward *trans*-enol and (iii) formation of solvated open enol conformer.

The third section deals with interactions of the fluorophores with bovine serum albumin (BSA). HPBI and HPIP-c bind in the hydrophobic site of BSA which is indicated by the red shift of the tautomer band in presence of BSA, but HPIP-b binds in the hydrophilic site of BSA. The fluorescence of both normal and tautomer bands increase upon increase in concentration of BSA. With increase in concentration of BSA, the intensity ratios of normal to tautomer bands of HPBI and HPIP-b decrease, whereas that of HPIP-c increases.

Chapter 6: Excited State Intramolecular Proton Transfer and Rotamerism of 2-(2'-Hydroxyphenyl)-3*H*-oxazo[4,5-*b*]pyridine

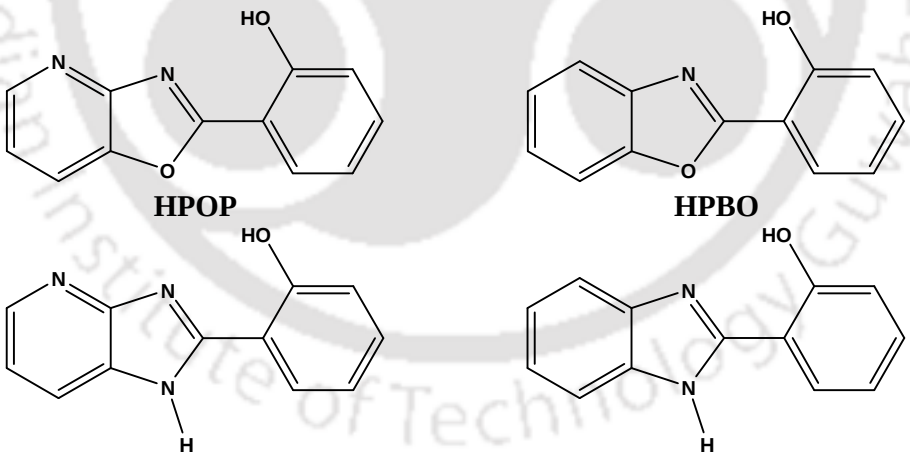

Chart 4. HPOP and its Parent Molecules.

In **Chapter 6**, the photophysical studies carried out in different solvents, pH and temperatures of a newly synthesized molecule, 2-(2'-hydroxyphenyl)-3*H*-oxazo[4,5-*b*]pyridine (HPOP) are reported. HPOP is a nitrogen substituted analogue of 2-(2'-hydroxyphenyl)benzoxazole (HPBO) and the structure of HPOP resembles that of HPIP-b' which is the isomeric form of HPIP-b (**Chart 4**).

HPOP also shows dual fluorescence viz. the normal and tautomer emissions due to emission from excited *trans*-enol and tautomer formed by ESIPT, respectively. In dioxane and polar solvents except glycerol, the tautomer form is observed in the ground state. The study shows that nonradiative decay is more efficient in the present molecule as compared to those in HPBO and HPIP-b. The fluorescence of HPOP decreases with increase in temperature except the normal emission in acetonitrile. This indicates the efficiency of the nonradiative deactivation increases with temperature. pH titration of HPOP shows the existence of equilibrium between neutral-monoanion.

				Page
Acknowledgements				ix
Synopsis				xi
List of Abbreviations				xxi
List of Tables				xxiii
List of Charts				xxv
List of Schemes				xxvi
List of Figures				xxviii
Chapter 1: Introduction				1
1.	1.	0.	Excited State Proton Transfer	2
		1.	Intrinsic Intramolecular Proton Transfer	2
		2.	Concerted Biprotonic Transfer	4
		3.	Proton Relay Tautomerization	8
1.	2.	0.	Excited State Intramolecular Proton Transfer	9
1.	2.	1.	Factors Affecting ESIPT	11
		1.	Effect of Intermolecular Hydrogen Bond	12
		2.	Effect of Substitution	13
1.	2.	2.	ESIPT and Charge Transfer	18
1.	2.	3.	Applications of ESIPT	21
		1.	Four Level Chemical Laser	22
		2.	Optoelectronic Devices	22
		3.	Molecular Switches	24
		4.	Photostabilizers	25
		5.	Fluorescent Probes	25
		6.	Fluorescent Sensors	26
1.	3.		Scope of the Present Work	30
Chapter 2: Materials, Methods and Intrumentations				31
2.	0.		Introduction	33
2.	1.	0.	Materials	33
		1.	Solvents	33
		2.	Metal Salts	33
		3.	Other Chemicals	34
		4.	Syntheses of 2-(2'-Hydroxyphenyl)benzimidazole, 2-(2'-Hydroxyphenyl)-3*H*-imidazo[4,5-*b*]pyridine and 2-(2'-Hydroxyphenyl)-3*H*-imidazo[4,5-*c*]pyridine	34
		5.	Synthesis of 2-(2'-Hydroxyphenyl)-3*H*-oxazo[4,5-*b*]pyridine	36
2.	2.	0	Preparation of Samples	37
		1.	In Solvents	37
		2.	Metal Solutions	38
		3.	Reverse Micelle	38
		4.	Protein Samples	38
2.	3.	0.	Methods	38
		1.	Quantum Yield (Φ_f)	38
		2.	Determination of Ionization Constant	39
		3.	Quantum Mechanical Calculations	40
2.	4.	0.	Instruments	43

1. pH Meter 43
2. Absorption Spectrometer 43
3. Steady State Spectrofluorimeter 43
4. Time Resolved Spectrofluorimeter 45
5. Other Instruments 48

Chapter 3: Excited State Intramolecular Proton Transfer and Rotamerism in 2-(2'-Hydroxyphenyl)benzimidazole and its Nitrogen Substituted Analogues 51

3. 0. Introduction 53
3 1. 0. Nitrogen Substitution in the Benzene Ring of HPBI 53
1. Molecular Geometries and Energies 54
2. Proton Transfer 59
3. Torsion Rotation of Keto Tautomer 62
4. Conclusion 66
3. 2. 0. Nitrogen Substitution in the Phenolic Ring of HPBI 66
1. Rotamers and Tautomers 66
2. Intramolecular Proton Transfer 71
3. Intermolecular Proton Transfer in 2',3'-HPyBI 75
4. Torsion Rotation of Keto Tautomer 76
5. Conclusion 79
3. 3. 0. Effect of Temperature on the Photophysics of HPBI, HPIP-b and HPIP-c 79
1. Population Ratio of Enol Conformers 80
2. Absorption Spectra 82
3. Fluorescence Emission Spectra 83
4. Fluorescence Quantum Yield 87
5. Fluorescence Excitation Spectra 89
6. Time Resolved Fluorescence 92
7. Conclusion 96

Chapter 4: Study of Fluorescence Sensing Ability of 2-(2'-Hydroxyphenyl) benzimidazole and its Nitrogen Substituted Analogues Toward Metal Ions 97

4. 0. Introduction 99
1. Absorption Spectra 100
1. Alkali and Alkaline Metal Ions 100
2. Ni^{2+}, Cu^{2+} and Zn^{2+} Metal Ions 102
4. 2. Fluorescence Spectra 105
1. Alkali and Alkaline Metal Ions 105
2. Ni^{2+}, Cu^{2+} and Zn^{2+} Metal Ions 107
4. 3. Fluorescence Intensity Ratio 114
4. 4. Metal Complexes 116
4. 5. Conclusion 118

Chapter 5: Photophysical Properties of 2-(2'-Hydroxyphenyl)benzimidazole and its Nitrogen Substituted Analogues in Microheterogeneous Media 119

5. 0. Introduction 121
5. 1. 0. HPBI, HPIP-b and HPIP-c in β-Cyclodextrin 123
1. Absorption Spectra 124
2. Fluorescence Emission Spectra 126
3. Binding Constants 135

		4.	pH Titration	136
		5.	Orientations of the Guests in Inclusion Complex and NMR Studies	138
		6.	Conclusion	141
5.	2.	0.	Effect of AOT Reverse Micelle	141
		1.	Solubility and Absorption Spectra	142
		2.	Fluorescence Emission Spectra	144
		3.	Fluorescence Excitation Spectra	147
		4.	Fluorescence Lifetime	151
		5.	Conclusion	154
5.	3.	0.	Effect of Bovine Serum Albumin	154
		1.	Absorption Spectra	155
		2.	Fluorescence Spectra	156
		3.	Binding Constants	163
		4.	Conclusion	164

Chapter 6: Excited State Intramolecular Proton Transfer and Rotamerism in 2-(2'-Hydroxyphenyl)-3*H*-oxazo[4,5-*b*]pyridine 165

6.	0.		Introduction	167
6.	1.	0.	Effect of Solvents	168
		1.	Absorption Spectra	168
		2.	Fluorescence Emission Spectra	169
		3.	Fluorescence Excitation Spectra	171
		4.	Binary Solvent Mixtures	173
		5.	Ground State Tautomer	176
		6.	Time Resolved Fluorescence Measurements	177
6.	2.	0.	Effect of Temperature	179
		1.	Absorption and Emission Spectra	179
		2.	Quantum Yield	182
		3.	Fluorescence Excitation Spectra	184
6.	3.	0.	Neutral-Monoanion Equilibrium	187
		1.	Absorption Spectra	188
		2.	Fluorescence Spectra	189
6.	4.		Conclusion	190

Chapter 7: Conclusion and Scope for Future Work 191

7.	1.		Conclusion	193
7.	2.		Scope for Future Work	195

References xxxv

Appendix A1: Assignment of Protons in NMR Spectrum of HPIP-c lvii

Appendix A2: Assignment of Protons in NMR Spectrum of HPIP-b lix

Appendix A3: Assignment of Protons in NMR Spectrum of HPBI lxi

Appendix A4: Parameters for Single Crystal of Ni(HPIP-b)$_2^{2+}$ Complex lxiii

Appendix A5: Determination of Binding Constants for HPBI, HPIP-b and HPIP-c with β-CD lxiv

List of Publications lxv

List of Abbreviations

ADC	Analogue to digital converter
AOT	Aerosol Orange T
AR	Analytical Reagent
BSA	Bovine Serum Albumin
CASSCF	Complete Active Space Self-Consistent Field
CCD	Charged Coupled Device
CD	Cyclodextrin
CIS	Configuration Interaction Singles
DFT	Density functional theory
DMF	*N*,*N*-Dimethylformamide
DMSO	Dimethylsulfoxide
ESIPT	Excited State Intramolecular Proton Transfer
ESPT	Excited State Proton Transfer
FRET	Fluorescence Resonance Energy Transfer
FT	Fourier Transform
FTIR	Fourier Transform Infrared
FWHM	Full Width at Half Maximum
HOMO	Highest Occupied Molecular Orbital
HPBI	2-(2'-Hydroxyphenyl)benzimidazole
HPBO	2-(2'-Hydroxyphenyl)benzoxazole
HPBT	2-(2'-Hydroxyphenyl)benzothiazole
HPIP-b	2-(2'-Hydroxyphenyl)-3*H*-imidazo[4,5-*b*]pyridine
HPIP-b'	2-(2'-Hydroxyphenyl)-1*H*-imidazo[4,5-*b*]pyridine
HPIP-c	2-(2'-Hydroxyphenyl)-1*H*-imidazo [4,5-*c*]pyridine
HPIP-c'	2-(2'-Hydroxyphenyl)-3*H*-imidazo [4,5-*c*]pyridine
HPOP	2-(2'-Hydroxyphenyl)-3*H*-oxazo[4,5-*b*]pyridine
HPO	2-(2'-Hydroxyphenyl)oxazole
HPT	2-(2'-Hydroxyphenyl)thiazole
HPP	8-(2'-Hydroxyphenyl)-9*H*-purine
HPP'	8-(2'-Hydroxyphenyl)-7*H*-purine
2',3'-HPyBI	2-(2'-Hydroxy-3'-pyridyl)benzimidazole
3',2'-HPyBI	2-(3'-Hydroxy-2'-pyridyl)benzimidazole
3',4'-HPyBI	2-(3'-Hydroxy-4'-pyridyl)benzimidazole
4',3'-HPyBI	2-(4'-Hydroxy-3'-pyridyl)benzimidazole
5',4'-HPymBI	2-(5'-Hydroxy-4'-pyrimidinyl)benzimidazole
ICT	Intramolecular Charge Transfer
IEF-PCM	Integral Equation Formalism-Polarizable Continuum Model

IPT	Intramolecular Proton Transfer
IR	Infrared
LED	Light Emitting Diode
LUMO	Lowest Unoccupied Molecular Orbital
MCP	Micro-Channel Plate
MO	Molecular Orbital
NMR	Nuclear Magnetic Resonance
OLED	Organic Light Emitting Diode
PES	Potential energy surface
PMT	Photomultiplier Tube
PT	Proton Transfer
RTIL	Room temperature ionic liquids
TAC	Time-to-Amplitude Converter
TCSPC	Time Correlated Single Photon Counting
TDDFT	Time Dependent Density Functional Theory
TLC	Thin Layer Chromatography
QY	Quantum Yield
UV	Ultraviolet
UV-Vis	Ultraviolet-Visible
λ_{em}	Monitoring wavelength of emission
λ_{exc}	Wavelength of excitation
μ_g	Ground state dipole moment
μ_e	Excited state dipole moment
Φ_f	Fluorescence quantum yield

List of Tables

Chapter 1:

Table 1.1. Functional groups that act as stronger acids and bases in the excited state.

Chapter 3:

Table 3.1. Relative energies (eV) of different forms of HPIP-b, HPIP-c, HPP and their respective isomers (HPIP-b', HPIP-c', HPP') with respect to their corresponding *cis*-enol forms of HPIP-b, HPIP-c, HPP isomers in the S_0 state.

Table 3.2. Optimized parameters for different enols and keto form of molecules in S_0 and S_1 states. Energy difference between other forms and *cis*-enol form (ΔE, eV), dipole moment (μ, D), interatomic distances (R_{xx}, Å) and charge on nitrogen. For the atom numbering, refer Scheme 3.1. Values in parenthesis are that correspond to S_1 state.

Table 3.3. Calculated excitation and fluorescence spectral data (nm) for different isomers along with corresponding experimental data.

Table 3.4. Energy difference between Keto and *cis*-Enol along the reaction coordinates and barrier for proton transfer reaction (eV).

Table 3.5. Properties of the energy minima and the transition state of tautomer rotamers and the values in parenthesis are that of ab initio calculations.

Table 3.6. Selected bond lengths and angles of the keto tautomers in the optimized S_0 and S_1 states. For the atom numbering, refer Figure 3.4.

Table 3.7. Transition energies for different enols and keto form of molecules in the S_0 and S_1 states in vacuum.

Table 3.8. Properties of the planar and twisted keto tautomers in vacuum.

Table 3.9. Important parameters of 2',3'-HPyBI for the keto forms K-1 and K-2 in the S_0 and S_1 states (Within Parentheses) in vacuum.

Table 3.10. Properties and nature of the transition of tautomer rotamers K-1 and K-2 of 2',3'-HPyBI in vacuum.

Table 3.11. Energy difference and barrier for proton transfer reaction (eV) in vacuum.

Table 3.12. Selected bond lengths and angles of the tautomers in the optimized S_0 and S_1 states (for the atom numbering, refer Figure 3.9).

Table 3.13. Absorption band maxima and Log(ε_{max}) of HPBI, HPIP-b and HPIP-c in different solvents at 293 Kelvin.

Table 3.14. Fluorescence band maxima of HPBI, HPIP-b and HPIP-c in different solvents at different temperatures.
Table 3.15. Lifetime data of HPBI in different solvents at different temperatures.

Table 3.16. Lifetime data of HPIP-b in different solvents at different temperatures.

Table 3.17. Lifetime data of HPIP-c in different solvents at different temperatures.

Chapter 4:

Table 4.1. Absorption maxima (λ_{max}^{abs}, nm) and fluorescence maxima (λ_{max}^{flu}, nm) of ligands and transition metal complexes of the HPBI, HPIP-b and HPIP-c.

Chapter 5:

Table 5.1. Lifetimes of HPBI, HPIP-b and HPIP-c in absence and presence of β-CD (15 mM) in DMSO.

Table 5.2. Fluorescence lifetime of HPBI, HPIP-b and HPIP-c in AOT reverse micelles monitored at normal and tautomer band maxima.

Table 5.3. Fluorescence excitation (λ_{max}^{exc} nm) and emission (λ_{max}^{fl} nm) band maxima of the red shifted band.

Chapter 6:

Table 6.1. UV-Visible absorption band maxima (λ_{max}^{ab}, nm) and molar absorption coefficient in Log ε_{max} of HPOP in different solvents.

Table 6.2. Fluorescence maxima (λ_{flu}, nm) and quantum yields of normal and tautomer emissions of HPOP in different solvents, λ_{exc} = 300 nm.

Table 6.3. Lifetime values for the normal and tautomer bands of HPOP in different solvents.

Table 6.4. Radiative rate (k_r, 10^7 s^{-1}) and nonradiative decay rate (k_{nr}, 10^7 s^{-1}) for the normal and tautomer bands of HPOP in different solvents.

List of Charts

Chapter 3:

Chart 3.1. HPBI and its nitrogen substituted molecules

Chart 3.2. HPBI and nitrogen substituted molecules.

Chart 3.3. Isomeric forms of nitrogen substituted analogues of HPBI.

Chart 3.4. Ground state keto tautomers of 2',3'-HPyBI.

Chart 3.5. *cis*- and *trans*-Tautomers of 2-(2'-Hydroxyphenyl)benzazoles.

Chapter 5:

Chart 5.1. Solvated structures.

Chart 5.2. Solvated open enol conformers.

Chapter 6:

Chart 6.1. Nitrogen Substituted Analogues of HPBI and HPBO.

Chart 6.2. Monoanionic Forms of HPOP and HPIP-b.

List of Schemes

Chapter 1:

Scheme 1.1. Excited-state intramolecular proton transfer.

Scheme 1.2. IPT in 3-hydroxyflavone.

Scheme 1.3. IPT in *o*-hydroxystyrene.

Scheme 1.4. Solvated structures of 7-azaindole.

Scheme 1.5. Proton transfer in dimer of 7-azaindole.

Scheme 1.6. Proton transfer in adenine catalyzed by acetic acid.

Scheme 1.7. Acetic acid catalyzed ESPT in lumichrome.

Scheme 1.8. Pyridine catalyzed proton transfer in lumichrome.

Scheme 1.9. Proton relay tautomerization.

Scheme 1.10. Proton transfer in 2-(hydroxyphenyl)-9*H*-fluorene.

Scheme 1.11. IPT in 3-hydroxyflavone.

Scheme 1.12. Rotameric forms of 2-(2'-hydroxyphenyl)benzazoles.

Scheme 1.13. Salicylic acid and methyl salicylate.

Scheme 1.14. Derivatives of salicyldehyde.

Scheme 1.15. 2-Amino-3-naphthoic acid.

Scheme 1.16. Hydroxybenzo[*h*]quinoline.

Scheme 1.17. 3-Hydroxychromone and 3-hydroxyflavone.

Scheme 1.18. 2-(2'-Hydroxynaphthyl)benzazoles.

Scheme 1.19. 2-(2'-Aminophenyl)benzimidazoles.

Scheme 1.20. *cis* and *trans*-conformers of 2-(2'-aminophenyl)benzimidazole.

Scheme 1.21. 2-(2'-Hydroxyphenyl)benzoxazole.

Scheme 1.22. 2-(2'-Hydroxy-4'-R-phenyl)benzothiazole.

Scheme 1.23. Intramolecular charge transfer induced ESIPT in 3-hydroxyflavones.

Scheme 1.24. Proton coupled charge transfer.

Scheme 1.25. Electron accepting and donating strengths in benzazoles and hydroxypyridines.

Scheme 1.26. 2-(2'-Hydroxyphenyl)benzotriazole.

Scheme 1.27. Derivatives of HPBO.

Scheme 1.28. Tautomerization of 2-(2'-hydroxyphenyl)benzoxazole.

Scheme 1.29. Molecular structures of SOX and DOX.

Scheme 1.30. Molecular logic gate operators based on ESIPT.

Scheme 1.31. ESIPT based UV stabilizers.

Scheme 1.32. 4-Hydroxy-5-azaphenanthrene.

Scheme 1.33. 2-(2-Furyl)-3-hydroxychromone.

Scheme 1.34. 4'-Dimethylamino-3-hydroxyflavone.

Scheme 1.35. Schiff base as chemosensor for Mg^{2+}.

Scheme 1.36. Chemosensors for detection of Na^{+} and Ca^{2+} ions.

Scheme 1.37. Inhibition of ESIPT in 2-(2'-phenylureaphenyl)benzoxazole in presence of fluoride ion.

Scheme 1.38. Inhibition of ESIPT by fluoride ion.

Chapter 2:

Scheme 2.1. Synthetic procedure for HPBI, HPIP-b and HPIP-c.

Scheme 2.2. Synthetic Procedure for HPOP.

Chapter 3:

Scheme 3.1. Interconversion of isomeric forms of nitrogen substituted analogues of HPBI.

Scheme 3.2. Kinetics schemes for the decay of *trans*-enol and ESIPT process in nitrogen substituted HPBI analogues.

List of Figures

Chapter 1:

Figure 1.1. Schematic diagram of vibronic transitions involving double minimum potential energy curves due to proton transfer.

Figure 1.2. ESIPT Process.

Chapter 2

Figure 2.1. ^{1}H NMR Spectra of HPBI, HPIP-b and HPIP-c in DMSO-d_6.

Figure 2.2. ^{1}H NMR Spectra of HPOP in DMSO-d_6/$CDCl_3$ (1:4 v/v).

Figure 2.3. Flowchart for quantum chemical calculations.

Figure 2.4. Block diagram of FSP 920 steady state fluorescence spectrophotometer from Edinburgh Instruments. Diagram was obtained from the catalogue of Edinburgh instruments FSP 920.

Figure 2.5. Block diagram of a TCSPC instrument.

Figure 2.6. Exponential decay model for three components.

Chapter 3:

Figure 3.1. Plot of molecular energy as a function of torsional angle between hydroxyphenyl plane and heterocylic plane for different molecules in S_0 state.

Figure 3.2. Simulated PES for proton transfer reaction tautomers in the S_1 and S_0 states for different molecules.

Figure 3.3. Simulated PES for torsion rotation of tautomers in the S_1 and S_0 states (a) HPBI, (b) HPIP-b, (c) HPIP-c and (d) HPP (left panel TDDFT calculations and right panel CIS calculations).

Figure 3.4. Optimized structures of (a) *cis*, (b) twisted minimum and (c) *trans* of keto on the excited state surface along with corresponding LUMO and HOMO for HPIP-b.

Figure 3.5. Plot of molecular energy as a function of torsional angle between the two aromatic rings for different molecules.

Figure 3.6. Frontier molecular orbitals of 2',3'-HPyBI and 5',4'-HPymBI involved in the longest wavelength transition. FMOs of the keto form of 5',4'-HPymBI [HOMO-1-LUMO ($n\pi^*$ excited state has lower energy than HOMO-LUMO ($\pi\pi^*$) excited state].

Figure 3.7. Simulated potential energy surfaces for IPT reaction for different molecules.

Figure 3.8. Water molecule assisted proton transfer in 2',3'-HPyBI.

Figure 3.9. Optimized structures of (a) Keto and (b) Twisted tautomer on the excited state surface along with corresponding frontier molecular orbitals for 3',2'-HPyBI.

Figure 3.10. Population ratio of *cis*-enol to *trans*-enol of (a) HPBI, (b) HPIP-b, and (c) HPIP-c in cyclohexane (-■-), dioxane (-●-), acetonitrile (-▲-), methanol (-■-), and ethylene glycol (-♦-) at different temperatures. The inset in each figure is the enlarged plot for acetonitrile, methanol, and ethylene gylcol.

Figure 3.11. Population ratio of *trans*-enol to open enol of (a) HPBI, (b) HPIP-b, and (c) HPIP-c in cyclohexane (-■-), dioxane (-●-), acetonitrile (-▲-), methanol (-■-), and ethylene glycol (-♦-) at different temperatures. The inset in each figure is the enlarged plot for acetonitrile, methanol, and ethylene gylcol.

Figure 3.12. UV-Visible absorption spectra of (a) HPBI in methanol, (b) HPIP-b in acetonitrile, and (c) HPIP-c in dioxane, and (d) HPIP-b in cyclohexane at different temperatures.

Figure 3.13. (a) 3-D Emission spectra of HPIP-c in methanol at room temperature, and (b) its corresponding contour diagram.

Figure 3.14. Emission spectra of HPIP-b in ethylene glycol at different temperatures (λ_{exc} = 310 nm).

Figure 3.15. Emission spectra of HPBI in cyclohexane at different temperatures (λ_{exc} = 310 nm).

Figure 3.16. Emission spectra of HPIP-b in acetonitrile at different temperatures (a) λ_{exc} = 310 nm, and (b) λ_{exc} = 340 nm.

Figure 3.17. Plot of quantum yield of normal band against temperature for (a) HPBI, (b) HPIP-b, and (c) HPIP-c in cyclohexane (purple), dioxane (green), acetonitrile (red), methanol (brown), and ethylene glycol (blue) at different temperatures.

Figure 3.18. Plot of quantum yield of tautomer band against temperature for (a) HPBI, (b) HPIP-b, and (c) HPIP-c in cyclohexane (purple), dioxane (green), acetonitrile (red), methanol (brown), and ethylene glycol (blue) at different temperatures.

Figure 3.19. Quantum yield ratio of normal to tautomer band of (a) HPBI, (b) HPIP-b, and (c) HPIP-c in cyclohexane (purple), dioxane (green), acetonitrile (red), methanol (brown), and ethylene glycol (blue) at different temperatures.

Figure 3.20. Fluorescence excitation spectra of HPBI in 1,4-dioxane at different temperatures (λ_{em} = 480 nm).

Figure 3.21. Fluorescence excitation spectra of (a) HPIP-c in ethylene glycol (λ_{em} = 355 nm), (b) HPIP-b in acetonitrile (λ_{em} = 360 nm), and (c) HPBI in 1,4-dioxane (λ_{em} = 365 nm) at different temperatures.

Figure 3.22. Decay profile of HPIP-b in methanol at different temperatures from 293 K to 333 K with interval of 10 K monitored at the (a) normal band (~ 355 nm), (b) tautomer band (~ 490 nm) and λ_{exc} = 308 nm.

Figure 3.23. Nonradiative decay plots of normal band against temperature for (a) HPBI, (b) HPIP-b, and (c) HPIP-c in cyclohexane (-■-), dioxane (-●-), acetonitrile (-▲-), methanol (-*-), and ethylene glycol (-♦-).

Figure 3.24. Nonradiative decay plots of tautomer band against temperature for (a) HPBI, (b) HPIP-b, and (c) HPIP-c in cyclohexane (-■-), dioxane (-●-), acetonitrile (-▲-), methanol (-*-), and ethylene glycol (-♦-).

Chapter 4:

Figure 4.1. Absorption spectra of HPBI in presence of Na^+.

Figure 4.2. Stepwise change in the absorption spectra of HPIP-b at (a) 0-5.2 μM, (b) 5.2-6.0 μM, (c) 6.0-7.3 μM, and (d) 7.3-9.7 μM of Na^+.

Figure 4.3. Absorption spectra of HPIP-c in presence of Mg^{2+}.

Figure 4.4. UV-Visible spectra of HPIP-b in presence of Zn^{2+}.

Figure 4.5. UV-Visible spectra of HPBI in presence of Cu^{2+} (a) from 0 μM to 13 μM, and (b) ≥ 13 μM.

Figure 4.6. Absorption spectra of HPIP-c in presence of Ni^{2+}.

Figure 4.7. Stepwise change in absorbance of HPIP-b in presence of Ni^{2+} in the range (a) 0 – 4 μM, (b) 4.3 – 8.7 μM, and (c) 8.7 – 130 μM.

Figure 4.8. Fluorescence spectra of HPIP-b in presence of Ca^{2+} (λ_{exc} = 308 nm).

Figure 4.9. Fluorescence spectra of HPBI in presence of Mg^{2+} (λ_{exc} = 300 nm). The inset shows the expanded spectra of normal band region.

Figure 4.10. Fluorescence spectra of HPIP-c in presence of Mg^{2+} (λ_{exc} = 308 nm).

Figure 4.11. Fluorescence spectra of HPBI in presence of Zn^{2+} (λ_{exc} = 300 nm).

Figure 4.12. Fluorescence spectra of HPIP-b in presence of Zn^{2+} (λ_{exc} = 308 nm).

Figure 4.13. Fluorescence spectra of HPIP-c in presence of Zn^{2+} (λ_{exc} = 310 nm).

Figure 4.14. Normalized fluorescence excitation spectra of HPIP-b in presence (solid lines) and absence (dotted lines) of Zn^{2+} (500 μM) monitored at (1) λ_{em} = 350 nm (blue), (2) λ_{em} = 440 nm (red), and (3) λ_{em} = 480 nm (green).

Figure 4.15. Fluorescence spectra of HPBI in presence of (a) 0-13 μM, and (b) above 13 μM of Cu^{2+} (λ_{exc} = 302 nm).

Figure 4.16. Fluorescence spectra of HPIP-b in presence of (a) 0-17 μM, and (b) above 17 μM of Cu^{2+} (λ_{exc} = 308 nm).

Figure 4.17. Fluorescence spectra of HPIP-c in presence of (a) 0-9 μM, and (b) above 9 μM of Cu^{2+} (λ_{exc} = 310 nm).

Figure 4.18. Fluorescence spectra of HPBI in presence of Ni^{2+} (λ_{exc} = 299 nm). Inset shows the enlarged spectra of normal band region.

Figure 4.19. Fluorescence spectra of HPIP-b increasing concentration of Ni^{2+} (λ_{exc} = 306 nm).

Figure 4.20. Fluorescence intensity ratio of normal (351 nm) to tautomer (462 nm) bands of HPBI at different concentration of metal ions.

Figure 4.21. Fluorescence intensity ratio of normal (355 nm) to tautomer (479 nm) bands of HPIP-b at different concentration of metal ions.

Figure 4.22. Fluorescence intensity ratio of normal (342 nm) to tautomer (476 nm) bands of HPIP-c at different concentration of metal ions.

Figure 4.23. Histogram plot of normal to tautomer band ratio at fluorophore to metal concentration ratio of 1:5.

Figure 4.24. Crystal structure of HPIP-b-Ni^{2+} complex.

Chapter 5:

Figure 5.1. Absorption spectra of (a) HPIP-b, and (b) HPIP-c at different concentrations of β-CD in water.

Figure 5.2. Absorption spectra of (a) HPBI, (b) HPIP-b, and (c) HPIP-c in increasing concentration of β-CD in DMSO.

Figure 5.3. Fluorescence spectra of (a) HPIP-b, and (b) HPIP-c at different concentrations of β-CD in water (λ_{exc} = 310 nm). Water Raman band is denoted by *.

Figure 5.4. Plot of quantum yield ratio of tautomer to normal bands of (a) HPIP-b, and (b) HPIP-c against [β-CD] in water (λ_{exc} = 310 nm).

Figure 5.5. Sites of hydrogen bond formation with the imidazopyridyl moiety of (a) HPIP-b, and (b) HPIP-c in β-CD nanocavity.

Figure 5.6. Fluorescence spectra of (a) HPBI, (b) HPIP-b, and (c) HPIP-c in DMSO as a function of [β-CD].

Figure 5.7. Fluorescence excitation spectra of HPBI in DMSO with increasing concentration of β-CD at (a) λ_{em} = 365 nm, (b) λ_{em} = 420 nm, and (c) λ_{em} = 465 nm.

Figure 5.8. Fluorescence excitation spectra of HPIP-b in DMSO with increasing concentration of β-CD at (a) λ_{em} = 365 nm, (b) λ_{em} = 415 nm, and (c) λ_{em} = 485 nm.

Figure 5.9. Fluorescence excitation spectra of HPIP-c in DMSO with increasing concentration of β-CD at (a) λ_{em} = 355 nm, (b) λ_{em} = 430 nm, and (c) λ_{em} = 465 nm.

Figure 5.10. Absorption spectra of (a) HPIP-b, and (b) HPIP-c in 15 mM aqueous β-CD at different pH.

Figure 5.11. Optimized geometry of HPIP-b obtained from DFT calculations.

Figure 5.12. Mode of 1:1 complexation of HPIP-b with β-CD with the heterocyclic imidazopyridine moiety (a) inside, and (b) outside the β-CD nanocavity.

Figure 5.13. ^{1}H NMR spectra of (a) HPBI, (b) HPIP-b, and (c) HPIP-c in the presence (solid line) and absence (dotted line) of β-CD in DMSO-d_6.

Figure 5.14. UV-Visible spectra of (a) HPBI, (b) HPIP-b, and (c) HPIP-c as a function of w_0.

Figure 5.15. Fluorescence emission spectra of (a) HPBI, (b) HPIP-b and (c) HPIP-c as a funtion of w_o, λ_{exc} = 310 nm.

Figure 5.16. Fluorescence emisson ratio of tautomer to normal emissions (solid curve) for HPBI, HPIP-b and HPIP-c excited at 310 nm as a function of w_o values. The dotted curves represent the normal to tautomer emission ratio.

Figure 5.17. Fluorescence excitation spectra of HPBI monitored at the (a) normal (λ_{em} = 365 nm), and (b) tautomer (λ_{em} = 465 nm) bands.

Figure 5.18. Fluorescence excitation spectra of HPIP-b monitored at the (a) normal (λ_{em} = 390 nm), and (b) tautomer (λ_{em} = 495 nm) bands.

Figure 5.19. Fluorescence excitation spectra of HPIP-c monitored at the (a) normal (λ_{em} = 360 nm), and (b) tautomer bands (λ_{em} = 475 nm).

Figure 5.20. Schematic diagram of the photophysical processes of HPBI occurring in AOT reverse micelle.

Figure 5.21. Absorption spectra of (a) HPBI, (b) HPIP-b, and (c) HPIP-c in presence of BSA.

Figure 5.22. Normalized fluorescence spectra of HPBI (A), HPIP-b (B) and HPIP-c (C) at pH ~ 7.1. Water Raman band is denoted by *.

Figure 5.23. Emission Spectra of (a) HPBI, (b) HPIP-b, and (c) HPIP-c in presence of BSA (λ_{exc} = 310 nm).

Figure 5.24. Fluorescence intensity ratio plot of normal to tautomer bands of HPBI (square), HPIP-b (circle) and HPIP-c (triangle) against concentration of BSA.

Figure 5.25. Fluorescence excitation spectra of (a) HPBI, (b) HPIP-b, and (c) HPIP-c monitored at the tautomer bands in presence of BSA.

Figure 5.26. Fluorescence spectra of (a) HPBI (λ_{exc} = 365 nm), (b) HPIP-b (λ_{exc} = 375 nm), and (c) HPIP-c (λ_{exc} = 375 nm) in presence of BSA.

Figure 5.27. Benesi-Hildebrand plot for the HPBI (●), HPIP-b (■), and HPIP-c (▲).

Chapter 6:

Figure 6.1. UV-visible absorption spectra of HPOP in (1) cyclohexane, (2) ethyl acetate, (3) methanol, (4) glycerol, (5) dimethylsulfoxide, and (6) water (pH ~ 7.2).

Figure 6.2. Normalized fluorescence spectra of HPOP excited at 300 nm in (1) cyclohexane, (2) 1,4-dioxane, (3) methanol, (4) acetonitrile, (5) glycerol, and (6) neutral (pH = 6.43). λ_{exc} = 300 nm (λ_{exc} = 315 nm for neutral solution). Water Raman band is denoted by *.

Figure 6.3. Normalized fluorescence spectra of HPOP in acetonitrile (1) λ_{exc} = 290 nm, (2) λ_{exc} = 300 nm, (3) λ_{exc} = 375 nm, and (4) λ_{exc} = 395 nm.

Figure 6.4. Normalized (1) absorbance, and fluorescence excitation spectra of HPOP in cyclohexane monitored at (2) normal (355 nm), and (3) tautomer (517 nm) bands.

Figure 6.5. Normalized fluorescence excitation spectra of HPOP in (1) glycerol, (2) 1,4-dioxane, (3) DMF, (4) DMSO, (5) acetonitrile, (6) methanol, (7) in water (pH ~ 6.43) monitored at the tautomer band, and (8) in water (pH ~12.93) monitored at the monoanion emission.

Figure 6.6. Normalized (1) absorbance and fluorescence excitation spectra of HPOP in DMSO monitored at (2) normal (387 nm), and (3) tautomer (480 nm) band.

Figure 6.7. UV-Visible absorption spectra of HPOP in water/glycerol binary solutions.

Figure 6.8. Fluorescence spectra of HPOP in water/glycerol binary solutions. λ_{exc} = 300 nm.

Figure 6.9. UV-Visible absorption spectra of HPOP in acetonitrile/DMSO binary solutions.

Figure 6.10. Fluorescence spectra of HPOP in acetonitrile/DMSO binary solutions. λ_{exc} = 300 nm.

Figure 6.11. Normalized fluorescence excitation spectra of (1) neutral (λ_{em} = 464 nm), and (2) monoanionic (λ_{em} = 481 nm) forms of HPOP in methanol.

Figure 6.12. Absorption spectra of HPOP in DMSO at different temperatures.

Figure 6.13. Fluorescence spectra of HPOP in acetonitrile at different temperatures, λ_{exc} = 300 nm.

Figure 6.14. Fluorescence spectra of HPOP in DMF at different temperatures, λ_{exc} = 300 nm.

Figure 6.15. Fluorescence spectra of HPOP in DMSO at different temperatures, λ_{exc} = 300 nm.

Figure 6.16. Fluorescence spectra of HPOP in glycerol at different temperatures, λ_{exc} = 300 nm.

Figure 6.17. Quantum yield of normal emission of HPOP in acetonitrile (-▲-), DMF (-♦-), DMSO (-■-), and glycerol (-●-) at different temperatures.

Figure 6.18. Quantum yield of tautomer emission of HPOP in acetonitrile (-▲-), DMF (-♦-), DMSO (-■-), and glycerol (-●-) at different temperatures.

Figure 6.19. Quantum yield ratio Φ_N/Φ_T of HPOP in acetonitrile (-▲-), DMF (-♦-), DMSO (-■-), and glycerol (-●-) at different temperatures.

Figure 6.20. Excitation spectra of HPOP in acetonitrile monitored at normal band (385 nm).

Figure 6.21. Excitation spectra of HPOP in DMF monitored at normal band (385 nm).

Figure 6.22. Excitation spectra of HPOP in DMSO monitored at tautomer band (480 nm).

Figure 6.23. Excitation spectra of HPOP in glycerol monitored at tautomer band (500 nm).

Figure 6.24. Intensity ratio of the ground state *cis*-enol and tautomer structures obtained from the excitation spectra recorded at the tautomer emission of HPOP in acetonitrile (triangle), DMF (diamond), and DMSO (square) at different temperatures.

Figure 6.25. UV-Visible absorption spectra of HPOP at from pH = 6.39 to pH 10.51.

Figure 6.26. Fluorescence spectra of HPOP (λ_{ex} = 370 nm) in pH range of 6.37 to 12.93. Water Raman band is denoted by *.

Chapter 1

Introduction

1.1.0. Excited State Proton Transfer

Proton transfer (PT) has been ubiquitously found in various chemical and biological reactions.[1-3] As a general rule, electron donating substituents in aromatic molecules become stronger donors in the excited state, while acceptors attract the electrons more strongly in the excited state (**Table 1.1**). In other words, PT can proceed in the excited state when both/either of the acid and/or base groups become stronger acids or bases in the excited state.

Table 1.1. Functional groups that act as stronger acids and bases in the excited state.

Stronger Bases in the Excited State	Stronger Acids in the Excited State
RCOOH, R-$COOH_2^+$, $R_2C{=}OH^+$, R-$SO_3H_2^+$, R-$AsO_3H_3^+$, RNO_2H	R-OH, R-NH_2, R-NH_3^+

One of the important characteristic of PT active molecules is that, depending on the solvent they show dual fluorescence - one band being the normal emission from the local excitation and the other called the keto or tautomer band due to emission from the tautomer structure that is formed after PT occurs which is more strongly Stokes-shifted than normal emission. The normal and tautomer emissions and subsequently their ratio depend heavily on the solvents[4,5] and the pH of the medium.[6-8]

Based on the PT mechanism, Michael Kasha[9] distinguished the phenomena of the excited state proton transfer (ESPT) into intrinsic intramolecular proton transfer (IPT), concerted biprotonic transfer and proton relay transfer. However, a particular molecule can exhibit more than one class of behavior depending on whether it acts individually or concerted with other molecules. Strictly speaking, only the intrinsic process is an intramolecular process is popularly called as excited state intramolecular proton transfer (ESIPT) and others are varieties of intermolecular proton transfer within microsolvent clusters.

1.1.1. Intrinsic Intramolecular Proton Transfer

ESIPT occurs in molecules containing both acidic and basic groups in close proximity forming an intramolecular hydrogen bonded cyclic ring where a covalently attached proton of the acid, typically of hydroxyl or amino group, migrates in the electronically excited state to a neighboring hydrogen bonded atom (base) less than 2 Å away to give phototautomer products. ESIPT is the very fast process of the order of femtosecond/picosecond[10,11-13] time scale. The phototautomer formed decays to the ground state in a radiative or non-radiative

manner, then the tautomer returns back to the original structure by reverse proton transfer thereby completing a cyclic four-level scheme as shown in **Scheme 1.1**.

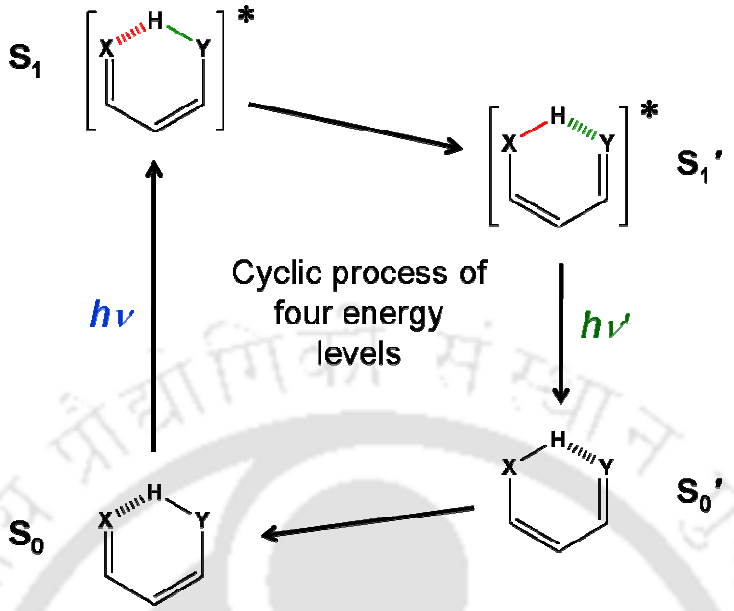

Scheme 1.1. Excited state intramolecular proton transfer.

In 3-hydroxyflavone, $\pi \rightarrow \pi^*$ is the lowest excited state. There is an increase in bond order of the phenyl ring linkage to the chromone moiety; this implies that the phenyl ring nearly planar to chromone in the excited state. There is no viscosity barrier to 3-hydroxyflavone on the $S_1 \rightarrow S_1'$ reaction coordinate and only green fluorescence due to the tautomer S_1' is observed in dry hydrocarbon solvents (**Scheme 1.2**).[13,14]

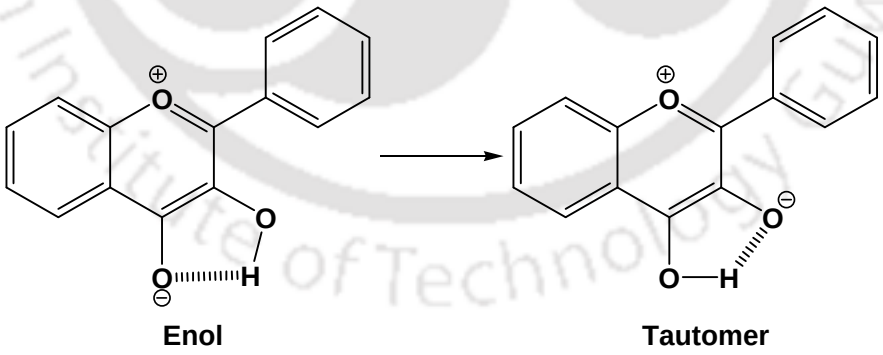

Scheme 1.2. IPT in 3-hydroxyflavone.

ESIPT from phenol OH to sp^2-carbon atoms of aromatic ring has also been observed. For example, the photolysis of *o*-hydroxystyrene in aqueous acetonitrile gave the hydration product via *o*-quinone methide (**Scheme 1.3**).[15,16] The primary photochemical event from S_1

is believed to be ESIPT from the phenol to the *β*-carbon of the alkene moiety. Reverse proton transfer is not observed, and instead the proton transferred product is quantitatively hydrolyzed by water to give alcohol.

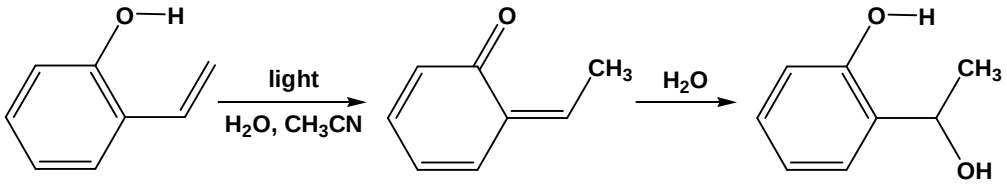

Scheme 1.3. IPT in *o*-hydroxystyrene.

However, molecules featuring intramolecular hydrogen bonds in non-polar solvents may lack such bonds in hydroxylic or protic solvents that are themselves capable of forming hydrogen bonds with the relevant groups of the molecule in question. As a result, ESIPT taking place along with intramolecular hydrogen bonds in nonpolar solvents may have to compete with intermolecular proton transfer to or from the solvent in hydroxylic/protic solvents.

1.1.2. Concerted Biprotonic Transfer

Concerted biprotonic transfer arises because of the large distance between the proton donor and acceptor group in a molecule which is unable to form intramolecular cyclic H-bonded ring. Thus, a molecular companion is needed which usually is a solvent molecule. The phenomenon can be clearly understood from 7-azaindole in alcohol (**Scheme 1.4**).[17-19] However, ethyl ether blocks tautomerization by locking up the pyrolo-H while water eliminates phototautomerization due to separate chain hydrogen bonding to the pyridine-N and pyrolo-NH groups.

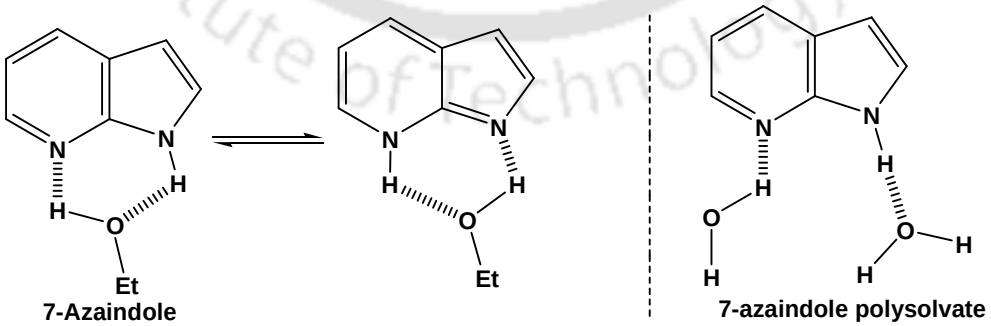

Scheme 1.4. Solvated structures of 7-azaindole.

In hydrocarbons like 3-methylpentane at 20°C, a doubly hydrogen bonded dimer is formed. It undergoes a concerted double proton transfer from the pyrrolo-N to the pyridine-N

within the S_1 state lifetime to give the tautomer dimer (**Scheme 1.5**). Hence, a concentration-dependent green fluorescence due to the tautomer dimer is observed in addition to the normal violet fluorescence.

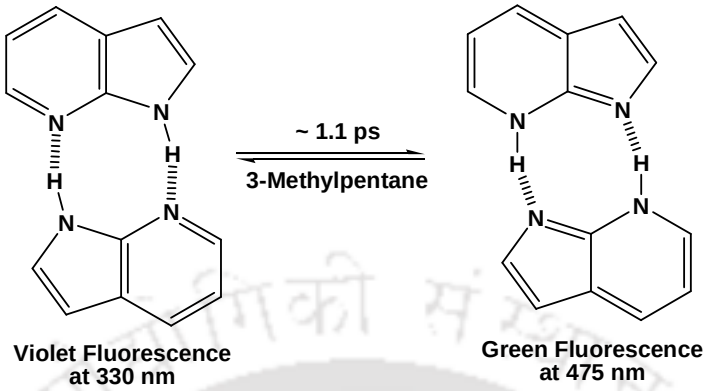

Scheme 1.5. Proton transfer in dimer of 7-azaindole.

Because of the skeletal resemblance of the 7-azaindole with those of purine bases adenine and guanine, this proton transfer in dimer for 7-azaindole has been widely studied for understanding the excimer formation, and the subsequent protonic tautomerization in DNA and polynucleotides due to the radiation.[19]

Solvent can catalyze the reaction either a static or dynamic way:

Static Catalysis

In static catalysis, the solvent molecule acts as a bifunctional acid-base catalyst for PT. The proton donor and acceptor groups of the fluorophore are hydrogen bonded to the acidic and basic moieties of the solvent molecule in such a way to form a cyclic hydrogen bonded ring structure. The concerted biprotonic transfer in a cyclic hydrogen bonded dimer, like the one case as in 7-azaindole dimer already discussed, can be considered as an example of static catalysis.

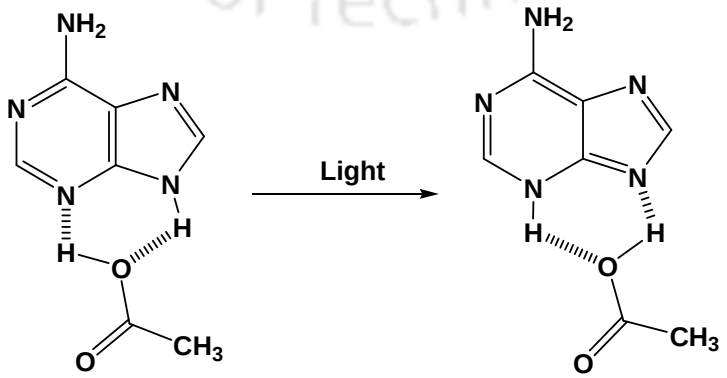

Scheme 1.6. Proton transfer in adenine catalyzed by acetic acid.

Adenine in hydrocarbon solution has absorption at 310 nm, in presence of acetic acid it fluoresces at 380 nm due to tautomer formation in the excited state. The use of acetic acid as a proton transfer agent is a simple case of static catalysis of concerted biprotonic transfer (**Scheme 1.6**).[9]

The multifunctional molecule lumichrome (7,8-dimethylalloxazine) which has several proton donor and proton acceptor sites also belongs to this category. In acetic acid, lumichrome undergoes ESPT to give flavin tautomer (**Scheme 1.7**).[20,21]

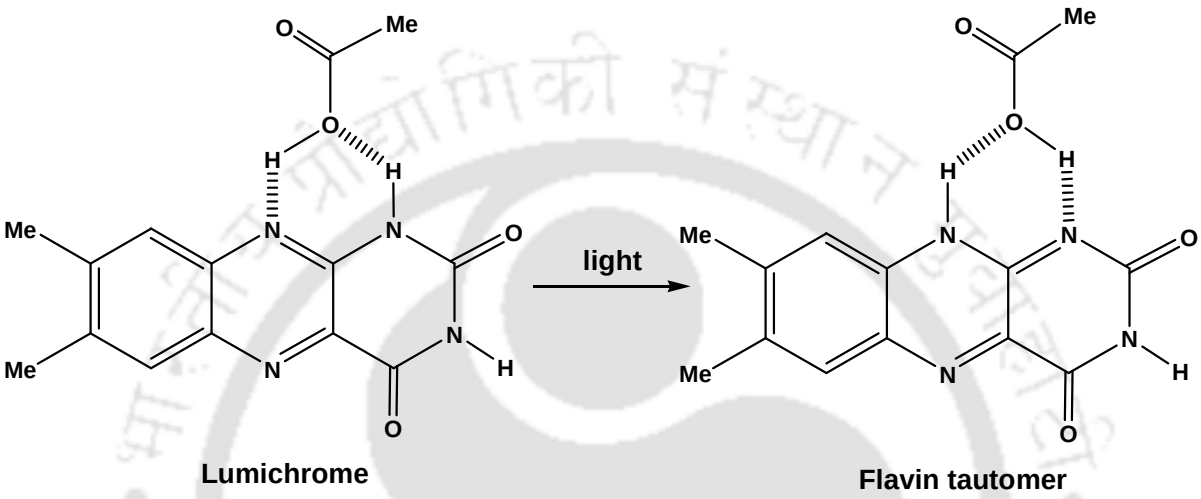

Scheme 1.7. Acetic acid catalyzed ESPT in lumichrome.

Dynamic Catalysis

In dynamic catalysis, the solvent molecule behaves as a general base catalyst for the PT. After accepting a proton from the proton donor site of the fluorophore the solvent molecule undergoes rotational relaxation to reorient itself so that it can donate the abstracted proton to the accepting site of the fluorophore. Dynamic catalysis of phototautomerism by pyridine in lumichrome is observed.[9,20,21] A ground state hydrogen bonded complex of pyridine with lumichrome on excitation forms an ion pair intermediate. On excitation, redistribution in the electronic structure of the lumichrome molecule increases the acidity of the N_1 proton in lumichrome, at the same time it increases the basicity of the N_{10} atom. This leads to the release of the N_1 proton to the pyridine molecule to form an ion pair complex. The protonated pyridine undergoes rotational relaxation to the S_1' equilibrium position from where the basic center of lumichrome can accept the proton (**Scheme 1.8**).

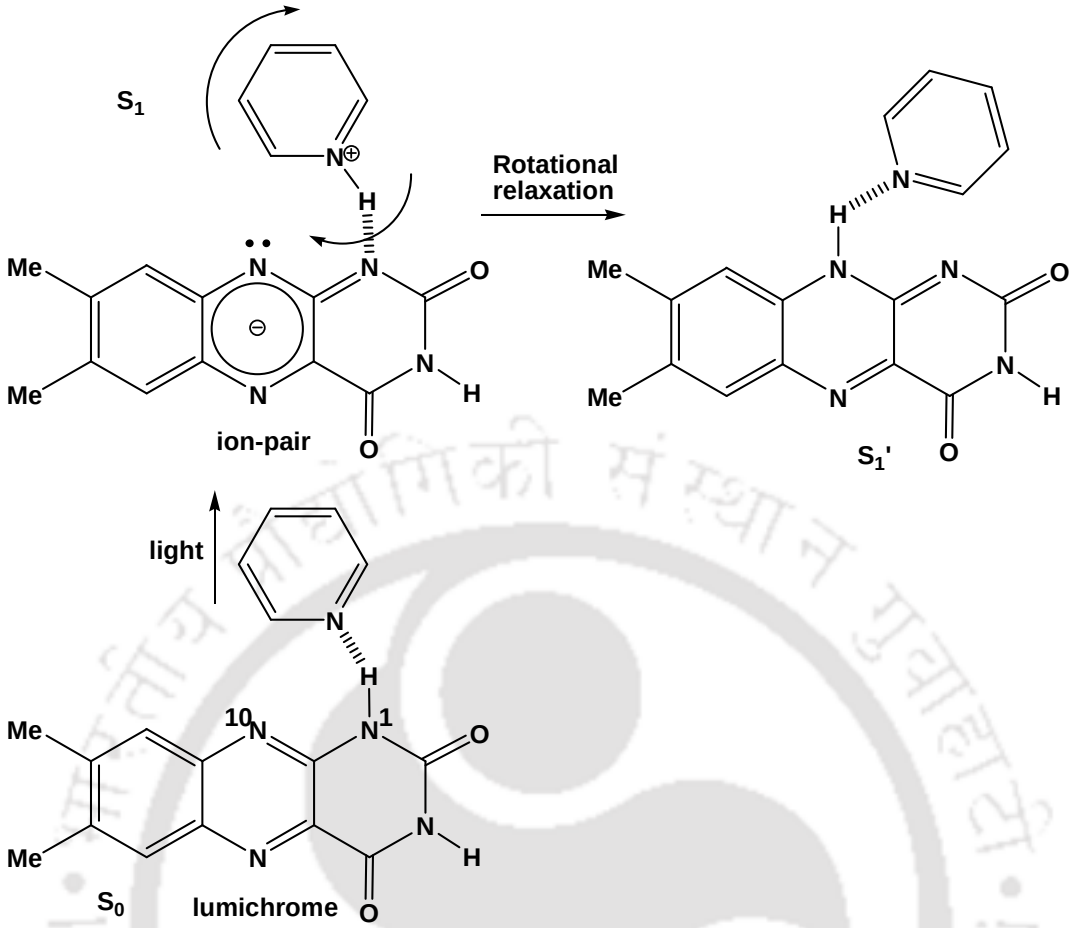

Scheme 1.8. Pyridine catalyzed proton transfer in lumichrome.

1.1.3. Proton Relay Tautomerization

Here, a proton, but not the same from the molecule, is transferred from one part to another part of a molecule through protic solvent molecules acting as bridges joining the donor and acceptor groups by cyclic hydrogen bonds. In fact, we could consider concerted biprotonic tautomerisation as a two-proton relay transfer. Three- and four-relay PTs mediated by methanol and water molecules respectively are shown in **Scheme 1.9**.[22,23]

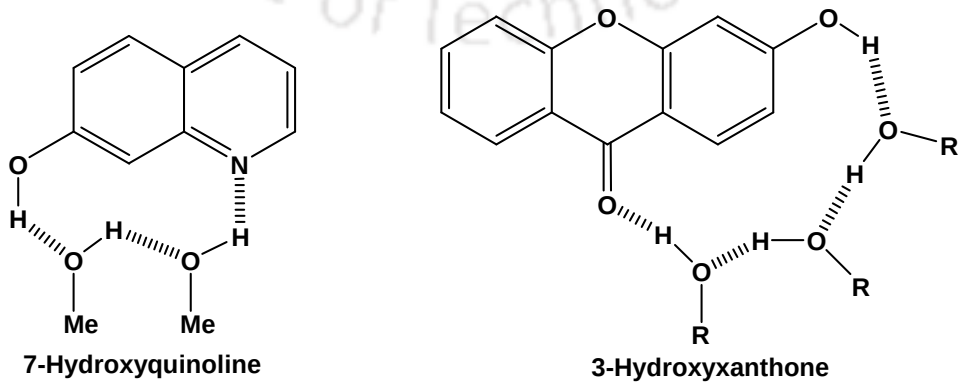

Scheme 1.9. Proton relay tautomerization.

Direct and water-mediated ESPT reactions from phenol OH to sp^2 carbon atom of extended ring are observed in 2-(hydroxyphenyl)-9*H*-fluorene (**Scheme 1.10**).[24] These ESPT reactions require the twisting of the biaryl structures in the ground state for the initial formation of hydrogen bonding interaction between the phenol and the π-system of the adjacent ring. This twisted geometry allows overlap of s-orbital of the acidic OH phenolic proton with the accepting π-system that subsequently facilitates the proton transfer. After PT in the excited state the molecule attains a more co-planar structure.

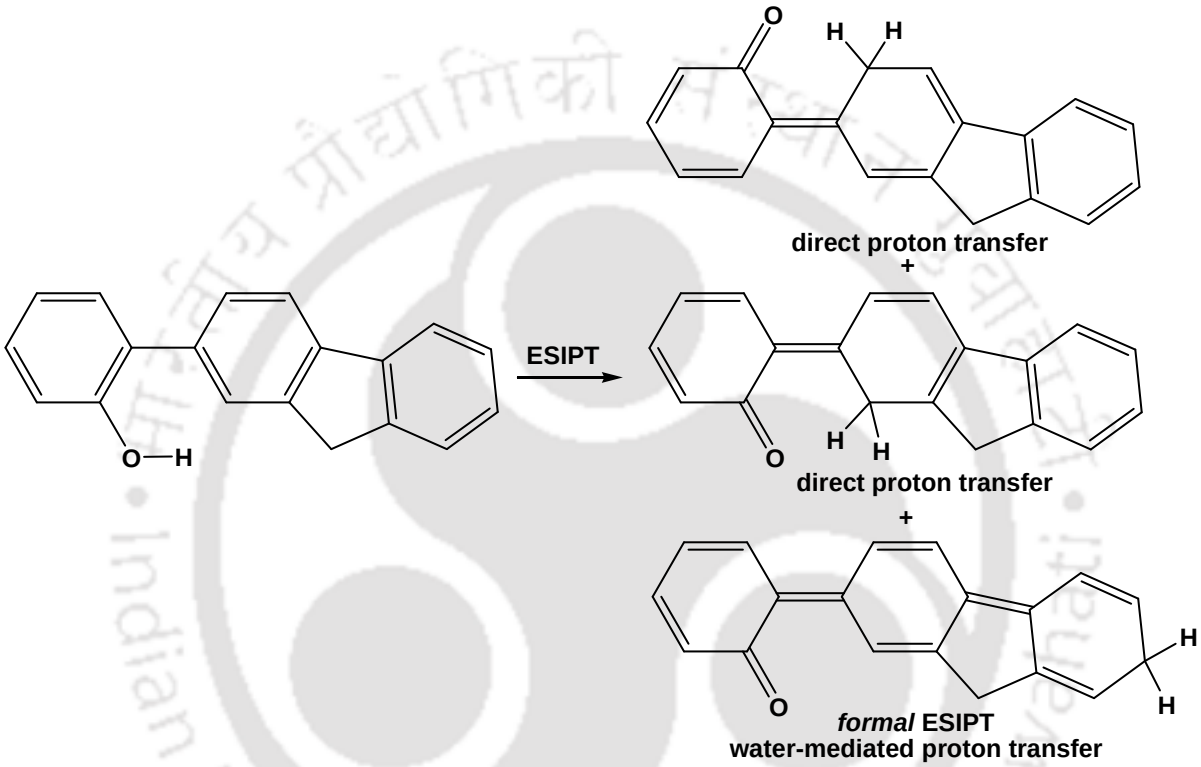

Scheme 1.10. Proton transfer in 2-(hydroxyphenyl)-9*H*-fluorene.

1.2. Excited State Intramolecular Proton Transfer

Among the various types of proton transfer patterns, the category relevant to ESIPT[9,10,25-32] has received much attention by photochemists and photophysicists owing to the simplicity and fundamental importance of its reaction pattern.

Molecules undergoing intramolecular PT exhibit double-minimum potential energy wells along the reaction coordinate – one minimum due to the normal structure and the other minimum due to the proton transfer product (**Figure 1.1**). Depending on the geometry and nature of the molecules, the double–minimum potential wells in both ground and excited state may be symmetric curve (where the two minima have the same energy), common asymmetric curve (where the lower minima in both the ground and excited state correspond to the same

structure) and the third possibility is the reversed asymmetry (where the lower minimum in the ground state become the upper minimum in the excited state).[33]

In **Figure 1.1**, O^+ and O^- are the vibrationless levels, the origin of these can be pictured as firstly the instantaneous movement of the proton with respect to the heavy atoms and then relaxation of these atoms into their new equilibrium positions.[33] By symmetry, O_+^+ and O_-^- are allowed vibronic transitions; the latter is the hot band. These transitions of the left and right oxygen atoms cannot be distinguished. In the case of common asymmetry, the allowed transitions become O_o^o (analogous to O_+^+) and T_o^1 (analogous to O_+ ', i.e. $O^+ \rightarrow O^-$).

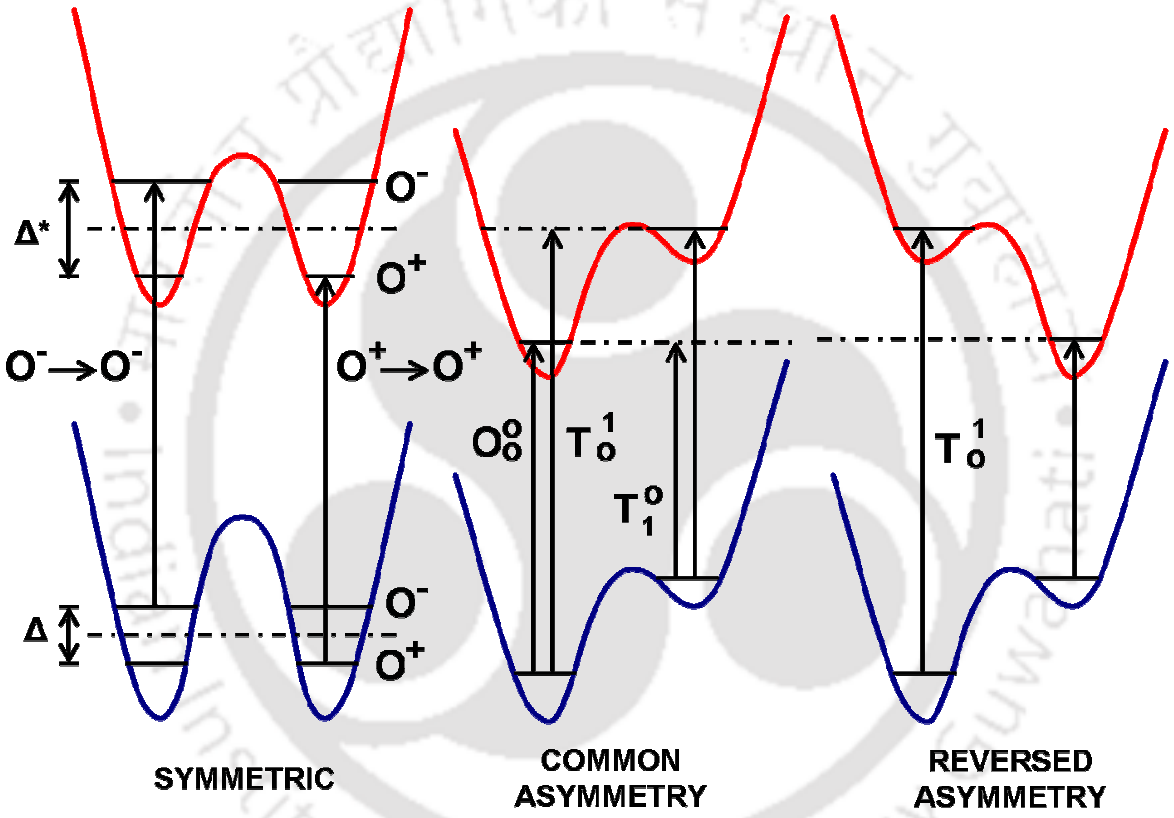

Figure 1.1. Schematic diagram of vibronic transitions involving double minimum potential energy curves due to proton transfer.

The reversed asymmetric type of double-minimum potential energy has implications on dual fluorescence of ESIPT exhibiting molecules. Therefore, it is the most investigated among the three. Several molecules such as *o*-hydroxybenzaldehydes,[34-36] methyl salicylate,[37-40] *o*-hydroxyacetophenone,[41] salicylamide,[41] 3-hydroxyflavones,[10,42-49] 2-(2'-hydroxyphenyl)benzazoles and analogues,[50-62] 1,5-dihydroxyanthraquinone,[63-65] exhibit ESIPT.

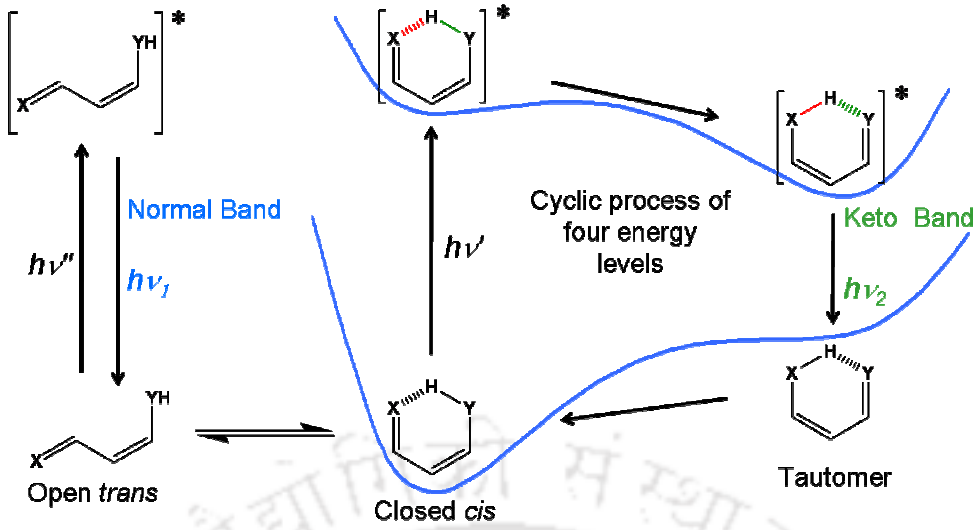

Figure 1.2. ESIPT Process.

The origin of dual fluorescence in ESIPT exhibiting molecules is demonstrated in **Figure 1.2**. ESIPT molecules have cyclic intramolecular hydrogen bonded ring. In aprotic solvents the hydrogen bonded ring is very strong. Upon excitation ESIPT occurs through the intramolecular hydrogen bonded ring to give the proton transferred phototautomer which exhibits highly Stokes shifted tautomer emission. However, protic solvents or other external perturbations such as temperature break the intramolecular hydrogen bond that lead to the open *trans*-structure which is in equilibrium with the closed *cis* form. Excitation of the *trans* form gives the normal emission band.

1.2.1. Factors Affecting ESIPT

PT highly depends on the nature and hydrogen bonding capability of the solvent.[4,5,42,66,67] Since in most of the ESIPT dyes intramolecular hydrogen bond forms a stable cyclic ring ESIPT is generally poorly dependent on viscosity. However, there has been one evidence of the strong effect of viscosity on the rate of ESIPT in polar environments.[68] Studies have also been done on ESIPT in room temperature ionic liquids (RTILS), which are organic salts that are in the liquid phase at room temperature.[69] RTILs possess solvation dynamics in a wide time range, and thus it is of interest to investigate the dynamics and kinetics involved in the proton transfer. The effects of solvent environment within a wide variety of pure and mixed homogeneous and microheterogeneous solvents on ESIPT in different molecules have been studied[68,70-72] and a number of theoretical studies from semi-empirical to density functional theory calculations have also been performed.[34,52-54,73-78] Apart from the environmental factors substitution also affects the ESIPT. The effect of solvent and substitution are briefly discussed here.

1.2.1.1. Effect of Intermolecular Hydrogen Bond

The cyclic intramolecular hydrogen bonded ring is the prerequisite for ESIPT reaction. Therefore, intermolecular hydrogen bonding with solvent molecules is the major factor that hampers the ESIPT reaction.[9,79-81] Therefore, the relative intensities of the normal and proton transferred bands of ESIPT molecules vary depending on the molecular structures and the nature of the environment surrounding the molecules mainly polarity and hydrogen bonding capacity of the solvent molecules.[82] The ratio of the two emissions can range from unity up to the complete disappearance of one of the forms. The ESIPT is more favored in non-polar solvents than in protic or polar solvents.[83,84]

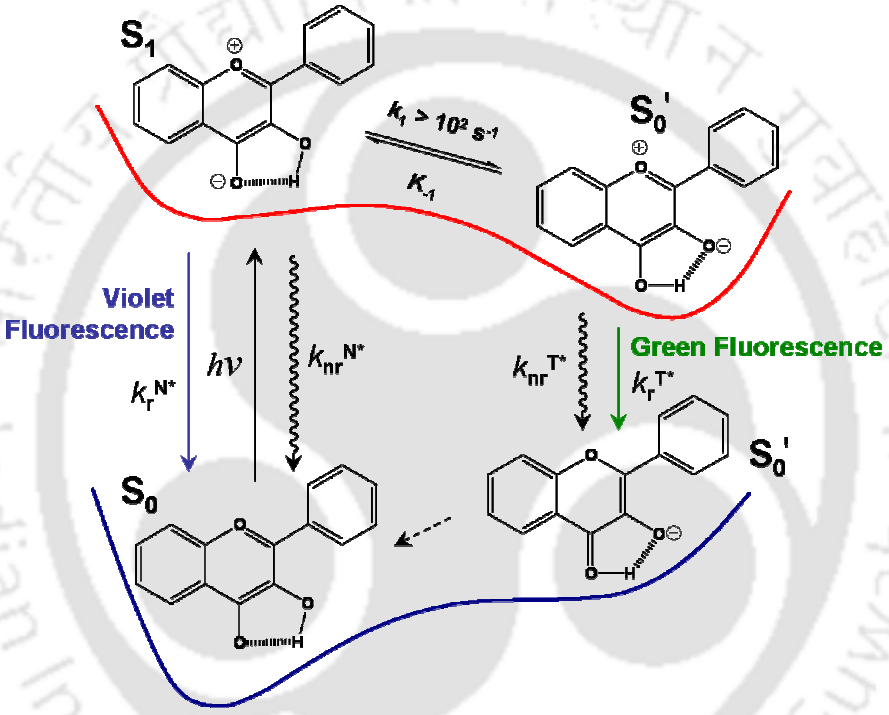

Scheme 1.11. IPT in 3-hydroxyflavone.

In polar or protic solvents like dimethylsulfoxide, methanol and water the cyclic intramolecular hydrogen bond in ESIPT molecules breaks and intermolecular hydrogen bond is formed between the proton donor/acceptor and the solvents molecules. This leads to the formation of solvated enol form resulting in the significant rise of the normal band at the cost of suppressed tautomer band. Such perturbation is greater in molecules with five-membered cyclic intramolecular hydrogen bonded ring structures as in 3-hydroxyflavone due to weak nature of intramolecular hydrogen bond.[9] As discussed in **Section 1.1.1** 3-hydroxyflavone which has ππ* absorption band at 335 nm in non-polar solvent 2-methylbutane exhibits a single emission large Stokes' shifted tautomer band[13,14] However in methanol, in addition to green tautomer band, a violet emission from enol form is observed (**Scheme 1.11**).[85]

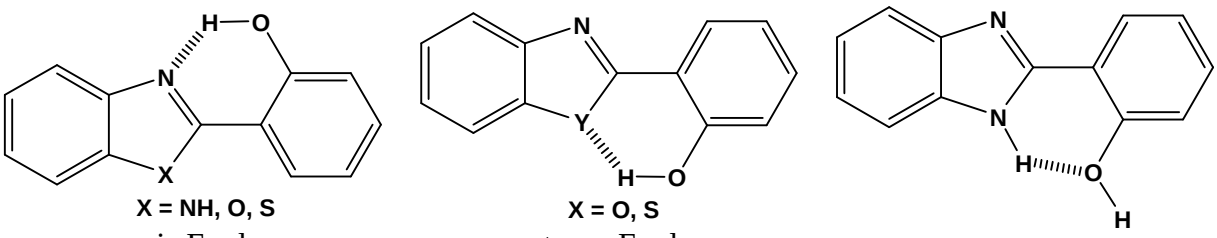

cis-Enol *trans*-Enol *trans*-Enol

Scheme 1.12. Rotameric forms of 2-(2'-hydroxyphenyl)benzazoles.

2-(2'-Hydroxyphenyl)benzazoles exists in two rotameric forms *cis*-enol and *trans*-enol (**Scheme 1.12**). *cis*-Enol forms hydrogen bond between the hydroxyl group and imidazole nitrogen atom and is responsible for ESIPT. *cis*-Enol is more stable than *trans*-enol due to its relatively stronger hydrogen bond. However the effect of protic solvent is less than that of five-membered cyclic intramolecular hydrogen bonded ring structures.

1.2.1.2. Effect of Substitution

Studies show that the fluorescence of ESIPT molecules is affected by substitution in terms of spectra position and quantum yield. Hence, introducing a suitable substituent in a specific position of the molecular framework will result in obtaining a compound with desired properties which can be utilized where ESIPT molecules find applications. Since ESIPT prone molecules find vast applications as laser dyes, probes, sensors, photostabilizers, and molecular devices, it is important to alter molecular structure to get the desired properties. One way is to involve modification of the molecular framework by substituents thus affecting the basicity and/or acidity of the reaction centers. On the other hand substitution within the molecular skeleton can be treated as selective perturbation, and its action can be helpful in elucidation of the reaction mechanisms. A few examples of substitution effects are briefed below:

Salicyl Derivatives

Since the pioneering work on the ESIPT reaction in methyl salicylate by Weller,[86] a vast number of works have been performed on the molecule and its derivatives to study the fundamental aspects and to explore the applications of ESIPT. Substitution of methoxy group at position 5 in salicylic acid and at positions 3 or 4 or 5 in methyl salicylate results in large Stokes shift of the phototautomer

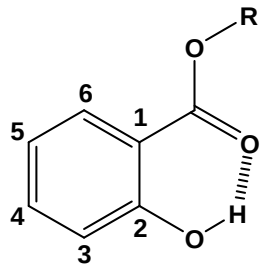

Scheme 1.13. Salicylic acid and methyl salicylate.

emission in nonpolar solvents (**Scheme 1.13**).[86,87] Further, substitution at position 5 also causes a decrease in the intensity of the phototautomer emission with an increase in the intensity of the fluorescence from the primary form.

The effect of methyl and methoxy substitution on the fluorescence of salicylic acid at position 5 has also been studied in supersonic molecular beams.[88] The phototautomer emission of methyl substituted compound is strongly red shifted as high as 10,000 cm^{-1}. However, for methoxy substituted compound the fluorescence is red-shifted only 3000 cm^{-1} indicating the ESIPT reaction is suppressed which is due to the electron donating effect of the methoxy group at the *para* position to the hydroxy group.

The effect of substitution on ESIPT in salicyldehyde and its derivatives was also studied (**Scheme 1.14**).[89] Replacing R and R' by electron withdrawing group decreases the quantum yield of the phototautomer compared to the parent molecule. But substitution with an electron donating group increases the quantum yield.

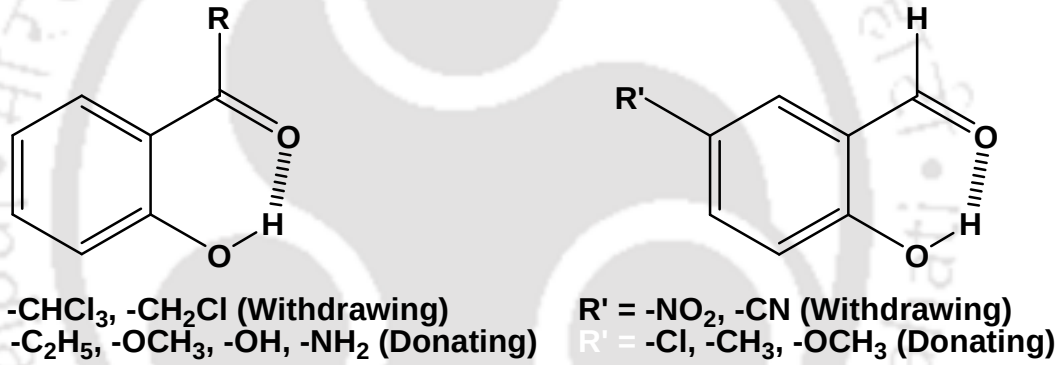

R = -CF_3, -$CHCl_3$, -CH_2Cl (Withdrawing)
-CH_3, -C_2H_5, -OCH_3, -OH, -NH_2 (Donating)

R' = -NO_2, -CN (Withdrawing)
R' = -Cl, -CH_3, -OCH_3 (Donating)

Scheme 1.14. Derivatives of salicyldehyde.

2-Amino-3-naphthoic acid and its methyl ester (**Scheme 1.15**) also show excited state prototropism similar to those of salicylates.[90] The conformer I undergoes ESIPT to give the tautomer emission while the conformer II gives the normal emission. The conformer II exists as a closed ring structure in non-polar solvent and an open structure in protic solvents.

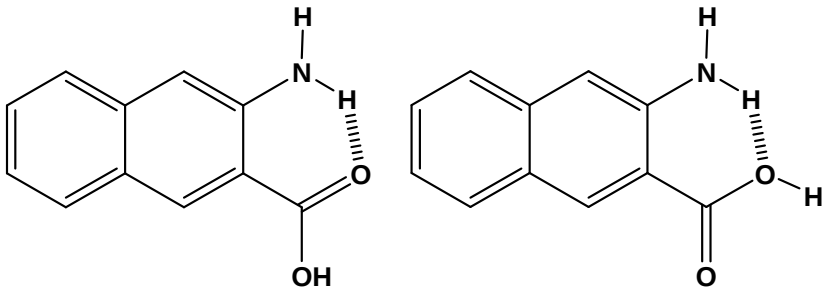

Conformer I **Conformer II**

Scheme 1.15. 2-Amino-3-naphthoic acid.

Hydroxybenzo[*h*]quinoline

Spectral tuning is also displayed by derivatives of 10-hydroxybenzo[*h*]quinoline with different electron donating and accepting substituents (**Scheme 1.16**).[12] The frontier molecular orbitals of the enol form are delocalized over the whole molecule. However, in the PT keto form the highest occupied molecular orbital (HOMO) is localized at the cyclohexa-2,4-dienone (Part A) and the lowest unoccupied molecular orbital (LUMO) at pyridine (Part B). Therefore, substituting electron withdrawing group at Part A moiety decreases the energy of HOMO while an electron donating group in Part B raises the LUMO both of which result in increase in transition energy of the keto form. Substituting an electron donating group to Part A decreases the transition energy of the keto form.

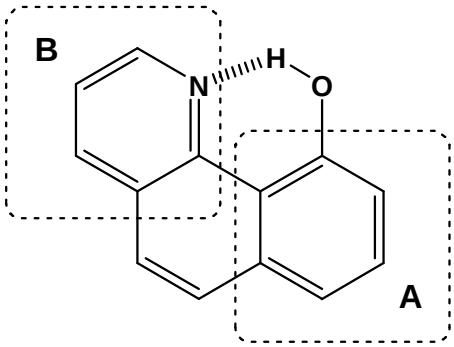

Scheme 1.16. Hydroxybenzo[*h*]quinoline.

Chromones and Flavones

Klymchenko et al. have shown that modulation of solvent dependent dual emission and sensing properties of 3-hydroxychromones can be obtained by the proper choice of subsitutents on the 3-hydroxychromone framework (**Scheme 1.17)**.[91] The ESIPT rate of 3-hydroxyflavone, the phenyl ring substituted derivative of 3-hydroxychromone at position 2, is slowed down compared to that of the parent molecule.[92] The *ortho* aryl substitution to hydroxyl group enhances the electron donating ability thus lowering the transfer ability of hydrogen atom. When the phenyl ring is replaced by the bigger naphthyl ring, the rate decreases further.

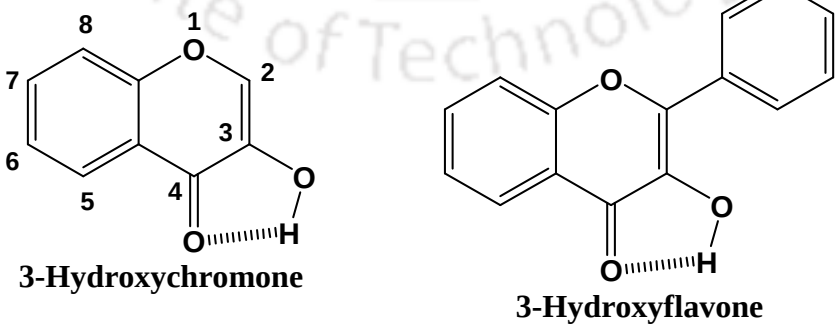

3-Hydroxychromone **3-Hydroxyflavone**

Scheme 1.17. 3-Hydroxychromone and 3-hydroxyflavone.

3-Hydroxyflavone displays laser action.[9,42] However, in 2-methyl-3-hydroxychromone the lasing activity cannot be achieved.[93] The authors explained this

observation in terms of fluorescence quenching due to molecular aggregation and transient parasitic absorption of the phototautomeric species. Besides, in flavonols (such as quercetin, and 3,5,7,3',4'-OH flavone), where 5-OH and 3-OH groups are simultaneously present, the hydrogen bond between the carbonyl oxygen and hydroxyl group of C-5 position interferes with that of carbonyl oxygen and hydroxyl group of C-3 position.[94] This prevents the ESIPT and consequently lowers the fluorescence quantum yield.

Azoles and Benzazoles

2-(2'-Hydroxyphenyl)benzimidazole (HPBI) exhibits single largely Stokes shifted tautomer emission in nonpolar hydrocarbons and dual emission consisting of normal and tautomer emissions in protic solvents.[95] But its analogues 2-(2'-hydroxyphenyl)benzoxazole (HPBO) and 2-(2'-hydroxyphenyl)benzthiazole (HPBT) emit dual emission even in non-polar hydrocarbons.[67,95-100] The normal emission is due to the *trans*-form (**Scheme 1.12**). Similar behavior is observed in their 2-hydroxynaphthyl derivatives also (**Scheme 1.18**).[101,102]

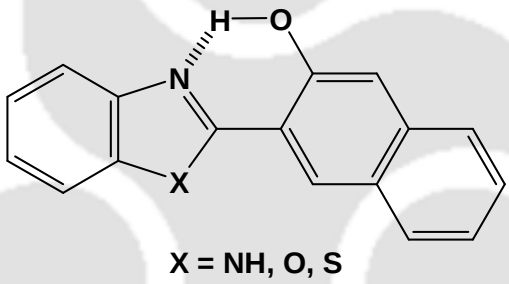

Scheme 1.18. 2-(2'-Hydroxynaphthyl)benzazoles.

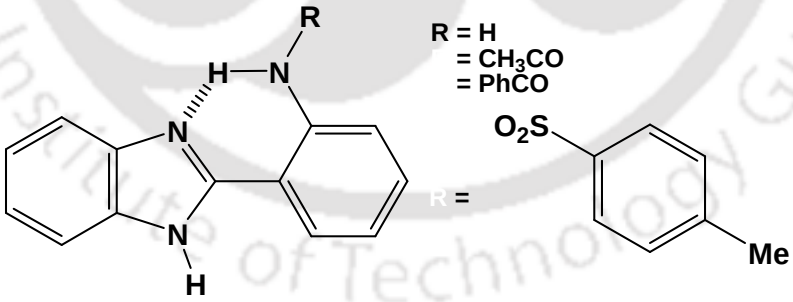

Scheme 1.19. 2-(2'-Aminophenyl)benzimidazoles.

The ESIPT is weakly observed in 2-(2'-aminophenyl)benzimidazole.[103,104] Substitution at the amino group of 2-(2'-aminophenyl)benzimidazole with electron withdrawing group enhances the ESIPT process and increases the quantum yield of the tautomer emission (**Scheme 19**).[55,105,106] The increase in quantum yield of the phototautomer is more in case of tosyl derivative.[55] One probable reason is the absence of *trans*-conformer in tosyl substituted derivative (**Scheme 1.20**). The aryl and benzimidazole moieties are out-

of-plane such that there is π-stacking between the tosylamide and benzimidazole rings. The conversion of *cis*- to *trans*-conformers requires rehybridization of the sulfonamide nitrogen and also result in loss of resonance stabilization energy between the nitrogen lone pair and the sulfone moiety.

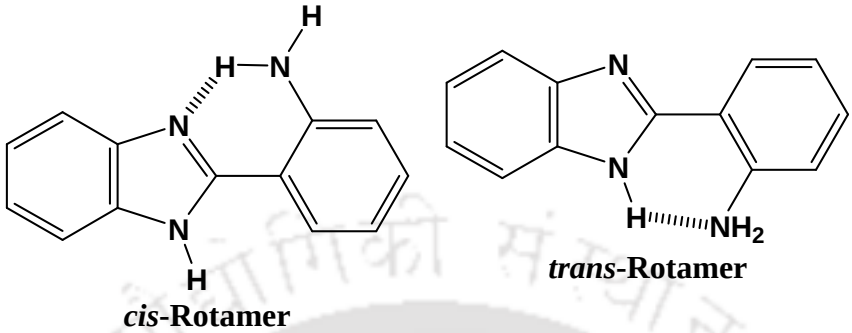

***cis*-Rotamer** ***trans*-Rotamer**

Scheme 1.20. *cis* and *trans*-conformers of 2-(2'-aminophenyl)benzimidazole.

The fluorescence yield of the 3'-methoxy substituted HPBO (**Scheme 1.21**) was found to be lower than that of the parent molecule.[107] However, when the methoxy group is substituted at 4'-position, the spectral characteristics are similar to HPBO. This difference is due to specific interaction between the hydrogen atoms of methoxy group and the phenolic oxygen.

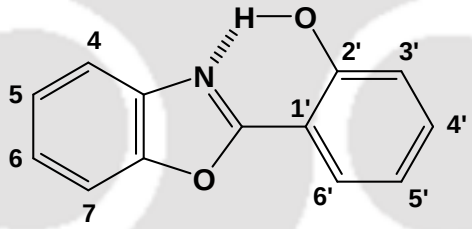

Scheme 1.21. 2-(2'-Hydroxyphenyl)benzoxazole.

Spectral tuning of HPBO was achieved from deep-blue to green by incorporating diethylamino or methoxy groups as electron donor, and aldehyde or ethylester groups as electron acceptor at 4′- and 6-positions of HPBO, respectively (**Scheme 1.21**).[27,108] The mesomeric effects of either electron-donating or accepting substituents decrease the electronic transition energy. The electron donating group raises the HOMO more than the LUMO while the electron accepting group stabilizes the LUMO more than the HOMO. As a result, the absorption maxima of the 4′- and 6-substituted derivatives are red-shifted compared to that of HPBO. The electron accepting substituent at 6-position caused a red-shift in the tautomer band and on the other hand, electron donating substituent at 4′-position resulted in blue shift. The HOMO and LUMO are delocalized over the whole molecule in

both enol and keto form, but the π-electron density at 4'-position of HOMO of keto form is extremely lower than that of enol form. Therefore, the negative inductive effect of donating group lowers the HOMO and caused the blue shift in the tautomer emission.

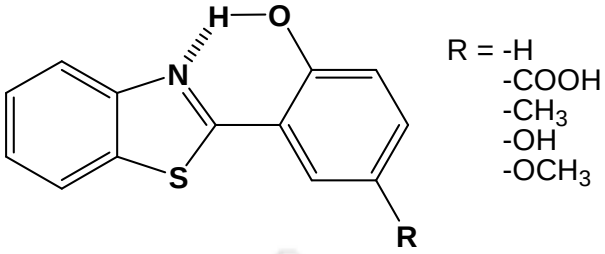

Scheme 1.22. 2-(2'-Hydroxy-4'-R-phenyl)benzothiazole.

The effects of substitution on the spectral change of ESIPT emission of HPBT nanoparticles was studied recently (**Scheme 1.22**).[109] A bathochromic shift is observed upon substitution with electron donating group and a hypsochromic shift is observed upon substitution with electron withdrawing group. The tautomer emission and its lifetime of the aggregated HPBT-R nanoparticles are strongly enhanced compared to those of the HPBT-R monomers. With rise in temperature, the equilibrium between the monomer enols and nanoparticles shifts toward monomer enol forms and thus the relative enol emission is increased.

1.2.2. ESIPT and Charge Transfer

Due to the involvement of large electronic and structural rearrangements during ESIPT reaction, introducing an electron donating or electron withdrawing group to ESIPT molecules may lead to intramolecular charge transfer (ICT) coupled reactions. According to the mechanism of the ICT coupled ESIPT reaction, the ICT could occur prior to or after ESIPT.[110-112] One such example for the former case is observed in 4'-*N*,*N*-diethylamino-3-hydroxyflavone and its analogues which has *N*,*N*-dialkylamino group as an electron donor and the carbonyl oxygen of the parent ESIPT molecule as an electron acceptor.[113-119]

The molecule upon photoexcitation first undergoes excited state ICT in femtosecond time scale after which ESIPT competes with the solvent relaxation process to the equilibrium ICT state (**Scheme 1.23**). After reaching the solvent equilibrium, ESIPT occurs from the ICT state as well. As a result, the molecule exhibits dual emission in polar aprotic solvents. The shorter wavelength emission band due to ICT shows strong positive solvatochromic shift while the longer wavelength emission band due to emission from EISPT product shows solvent polarity independent emission.[120] 7-*N*,*N*-Diethylamino-3-hydroxyflavone, where here

the position of the diethylamine is changed from C(4') to C(7) position, also exhibits dual emission but here a precursor–successor relationship exists between the ICT state and the phototautomer.[121,122] However, when the diethylamine is substituted at both the C(4') and C(7) positions, the fluorophore exhibits predominantly the proton-transfer emission only.[122]

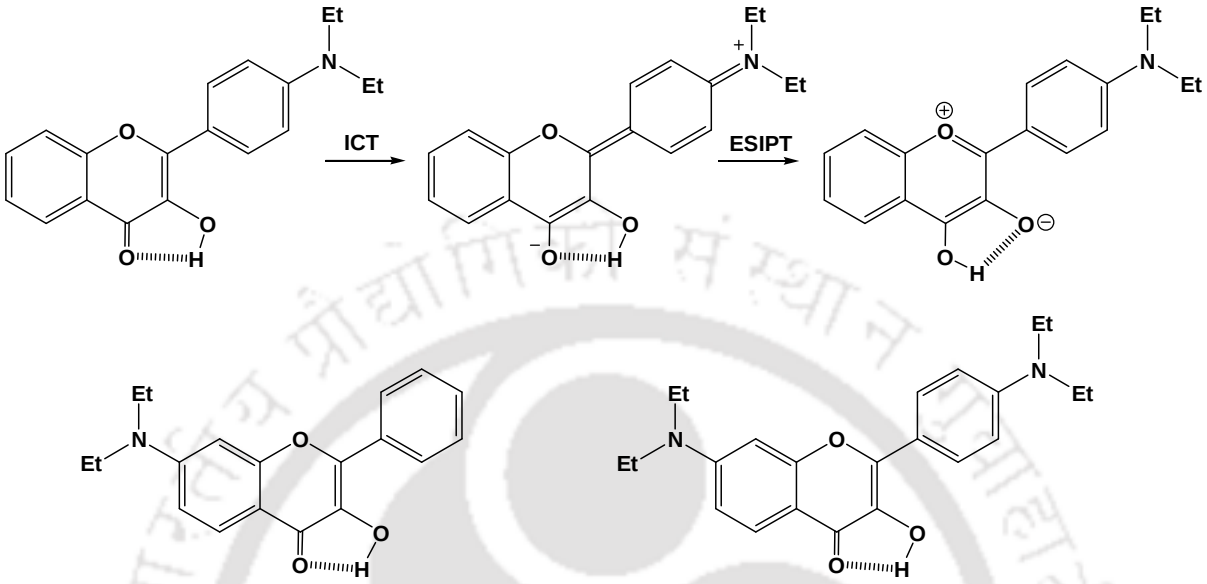

Scheme 1.23. Intramolecular charge transfer induced ESIPT in 3-hydroxyflavones.

In 2'-hydroxyphenylazoles the ICT occurs after ESIPT.[67,50-52,95-100] The ICT is shown to be associated with the conformational change of the ESIPT product by torsion rotation between the two aromatic rings (**Scheme 1.24**).[123] The torsional rotation leads to the formation of a twisted nonfluorescent charge transfer intermediate having a structure with suitable redox pair. The phenyl ring of the molecules is electron rich while the azole ring is electron deficient. The electron-donating and electron accepting strengths of the substituents are shown in **Scheme 1.25**. 2'-Hydroxyphenyloxazole and 2'-hydroxyphenylthiazole are shown to undergo torsion rotation of the tautomer in the first excited singlet state overcoming a small energy barrier to give a twisted tautomer that possesses a biradicaloid nature.[96]

2-Hydroxyarylbenzotriazoles (**Scheme 1.26)** show ICT induced PT.[124,125] Complete active space self consistent field (CASSCF) study of the reaction path for ESIPT of 2-(2'-hydroxyphenyl)triazole predicted that the ESIPT is triggered by the ICT from the phenol to the triazole moiety. The ESIPT reaction results in the phototautomer that decays nonradiatively.[125] The increase of blue fluorescence in 2-(2'-hydroxyphenyl)benzotriazole in strongly polar media was attributed to the formation of a long-lived intermediate of a twisted ICT state. In solution the intramolecular hydrogen bond breaks and the intermolecular hydrogen bond is formed between the hydroxyl group and the solvent molecules.[126,127] This

render the molecule lose its planarity and the nonplanar enol emits luminescent from its excited state. Substitution by methyl and *t*-butyl groups at 3'-positon of 2-(2'-hydroxyphenyl)benzotriazole hinders the rotation of hydroxyl group and thus strengthen the intramolecular hydrogen bond which favors the ESIPT reaction.[126,128]

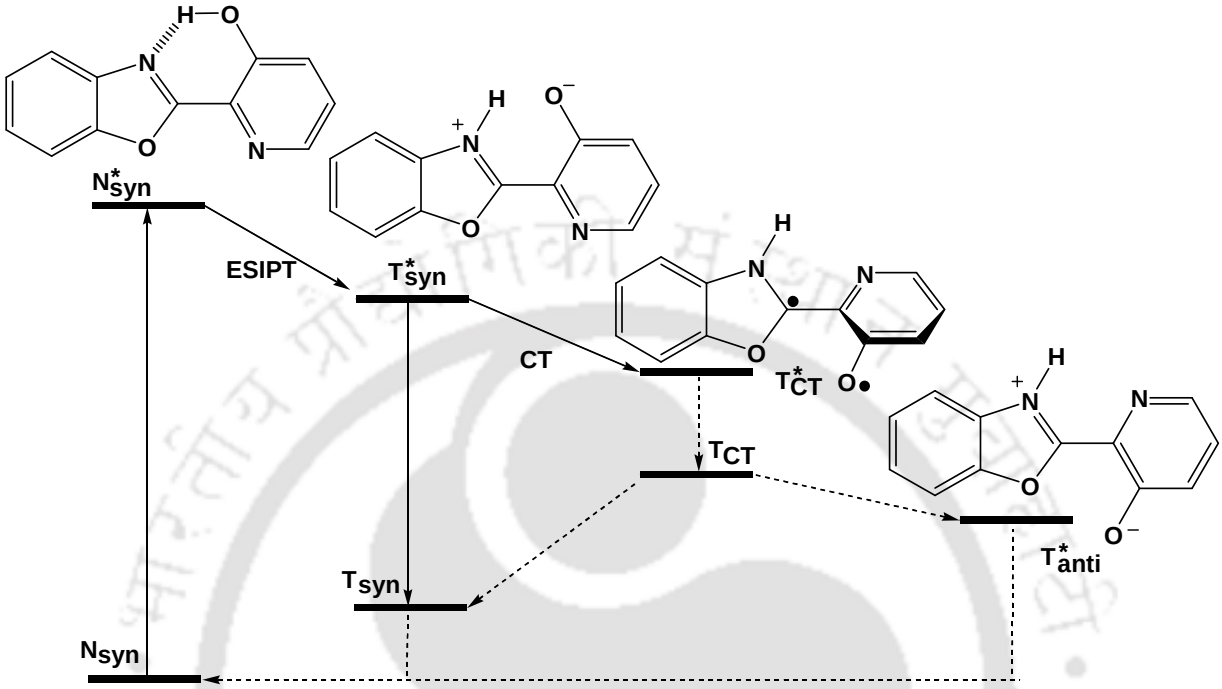

Scheme 1.24. Proton coupled charge transfer.

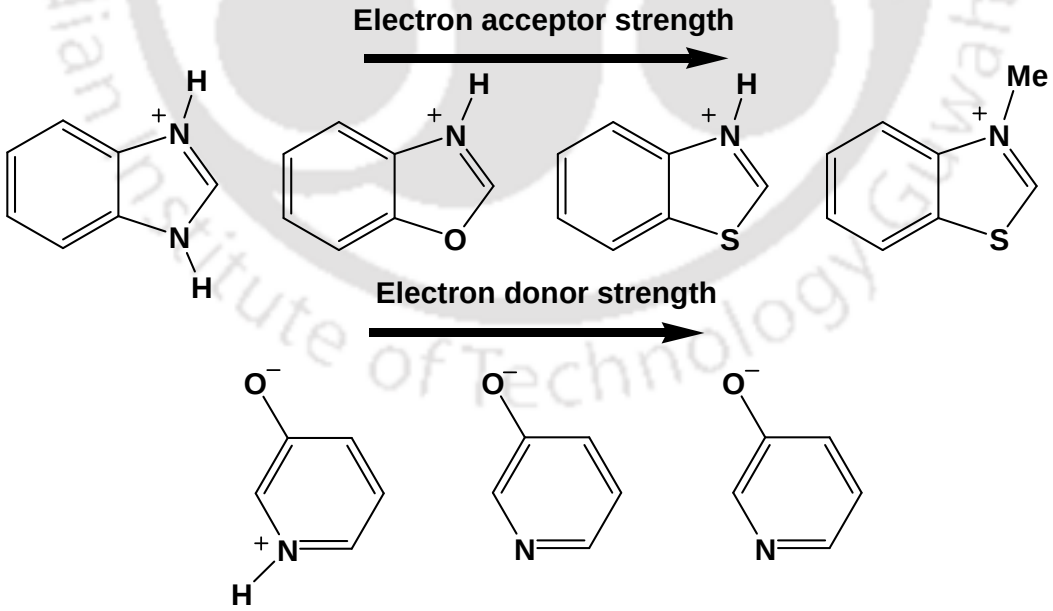

Scheme 1.25. Electron accepting and donating strengths in benzazoles and hydroxypyridines.

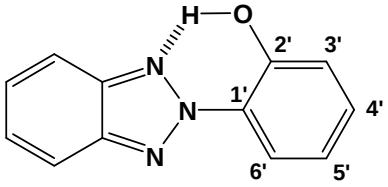

Scheme 1.26. 2-(2'-Hydroxyphenyl)benzotriazole.

The phototautomer emission usually shows small negative solvatochromism. However, introduction of conjugative electron acceptor groups at the 6-position of HPBO resulted in molecules (**Scheme 1.27**) those exhibit a strong positive solvatochromism in the phototautomer emissions due to consecutive ICT and ESIPT process. But their normal emission bands are independent of solvent polarity.[4]

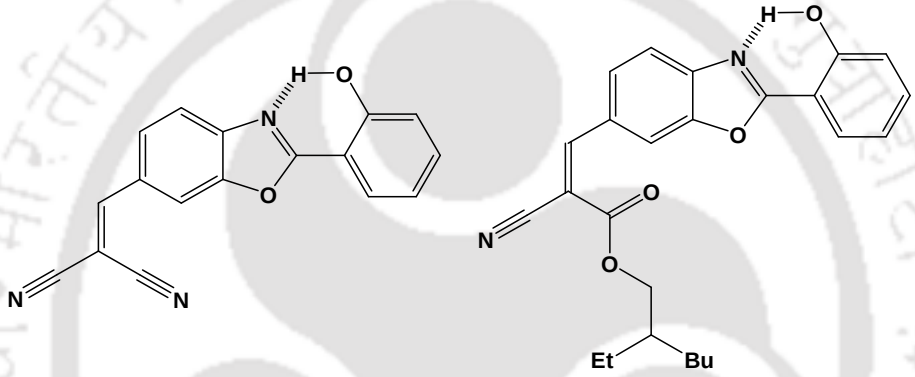

Scheme 1.27. Derivatives of HPBO.

1.2.3. Applications of ESIPT

In general, fluorophores with large Stokes shift are desired because self-absorption or the inner filter effect can be avoided. This will improve the fluorescence analysis. Since it is difficult to increase the Stokes shift of the conventional fluorophores by chemical modification, utilization of ESIPT exhibiting fluorophores can be a substitute. ESIPT is accompanied by large electronic and structural rearrangements; hence, is associated with change in dipole moment and molecular geometry. This strong and fast reorganization of the charge distribution resulting from the PT makes the molecules exhibiting ESIPT very attractive as potential implications in lasing systems as tunable laser dyes and light emitting diodes (LEDs),[42,129,130] molecular switches,[66] photostabilizers,[13,78,131,132] probes,[133-137] and sensors.[138-141]

1.2.3.1. Four Level Chemical Laser

Organic laser dyes often suffer from serious limitations arising due to occurrence of

self-absorption and concentration quenching.[27,28,142] However, four-level proton-transfer laser dyes have been found to be extraordinarily efficient. This can be considered to be a true chemical laser because the flash-photolysis pulse produces a new chemical species - the excited tautomer state (S_1'), easily attaining a complete population inversion with respect to the ground S_0' state which initially has zero population and is rapidly depopulated thereafter to the original ground state S_0. A stimulated emission is easily obtained. The working of a four level PT laser is schematically illustrated in **Scheme 1.11**. The whole PT becomes a cyclic process and thus, ESIPT molecules are photostable unlike other organic dye lasers which undergo photobleaching on prolong exposure to radiation.

The strong and rapid reorganization of charge distribution in the excited state render large Stokes' shift in fluorescence. Besides, it has a tunable range, as for instance, desired wavelength between 518 and 545 nm can be obtained from 3-hydroxyflavone in hydrocarbon solvent.[42] Such properties are also observed in other ESIPT molecules salicylamide,[143] sodium salicylate,[144] HPBI and its anologues,[58,144] and quinoline-based ESIPT moiety containing dendrimer neat films[145,146] and highly doped polymer films.[147]

1.2.3.2. Optoelectronic Devices

The cyclic process in ESIPT can be controlled by light to halt at one point of the reaction where the material has different structures and functions. Hence, this principle finds use in molecular switches, energy and information storage systems at molecular level[148-150] and organic light emitting diodes (OLED).[27,151-155]

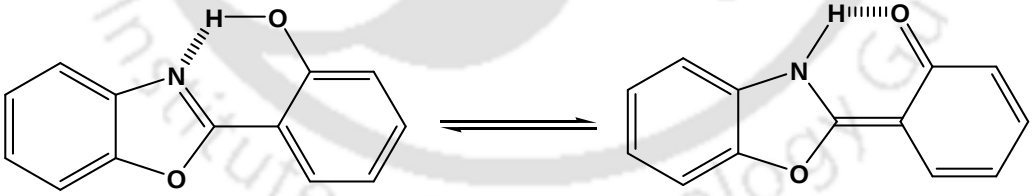

Scheme 1.28. Tautomerization of 2-(2'-hydroxyphenyl)benzoxazole.

The optical switching effect in HPBO (**Scheme 1.28**) originates from the beam deflection of the probe beam (632 nm) when a third-harmonic generation laser (355 nm) is used as the pump beam used for irradiation.[66] This is due to ESIPT process, and not the thermal effect because of absorption of the pump beam which was assumed earlier. This causes the change in refractive index under the pump beam. As the ESIPT process is very fast, HPBO might be an excellent material for high-speed optical switching.

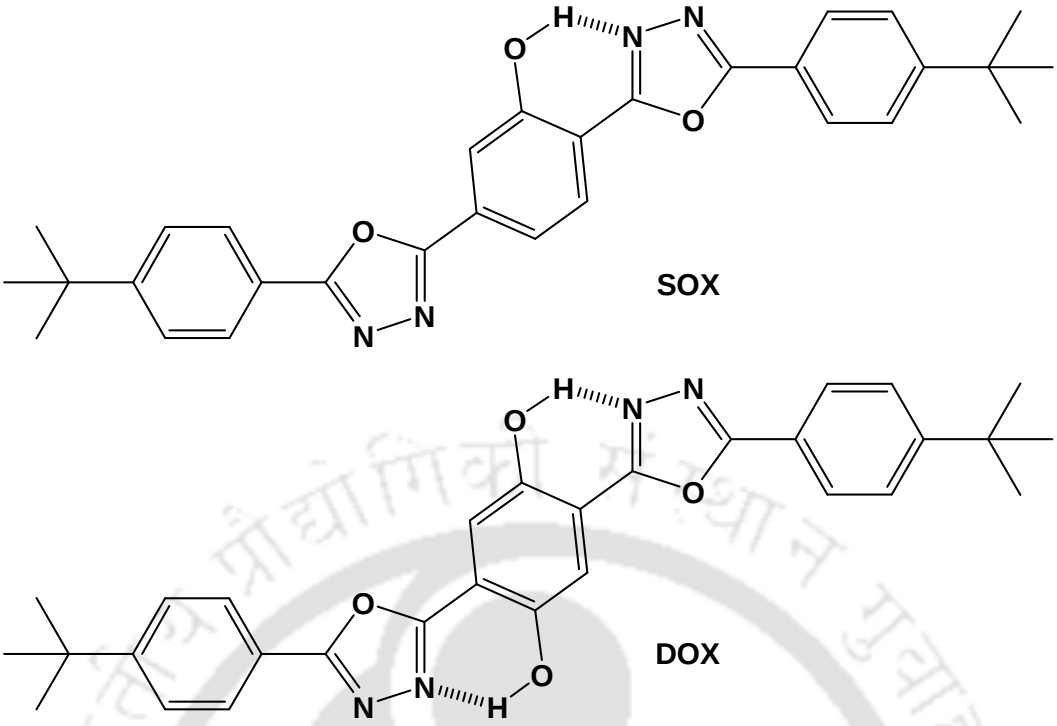

Scheme 1.29. Molecular structures of SOX and DOX.

White luminescence is one significant application of ESIPT chromophores because of their large Stokes shift and the transient feature of the ground states of the emissive species.[27,28] It is difficult to obtain a luminophore that gives emission over the whole range of the visible spectrum. To obtain white light emission, at least two luminophores that show different emission colors are mixed. It is important to note that energy transfer irrespective of its actual mechanism (Förster, Dexter or trivial) can occur between the component luminophores if there is overlap between the emission of one (donor) with the absorption of the other luminophore (acceptor). In two level fluorescent chromophores, the S_1 state of the donor and the S_0 state of the acceptor are highly populated under illumination and thus the energy transfer cannot be frustrated. However, in four level fluorescent chromophores like ESIPT molecules consisting of S_0, S_1, S_0' and S_1' states (**Scheme 1.1**) the energy transfer is frustrated in the sense that the population of the ground state K form of the acceptor is negligible since the ground state tautomer form instantly reverses back the transferred proton to the normal form after radiative relaxation. Therefore, ESIPT luminophores are ideal for construction of white luminescent materials. For example, highly efficient OLED can be fabricated by doping two ESIPT luminophore molecules SOX and DOX in 9:1 by weight (**Scheme 1.29**).[155] The SOX has one phenolic hydroxyl group (i.e. one ESIPT chromophore) while DOX has two. SOX gives a broad tautomer emission band at 492 nm and DOX exhibits the tautomer emission band at 583 nm with a minor emission 450 nm due

to the enol form. The longer wavelength of the tautomer emission in DOX is explained by the enhanced coplanarity of the molecule due to the extra phenolic hydroxyl group.

1.2.3.3. Molecular Switches

Any chemical system that can exist in at least two quasi-stable states of different chemical or physical properties can be regarded as a molecular switch. However, these states should be relatively stable and reversibly interconvertible caused by an external stimulus. The existence in different states could be due to different processes such as protonation/deprotonation, geometrical isomerization, proton transfer, charge transfer, change in spin state, bond formation/cleavage, photoexcitation, oxidation/reduction, luminescence or specific interactions with ions and molecules.[156-160] Therefore, the switching of one state to another can be used build a molecular logic gate. One state of the switch can be assigned as ON and the other as OFF. In terms of digital information processing, the ON or OFF can represent as the signal 1 or 0, respectively or vice versa depending on state assignment.

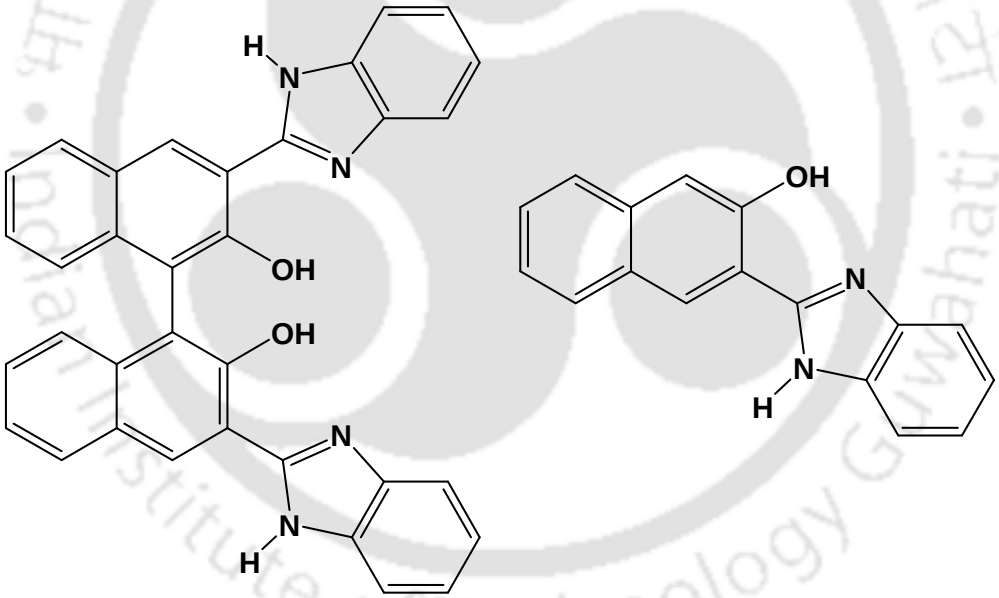

Scheme 1.30. Molecular logic gate operators based on ESIPT.

Since ESIPT molecules often exist in different rotameric and tautomeric forms, they are good examples of molecular switches and they can be used to construct molecular logic gates. For example, the fluorophore 3,3'-*bis*(1*H*-benzimidazolyl-2-yl)[1,1']binaphthalenyl-2,2'-diol (**Scheme 1.30**) consisting of 2,2′-binaphthol and benzimidazole moieties has been suggested for molecular arithmetic half-subtractor logic operator that can operate INHIBIT,

XOR, and XNOR gates by manipulating the neutral, acidic and basic conditions of the fluorophore.[161] The fluorophore consisting of naphthol and imidazopyridine moieties has been used as INHIBIT, INVERTOR, and XOR half-subtractor on based on selective emission changes of the fluorophore on interaction with Cu^{2+} and F^- ions.[162]

1.2.3.4. Photostabilizers

To prevent destructive degradation of polymeric materials by ultraviolet (UV) light absorption, the product materials are coated with UV absorbers like derivatives of hydroxyphenyltriazole/triazine (**Scheme 1.31**).[78,132,59-61] The coated material (light stabilizer) filters off the UV radiation by ultrafast dissipation of the absorbed light via an internal conversion mechanism of intramolecular rearrangement.

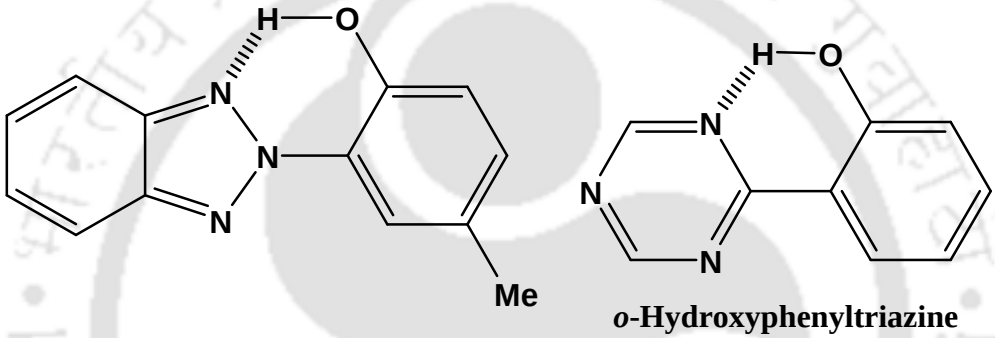

Tinuvin ***o*-Hydroxyphenyltriazine**

Scheme 1.31. ESIPT based UV stabilizers.

1.2.3.5. Fluorescent Probes

The ESIPT process is affected by interaction with the surrounding environment, such as intermolecular hydrogen bond formation with solvent molecules and deprotonation by basic media. This leads to the formation of various isomers. Therefore, multiple emissions are obtained from an ESIPT molecule due to emission from the initial and proton-transferred form as well its rotamers and protomers. In addition, the emission intensities and wavelength of each band are subjected to vary with change in the surrounding environment due to large structural and electronic changes involved during ESIPT. Such a unique sensitivity of ESIPT process to the environmental factors is very beneficial in designing fluorescence probes for polarity, viscosity, pH, ions, biological systems, etc couple of examples are discussed here.[28,163,164]

ESIPT exhibiting 4-hydroxy-5-azaphenanthrene is shown to act as a good fluorescent probe for human serum albumin and beaver apomyoglobin.[135] The ESIPT of 4-hydroxy-5-azaphenanthrene is free from hydrogen bonding solvent interference, hence can give dynamic

information about the surrounding (**Scheme 1.32**). It is blue shifted with increased polarity, thus acts as ideal probe for prediction of the polarity properties of protein binding sites and their conformational stability.

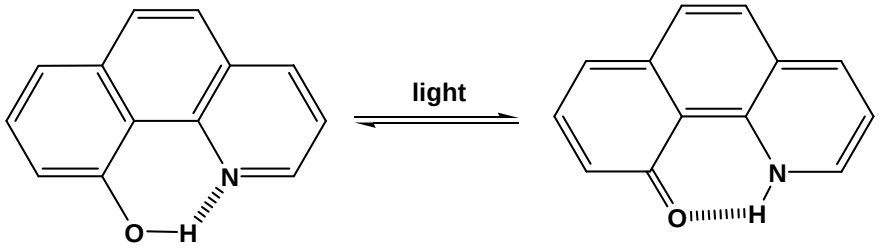

Scheme 1.32. 4-Hydroxy-5-azaphenanthrene.

Derivatives of 2-(2-furyl)-3-hydroxychromone (**Scheme 1.33**) are used as hydration-sensitive probes for the interaction between peptide and oligonucleotide based on ratiometric response of the normal and tautomer emissions.[165] In lower hydration environment, dual fluorescence consisting of both normal and tautomer emissions is observed. However, in aqueous environment, the tautomer emission disappears and only the normal emission is detected. The ESIPT chromophore tagged in the protein is shielded by the protein-oligonucleotide interaction from the aqueous environment. This changes the fluorescence intensity ratio of normal to tautomer which acts a tool in quantification of the hydration environment of the biomolecules.[166-168]

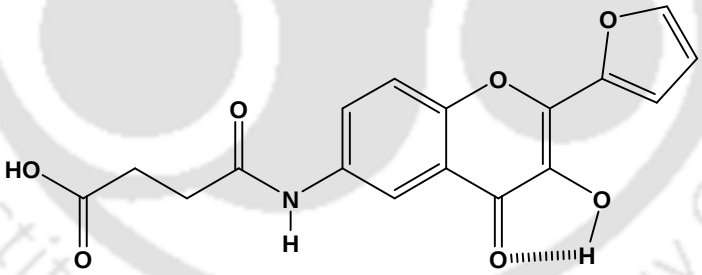

Scheme 1.33. 2-(2-Furyl)-3-hydroxychromone.

1.2.3.6. Fluorescent Sensors

Since ESIPT results in dual emission, molecules exhibiting ESIPT can be used as ratiometric sensors. Ratiometric fluorescent recognition has advantages over conventional single wavelength monitoring as the ratiometric method is free from the errors associated with receptor concentration, photobleaching and environmental effects. Most of the applications of ESIPT chromophores are based on the perturbation of the ESIPT process upon interaction with the analytes. A variety of ESIPT based sensors have been reported in the literature, some of these sensors are discussed in the following.

Hydrogen Bonding Sensors

Molecular hydrogen bonding sensors are highly desired by modern science and technology. The equilibrium between the hydrogen bonded and non hydrogen bonded forms of 4'-dialkylamino-3-hydroxyflavone dyes (**Scheme 1.34**) in mixed solvents in the ground state remain almost unchanged upon excitation to the normal excited state S_1.[169] In the excited state no new hydrogen bond forms, but those already existing undergo slow ESIPT reaction. The fluorescence spectra of the dye provide a measure of the ground state distribution between its hydrogen bonded and non hydrogen bonded forms, which in turn reflects the hydrogen bonding potential of the environment. Due to this feature, these dye derivatives can serve not only as a calibrator of solvent properties but also as a unique sensor of hydrogen bonding potential in unknown media.

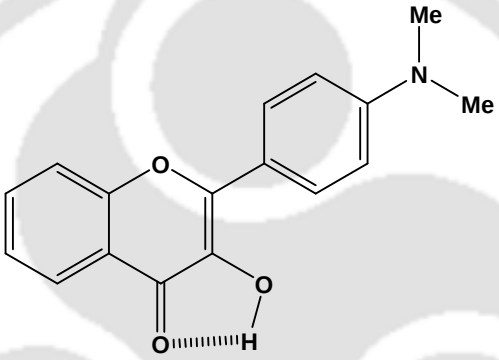

Scheme 1.34. 4'-Dimethylamino-3-hydroxyflavone.

Metal Ion Sensors

Some metal ions are found as environment pollutants and some are essential trace elements in biological systems. For the detection and measurement of metal ions fluorescence sensors are highly investigated.[139,140,170] Using a Schiff base, Mg^{2+} ion is recognized based on the fluorescence intensity ratio of the keto and enol emissions.[139] The sensor Schiff base in THF/water (9:1 v/v) when excited at 275 nm exhibits dual emission at 355 and 427 nm, due to normal enol and keto tautomer forms, respectively (**Scheme 1.35**). Upon addition of Mg(II) ion to the solution, the intensity of the emission band at 355 nm decreases along with the concomitant increase of the band at 427 nm. However, other metal ions including alkali (Na^+, K^+), alkaline earth (Ca^{2+}, Sr^{2+}) and transition metal ions (Mn^{2+}, Fe^{3+}, Co^{2+}, Ni^{2+}, Cu^{2+}, Zn^{2+}) give no such significant change in the fluorescence spectrum under the same conditions.[139] The sensor could potentially be used to detect conditions such as hypermagnesaemia.

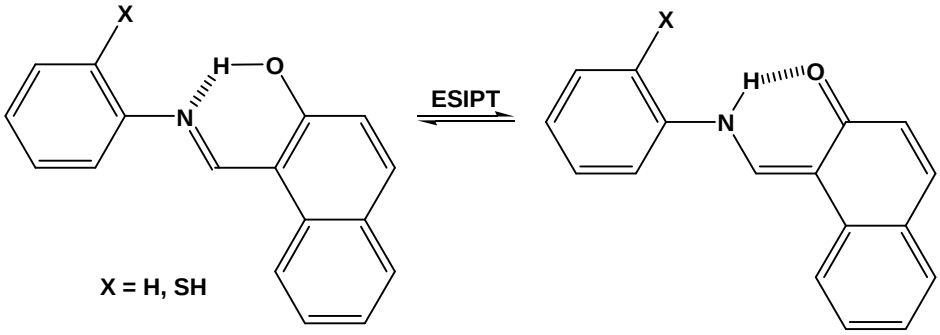

Scheme 1.35. Schiff base as chemosensor for Mg^{2+}.

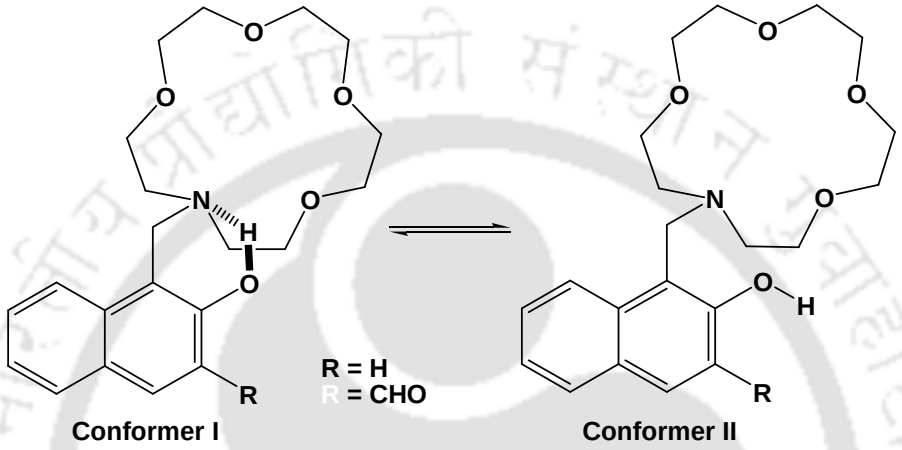

Scheme 1.36. Chemosensors for detection of Na^+ and Ca^{2+} ions.

ESIPT molecules containing aza crown ether moiety (**Scheme 1.36**) have been exploited as chemosensors for Na^+ and Ca^{2+} ions.[171] The conformer I is the dominant species in acetonitrile and undergoes ESIPT to give its zwitternionic form responsible for the large stokes' shifted emission. On addition of Na^+ ion, the equilibrium shifts towards the conformer II and the ESIPT process is inhibited and the normal emission which occurs from conformer II is enhanced. When R group is the formyl moiety, another ESIPT channel is switched on in the conformer II where the aldehyde group acts as proton acceptor and the hydroxyl group as donor. This gives another ESIPT emission.

Anion Sensors

2-(2'-Phenylureaphenyl)benzoxazole (**Scheme 1.37**),[138] is a good hydrogen-bond donor, can be used as sensor for fluoride and acetate anions. In fluoride and acetate anions the different mechanisms operates to inhibit the ESIPT. The inhibition of ESIPT occurs either by the fluoride induced deprotonation of the urea unit or by the formation of a strong acetate-urea intermolecular hydrogen bond complex. This changes the ratiometric responses of the normal and tautomer emissions.

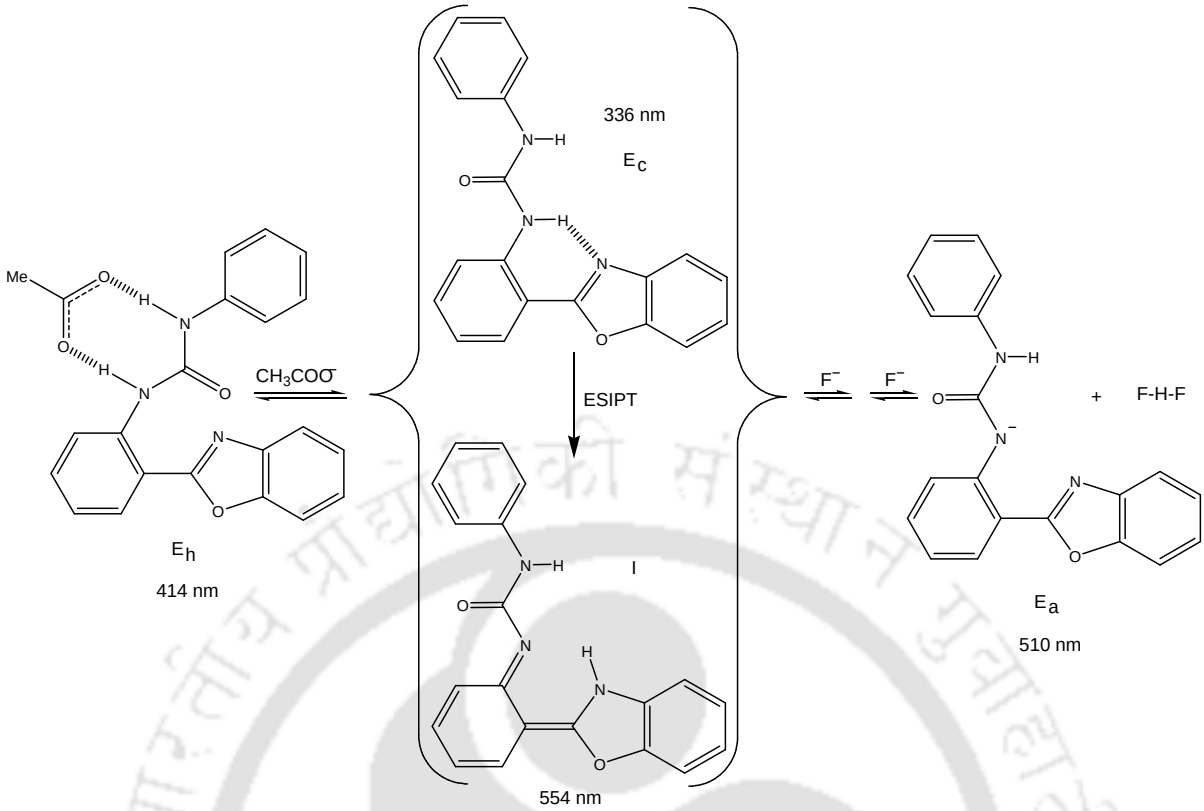

Scheme 1.37. Inhibition of ESIPT in 2-(2'-phenylureaphenyl)benzoxazole in presence of fluoride ion.

Thiazole-based ESIPT molecule (**Scheme 1.38**) has been used as a chemosensor for selective detection of fluoride anion in acetonitrile.[172] The fluoride anion deprotonates the phenolic hydroxyl group, therefore inhibits the ESIPT reaction. Upon addition of fluoride anion, the normal and tautomer bands disappear and a new emission corresponds to phenolic anion form starts to appear. Such changes are not observed in case of other halides.

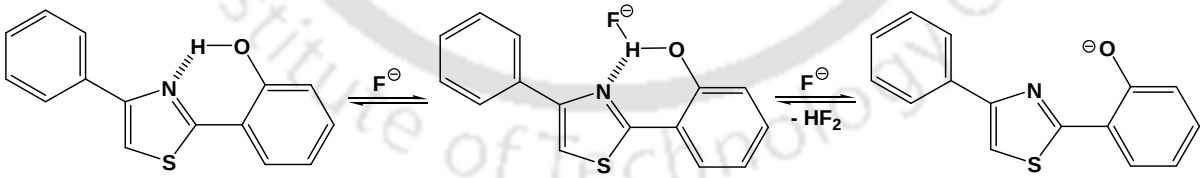

Scheme 1.38. Inhibition of ESIPT by fluoride ion.

A Zn^{2+} complex of HPBO derivative has been used as a ratiometric fluorescent probe for selective detection of pyrophosphate anions.[173] In the Zn^{2+} bonded form the phenolic hydroxyl group is deprotonated thus the ESIPT is inhibited. Binding with pyrophosphate anions frees the phenolic hydroxyl group which in turn triggers the ESIPT. The pyrophosphate bonded sensor gives emission at 518 nm due to tautomer emission.

1.3. Scope of the Present Work

As discussed earlier, HPBI exhibits clear four distinct energy levels due to ESIPT it undergoes. Hence, HPBI is used as a source for four level chemical lasers. The photophysics of HPBI is studied by replacing the NH group with O (HPBO) and S (HPBT) hetero atoms, respectively. These molecules show different photophysical properties in terms of quantum yield, Stokes' shift, photostability and ESIPT pattern they undergo. Further substitution with hetero atoms in these molecules will further alter their photophysics. Besides, the substitution creates a new binding site in the molecule which develops a new dimension in exploring the potential implications of these molecules as probes and sensors. It also helps better in understanding the photophysical properties of these molecules.

The primary scope of the present work is to understand the ESIPT reaction and the related photophysics of HPBI and its analogues. Earlier studies carried out by Dogra et al.[6,95,174-176] and Rodriguez et al.[177,178] revealed that presence of N-heteroatom in the benzene ring of HPBI reduces the quantum yield of the phototautomer while the nitrogen substitution on the phenolic ring increases its yield. Therefore, theoretical calculations have also been performed to understand the photophysical processes those occur in these molecules.

In the literature, many physical and chemical techniques such as X-ray diffraction,[177] nuclear magnetic resonance (NMR),[178] electron paramagnetic resonance,[179] electrophoresis,[180] ultrafiltration,[181] light scattering,[182] absorption[183] or emission spectroscopy[184] are used to study the characteristics of microenvironments. Fluorescence is more popular than other techniques not only due to simplicity in measurement but also due to the high sensitivity of the technique. Since emission intensity depends on factors such as concentration, bleaching, optical path length, and illumination intensity, ratiometric sensing are more desired over single wavelength measurement. In this aspect ESIPT exhibiting molecules can be used as probes or sensors. Making use of the ratiometric measurements the interactions of HPBI and its nitrogen substituted analogues with metal ions and different microheterogeneous media viz. cyclodextrin (CD), reverse micelle and bovine serum albumin (BSA) protein were investigated. In the process, potential implications of these molecules as sensors and probes were also explored. A new fluorophore 2-(2'-hydroxyphenyl)-3*H*-oxazo[4,5-*b*]pyridine (HPOP) was synthesized and studied to understand the effects of substituent on ESIPT.

Chapter 2

Materials, Methods and Instrumentations

2.0. Introduction

The chapter provides the details of the materials used in the present work and the synthetic procedures of the fluorophores. Methods used for the analysis, calculations and preparation of the samples are also elaborated. The chapter also describes the methods used for the quantum chemical calculations and in addition, brief descriptions of the instrumentations such as UV-Visible absorption spectrophotometer, and steady-state and time-resolved fluorimeters are provided.

2.1.0. Materials

Details of the materials utilized in the present work are given below.

2.1.1. Solvents

- Acetonitrile,CH_3CN (HPLC grade, Spectrochem Pvt. Ltd., India)
- 1-Butanol, $CH_3CH_2CH_2CH_2OH$ (HPLC grade, Spectrochem Pvt. Ltd., India)
- Chloroform, $CHCl_3$ (HPLC grade, Rankem India)
- Cyclohexane, C_6H_{12} (HPLC grade, Rankem India)
- *N*,*N*-Dimethylformamide, $N(CH_3)_2CHO$ (HPLC grade, Rankem India)
- Dimethylsulfoxide, $(CH_3)_2SO$ (HPLC grade, Rankem India)
- 1, 4-Dioxane, $C_2H_4O_2C_2H_4$ (AR grade, Spectrochem Pvt. Ltd., India)
- Ethylene Glycol, $(CH_2OH)_2$ (AR grade, Rankem India)
- Ethyl Acetate, $CH_3COOCH_2CH_3$ (HPLC grade, Rankem India)
- Ethyl Alcohol, CH_3CH_2OH (ACS grade, Merck India)
- Glycerol, $CH_2OHCHOHCH_2OH$ (AR grade, Rankem India)
- Methyl Alcohol, CH_3OH (HPLC grade, Rankem India)
- Tetrahydrofuran, C_4H_8O (HPLC grade, Rankem)
- Toluene, $C_6H_5CH_3$ (HPLC grade, Rankem India)
- 1-Propanol, $CH_3CH_2CH_2OH$ (AR grade, Rankem India)
- Water, H_2O (Millipore water)

All the solvents were tested and found free of spurious fluorescence in the region of spectral measurement before use.

2.1.2. Metal Salts

- Barium perchlorate hydrate, $Ba(ClO_4)_2.xH_2O$ (99.0%, Sigma Aldrich)

- Calcium perchlorate tetrahydrate, $Ca(ClO_4)_2.4H_2O$ (99.0%, Sigma Aldrich)
- Copper perchlorate hexahydrate, $Cu(ClO_4)_2.6H_2O$, (98.0% Sigma Aldrich)
- Magnesium perchlorate hexahydrate, $Mg(ClO_4)_2.6H_2O$ (> 99 %, Sigma Aldrich)
- Nickel perchlorate hexahydrate, $Ni(ClO_4)_2.6H_2O$ (98.0% Sigma Aldrich)
- Sodium perchlorate monohydrate, $NaClO_4.H_2O$ (99.0%, Sigma Aldrich)
- Sodium sulphate anhydrous, Na_2SO_4 (99.5 %, Merck India)
- Zinc perchlorate hexahydrate, $Zn(ClO_4)_2.6H_2O$ (98.0%, Sigma Aldrich)

2.1.3. Other Chemicals

- Aerosol Orange T, (AOT, Sigma Aldrich)
- Bovine serum albumin (BSA, 98%, Merck India)
- β-Cyclodextrin (β-CD, Sigma Aldrich)
- 2,3-Diaminopyridine (98%, Sigma Aldrich)
- 3,4-Diaminopyridine (98%, Sigma Aldrich)
- Diphosphorous pentoxide (97%, Merck India)
- *ortho*-Phenylenediamine (98%, Merck India)
- ortho-Phosphoric Acid, (AR grade, Rankem India)
- Phosphorous oxychloride (Spectrochem)
- Potassium hydroxide (Merck India)
- Salicylic Acid, (98%, Merck India)
- Sodium hydroxide (Merck India)
- Sulphuric Acid (AR grade, Rankem India)

2.1.4. Syntheses of 2-(2'-Hydroxyphenyl)benzimidazole, 2-(2'-Hydroxyphenyl)-3*H*-imidazo[4,5-*b*]pyridine and 2-(2'-Hydroxyphenyl)-3*H*-imidazo[4,5-*c*]pyridine

HPBI, 2-(2'-Hydroxyphenyl)-3*H*-imidazo[4,5-*b*]pyridine (HPIP-b) and 2-(2'-Hydroxyphenyl)-3*H*-imidazo[4,5-*c*]pyridine (HPIP-c) were synthesized following the reaction scheme shown in **Scheme 2.1**.[187-189] Equimolar mixture of appropriate diamine and salicylic acid was heated in polyphosphoric acid at 160-200 ^oC until the reaction was completed (~ 4.5 hours). The reaction was monitored by thin layer chromatography (TLC). The reaction mixture was cooled to room temperature. To the reaction mixture, 2 heaps of ice cold water were added and stirred well so that the mixture become a complete slurry. The acidic grey colored slurry was neutralized with aqueous KOH solution to neutral pH at which

the product precipitated out. The precipitate was vacuum suctioned and dried for overnight in a dessicator. The dried precipitate was thrice recrystallized. The identities and purity of the synthesized compounds were confirmed by TLC, Fourier Transform Infrared (FT-IR), and NMR. The ^{1}H NMR peaks were assigned based on the decoupling experiments performed (**Appendices A1**, **A2**, and **A3**). **Figure 2.1** shows the NMR spectra of HPBI, HPIP-b and HPIP-c in the aromatic region.

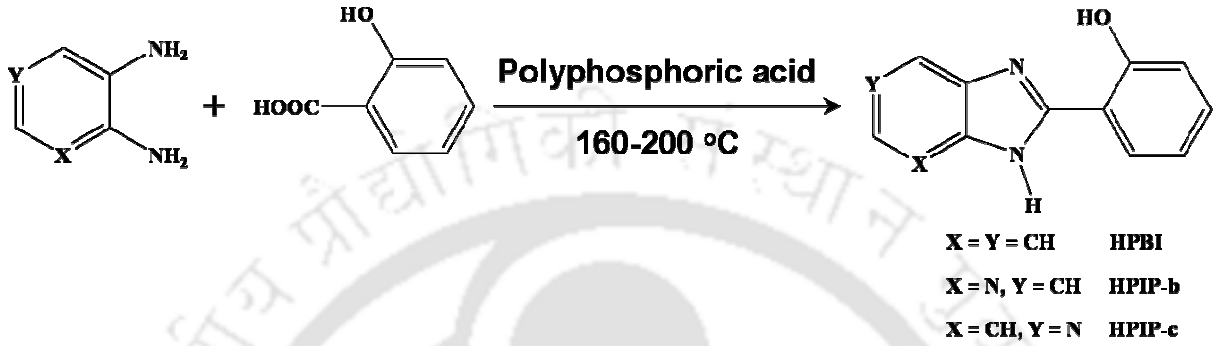

Scheme 2.1. Synthetic procedure for HPBI, HPIP-b and HPIP-c.

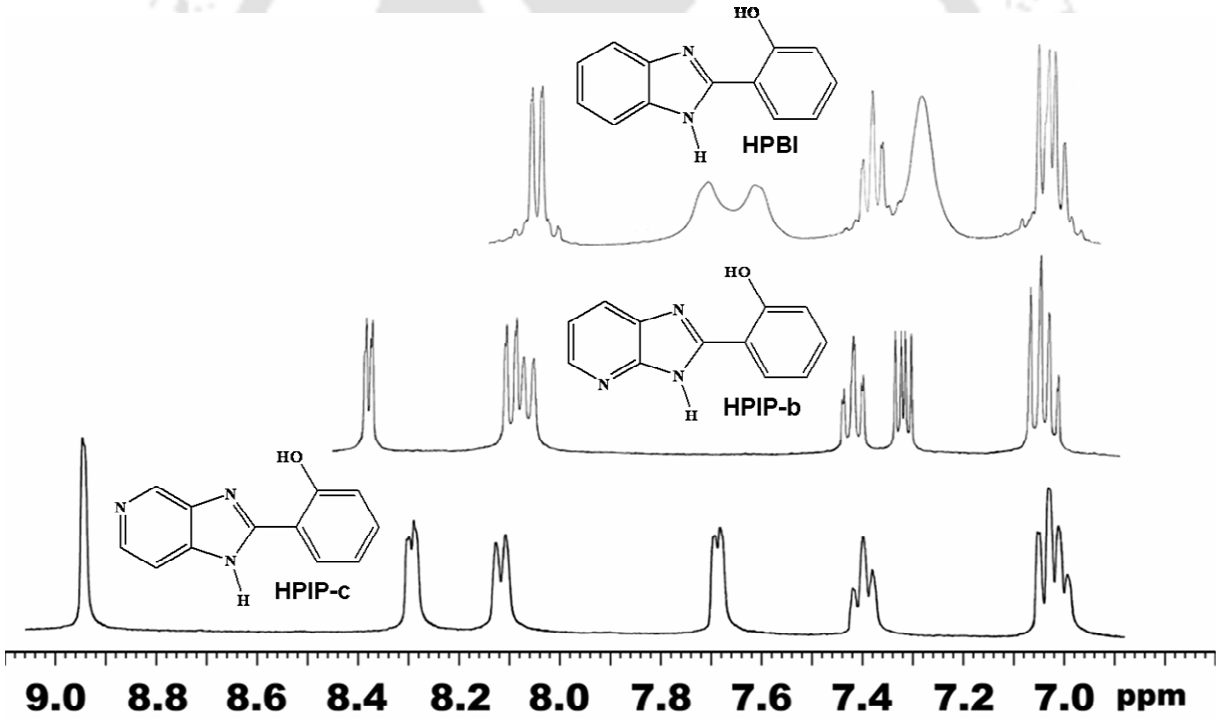

Figure 2.1. ^{1}H NMR Spectra of HPBI, HPIP-b and HPIP-c in DMSO-d_6.

HPBI: White solid; ^{1}H NMR (400 MHz, DMSO-d_6/$CDCl_3$, 1:7) δ = 7.01 (1H, d, Ar-H), 7.05 (1H, d, Ar-H), 7.28 (2H, br, Ar-H), 7.38 (1H, m, Ar-H), 7.61 (1H, br, Ar-H), 7.70 (1H, br, Ar-H), 8.02 (1H, d, ArN-H).

IR (KBr): 3325, 3056, 2508, 1602, 1590, 1492, 1395, 1262, 726 cm^{-1}.

HPIP-b: Light green solid; ^{1}H NMR (400 MHz, DMSO-d_6) δ = 7.02 (2H, d, Ar-H), 7.30 (1H, m, Ar-H), 7.42 (1H, t, Ar-H), 8.04 (1H, d, Ar-H), 8.11 (1H, d, Ar-H), 8.39 (1H, d, Ar-H).
IR (KBr): 3432, 3064, 1634, 1588, 1491, 1422, 1259, 740 cm^{-1}.

HPIP-c: White solid; ^{1}H NMR (400 MHz, DMSO-d_6, 1:7) δ = 6.98 (1H, d, Ar-H), 7.04 (1H, d, Ar-H), 7.39 (1H, t, Ar-H), 7.69 (1H, d, Ar-H), 8.11 (1H, d, Ar-H), 8.28 (1H, d, Ar-H), 8.92 (1H, s, Ar-H).
IR (KBr): 3505, 3044, 1632, 1590, 1491, 1415, 1288, 1259, 754 cm^{-1}.

2.1.5. Synthesis of 2-(2'-Hydroxyphenyl)-3*H*-oxazo[4,5-*b*]pyridine

2-(2'-Hydroxyphenyl)-3*H*-oxazo[4,5-*b*]pyridine (HPOP) was synthesized by following the procedure reported earlier for the synthesis of the similar compound.[190] The reaction scheme is presented in **Scheme 2.2**. Salicylic acid (1.4 gram) was dissolved and stirred in $POCl_3$ (2 mL) for ~ 3 minutes. Then 2-amino-3-hydroxypyridine (1.1 gram) was added to the solution. The reaction mixture was heated at 90 ºC and heated until the reaction was complete (6 hours). The reaction was monitored by TLC. After completion of the reaction the mixture was cooled. 2-3 heaps of ice was added, stirred and scratched with spatula to mix the hardened solid. White precipitate was formed. The precipitate was filtered and dried. The dried residue (1.3 gram) was dissolved in dichloromethane leaving behind insoluble sticky solids. The filtrate was dried with anhydrous $NaSO_4$ and filtered. The product was dried from the solvent to give greenish flakes (600 mg). The compound was doubly recrystallized in methanol.

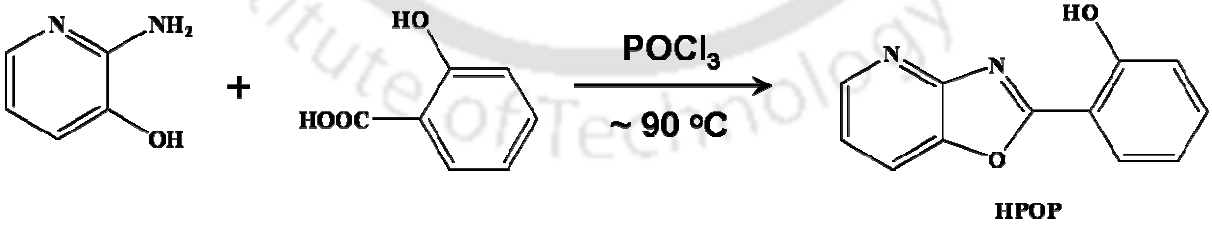

Scheme 2.2. Synthetic Procedure for HPOP.

The identities and purity of the synthesized compound 2-(2'-Hydroxyphenyl)-3*H*-oxazo[4,5-*b*]pyridine (HPOP) were confirmed by TLC, LC-MS, FT-IR, and NMR. The ^{1}HNMR spectrum of HPOP is shown in **Figure 2.2**.

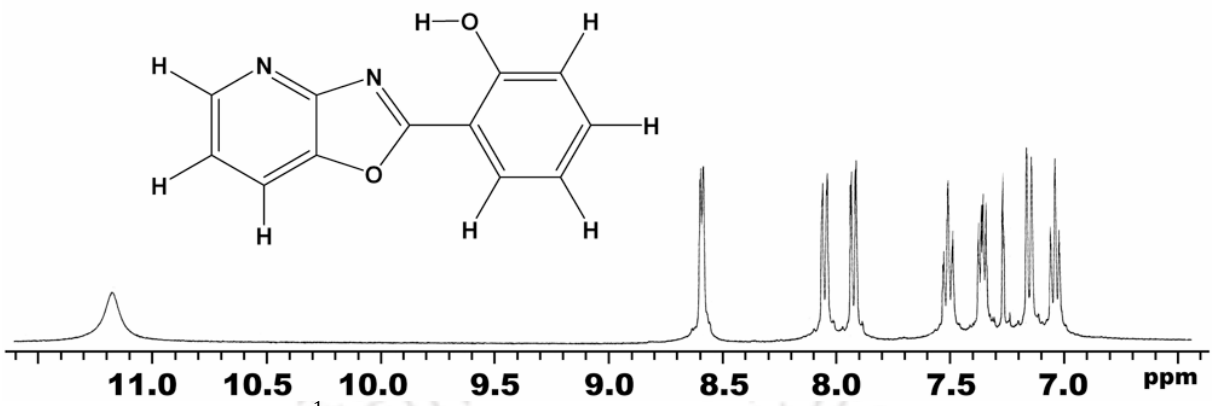

Figure 2.2. ^{1}H NMR Spectra of HPOP in DMSO-d_6/$CDCl_3$ (1:4 v/v).

HPOP: Yellowish green; ^{1}H NMR (400 MHz, DMSO-d_6/$CDCl_3$, v/v = 1:4) δ = 7.0 (1H, t, Ar-H), 7.15 (1H, m, Ar-H), 7.35 (1H, m, Ar-H), 7.5 (1H, t, Ar-H), 7.9 (1H, d, Ar-H), 8.08 (1H, d, Ar-H), (1H, br s, ArO-H).

IR (KBr): 3452, 1631, 1544, 1485, 1404 cm^{-1}.

ESI-MS, m/z: 213.07 $(M+1)^{+}$.

2.2.0. Preparation of Samples

2.2.1. In Solvents

A stock solution of the fluorophore of 1 mM concentration was prepared in methanol. 10^{-4} M of the fluorophore solution was further prepared in methanol by pipetting out 1 ml of the stock solution to a 10 ml volummetric flask and filling the flask upto the mark by adding methanol. From the 10^{-4} M solution, 500 µL of the solution was pipetted out to another 10 ml volummetric flask. The solution was kept in the oven overnight at ~ 50 ºC to remove the methanol. After complete removal of methanol, 10 ml of different solvents was added to each volumetric flask containing the dried compound. The flask was shaken well to dissolve the compound completely in the solvent. For pH titration, a small amount of H_3PO_4 or NaOH solution was added to obtain the desired pH. The final concentration of HPBI/HPIP-b/HPIP-c for any absorption or fluorescent measurement was 5 µM unless otherwise mentioned. In the case of HPOP, 100 µL of 1 mM solution in methanol was pipetted out to a 10 mL volummetric flask. The final concentration of HPOP in a given solvent for the study was 10 µM.

2.2.2. Metal Solutions

Metal perchlorate solutions were prepared in acetonitrile. The compound was completely dissolved in acetonitrile. Metal ion titrations were carried out by mixing appropriate amount of the metal ion solutions to the fluorophore solution. The fluorophore concentration was maintained at 5 μM.

2.2.3. Reverse Micelle

AOT/*n*-heptane/water reverse micelles were prepared by systematically adding desired amount of water to a solution of AOT in *n*-heptane. The amount of water present in the mixture is expressed as the molar ratio of water to AOT surfactant (w_0). The concentrations of the fluorophore and AOT in the reverse micelle system were maintained at 5 μM and 0.1 M, respectively throughout the experiments.

2.2.4. Protein Samples

10 mM of aqueous phosphate buffer of pH 7.0 ± 0.1 was used to prepare the protein samples. For fluorescence resonance energy transfer (FRET) experiments, the concentration of bovine serum albumin (BSA) was kept constant of 10 μM and fluorophores concentrations were varied. For other studies the ligands concentrations were kept constant at 5 μM and BSA concentrations were varied.

2.3.0. Methods

2.3.1. Quantum Yield (Φ_f)

The excited molecules after absorption of light dissipate their absorbed energy by decomposition, reaction, emission or nonradiative de-excitation. The efficiency with which these processes take place is called the quantum efficiency. Quantum yield of fluorescence (Φ_f) is defined as the ratio of the number of photons emitted to the number of photons absorbed as given by the following equation.

$$\Phi_f = \frac{\text{Number of photons emitted}}{\text{Number of photons absorbed}} \qquad (2.1)$$

The fluorescence quantum yield of a sample (Φ_s) is determined with respect to that of a standard known fluorophore using the **Equation 2.2** given below

$$\frac{\Phi_s}{\Phi_r} = \frac{I_s A_r n_s^2}{I_r A_s n_r^2} \qquad (2.2)$$

where Φ_s is the fluorescence quantum yield of the sample, I_s and I_r are the integrated fluorescence area, and A_s and A_r are the absorbance values for the sample and reference solutions, respectively. n_s and n_r are the refractive indices for the sample and reference solutions, respectively. Quinine sulphate in 1N sulphuric acid solution (Φ_r = 0.546) was used as the reference for fluorescence quantum yield determination.[191] The dielectric constants and refractive indices of different solvents at different temperatures for the determination of fluorescence quantum yields were obtained from the literature.[192,193]

2.3.2. Determination of Ionization Constant

The acid dissociation constant or pK_a is a measure of the strength of an acid or a base. The pK_a measurements are useful parameters for understanding the behavior of probe molecules. Different ionic species of a molecule differ in physical, chemical and biological properties and so it is important to find which ionic form of the molecule is present at the site of action. The most familiar Hammette equation used for the determination of ionization constant (pK_a) of the dissociation reaction of an acid in water is given below:

$$BH^+ + H_2O \rightleftharpoons B + H_3O^+ \qquad (2.3)$$

$$H_0 = pK_a + \log\frac{[B]}{[BH^+]} \qquad (2.4)$$

where $[BH^+]$ and [B] are the molar concentration of conjugate acid and base, respectively as described by the reaction given in **Equation 2.3**. H_0 is called the Hammette acidity function, which is given by the following **Equation 2.5**

$$H_0 = -\log\frac{a_{H^+} f_B}{f_{BH^+}} \qquad (2.5)$$

where f_B and $f_{BH}{}^+$ are the acidity co-efficients of conjugate base and acid, respectively. $a_H{}^+$ is the activity of the proton. For dilute solution, H_0 can be replaced by pH. A plot of pH versus $\log\frac{[B]}{[BH^+]}$ gives a straight line with unit slope and the pH is equal to pK_a when $[B] = [BH^+]$.

The factor $\frac{[B]}{[BH^+]}$ can be determined from following relation.

$$\frac{[B]}{[BH^+]} = \frac{[A_B - A]}{[A - A_{BH^+}]} \qquad (2.6)$$

where $A_{BH}+$ and A_B are the absorbances (at the analytical wavelength) of pure BH^+ and B, respectively and A is the absorbance (at same wavelength) of any solution in which BH^+

is partially ionized. The factor $\frac{[B]}{[BH^+]}$ can also be expressed as

$$\frac{[B]}{[BH^+]} = \frac{[B]}{[C]-[B]} \qquad (\mathbf{2.7})$$

where [C] = molar concentration of the compound in the experimental solution.

The concentration of the conjugate base is given by

$$[B] = \frac{A(\lambda_1)\varepsilon^+_{BH}(\lambda_2) - A(\lambda_2)\varepsilon^+_{BH}(\lambda_1)}{\varepsilon_B(\lambda_1)\varepsilon^+_{BH}(\lambda_2) - \varepsilon_B(\lambda_2)\varepsilon^+_{BH}(\lambda_1)} \qquad (\mathbf{2.8})$$

ε is the molar extinction coefficient. Generally, two wavelengths (λ_1 and λ_2) are chosen on both side of the isosbestic point.

2.3.3. Quantum Mechanical Calculations

Density functional theory (DFT) methods for solving molecular parameters in the electronic ground state have gained rapid momentum in modern computational chemistry due to their accuracy and lower computational cost. Density functional calculations are based on electron probability density function or electron density function unlike *ab initio* methods which are based on solving wavefunctions. The basic principles on developing the methods and solving the electronic structure of a molecule are discussed in details by Lewar,[194] Cramer[195] and Szabo et al[196] and Gaussian Manuals[197,198] in their books.

However, calculating molecular parameters for an electronic excited complex molecular system is difficult in terms of accuracy and computational cost and time. Configuration interaction singles (CIS)[199] is a common method for calculations of excited state parameters.[96,200] CIS is an analytic gradient method which allows optimization of the excited state geometries and is less expensive. The geometries obtained at the CIS level are quite reasonable and correct at least as a first approximation for a variety of molecules.[201-204] But CIS has certain limitations such as significant difference of the calculated energies from the experimental data, and incorrect order of the excited states.[199,204,205] To be more specific, CIS overestimates the energy barrier for PT and fail to describe the breaking of bond.[206-210] The multireference complete active space self consistent field (CASSCF)[211] method gives better accuracy and optimization in the electronic excited state is also possible with the method. The nondynamic electron correlation effects due to degenerate configurations are also taken into account in CASSCF. However, in this method only selected few orbitals can be included in the molecular orbital (MO) active space.[62,212-215] The active orbitals in the active space can change during geometry optimization.[62] Therefore, extreme caution should

be taken in choosing the active space. Moreover, the method is computationally expensive for large systems.[78,216-217] During the past decade, there has been significant rise in development of time-dependent density functional theory (TDDFT) methods which are DFT based for calculations of excited state properties.[218,219] TDDFT proves good for electronic structure calculations in the excited states including proton transfer even for large molecular system due to its moderate efficiency and accuracy.[220-226] Lately, excited state gradients have been implemented in TDDFT,[224,227] but it is reported that optimization by TDDFT method gives incorrect ordering of energies in few cases.[228] TDDFT calculations over CIS optimized geometries have been proven to be an efficient approach in predicting energy parameters for various systems.[202,229-232] Moreover, TDDFT method employing B3LYP functional is shown to be reliable in treating vertical excitation energies even for charge transfer states.[221] Therefore, the hybrid method TDDFT//CIS for energy calculations in the excited state was implemented in the entire work. The excited S_1 state geometries were optimized using *ab initio* restricted configuration interaction singles RCIS/6-31G(d) approach.

In all the cases for optimization, the 6-31G(d) basis set was used but the molecular energies and other properties were obtained using 6-31+G(d,p) basis set. The minimum energy nature of the geometries was confirmed by vibration frequency calculations performed on the optimized stationary point geometries and first-order transition states using the same basis set 6-31G(d) used during the geometry optimization.[196,197] Vertical excitation energy calculations were performed on the optimized ground and S_1 state geometries by TDDFT/B3LYP/6-31+G(d,p) for the assignment of excitation and emission energies, respectively. The convergence threshold for the energies and residual forces on the atoms during geometry optimization (both the ground and the excited states) were 10^{-8} hartree and 4.5×10^{-4} hartree/bohr, respectively.

Solvent stabilization effects were also studied in cyclohexane, 1,4-dioxane, acetonitrile, methanol and ethylene glycol using the integral equation formalism-polarizable continuum model (IEF-PCM).[233,234] The dielectric constants available from the literature,[191] were used for these calculations. In all the cases for optimization, the 6-31G(d,p) basis set was used but the molecular energies and other properties were obtained using 6-31+G(d,p) basis set.

Theoretical calculations were performed using Gaussian 03W program[235] throughout the work to obtain the molecular parameters. Molecular modeling software GaussView 4.1[236] was used for drawing the molecules to obtain the coordinates and to give inputs for the calculations. The flowchart for a typical quantum chemical calculation employed in this work

is schematically described in **Figure 2.3**. The ground state geometries of the molecules were obtained by full optimization of structural parameters employing Berny optimization algorithm by DFT utilizing Pople's split-valence polarized basis set[237] 6-31G(d) in a spin restricted shell wavefunction manner.[238,239] The calculations in the ground state were carried out using the hybrid functional B3LYP containing Becke's gradient corrected three-parameter exchange functional B3 with 20% of Hartree-Fock exchange,[240] and nonlocal correlation functional of Lee, Yang, and Parr (LYP),[241] given by the expression below.

$$aE_X^{Slater} + (1-a)E_X^{HF} + b\Delta E_X^{Becke} + E_C^{VWN} + c\Delta E_C^{LYP} \qquad (\mathbf{2.9})$$

The constants *a*, *b* and *c* are semiempirical coefficients with values 0.8, 0.72 and 0.81, respectively.

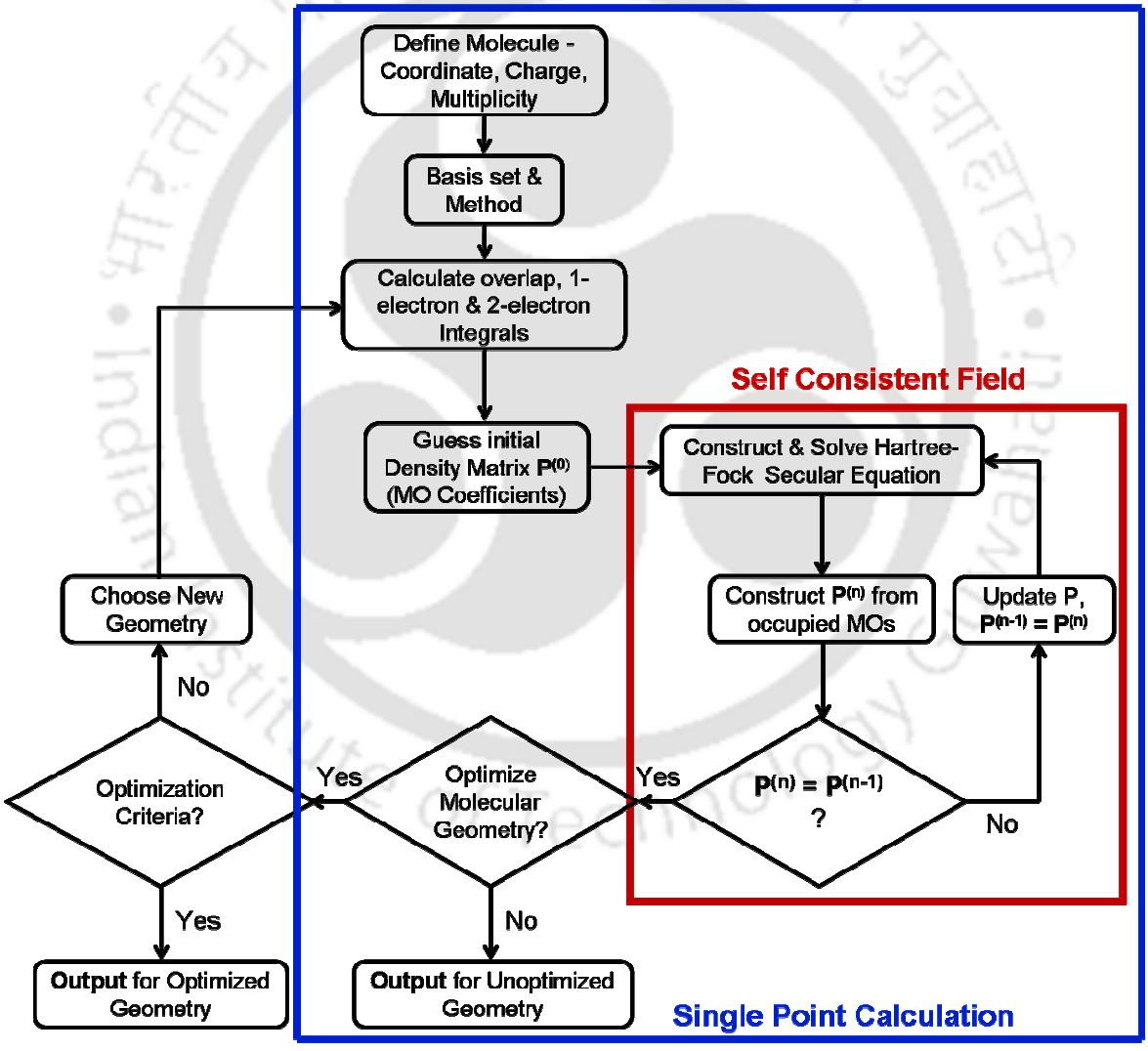

Figure 2.3. Flowchart for quantum chemical calculations.

2.4.0. Instruments

2.4.1. pH Meter

The pH of different solutions was measured using Jenway pH Meter (Model No 3510). The pH meter was calibrated by using three different standard buffer solutions (pH 4.0, pH 7.0 and pH 10.0) within a range of ± 0.01-0.02 pH units before a measurement was performed.

2.4.2. Absorption Spectrometer

Absorption spectroscopy is the most widely used spectroscopic tool which provides the wavelength of a transition and the corresponding molar extinction coefficient (ε_λ) of a chromophore under investigation. The modern Ultra Violet-Visible (UV-Vis) spectrometer consists of light source, monochromator, detector, amplifier and recording devices. Quartz cells to hold the sample are used for the measurement of the absorption spectra.

In the present work, the absorption spectra were recorded on a double beam UV-Vis spectrometer Cary 100 from Varian. Deuterium and tungsten lamps are used as UV and visible sources, respectively. In the Cary 100, a photomultiplier tube (PMT) is used as detector. The error limits in absorption maximum wavelength were ± 1 nm

2.4.3. Steady State Spectrofluorimeter

Steady state fluorescence spectra were recorded on Edinburgh Instruments FSP 920, Jobin Yvon Spex Fluoromax 4 and Cary Eclipse spectrophotometers. As an illustration for the instrumentation of a spectrofluorimeter, description of FSP 920 instrument is shown in **Figure 2.4**. In the experiments, both emission and excitation slit widths were of same width and were maintained at 1 nm, 2 nm, and 5 nm in the above three instruments, respectively.

Optical System

The most common light source for fluorimeters is xenon arc lamp. These lamps provide a relatively uniform intensity over a broad spectral range from UV to near infrared (IR). Excitation monochromator is used to select the excitation wavelength. Fluorescence is collected at right angles with respect to the incident beam and the emitted light is detected through a monochromator by a PMT. Motorized monochromator is used for automatic scanning of wavelengths. The monochromators are controlled by the electronic devices and the computer. The optical module contains various parts: a sample holder, shutters, polarizers

if necessary, and a beam splitter consisting of a quartz plate reflecting a few percent of the exciting light towards a quantum counter or a photodiode.

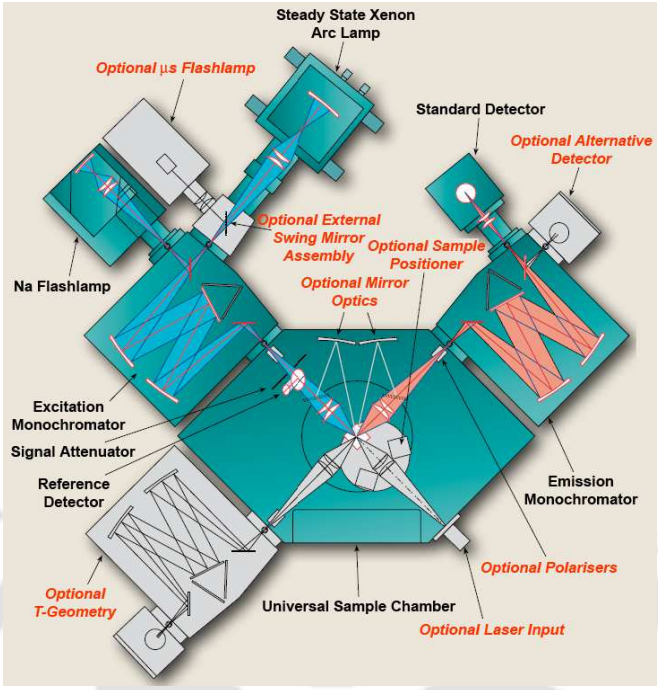

Figure 2.4. Block diagram of FSP 920 steady state fluorescence spectrophotometer from Edinburgh Instruments. Diagram was obtained from the catalogue of Edinburgh instruments FSP 920.

The emission spectrum reflects the variation of fluorescence intensity as a function of λ_{em} (the wavelength at which the fluorescence is observed) when the excitation wavelength (λ_{exc}) is fixed. The excitation spectrum shows the variation of fluorescence intensity as a function of λ_{exc} with fixed λ_{em}. The spectra are recorded as a function of wavelength and not wavenumber because the monochromators of spectrofluorimeter are equipped with gratings, so that for a given width of the input and output slits, the monochromators operate at a constant band pass expressed in wavelength. The fluorescence spectra are needed to be corrected for the distortion by the wavelength dependence of several components of the instrument.

Correction for Emission Spectra

The emission spectrum is distorted by the wavelength dependence of the emission monochromator efficiency and the photomultiplier response. In general, the correction factors are measured using a calibrated tungsten lamp or by a standard fluorescent dye whose corrected emission spectrum has been reported. Emission correction factors are provided by the manufacture in all the three instruments used.

Correction for Excitation Spectra

The excitation spectrum is distorted by the variations of the intensity of the exciting light. These variations are due to the wavelength dependence of the lamp intensity and of the transmission efficiency of the excitation monochromator. Because the quantum counter circumvents the wavelength dependence of the sensitivity of the sample and the reference photomultiplier. The ratio of the fluorescence signal from the sample to that from the quantum counter or photodiode, as a function of the excitation wavelength, provides in principle corrected excitation spectra. However, such correction procedures may be insufficient when very accurate measurements are needed (for instance when information is expected from the comparison of the absorption and excitation spectra). In fact, the optical geometry of the reference channel is not identical to that of the main channel, and the wavelength dependence of optical parts (e.g. focal length of lenses) may introduce some distortion into the excitation spectrum. It is then recommended to use correction factors obtained by using a fluorophore absorbing in the same wavelength range as that of the sample to be studied, and whose absorption spectrum is identical to its excitation spectrum. The ratio of the measured excitation spectrum of this reference compound – as described above using the quantum counter – to the absorption spectrum provides the correction factors that can be stored in the computer. It should be noted that most commercially available instruments are delivered with a file containing the correction factors and the manufacture provided the correction file for all three molecules.

FSP 920 is equipped with double excitation monochromator and the other instruments used for the measurements have single excitation monochromator. FSP 920 and Fluoromax 4 have 450 W and 150 W Xe arc lamps, respectively as light source. But Cary Eclipse employs 75 W pulsed Xe lamp as light source. All three instruments use Hamamatsu red sensitive PMT R928 as detector.

2.4.4. Time Resolved Spectrofluorimeter

Fluorescence lifetime is the time required by a population of *N* electronically excited fluorophores to decrease exponentially by a factor of *e* to *N/e* via the loss of energy through fluorescence and other nonradiative processes. The fluorescence lifetime may vary from tens of femtoseconds to nanoseconds. It is an intrinsic property of a fluorophore and is independent the way it is measured. It is considered as a state function, as it is independent of the initial perturbation conditions like excitation wavelength, one or multiphoton excitation, duration of light exposure, fluorescence intensity and fluorophore concentration. Moreover, it

is not affected by photobleaching. Since fluorescence occurs from an energetically unstable state, fluorescence lifetime is sensitive to internal and external factors. The internal factor comprises of the fluorophore structure and the external factors include temperature, polarity, viscosity and the presence of fluorescence quenchers.

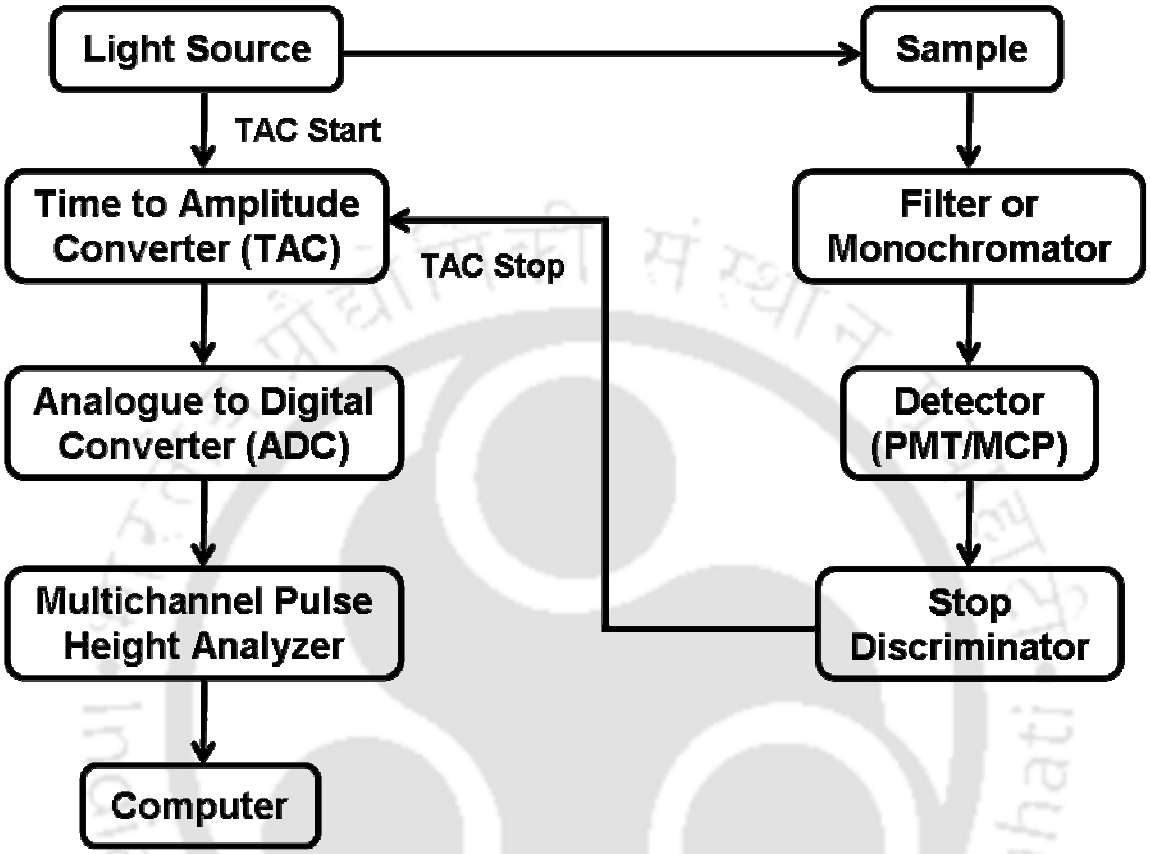

Figure 2.5. Block diagram of a TCSPC instrument.

There are two ways to determine the fluorescence lifetime of the fluorophores, frequency-domain and time-domain.[242-248] They have different instrumentation setups and follow different data acquisition methods, however, both approaches are mathematically equivalent and their data can be interconverted by Fourier transform. In frequency domain method, the incident light is sinusoidally modulated at high frequencies such that the emission occurs at the same frequency as the incident light. The difference between the incident and emitted light is that the emitted light experiences a phase delay and change in the amplitude relative to the excitation light (demodulation). Data are acquired with photomultipliers or charge-coupled devices (CCD) equipped with a gain modulator.

In time-domain, the sample to be analyzed is excited with a short light pulse from a light source with sufficient delay between pulses. The light source can be flash lamp, pulsed laser, laser diode, or LED. Various methods are available for data collection. The most common technique is the time correlated single photon counting (TCSPC) which is applied in

this work.[247,248] **Figure 2.5** explains schematically the working principle of a TCSPC instrument. In TCSPC method, the light source beam is split into start and stop signal pulses. The start signal pulse travels to a PMT or micro-channel plate (MCP) photomultiplier which activates the time-to-amplitude converter (TAC). The stop signal pulse travels through the sample. The growth of ramp signal in TAC is stopped by this pulse. The TAC output can be amplified by an amplifier, and this analogue pulse of height corresponding to a measured time of the signal goes through further processing to convert to digital pulse through the analogue to digital converter (ADC).

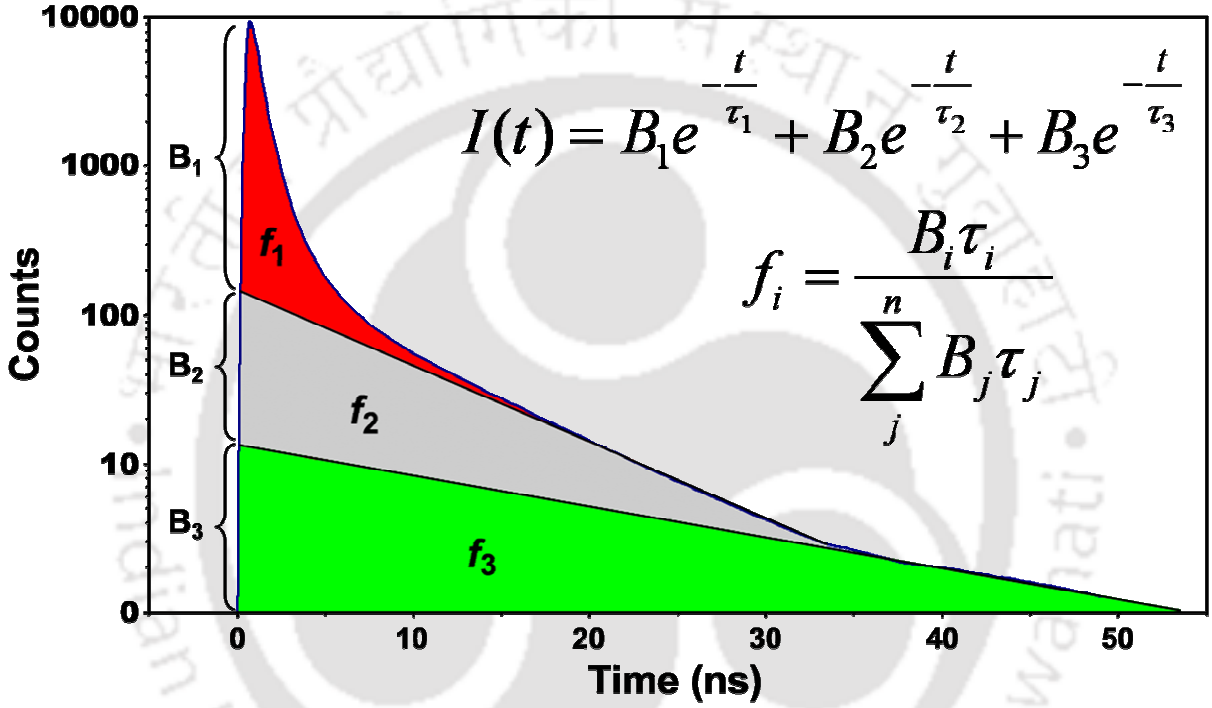

Figure 2.6. Exponential decay model for three components.

Since the fluorophores emit photons at different relaxation times following their excitation by radiation, the decay time of single molecules must have a certain rate rather than occurring at a specific time with excitation. The principle of TCSPC is the detection of single photons and the measurement of their arrival times in respect to a reference signal from the light source. The TCSPC method needs a high repetitive light source to accumulate a sufficient number of photons since this is a statistical method and requires many numbers of statistical data precision. The time measurement of the start and stop sequence is represented by an increase of a memory value in a histogram. Thus, this experiment must be repeated many times to gather sufficient photons in the full range of delays between excitation and emission. The resulting histogram counts versus the time channels on the x-axis represents

the curve of fluorescence decay profiles. A typical emission decay of a fluorophore consisting of three components obtained from TCSPC method is shown in **Figure 2.6**.

In most cases, the TCSPC technique has limits for the temporal resolution and lifetime range measurable for the fluorescence lifetimes. Therefore, for the curve fittings the method involving linearization of the fitting function and least-squares fitting is the most widely used deconvolution technique. The fluorescence temporal profiles were derived by deconvolution procedures with the instrument response using nonlinear least-squares fittings.

In the entire work, fluorescence lifetimes were measured with the use of *LifeSpec II* from Edinburgh Instruments. *LifeSpec II* employs Hamamatsu MCP detector that has response time of 50 ps. The light sources used to excite the sample were 308 nm LED from PicoQuant and 375 nm laser diode from Edinburgh with full pulse widths of 635 ps and 2 ps, respectively at half-maximum. Time-resolved data were analyzed with reconvolution method based on discrete components analysis model using the FAST software[249] developed by the Edinburgh Instruments Ltd. The goodness of fit was determined by the reduced χ^2 values and weighted residuals (X) which were between the range of ± 6. The reduced χ^2 and weighted residuals (X) are given by the following equations.

$$\chi^2 = \sum_i w_i^2 \frac{[S_i - F_i]^2}{n} \qquad \textbf{(2.10)}$$

$$X_i = w_i(S_i - F_i) \qquad \textbf{(2.11)}$$

where w_i, F_i, and S_i are the weighting factor, measured value, and fitted value, respectively and n is the number of fitted data points subtracted by the number of lifetime parameters used in the fit. The error limits in the lifetime values were ± 0.05 ns.

2.4.5. Other Instruments

Fourier transform infra red (FTIR) spectra in the range 450-4000 cm^{-1} were recorded in KBr pellets on Nicolet Impact-410. Fourier transform NMR spectra of the synthesized compounds (~ 5 mg) were recorded in ~ 400 μL of $CDCl_3$ or DMSO-d_6 with tetramethylsilane as the standard for ^1H nuclei on Varian instrument of 400 MHz. The chemical shifts were recorded in parts per million (ppm) on the scale using tetramethylsilane (TMS) or residual solvent peak as the reference.

For single crystal structure determination the intensity data were collected using Bruker SMART APEX-II CCD diffractometer equipped with a fine focus 1.75 kW sealed tube graphite monochromated Mo-K_α radiation (λ = 0.71073 Å) at 298 K with increasing ω

(width of 0.3^{o} per frame) at a scan speed of 5 second per frame. Cell parameters were retrieved using SMART software[250] and refined with SAINT on all observed reflections. Data reduction was performed with the SAINT software and corrected for Lorentz and polarization effects. Absorption corrections were applied with the program SADABS.[251] The structure was solved by direct method implemented in SHELXS-97 program[252] and refined by full-matrix least-square method on F_2 using SHELXL-97.[253] All non-hydrogen atomic positions were located in difference Fourier map and refined anisotropically. The hydrogen atoms were placed in their geometrically generated positions. The positional and temperature factors were refined isotropically. Structural illustrations have been drawn with MERCURY 2.3 for Windows.[254]

Chapter 3

Excited State Intramolecular Proton Transfer and Rotamerism in 2-(2'-Hydroxyphenyl)benzimidazole and its Nitrogen Substituted Analogues

3.0. Introduction

Since the first report of Dogra et al. on ESIPT in HPBI,[95] several groups investigated HPBI.[99,255-258] Dogra's group and Rodriguez's group studied the role of nitrogen substitution in different parts of HPBI. Dogra's group concentrated on nitrogen substitution in the benzene ring of HPBI by synthesizing and studying HPIP-b[6,174] and HPIP-c.[175] Their works revealed that N-heteroatom substitution in the benzene ring reduces the quantum yield, and the excited state lifetimes also strongly depend not only on the presence of nitrogen but also its position. Rodriguez's group[177,178] examined the role of nitrogen substitution on the phenolic ring by studying 2-(3'-hydroxy-2'-pyridyl)benzimidazole (3',2'-HPyBI) and they found that the quantum yield of the phototautomer product increases by nitrogen substitution. However, Dogra found that when the position of substitution changed, 2-(2'-hydroxy-3'-pyridyl)benzimidazole (2',3'-HPyBI) does not undergo ESIPT.[176] All these results clearly suggest that the presence and position of nitrogen atom strongly perturb the ESIPT process and the related photophysics of these molecules.

Several *ab initio* and semiempirical calculations have been performed on HPBI and other 2-hydroxyphenylbenzazoles to demonstrate various aspects of their photophysics.[57,98,259-261] Recently Chattopadhyay et al. carried out AM1-SCI calculations on 2-hydroxyphenylbenzazoles including HPBI and compared the calculated results with experimental results.[51,52] Dogra et al. performed semiempirical calculations on HPIP-b and HPIP-c to rationalize the experimental findings.[6,174]

In this chapter, the role of nitrogen substitution in HPBI on ESIPT and rotamerism are investigated by DFT calculation and temperature studies. The chapter is divided into three sections. The theoretical study on the effect of nitrogen substitution in benzene ring of HPBI is carried out in the first section. The second section is the extension of the DFT study to examine theoretically the role of nitrogen substitution in the phenolic ring of HPBI on ESIPT and rotamerism. The third section is an experimental study of temperature effect on ESIPT in HPBI and its nitrogen substituted analogues viz. HPIP-b and HPIP-c.

3.1.0. Nitrogen Substitution in the Benzene Ring of HPBI

The common characteristics of HPBI and azo substituted compounds HPIP-b, HPIP-c and 8-(2'-hydroxyphenyl)-9*H*-purine (HPP, **Chart 3.1**) are summarized below: *cis*-enol, the intramolecularly hydrogen bonded form is the most stable form of these compounds. Upon excitation, ultrafast IPT occurs in *cis*-enol to give the phototautomer. In polar solvents *trans*-enol conformer was observed, and is responsible for the normal emission. But the quantum

yields and the excited state lifetimes strongly depend not only on the presence of nitrogen but also its position.

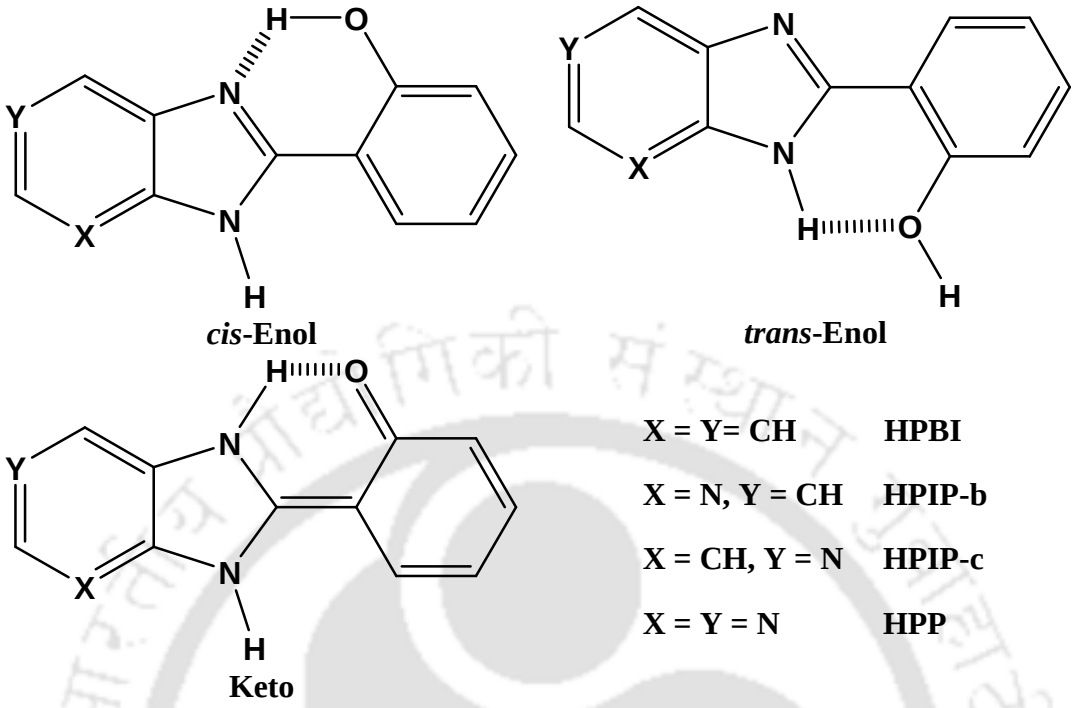

Chart 3.1. HPBI and its nitrogen substituted molecules.

3.1.1. Molecular Geometries and Energies

Two isomeric forms are possible for HPIP-b, HPIP-c and HPP and we labeled the respective isomeric forms as HPIP-b', HPIP-c' and HPP' (**Scheme 3.1**). The optimized energies calculated for all the forms of both the isomers are compared in **Table 3.1**. For all rotameric and tautomeric forms, HPIP-b, HPIP-c and HPP isomers are more stable than their respective forms of HPIP-b', HPIP-c' and HPP' isomers. The keto forms of the isomers are interconvertable by torsional rotation of phenolic moiety. Torsional rotation of keto form followed by reverse proton transfer will lead to the other isomer (**Scheme 3.1**).

Table 3.1. Relative energies (eV) of different forms of HPIP-b, HPIP-c, HPP and their respective isomers (HPIP-b', HPIP-c', HPP') with respect to their corresponding *cis*-enol forms of HPIP-b, HPIP-c, HPP isomers in the S_0 state.

Molecule	*cis*-Enol	*trans*-Enol	Keto
HPIP-b	0.0	0.2526	0.4343
HPIP-b'	0.1497	0.4031	0.5475
HPIP-c	0.0	0.4485	0.2259
HPIP-c'	0.0044	0.2329	0.4365
HPP	0.0	0.2176	0.4700
HPP'	0.1368	0.3560	0.5637

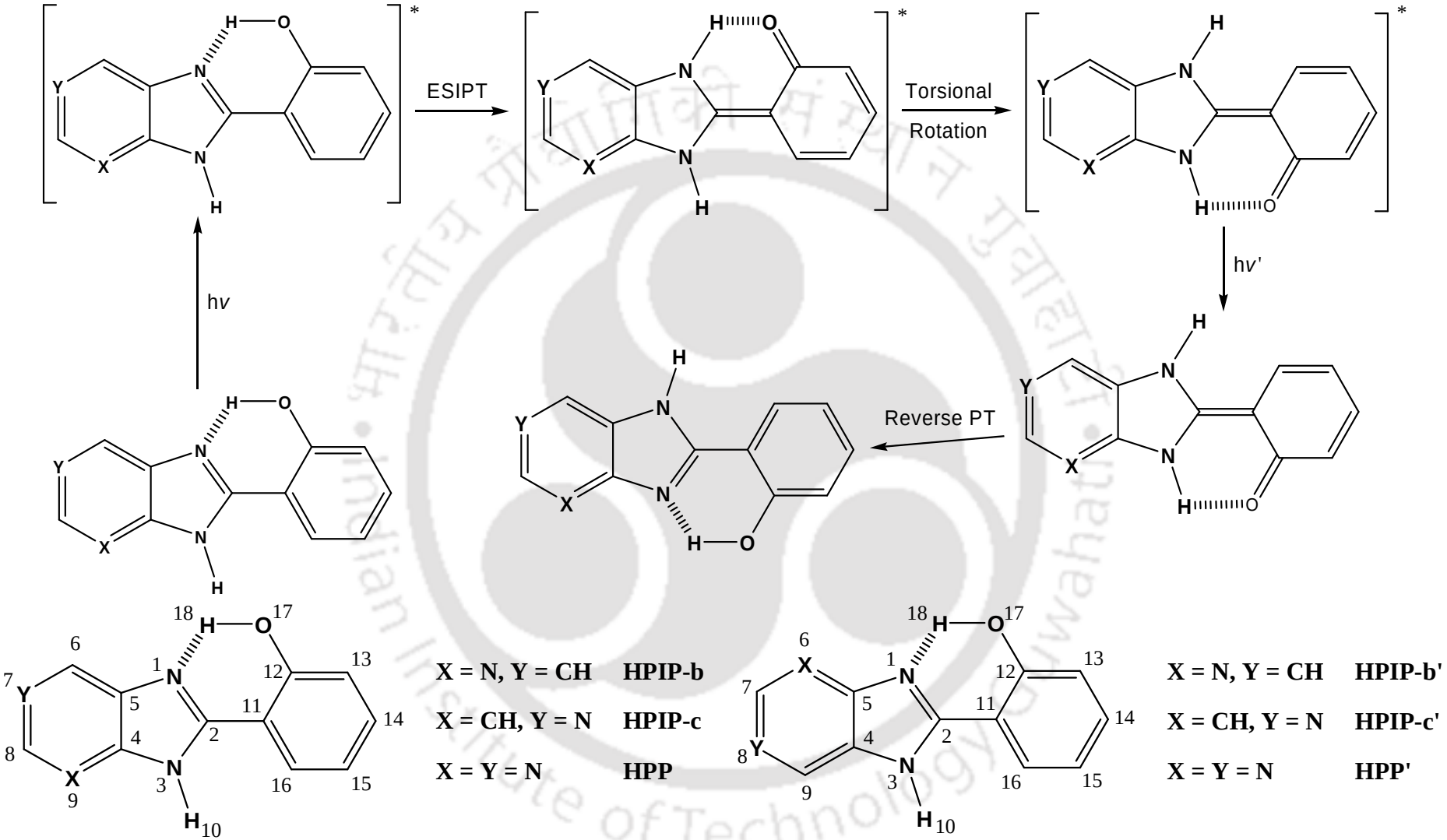

Scheme 3.1. Interconversion of isomeric forms of nitrogen substituted analogues of HPBI.

The optimized parameters of *cis*-enol, *trans*-enol and keto forms for all the molecules in the ground state are compiled in **Table 3.2**. The calculation predicts the *cis*-enol as the most stable geometry in all the molecules and further the dihedral angles between the imidazole ring and phenyl ring as 0° and 180° in *cis*- and *trans*-enol conformers in all the molecules. The corresponding angles reported from semiempirical calculations for HPBI,[52,98] HPIP-b[174] and HPIP-c[175] are about 40° and 140°. The relative stability of the *cis*-enol to *trans*- enol decreases with nitrogen substitution and follows the order HPBI > HPIP-b' > HPIP-b > HPIP-c' > HPIP-c > HPP' > HPP. This may be due to relative weakening of hydrogen bond between N_1 and H_{18} in *cis* conformer of enol (**Table 3.2**). Thus substitution of nitrogen in benzene ring affects the relative population of the two rotamers in the ground state. The potential energy surfaces (PES) for conversion of *cis*-enol to *trans*-enol are constructed by optimizing the molecular geometries with different preset torsional angle between the hydroxyphenyl plane and the heterocyclic plane. The PES thus constructed are shown in **Figure 3.1**. The barrier height for the conversion of *cis*-enols to *trans*-enols are found to be 0.512, 0.522, 0.538, 0.501, 0.511, 0.515, 0.541 eV for HPBI, HPIP-b, HPIP-b', HPIP-c, HPIP-c', HPP and HPP' respectively. The barrier heights for the reverse transformation for the compounds are 0.252, 0.270, 0.285, 0.275, 0.283, 0.297, 0.322 eV respectively.

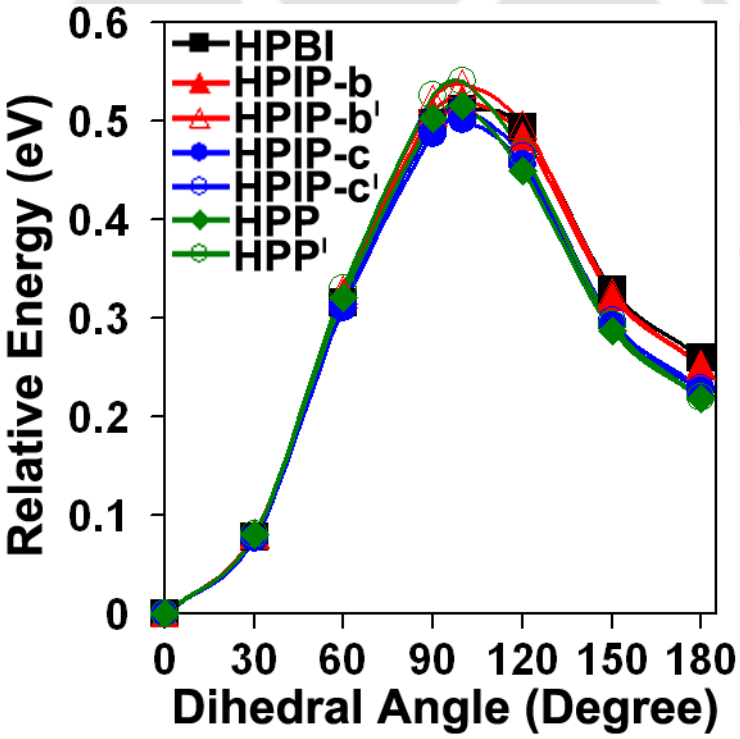

Figure 3.1. Plot of molecular energy as a function of torsional angle between hydroxyphenyl plane and heterocylic plane for different molecules in S_0 state.

Table 3.2. Optimized parameters for different enols and keto form of molecules in S_0 and S_1 states. Energy difference between other forms and *cis*-enol form (ΔE, eV), dipole moment (μ, D), interatomic distances (R_{xx}, Å) and charge on nitrogen. For the atom numbering, refer Scheme 3.1. Values in parenthesis are that correspond to S_1 state.

Molecule	Parameter	*cis* -enol	*trans*-enol	Keto
HPBI	ΔE	0.0 (0.0)[1]	0.2597 (0.2621)	0.4075 (-0.3387)
	μ	3.9 (3.8)	4.7 (3.9)	5.9 (4.9)
	R_{OH} (17,18)	0.998 (0.964)	0.970 (0.948)	1.630 (1.963)
	R_{NH} (1,18)	1.732 (1.825)	-	1.057 (1.001)
	R_{OH} (17,10)	-	2.038 (2.097)	-
HPIP-b	ΔE	0.0 (0.0)	0.2526 (0.3884)	0.4343 (-0.3884)
	μ	1.6 (1.5)	3.6 (2.6)	3.9 (2.7)
	R_{OH} (17,18)	0.996 (0.964)	0.970 (0.948)	1.611 (1.953)
	R_{NH} (1,18)	1.736 (1.824)	-	1.357 (1.001)
	R_{OH} (17,10)	-	2.050 (2.112)	-
HPIP-b'	ΔE	0.0 (0.0)	0.2534 (0.3574)	0.3979 (-0.4393)
	μ	6.1 (5.8)	6.8 (6.5)	7.4 (6.5)
	R_{OH} (17,18)	0.998 (0.966)	0.970 (0.948)	1.685 (1.987)
	R_{NH} (1,18)	1.735 (1.820)	-	1.048 (1.001)
	R_{OH} (17,10)	-	2.030 (2.089)	-
HPIP-c	ΔE	0.0 (0.0)	0.2259 (0.3685)	0.4485 (-0.3531)
	μ	5.3 (4.8)	7.3 (5.9)	5.7 (5.1)
	R_{OH} (17,18)	0.996 (0.965)	0.970 (0.948)	1.626 (1.961)
	R_{NH} (1,18)	1.743 (1.821)	-	1.058 (1.001)
	R_{OH} (17,10)	-	2.030 (2.102)	-
HPIP-c'	ΔE	0.0 (0.0)	0.2286 (0.4001)	0.4321 (-0.3882)
	μ	3.6 (3.9)	6.4 (5.5)	3.5 (2.9)
	R_{OH} (17,18)	0.997 (0.968)	0.970 (0.948)	1.621 (1.954)
	R_{NH} (1,18)	1.737 (1.800)	-	1.060 (1.954)
	R_{OH} (17,10)	-	2.029 (2.097)	-
HPP	ΔE	0.0 (0.0)	0.2176 (0.2980)	0.4700 (-0.3912)
	μ	3.6 (3.7)	6.5 (5.3)	3.2 (2.9)
	R_{OH} (17,18)	0.995 (0.966)	0.970 (0.948)	1.617 (1.952)
	R_{NH} (1,18)	1.746 (1.816)	-	1.060 (1.002)
	R_{OH} (17,10)	-	2.038 (2.117)	-
HPP'	ΔE	0.0 (0.0)	0.2193 (0.2946)	0.4270 (-0.4346)
	μ	5.9 (6.4)	8.1 (7.9)	5.7 (5.4)
	R_{OH} (17,18)	0.996 (0.970)	0.970 (0.949)	1.677 (1.973)
	R_{NH} (1,18)	1.741 (1.790)	-	1.050 (1.002)
	R_{OH} (17,10)	-	2.022 (2.089)	-

[1]Energy of *cis* enol in S_0 and S_1 states are -18672.8614 eV and -18672.5751 eV, respectively.

On the other hand the relative stability of *cis*-enol to keto tautomer increases in the order HPIP-b' < HPBI < HPP' < HPIP-c' < HPIP-b < HPIP-c < HPP. In general, the relative

stability of *cis*-enol to keto tautomer increases with nitrogen substitution. Exceptional behavior of HPIP-b' and HPP' may be due to the presence of pyridine ring nitrogen (N_6) with lone pair near the imidazole nitrogen (N_1) that also has lone pair and the proton transfer reduces the lone pair-lone pair repulsion.

Table 3.3. Calculated excitation and fluorescence spectral data (nm) for different isomers along with corresponding experimental data.

Molecule	Excitation		Fluorescence	
	Cal.	Exp. (Dioxane)	Cal.	Exp. (Dioxane)
HPBI				
cis-enol	316	293, 318, 332[a]	341	
trans-enol	307	304, 326[a]	343	360[a,b]
Keto	389		429	458[a,b]
HPIP-b				
cis-enol	324	318, 327[C]	344	
trans-enol	307	315, 329 (sh)[C]	340	335, 350, 363[c]
Keto	409		450	485[c]
HPIP-b'				
cis-enol	326		344	
trans-enol	306		337	
Keto	412		451	
HPIP-c				
cis-enol	315	327[d]	337	
trans-enol	302	299, 309 (sh)[d]	340	337, 342, 355[d]
Keto	392		434	476[d]
HPIP-c'				
cis-enol	318		336	
trans-enol	293		326	
Keto	395		439	
HPP				
cis-enol	326		341	
trans-enol	309		339	
Keto	411		456	
HPP'				
cis-enol	330		344	
trans-enol	317		342	
Keto	416		461	

[a]Data from present work. [b]Ref. 98, [c]Ref. 174, [d]Ref. 175.

Since the experimental excitation energies are available in the literature for both conformers (except for HPP) we calculated and compared the excitation energy of different forms with the experimental values (**Table 3.3**). The calculated data show that the excitation

spectrum was red shifted on moving from HPBI to HPIP-c to HPIP-b and is consistent with the experimental report. The excitation energies predicted by the calculations are also in reasonable agreement with the experimental data.

The parameters obtained for optimized molecular geometries in the first excited state are compiled in **Table 3.2**. The energy difference between *cis*-enol and keto increases with nitrogen substitution. The fluorescence data calculated for different isomers are in reasonable agreement with the available experimental spectral data (**Table 3.3**).

3.1.2. Proton Transfer

The CIS method is known to overestimate the energy barriers for proton transfer reactions.[57,262,263] The TDDFT has been proven much more reliable with proton transfer reactions.[57,213,220,262,263] Thus the PES for proton transfer process have been generated in S_0 and S_1 states using the distinguished coordinate approach with the OH bond elongation as the primary reaction coordinate by TDDFT/B3LYP/6-31G+(d,p) calculations. The diagrams are shown in **Figure 3.2** and the data are compiled in **Table 3.4**.

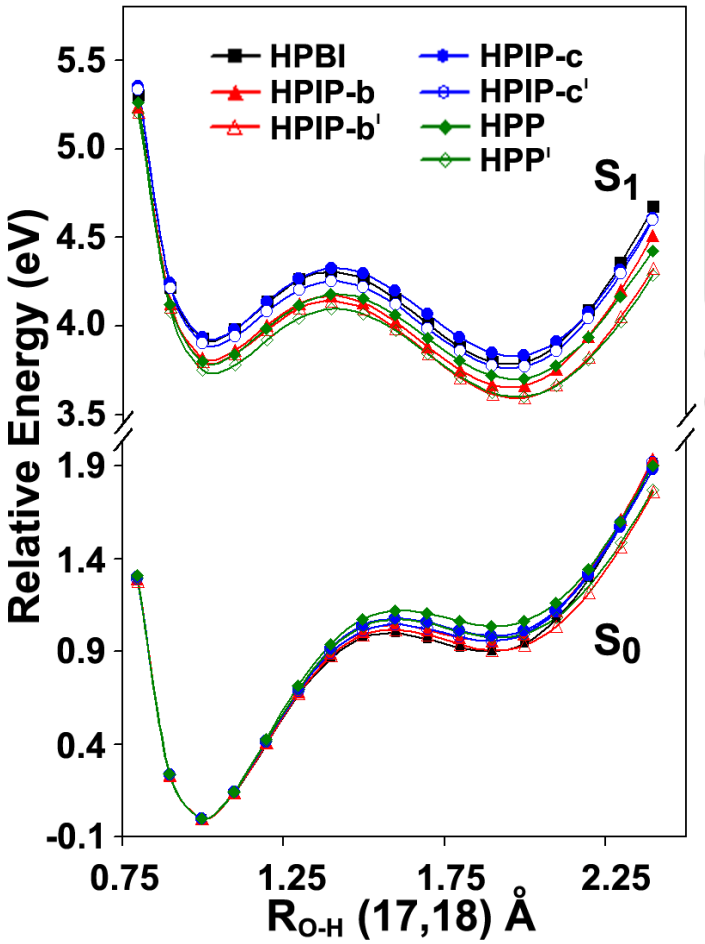

Figure 3.2. Simulated PES for proton transfer reaction tautomers in the S_1 and S_0 states for different molecules.

Table 3.4. Energy difference between Keto and *cis*-Enol along the reaction coordinates and barrier for proton transfer reaction (eV).

Molecule	Energy Difference between Keto and *cis*-Enol	Energy Barrier	
		***cis*-Enol**	**Keto**
HPBI			
S_1 State	-0.1326	0.3778	0.5104
S_0 State	0.9195	0.9986	0.0790
HPIP-b			
S_1 State	-0.1557	0.3521	0.5078
S_0 State	0.9535	1.0433	0.0898
HPIP-b'			
S_1 State	-0.2052	0.3380	0.5431
S_0 State	0.9053	1.0177	0.1124
HPIP-c			
S_1 State	-0.0985	0.3902	0.4887
S_0 State	0.9851	1.0789	0.0939
HPIP-c'			
S_1 State	-0.1307	0.3521	0.4829
S_0 State	0.9566	1.0463	0.0897
HPP			
S_1 State	-0.0972	0.3761	0.4733
S_0 State	1.0357	1.1195	0.0838
HPP'			
S_1 State	-0.1518	0.3448	0.4966
S_0 State	0.9744	1.0743	0.0999

The general features of PES are summarized below: The proton transfer process is endothermic in the ground state and exothermic in the first excited state. Thus thermodynamically unfavorable proton transfer process becomes thermodynamically favorable in the S_1 state. The potential energy barrier for the proton transfer reaction is also appreciably lowered in the S_1 state compared to S_0 state and the proton transfer become favored in the S_1 state. The barrier for reverse transfer is very small in the S_0 state, but increases in the S_1 state. The energy difference between the enol and keto tautomers along the reaction coordinates in S_0 state increase in the order HPIP-b' < HPBI < HPIP-b < HPIP-c' < HPP' < HPIP-c < HPP. On the other hand, the thermodynamic feasibility of proton transfer in the S_1 state decreases with nitrogen substitution except HPIP-b, HPIP-b' and HPP'. A similar effect was also found when –NH– is replaced by more electronegative –S– and –O– in HPBI.[57] The difference in behavior of HPIP-b' and HPP' may be due to the reduced lone pair-

lone pair repulsion in keto tautomer as mentioned earlier. This was further supported by fact that the barrier height for reverse proton transfer follows the order HPIP-b' > HPBI > HPIP-b > HPP' > HPIP-c > HPIP-c' > HPP i.e. for HPIP-b' is higher than HPBI and for HPP' is higher than HPIP-c'.

Table 3.5. Properties of the energy minima and the transition state of tautomer rotamers and the values in parenthesis are that of ab initio calculations.

	***cis*-keto**	**twisted- keto**	***trans*-keto**
	HPBI		
Relative Energy (eV)	0.0	-0.2619 (0.3769)	
$S_1 \rightarrow S_0$ Transition energy (eV)	2.89 (3.93)	0.75 (2.19)	
Oscillator Strength	0.3300 (0.6100)	0.0001 (0.0010)	
	Dipole Moment (D)		
S_1 State	(4.9)	(3.6)	
S_0 State	5.9	8.2	
	Charge on Benzimidazole ring		
S_1 State	(0.5423)	(0.0816)	
S_0 State	0.8496	(0.6536)	
ϕ_f[1]	0.65 (ref 24)		
	HPIP-b		
Relative Energy (eV)	0.0	- 0.2589 (0.3391)	0.0870 (0.0704)
$S_1 \rightarrow S_0$ Transition energy (eV)	2.76 (3.88)	0.70 (2.21)	2.75 (3.86)
Oscillator Strength	0.3024 (0.6324)	0.0003 (0.0011)	0.3122 (0.6438)
	Dipole Moment (D)		
S_1 State	(2.7)	(4.3)	(6.5)
S_0 State	3.9	7.6	7.4
	Charge on Imidazopyridine ring		
S_1 State	(0.3754)	(0.0763)	(0.3759)
S_0 State	0.8895	(0.6808)	0.9173
ϕ_f[1]	0.26 (ref 30)		
	HPIP-c		
Relative Energy (eV)	0.0	- 0.3422 (0.2711)	-0.0355 (-0.0194)
$S_1 \rightarrow S_0$ Transition energy (eV)	2.85 (3.91)	0.67 (2.12)	2.83 (3.90)
Oscillator Strength	0.2941 (0.5591)	0.0001 (0.0006)	0.2891 (0.5684)
	Dipole Moment (D)		
S_1 State	(5.1)	(6.2)	(2.9)
S_0 State	5.7	6.2	3.5
	Charge on Imidazopyridine ring		
S_1 State	(0.3780)	(0.0734)	(0.2343)
S_0 State	0.3711	(0.6430)	0.3701
ϕ_f[1]	0.22 (ref 31)		
	HPP		
Relative Energy (eV)	0.0	-0.3437 (0.2124)	0.0544 (0.0470)
$S_1 \rightarrow S_0$ Transition energy (eV)	2.72 (3.85)	0.57 (2.09)	2.69 (3.82)
Oscillator Strength	0.2684 (0.5689)	0.0002 (0.0006)	0.2761 (0.5912)
	Dipole Moment (D)		
S_1 State	(2.9)	(6.6)	(5.4)
S_0 State	3.2	5.3	5.7
	Charge on Purine ring		
S_1 State	(0.3469)	(0.0642)	(0.3431)
S_0 State	0.7933	(0.5019)	0.7972

[1]Fluorescence quantum yields (Φ_f) are that of tautomers in dioxane.

3.1.3. Torsion Rotation of Keto Tautomer

One of the important consequences of nitrogen substitution is the decrease in the fluorescence quantum yield (**Table 3.5**). Several mechanisms for nonradiative transition of

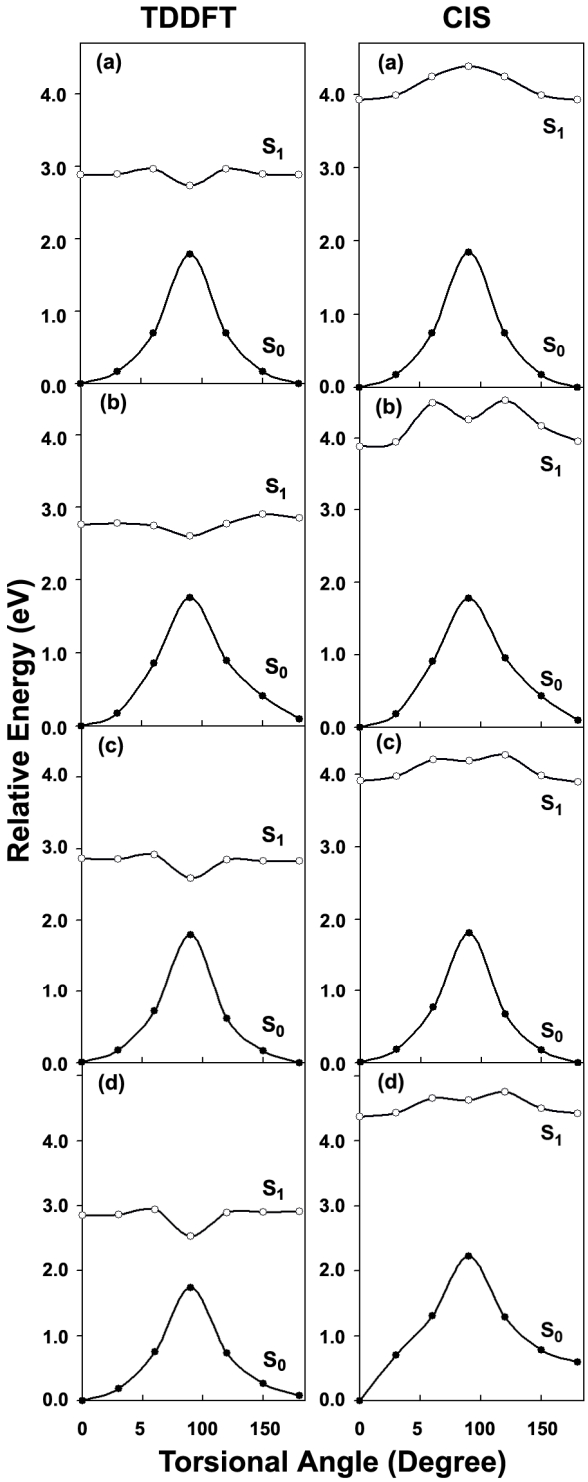

Figure 3.3. Simulated PES for torsion rotation of tautomers in the S_1 and S_0 states (a) HPBI, (b) HPIP-b, (c) HPIP-c and (d) HPP (left panel TDDFT calculations and right panel CIS calculations).

ESIPT molecules have been proposed but still unproven. The ICT reaction in the excited state keto form which results in twisted geometry is proposed as one of the possible paths for quenching in 2-(2'-hydroxyphenyl)-oxazole (HPO) and thiazole (HPT).[96] Ab initio calculations on HPO and HPT predicted twisted conformations have a biradicaloid nature and have the minimum energy in the S_1 state. Vazquez et al. investigated the effect of substituting nitrogen on the phenyl ring of 2-(2'-hydroxyphenyl)benzazoles and suggested that the radiationless decay involves a proton coupled charge transfer process from dissociated phenol or pyridinol moiety to protonated benzazole moiety.[264]

Dissociated phenol being a better donor than the dissociated pyridinol moiety, with increase in electron accepting strength by nitrogen substitution in protonated benzimidazole the feasibility of such a process increases in the present systems. We have constructed the potential energy surface for torsional motion of hydroxyphenyl moiety relative to the heterocyclic ring from the relaxed keto tautomers by performing partial optimization on different geometries that have preset torsional angle. As mentioned earlier such a rotational motion of HPIP-b, HPIP-c and HPP keto tautomers result in the respective keto tautomers obtained from HPIP-b', HPIP-c' and HPP'. Then, as in other cases we have performed single point TDDFT calculations over CIS optimized geometries. From these calculations, it is found that the first electronic transition ($S_1 \leftarrow S_0$) corresponded only to the promotion of an electron from HOMO to LUMO in all of these molecules. The PES constructed by TDDFT predict that c*is*- and *trans*-rotamers are stable forms of keto tautomer in S_0 as well as in S_1 states (**Figure 3.3**). The perpendicular geometry of tautomer possesses the maximum energy in S_0 state and the minimum energy in S_1 state. The full optimization of S_1 minimum starting with the perpendicular structure of the S_0 state leads to a bent or twisted structure with nonplanar heterocyclic subsystems (**Table 3.6** and **Figure 3.4**). This twisted structure is the result of pyramidalization of imidazole ring subsystem by rehybridization. Such a rehybridization is due to increase in electron density of five member ring and is consistent with the literature report.[96,265] The charge calculations on heterocyclic and phenolic moieties indicate the dot-dot electronic configuration for the perpendicular geometry in the S_1 state. The dot-dot electronic configuration is consistent with previous finding of HPO and HPT.[96] However, it was reported for HPO and HPT that the $S_1 \rightarrow S_0$ transition corresponds to the transfer of nearly a full electron. In the present cases the charges on the individual moieties in the ground state suggests that $S_1 \rightarrow S_0$ transition corresponds to partial electron transfer from heterocyclic moiety to phenolic moiety.

Table 3.6. Selected bond lengths and angles of the keto tautomers in the optimized S_0 and S_1 states. For the atom numbering, refer Figure 3.4.

Geometry Parameters	*cis*-keto		Twisted-Keto		*trans*-Keto	
	S_0 State	S_1 State	S_0 State	S_1 State	S_0 State	S_1 State
HPBI						
N1 C2	1.353	1.358	1.350	1.409	-	-
N3 C2	1.370	1.370	1.350	1.410		
C2 C11	1.416	1.406	1.448	1.436	-	-
C11 C12	1.463	1.502	1.461	1.488	-	-
C11 C16	1.420	1.394	1.407	1.421	-	-
C12 O17	1.273	1.230	1.258	1.207	-	-
N1 C2 C11 C12	0.00	-0.10	88.0	67.7	-	-
C5 N1 C2 C11	180.0	180.0	-174.93	-151.8	-	-
HPIP-b						
N1 C2	1.358	1.360	1.354	1.411	1.376	1.371
N3 C2	1.371	1.371	1.350	1.402	1.356	1.360
C2 C11	1.414	1.406	1.446	1.438	1.410	1.407
C11 C12	1.463	1.499	1.462	1.488	1.466	1.499
C11 C16	1.421	1.392	1.407	1.419	1.423	1.392
C12 O17	1.274	1.231	1.258	1.207	1.267	1.229
N1 C2 C11 C12	0.1	0.0	88.4	67.9	180.0	180.0
C5 N1 C2 C11	179.8	180.0	-174.4	-149.1	180.0	180.0
HPIP-c						
N1 C2	1.353	1.357	1.349	1.410	1.370	1.368
N3 C2	1.376	1.376	1.355	1.410	1.359	1.364
C2 C11	1.413	1.406	1.445	1.435	1.413	1.406
C11 C12	1.464	1.501	1.462	1.488	1.464	1.501
C11 C16	1.421	1.391	1.407	1.421	1.422	1.391
C12 O17	1.272	1.230	1.258	1.207	1.272	1.230
N1 C2 C11 C12	-0.02	-0.01	87.6	68.1	180.0	180.0
C5 N1 C2 C11	180.0	180.0	-174.5	-151.7	180.0	180.0
HPP						
N1 C2	1.358	1.359	1.353	1.412	1.376	1.370
N3 C2	1.378	1.377	1.356	1.404	1.363	1.365
C2 C11	1.409	1.406	1.443	1.436	1.406	1.407
C11 C12	1.465	1.498	1.462	1.488	1.468	1.498
C11 C16	1.423	1.390	1.408	1.419	1.389	1.425
C12 O17	1.271	1.230	1.258	1.207	1.266	1.229
N1 C2 C11 C12	0.0	0.0	87.9	69.3	180.0	180.0
C5 N1 C2 C11	180.0	180.0	-174.0	-149.5	180.0	180.0

It is reported in the literature that TDDFT poorly describes some charge transfer situations, in which little or no overlap between the atomic orbitals contributing to the HOMO and those to the LUMO.[266,267] Since we have also constructed the potential energy surface by performing single point over CIS optimized geometries, we have presented the CIS energy curves also (**Figure 3.3**). CIS curve for HPBI differs significantly from that of TDDFT in the sense that the unlike TDDFT no minimum is observed at the twisted geometry by CIS. Similarly a barrier was found at twisted keto for 2-(2'-hydroxyphenyl)-4-methyloxazole by CIS calculation.[220] On the other hand in nitrogen substituted analogues CIS

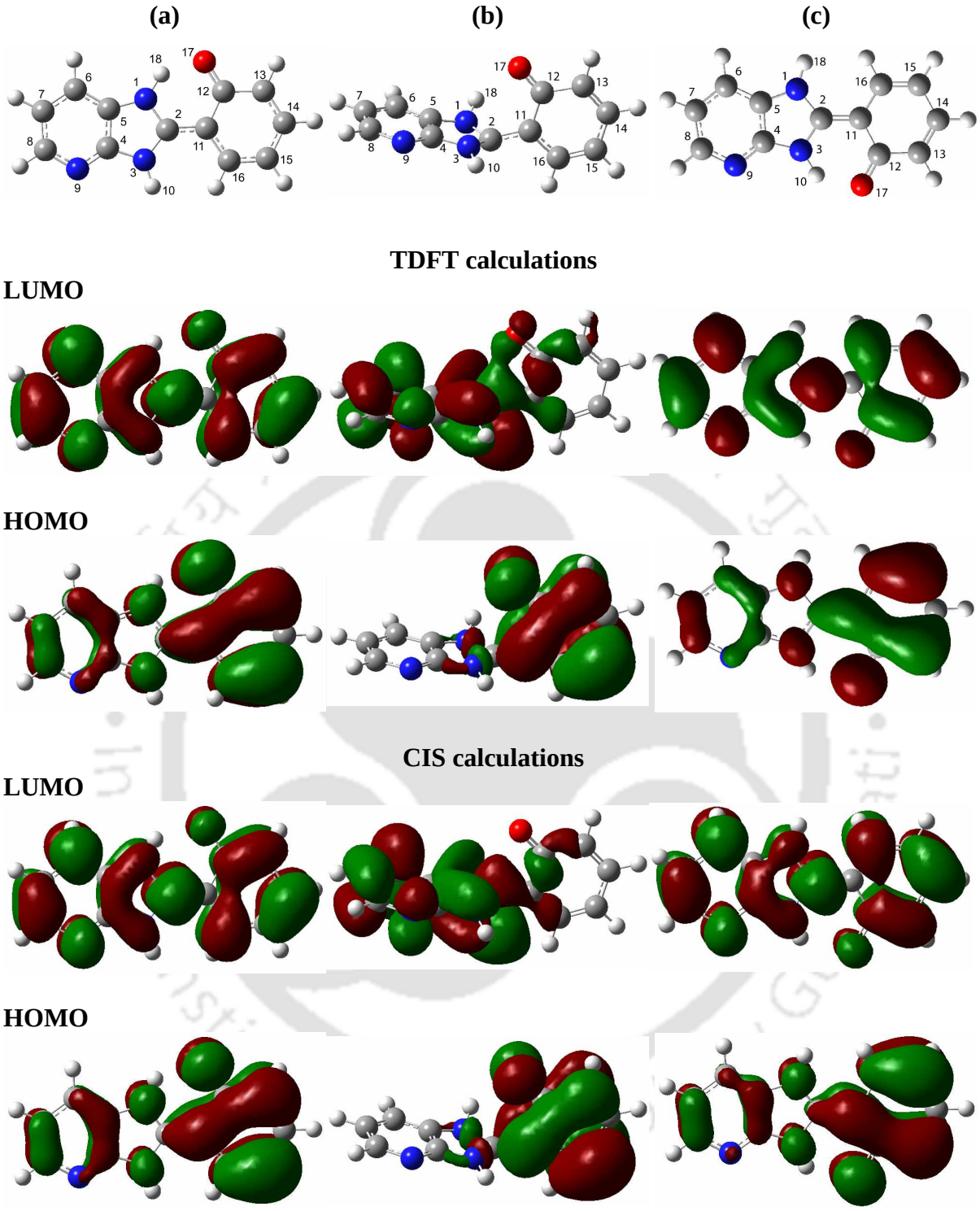

Figure 3.4. Optimized structures of (a) *cis*, (b) twisted minimum and (c) *trans* of keto on the excited state surface along with corresponding LUMO and HOMO for HPIP-b.

also predicted a minimum for twisted geometry. But the energies of the twisted geometries are higher than that of planar isomers. While the transition energies calculated for planar keto by TDDFT is closer to experimental values the CIS method overestimates them. It is difficult to predict whether TDDFT or CIS is closer to the correct description. However, both the calculations predict that the S_1-S_0 energy gap decreases in order HPBI > HPIP-b > HPIP-c >

HPP (**Table 3.5**). According to energy gap law[267b] the decrease in energy gap would lead to increase in non radiative rate. Thus the nitrogen substitution in benzene ring of HPBI increases the torsion induced nonradiative decay of keto tautomer in the order HPBI < HPIP-b < HPIP-c < HPP. The results are in good agreement with the experimental findings that the fluorescence quantum yield for tautomer decreases in the order HPBI > HPIP-b > HPIP-c.[174,175]

3.1.4. Conclusion

A comparative theoretical study of nitrogen substitution in the benzene ring of HPBI is presented. The calculated excitation and fluorescence spectral data agree well with the available experimental results. The present study also reveals: (i) All molecules have two stable rotameric forms in the ground state and the relative stability of *cis*-enol decreases with nitrogen substitution. (ii) For all the molecules the intramolecular proton transfer is unfavorable in the S_0 state and becomes feasible in the S_1 state. (iii) The energy difference between the keto and enol forms along the proton transfer coordinates in the S_1 state decreases in the order HPIP-b' > HPIP-b > HPP' > HPBI > HPIP-c' > HPIP-c > HPP (iii) Torsion rotation of the tautomer to form twisted structure at 90° is one of the nonradiative channels for the tautomer. At this conformation, the S_1-S_0 energy gap is reduced in the order HPBI > HPIP-c > HPIP-b > HPP. (iv) The influence of nitrogen substitution on photophysics of HPBI depends not only on the number of nitrogen atom present in the benzene ring but also on the position of nitrogen atom.

3.2.0. Nitrogen Substitution in the Phenolic Ring of HPBI

The role of nitrogen substitution in the phenolic ring of HPBI on ESIPT and rotamerism are studied in this section. The molecules considered in this work are 2',3'-HPyBI, 2-(3'-hydroxy-4'-pyridyl)benzimidazole (3',4'-HPyBI), 2-(4'-hydroxy-3'-pyridyl) benzimidazole (4',3'-HPyBI), 3',2'-HPyBI, and 2-(5'-hydroxy-4'-pyrimidinyl)benzimidazole (5',4'-HPymBI, **Chart 3.2**).

3.2.1. Rotamers and Tautomers

The important stationary point molecular structures for all the molecules (except 2',3'-HPyBI) are *cis*, open and *trans*-enols and the keto form (**Chart 3.3**). The optimized energy parameters for all these forms in the S_0 state as well as the S_1 state are compiled in **Table 3.7** along with the transition energies for different transitions. The dihedral angle

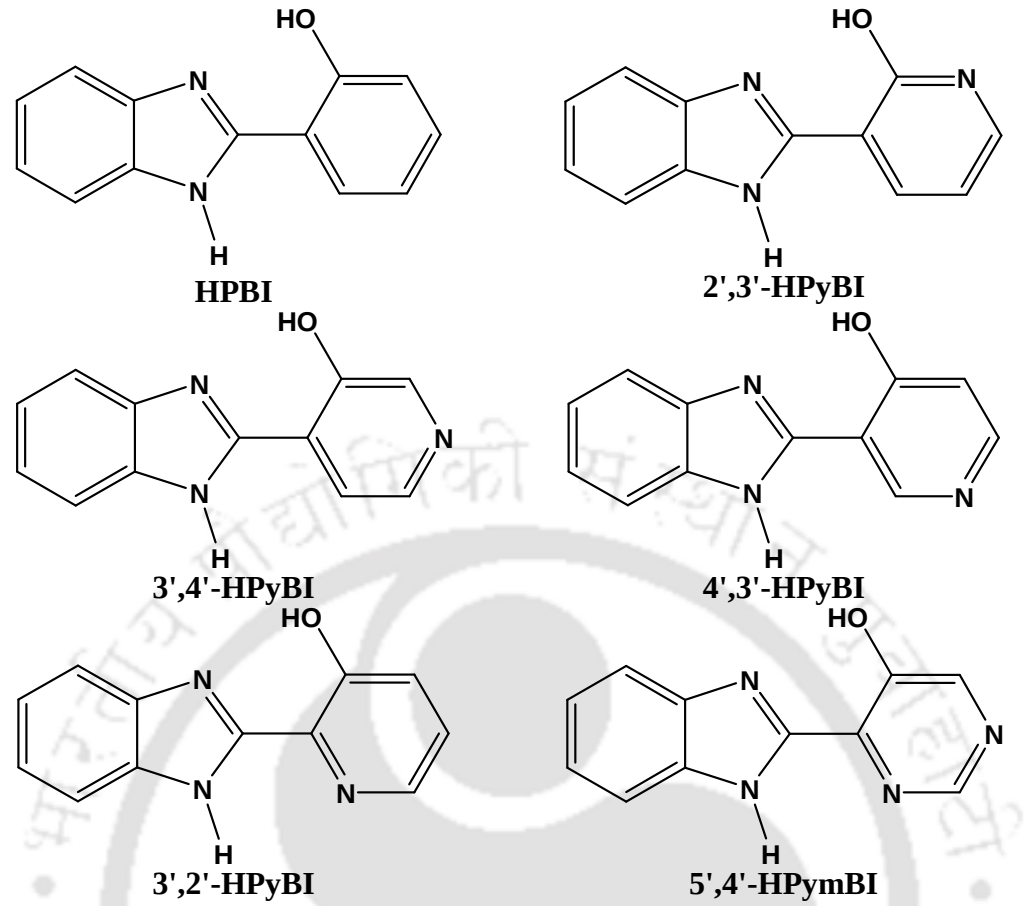

Chart 3.2. HPBI and nitrogen substituted molecules.

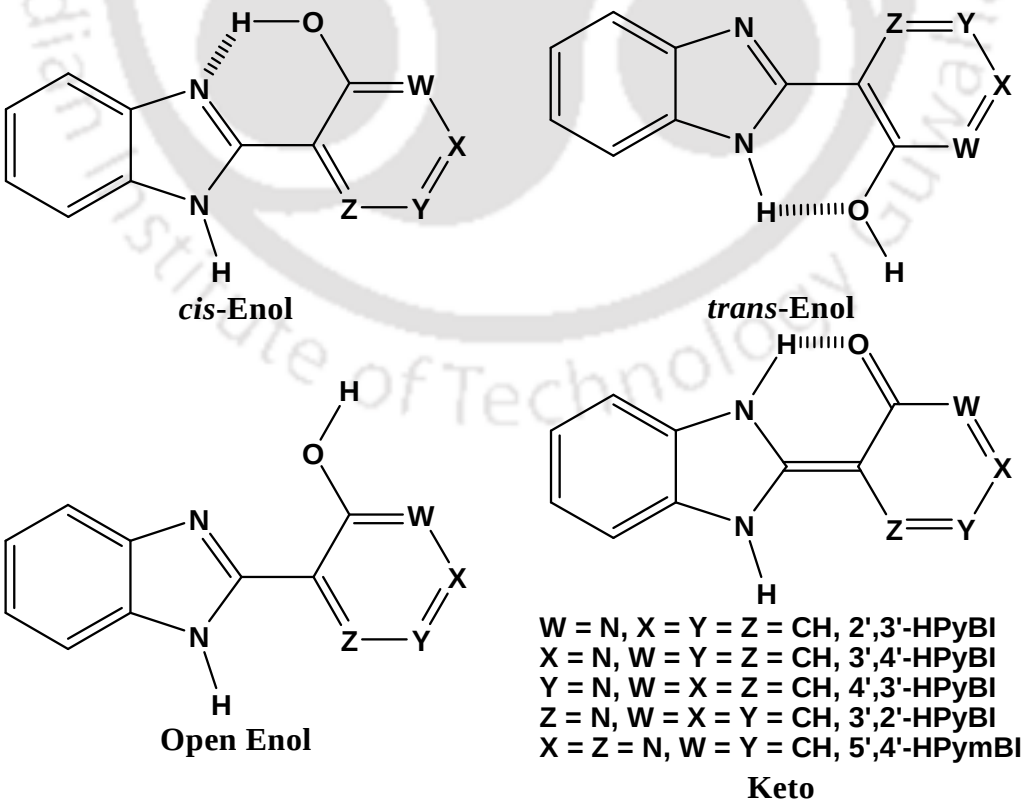

Chart 3.3. Isomeric forms of nitrogen substituted analogues of HPBI.

Table 3.7. Transition energies for different enols and keto form of molecules in the S_0 and S_1 states in vacuum.[a]

Parameter	*cis* -Enol	Open-enol	*trans*-Enol	Keto
		HPBI		
ΔE (eV)	0.0 (0.0)[b]	0.6303 (0.6137)	0.2597 (0.2621)	0.4075 (-0.3387)
Excitation[c]	316 (293, 318, 332)	311	307 (304, 326)	389
Emission[c]	341	344	343 (360)	429 (458)
		2',3'-HPyBI		
ΔE (eV)	0.0 (0.0)	0.3600 (0.2967)	-0.0411 (-0.1062)	0.4014 (-0.1705)
Excitation	317	321	321	379
Emission	347	354	355	406
		3',4'-HPyBI		
ΔE (eV)	0.0 (0.0)	0.5755 (0.5669)	0.2227 (0.2243)	0.4106 (-0.3635)
Excitation	320	317	315	398
Emission	343	345	345	438
		4',3'-HPyBI		
ΔE (eV)	0.0 (0.0)	0.6307 (0.5310)	0.3319 (0.2011)	0.3368 (-0.2991)
Excitation	299	306	307	358
Emission	332	340	343	394
		3',2'-HPyBI		
ΔE (eV)	0.0 (0.0)	0.6075 (0.5164)	0.7257 (0.6795)	0.3682 (-0.2500)
Excitation[c]	320 (328)[d]	330	326	386
Emission[c]	347	357	353	415 (458)[d]
		5',4'-HPymBI		
ΔE (eV)	0.0 (0.0)	0.5505 (0.4592)	0.6685 (0.5873)	0.3680 (-0.7086)
Excitation	323	337	336	439
Emission	347	354	354	490

[a]Energy difference, ΔE in eV with respect to *cis*-enol. Values in parentheses are that correspond to the S_1 state. Transition energies are in nm. All experimental data are that of molecule in dioxane. [b]Energy of *cis*-enol in the S_0 and the S_1 states are -18671.5598 eV and -18667.5684 eV respectively. [c]Values in parentheses are experimental data. [d]Ref. 54.

between the benzimidazole and phenyl rings is 0° in *cis* and open enol conformers and is 180° in *trans*-enol conformer. The dipole moment of *trans*-enol is higher than that of *cis*-enol in all the molecules. 3',4'-HPyBI and 2',3'-HPyBI are exceptions where the dipole moment of *trans*-enol is less than that of *cis*-enol. In all of the molecules, *cis*-enol which forms intramolecularly hydrogen-bonded structure is the most stable geometry in the ground state. 2',3'-HPyBI is an exception which will be discussed later. Compared to HPBI the relative stability of *cis* to *trans*-enol decreases in 3',4'-HPyBI and 2',3'-HPyBI. However, the relative stability of *cis* to *trans* enol increases in 3',2'-HPyBI, 5',4'-HPymBI and 4',3'-HPyBI. In particular the *trans*-enol is the most unstable form of 3',2'-HPyBI and 5',4'-HPymBI due to lone pair-lone pair repulsion between the imidazo nitrogen and the pyrido nitrogen. The presence of additional nitrogen reduces the repulsion in 5',4'-

HPymBI, hence the relative stability of *cis* to *trans*-enol increases in 5',4'-HPymBI when compared to 3',2'-HPyBI. Except 5',4'-HPymBI and 3',2'-HPyBI, in the other four molecules *trans*-enol is more stable than open-enol and keto form in the ground state. The open enols are expected to be dominant only in protic solvent.[178] Rodríguez-Prieto et al. showed that in nonaqueous solvents, 3',2'-HPyBI exists only as *cis*-enol in the ground-state and as keto in the excited state.[198] Their Hartree-Fock calculations also predicted planar structure for the molecule.

The potential energy pathways for conversion of *cis*-enol to *trans*-enol for different molecules were constructed by optimizing the molecular geometries with different preset torsional angle between the two aromatic planes (**Figure 3.5**). The calculations suggest that like HPBI, all these nitrogen substituted molecules can also be present in these two rotameric forms. The barrier height for the conversion increases with nitrogen substitution. 2',3'-HPyBI is an exception and it has lower energy barrier than HPBI. Relative to other molecules the barrier height for conversion is nearly 1.6 times greater in 5',4'-HPymBI and 3',2'-HPyBI, where the lone pair repulsion reduces the stability of *trans*-enol. Reduction of repulsion due to additional nitrogen in 5',4'-HPymBI also increases the barrier for the reverse process.

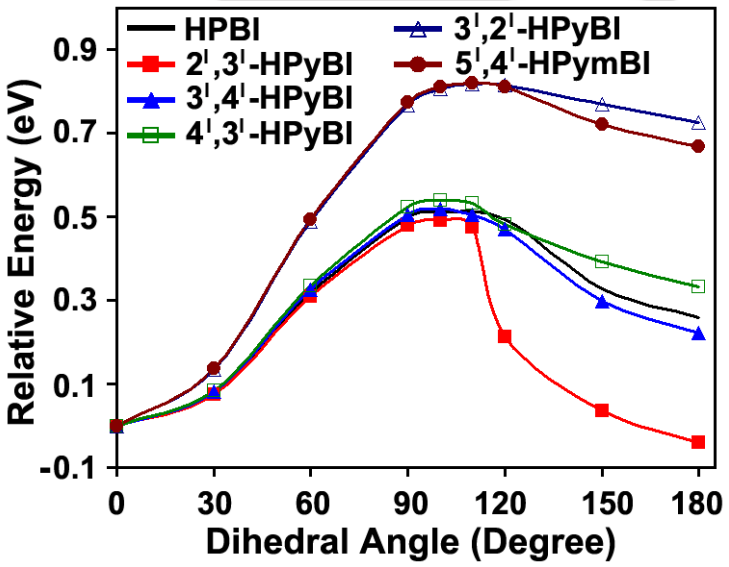

Figure 3.5. Plot of molecular energy as a function of torsional angle between the two aromatic rings for different molecules.

The photoexcited molecule from the Franck-Condon region undergoes vibration transitions to reach the relaxed geometry in the first excited state or relax to keto tautomer through ESIPT. The energies of those conformationally relaxed states for all of the isomers are also presented in **Table 3.7**. The distance between the proton donor (oxygen

atom) and the proton acceptor (nitrogen atom) in keto form increases in the S_1 state. Also in the first excited singlet state, as expected, the keto form is the most stable form. Although *cis*-enol is more stable than *trans*-enol, the relative stability of *trans*-enol for the nitrogen substituted molecules increases in the S_1 state relative to that in the ground state. It is opposite to that observed in HPBI, where the relative stability of *trans*-enol decreases in the S_1 state relative to that in the ground state.

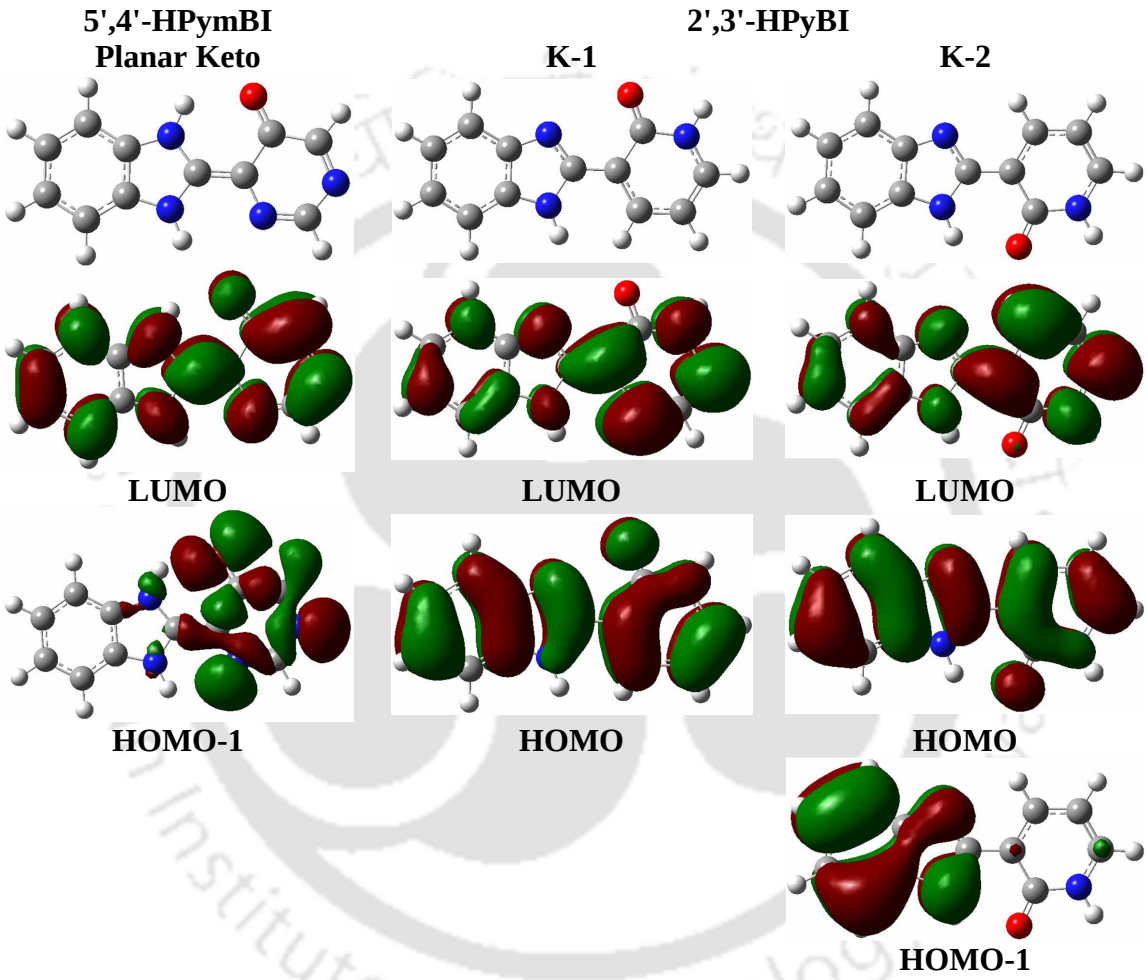

Figure 3.6. Frontier molecular orbitals of 2',3'-HPyBI and 5',4'-HPymBI involved in the longest wavelength transition. FMOs of the keto form of 5',4'-HPymBI [HOMO-1-LUMO (nπ* excited state has lower energy than HOMO-LUMO (ππ*) excited state].

The longest wavelength transitions of the enolic forms in all the molecules have ππ* character. Although the keto forms of mono nitrogen substituted molecules have ππ* state as emiting state, in dinitrogen substituted 5',4'-HPymBI the keto form has the nπ* state as lowest excited state and ππ* state as higher excited state (**Figure 3.6** and **Table 3.8**). The excitation and emission maxima in all the isomeric forms are red shifted on

nitrogen substitution. The red shifts suggest that the lone pair of electrons in the substituted nitrogen are involved in conjugation. 4',3'-HPyBI, where the nitrogen is substituted at meta position to the electron withdrawing benzimidazole, is an exception. The spectral maxima for all the forms of 4',3'-HPyBI are blue shifted relative to HPBI.

2',3'-HPyBI is a special case, in the sense that it can exist in two additional keto forms (K-1 and K-2, **Chart 3.4**). Dogra has studied the photophysics of 2',3'-HPyBI and found that K-2 keto tautomer is the most stable form in both S_0 and S_1 states.[176] Our calculated results were consistent with his observation that K-2 form is most stable in the ground state and its stability increases further more in the excited state (**Table 3.7** and **Table 3.9**). Interestingly *cis*-enol, the most stable form in other molecules, is less stable than *trans*-enol by 0.0149 eV.

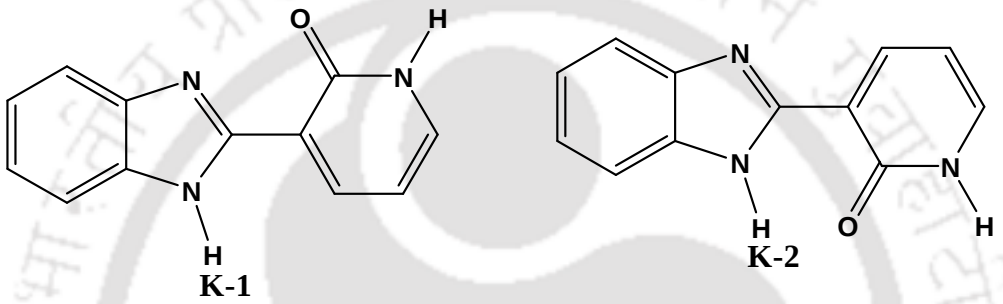

Chart 3.4. Ground state keto tautomers of 2',3'-HPyBI.

The experimental excitation and emission wavelengths for 0-0 transition of K-2 keto in dioxane are 386 nm and 404 nm respectively.[176] Our present calculated values 372 nm and 407 nm for excitation and emission respectively are in better agreement with the experimental values than the theoretical values, 367 nm and 443 nm respectively reported earlier by Dogra.[176] Alike the keto tautomer formed by ESIPT, in K-2 keto the lowest energy transition is mainly described by $\pi\pi^*$, with small contribution (16%) from the local excitation of benzimidazole moiety (LE_B) to π^* (**Table 3.10** and **Figure 3.7**).

3.2.2. Intramolecular Proton Transfer

After photoexcitation, *cis*-enol undergoes ultrafast proton transfer that results in keto tautomer.[34,56] In most of the molecules, ESIPT process is very fast, happening in femto- to subpicosecond timescale. The PES of the IPT process in both the ground and excited states were generated as a function of the distance between the dissociable hydrogen and oxygen of the phenolic hydroxyl group of *cis*-enol geometries. As the distance between the phenolic oxygen and proton gets larger, the proton comes closer to the imidazole nitrogen i.e. the hydrogen bond between the dissociable hydrogen and the imidazo nitrogen becomes

Table 3.8. Properties of the planar and twisted keto tautomers in vacuum.

	HPBI		2',3'-HPyBI		3',4'-HPyBI		4',3'-HPyBI		3',2'-HPyBI		5',4'-HPymBI	
	Planar	**Twisted**	**Planar**	**Twisted**	**Planar**	**Twisted**	**Planar**	**Twisted**	**Planar**	**Twisted**	**Planar[e]**	**Twisted**
S_1 Energy[a] (eV)	0.0	-0.2619	0.0	-0.1961	0.0	-0.1846	0.0	-0.0134	0.0	0.0462	0.0	0.5584
$S_1 \leftarrow S_0$ (eV)	2.89	0.75	3.05	0.90	2.83	0.85	3.15	1.34	2.99	0.93	2.53	1.09
State nature	ππ*	biradicaloid	ππ*	biradicaloid	ππ*	biradicaloid	ππ*	biradicaloid	ππ*	biradicaloid	nπ* ππ*	biradicaloid
Oscillator Strength	0.3300	0.0001	0.4426	0.0001	0.3279	0.0001	0.3107	0.0001	0.4494	0.0005	0.0007[d]	0.0003
						Dipole Moment (D)						
S_1 State	4.92	3.62	7.84	5.04	7.17	2.46	5.31	1.22	4.02	3.33	6.55	0.68
S_0 State	5.88	8.18	8.62	9.53	8.82	10.71	7.19	9.1	4.81	7.28	7.64	9.93
						Charge on hydroxypyridine/pyrimidine moiety						
S_1 State	-0.5423	-0.0816	-0.4601	-0.0974	-0.4418	-0.0997	-0.4337	-0.1052	-0.4796	-0.1211	-0.5068	-0.1357
S_0 State	-0.8496	-0.6536	-0.2510	-0.5304	-0.8196	-0.1283	-0.5377	-0.1931	-0.4859	-0.4198	-0.5888	-0.2816
ϕ_f[b]	0.22[c]								0.49[c]			

[a]Relative energy with respect to the planar keto. [b]Fluorescence quantum yields (ϕ_f) are that of tautomers in acetonitrile. [c]Ref. 54. [d]The lowest excited state is nπ* with oscillator strength 0.0007, the second excited state is ππ* that has oscillator strength 0.4475.

Table 3.9. Important parameters of 2',3'-HPyBI for the keto forms K-1 and K-2 in the S_0 and S_1 states (Within Parentheses) in vacuum.[a]

Parameter	K-1	K-2
ΔE[a] (eV)	0.3985 (-0.1024)	-0.2445 (-0.7817)
	Excitation (nm)	
Theoretical	363	372
Experimental[b]	-	386
	Emission (nm)	
Theoretical	400	407
Experimental[b]	-	404

[a]Energy difference in eV is with respect to *cis*-enol. [b]Experimental data (0-0 transition) are that of molecule in dioxane (Ref. 176).

Table 3.10. Properties and nature of the transition of tautomer rotamers K-1 and K-2 of 2',3'-HPyBI in vacuum.

	K-1	K-2
$S_1 \leftarrow S_0$ (eV)	3.10	3.05
State nature	ππ*	ππ* (84%) $LE_B\pi^*$ (16%)
Oscillator Strength	0.6196	0.5033
ϕ_f		0.48[a]
	Dipole Moment (D)	
S_1 State	5.71	2.09
S_0 State	6.68	4.49

[a]Fluorescence quantum yield in dioxane from Ref. 176.

covalent bond. After relaxation, the keto product decays to the Franck-Condon region in its ground state. In the ground state keto form is unstable and reverses back the proton transfer to form *cis*-enol.

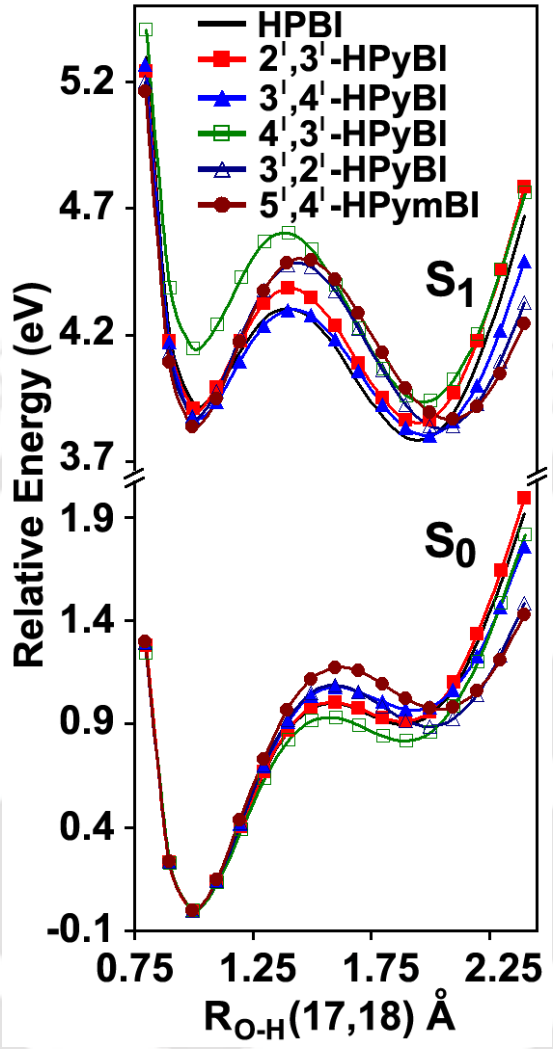

Figure 3.7. Simulated potential energy surfaces for IPT reaction for different molecules.

Although 2',3'-HPyBI and 3',2'-HPyBI have been examined theoretically,[54,176] complete PES for proton transfer process were not simulated for any of these nitrogen substituted molecules. The PES for different molecules are shown in **Figure 3.7** and the energy difference and the energy barriers are given in **Table 3.11**. In all of the molecules, *cis*-enol is the stable form in the S_0 state while keto, the proton transfer product, is more stable in the S_1 state (except that of 5',4'-HPymBI). This shows that IPT is thermodynamically not favored in the ground state but favored in the S_1 state. However, the *cis*-enol form of 5',4'-HPymBI is more stable than keto in both S_0 and S_1 states.

Contrary to nitrogen substitution in the benzene ring, the relative stability of the keto form with respect to *cis*-enol form in the S_1 state decreases upon nitrogen substitution in the phenolic ring. The exception is 4',3'-HPyBI, where nitrogen is substituted at *para* position to hydroxyl group and the electron withdrawing nature of nitrogen make it more acidic. In 2',3'-HPyBI, although the keto form is relatively more stable than *cis*-enol in the S_1 state, no ESIPT was observed. The absence of ESIPT in 2',3'-HPyBI is due to the absence of *cis*-enol in the ground state which has the prerequisite intramolecular hydrogen bond that is essential of ESIPT (as mentioned earlier K-2 keto is the most stable form).[176] Water assisted relay transfer of proton in 2',3'-HPyBI is discussed in the next section.

Table 3.11. Energy difference and barrier for proton transfer reaction (eV) in vacuum.

Energy Sate	ΔE	Energy Barrier	
		cis-Enol	Keto-Tautomer
		HPBI	
S_1	-0.1326	0.3778	0.5104
S_0	0.9195	0.9986	0.0790
		2',3'-HPyBI	
S_1	-0.0468	0.4743	0.5211
S_0	0.9100	1.0066	0.0966
		3',4'-HPyBI	
S_1	-0.0743	0.4207	0.4950
S_0	0.9701	1.0806	0.1105
		4',3'-HPyBI	
S_1	-0.2025	0.4596	0.6621
S_0	0.8166	0.9317	0.1151
		3',2'-HPyBI	
S_1	-0.0346	0.6000	0.6345
S_0	0.8874	1.0896	0.2022
		5',4'-HPymBI	
S_1	0.0297	0.6572	0.6275
S_0	0.9747	1.1734	0.1986

[a]Energy difference between cis-enol and keto-tautomer.

The energy barrier for the IPT in the S_0 state also increases upon nitrogen substitution, 4',3'-HPyBI is an exception. In the excited S_1 state the barrier decreases with respect to the ground state. This is consistent with the fact that the interconversion of the enol form to the keto form is more favorable in the S_1 state. Unlike the S_0 state, in the S_1 state the barrier increases in all the nitrogen substituted molecules and it is highest in dinitrogen substituted 5',4'-HPymBI. Thus, substitution of nitrogen in the phenolic ring decreases the IPT process. The effect is just opposite to that observed when nitrogen is substituted in the benzene ring of HPBI. Despite this, the opposite trend is observed in the fluorescence quantum yield of the keto form.[6,174,175,177] The fluorescence yield decreases when nitrogen is substituted in benzene ring and increases on substitution in the phenolic ring.

3.2.3. Intermolecular Proton Transfer in 2',3'-HPyBI

As reported by Dogra,[176] the absence of ESIPT in 2',3'-HPyBI can be attributed to the non-existence of *cis*-enol in the ground state. In the ground state the molecule is predominately present in K-2 form, which is the *trans* conformer of K-1. Both K-1 and K-2 are keto tautomeric form of 2',3'-HPyBI and are different from the one that is formed by ESIPT. This renders a special interest on the interconversion of different forms of 2',3'-HPyBI in ground state. In absence of intramolecular hydrogen bonding between the proton donor and the proton acceptor, the transfer should be assisted by protic solvents. We have examined water mediated conversion of open- and *trans*-enol to K-1 and K-2 tautomers respectively by adding a water molecule.

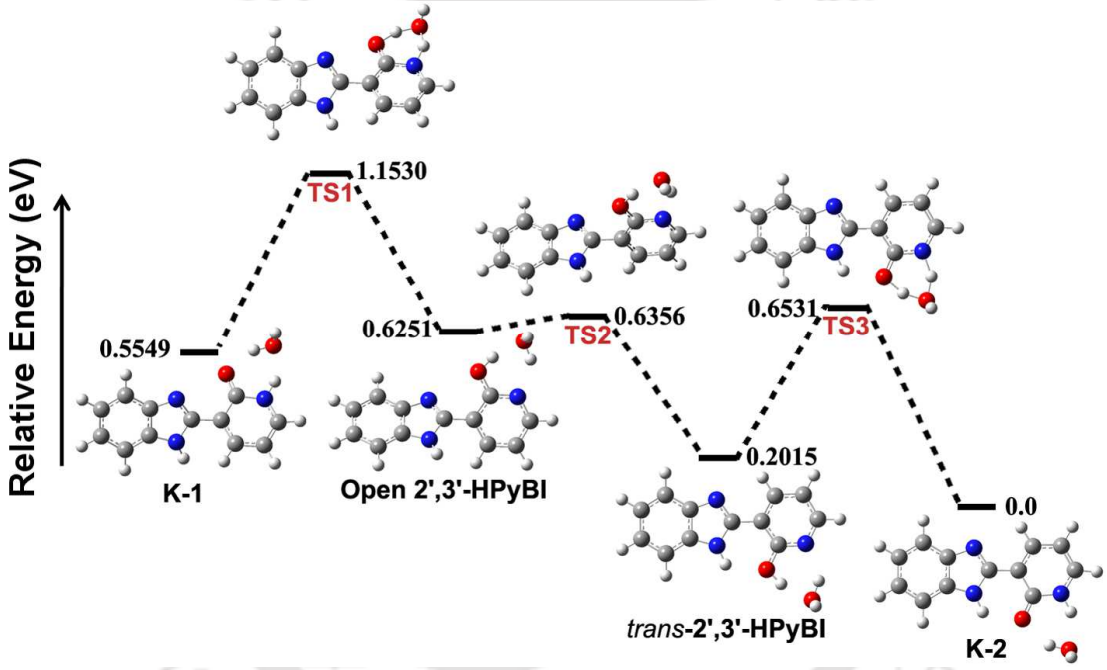

Figure 3.8. Water molecule assisted proton transfer in 2',3'-HPyBI.

In absence of water molecules, the open-enol structure is more stable than K-1 (**Tables 3.7** and **3.9**). Upon addition of a water molecule K-1 becomes more stable than open-enol by 0.0703 eV. The geometry of open enol also changes to a measurable extend mainly the dihedral angle between the two aromatic rings which was 0^{o} in absence of water increases to 37.4^{o}. The activation energy for the conversion to K-1 from open-enol is 0.5278 eV in case of simultaneous double proton transfer that occurs via TS1 transition state (**Figure 3.8**). Proton transfer can also occur step wise through two different path ways: (i) the open enol loses its phenolic proton to solvent molecule to form a phenolate-hydronium complex, followed by proton transfer from the hydronium ion to the fluorophore to form K-1 tautomer, (ii) proton is first transferred from water molecule to pyridine nitrogen of 2',3'-HPyBI

forming a pyridinium-hydroxyl ion pair and in the next step the phenolic proton is transferred to hydroxyl ion to give K-1. The activation energies of these step wise proton transfer processes are same and are 0.5412 eV.

The energy barrier for rotation of hydrated open-enol to *trans*-enol is 0.0121 eV and *trans*-enol is more stable than the K-1 tautomer. However, the K-2 tautomer is the most stable form in hydrated state also. The barrier for conversion from *trans*-enol to K-2 is also less than that of open-enol to K-1. Here the barrier for simultaneous proton transfer is 0.4617 eV (**Figure 3.8**). On the other hand the activation energies for step wise proton transfer via phenolate-hydronium and pyridinium-hydroxyl ion pairs are 0.4518 eV and 0.4516 eV, respectively.

3.2.4. Torsional Rotation of Keto Tautomer

As discussed in **Section 3.1.4** the torsional relaxation of the keto tautomer to a twisted state competes with radiative transitions and leads to fluorescence quenching. Vázquez et al., based on their experimental work, proposed that the excited state intramolecular coupled proton and charge transfer leads to a non fluorescent intermediate in 2-(2'-hydroxyphenyl)benzazoles and 3',2'-HPyBI.[264] It was also suggested that the relative efficiency of this radiationless decay is less favored in 3',2'-HPyBI compared to 2-(2'-hydroxyphenyl)benzazoles. We have optimized the geometry of twisted keto in the S_1 state. As shown in **Figure 3.9**, the increase in the electron density of the five member ring leads to its pyramidalization, borne out by the angle ~ 67° and 150° (in the S_1 state) deviation from ~ 90° and 180° (**Table 3.12**). This is consistent with the pyramidalization with increase in electron density on the azole rings observed earlier (**Section 3.1.4**). The energies obtained from the present TDDFT calculations predict that like HPBI, the twisted keto is more stable than planar keto in 2',3'-HPyBI, 3',4'-HPyBI and 4',3'-HPyBI. But twisted keto of 3',2'-HPyBI and 5',4'-HPymBI are less stable than corresponding planar conformer in the S_1 state (**Table 3.8**).

The present results depict a different scenario from the earlier one (**Section 3.1.4**), where the benzene ring of benzimidazole moiety in HPBI is substituted by nitrogen. There the twisted keto form is more stable than the planar one in all the molecules and the relative stability increases with nitrogen substitution. The energy difference between the S_0 and S_1 at the twisted geometry decreases with nitrogen substitution. This provides a route for nonradiative deactivation to the ground state from the S_1 state. Thus, the radiationless decay

involves large-angle motion of the excited tautomer associated with intramolecular charge transfer from the deprotonated phenol to the protonated benzimidazole ring to form the twisted keto. However the efficiency of the process is related to the strength of the electron donor (dissociated phenol moiety) and electron acceptor (protonated azole).

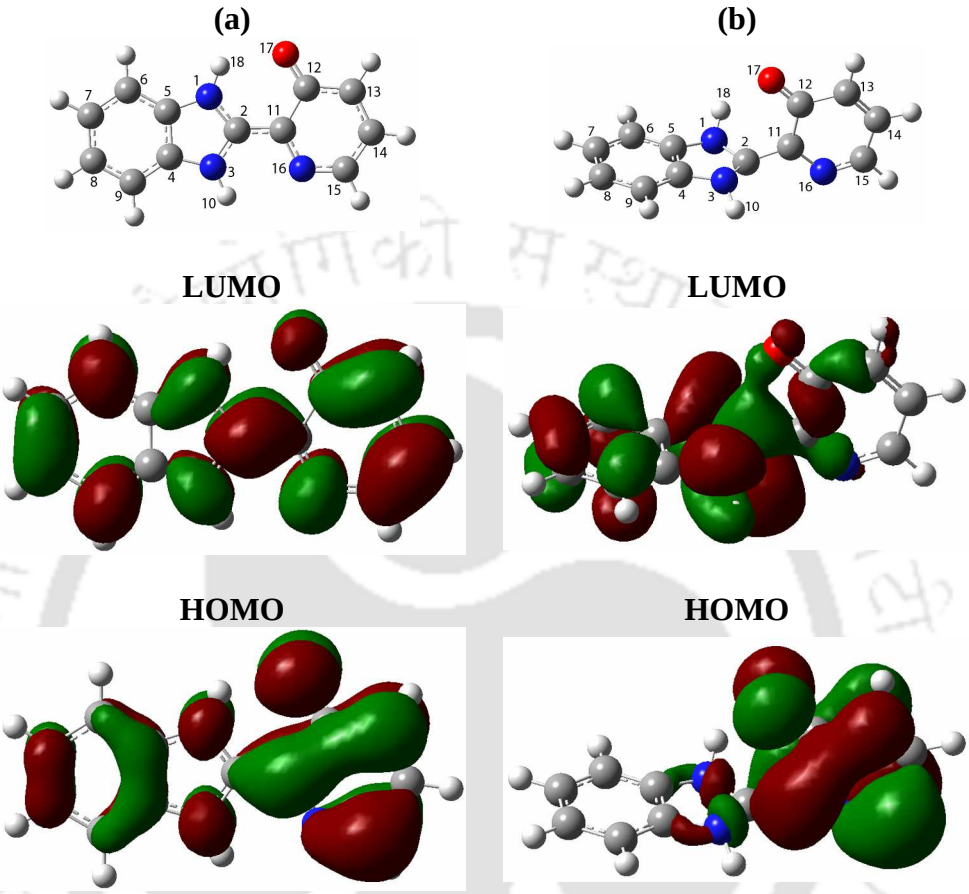

Figure 3.9. Optimized structures of (a) Keto and (b) Twisted tautomer on the excited state surface along with corresponding frontier molecular orbitals for 3',2'-HPyBI.

Substitution of nitrogen in the benzimidazole ring favors the formation of the twisted form. In the present case, due to incorporation of more electronegative nitrogen in the phenolic ring, the charge donating capacity of the dissociated pyridinol or pyrimidinol moiety is less than the dissociated phenol. Hence, the charge transfer is less in the present systems and thus the twisted keto tautomer is less stabilized.

Contrary to the nitrogen effect on benzene ring, the S_1-S_0 energy gap for the twisted keto also increases by nitrogen substitution on phenolic moiety (**Table 3.8**). Hence, it is clear that the non radiative deactivation through twisted keto is less important in the present system. This result is consistent with the observed higher quantum yield for 3',2'-HPyBI (Φ_f = 0.49 in acetonitrile) compared to HPBI (Φ_f = 0.22 in acetonitrile).[264] It may also be noted that the fluorescence quantum yield of 2-(2'-hydroxyphenyl)benzoxazole strongly depends on

temperature and viscosity. On the other hand, the fluorescence quantum yield of corresponding hydroxypyridinyl analogue, whose electron donating capacity decreases due to

Table 3.12. Selected bond lengths and angles of the tautomers in the optimized S_0 and S_1 states (for the atom numbering, refer Figure 3.9).

Geometry Parameters	Keto		Twisted Tautomer	
	S_0 State	S_1 State	S_0 State	S_1 State
		2',3'-HPyBI		
N1 C2	1.35148	1.35685	1.35087	1.40842
N3 C2	1.36952	1.36830	1.35089	1.41004
C2 C11	1.41744	1.40534	1.44595	1.43209
C11 C12	1.47001	1.51001	1.47101	1.49396
C11 C16	1.41041	1.40079	1.39493	1.42450
C12 O17	1.25922	1.22002	1.24600	1.19754
N1 C2 C11 C12	-0.01990	-0.01137	87.65675	66.48273
C5 N1 C2 C11	179.99811	179.99047	-174.09121	-152.49942
		3',4'-HPyBI		
N1 C2	1.35180	1.35553	1.34938	1.40602
N3 C2	1.36768	1.36650	1.34939	1.40959
C2 C11	1.41812	1.40491	1.44780	1.43868
C11 C12	1.45214	1.48856	1.45497	1.47364
C11 C16	1.41788	1.39092	1.40709	1.41547
C12 O17	1.26986	1.23010	1.25400	1.20461
N1 C2 C11 C12	0.00103	-0.00060	87.47633	67.61629
C5 N1 C2 C11	-180.00000	-179.99689	-174.45755	-150.05776
		4',3'-HPyBI		
N1 C2	1.35067	1.36125	1.35019	1.40832
N3 C2	1.36710	1.37070	1.35018	1.41025
C2 C11	1.41879	1.40076	1.44495	1.42684
C11 C12	1.46159	1.49712	1.46559	1.48964
C11 C16	1.41327	1.40157	1.40196	1.44774
C12 O17	1.26705	1.22591	1.25021	1.20418
N1 C2 C11 C12	0.00302	-0.00121	88.08348	68.30817
C5 N1 C2 C11	-179.99962	-179.99877	-175.52207	-153.17114
		3',2'-HPyBI		
N1 C2	1.35058	1.35406	1.34614	1.40567
N3 C2	1.35872	1.35709	1.34615	1.40948
C2 C11	1.41819	1.40972	1.46840	1.43429
C11 C12	1.45276	1.49196	1.44735	1.48415
C11 C16	1.35946	1.33170	1.34348	1.35814
C12 O17	1.26741	1.22956	1.25833	1.20610
N1 C2 C11 C12	0.00077	0.00283	89.70911	68.10541
C5 N1 C2 C11	-180.00000	179.99906	-178.23576	-151.66542
		5',4'-HPymBI		
N1 C2	1.34957	1.35250	1.34526	1.40265
N3 C2	1.35660	1.35523	1.34525	1.40880
C2 C11	1.41985	1.40794	1.46778	1.43584
C11 C12	1.44233	1.47674	1.44199	1.47002
C11 C16	1.35941	1.33215	1.34680	1.35666
C12 O17	1.26493	1.22972	1.25397	1.20366
N1 C2 C11 C12	-0.00564	0.00647	89.04696	68.09616
C5 N1 C2 C11	179.99927	179.99212	-177.50183	-149.74740

nitrogen substitution, is independent of temperature and viscosity.[264] Thus, it may be concluded the decrease in the non radiative rate due to formation of twisted keto is responsible for the different dependence on viscosity and temperature between 2-(2'-hydroxyphenyl)benzoxazole.

3.2.5. Conclusion

Studies on the role of nitrogen substitution in the phenolic ring of HPBI were performed theoretically. The theoretical calculations for excitation and emission energies are in agreement with available literature data. The calculations show that *cis*-enol is the most stable geometry in the S_0 state in all the molecules except in 2',3'-HPyBI where K-2 keto is the most stable form. In 2',3'-HPyBI, *trans*-enol is also more stable than *cis*-enol. The energy barrier predicted for water molecule assisted interconversion of *trans*-enol to K-2 form is lower than that of open-enol to K-1. In all the molecules except 5',4'-HPymBI, the ESIPT process is favored in the S_1 state thermodynamically with the energy barrier increasing with nitrogen substitution. The energy difference between the enol form and the keto form along the proton transfer coordinates in the S_1 state decreases with nitrogen substitution except in the case of 4',3'-HPyBI. The calculations suggest that the non radiative decay through torsional rotation of the excited keto tautomer to the twisted structure is less important in these molecules. This is consistent with the experimental fact that the quantum yield of 3',2'-HPyBI is higher than that of HPBI.

3.3.0. Effect of Temperature on the Photophysics of HPBI, HPIP-b and HPIP-c

1-Hydroxy-2-naphthaldehyde shows remarkable sensitivity towards variation of temperature.[268] With an increase in temperature, the intensity of the phototautomer emission decreases with a simultaneous slight increase of the normal emission band in both polar and nonpolar solvents. It was explained that the change in the intensities may be due to (i) temperature induced breaking of intramolecular hydrogen bond which leads to enhancement of the enol form, and (ii) increase in nonradiative rate leading to decrease of fluorescence. Besides, in protic solvent the phototautomer emission is blue shifted indicating the formation of unsolvated structures which are energetically less stable than their solvated counterparts.

The increase in temperature decreases the quantum yields of HPBO and HPBT and their derivatives 2-(3′-hydroxy-2′-pyridyl)benzoxazole and 2-(3-methyl-1,3-benzothiazol-3-ium-2-yl)benzenolate.[123,269] The decrease in the quantum yield has been associated with the temperature-dependent radiationless deactivation of the phototautomer. However, the

mechanism of the deactivation process is still not clear.[25,269-274] However, it was predicted that *cis*-*trans* isomerization of the phototautomer may be the cause of the thermally activated decay after formation of the ICT state having a twisted tautomer structure.[102,271,275,276] The *trans*-tautomer (**Chart 3.5**) has been experimentally detected by transient absorption measurements and two-step laser excitation as a long-lived transient ground-state species for HPBT and HPBO.[102,271,272,276-278] Recently photophysical properties of two different polymorphic crystalline forms of HPBI have been studied from liquid nitrogen temperature to room temperature by Sekiya et al.[279] They found that the fluorescence quantum yield of the tautomer emission is dependent on the polymorph and the value decreases with increase in temperature. Further, they proposed that the decrease in the quantum yield is associated with ICT.

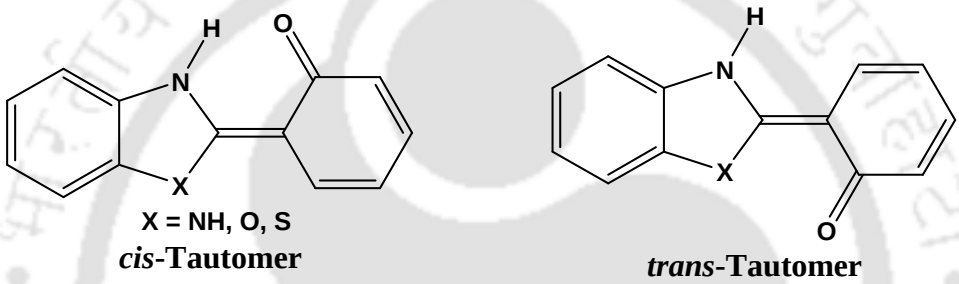

Chart 3.5. *cis*- and *trans*-Tautomers of 2-(2'-hydroxyphenyl)benzazoles.

As discussed earlier (**Section 3.1.4**), the torsion rotation of the phototautomer is favored when the benzene ring of HPBI is substituted with a nitrogen atom. Therefore, the effect of temperature on the spectral characteristics of HPBI and its nitrogen substituted analogues viz. HPIP-b and HPIP-c was studied. Although, the spectral characteristics of HPBI, HPIP-b and HPIP-c were investigated earlier,[6,95,174,175] the effect of temperature was not studied. The studies were carried out in non-polar solvents cyclohexane (due to poor solubility HPIP-c was not studied in cyclohexane) and dioxane, polar aprotic solvent acetonitrile and protic solvents ethylene glycol and methanol. Such a study may lead to a better understanding of the ESIPT induced charge transfer observed in these molecules. Temperature effects on the ground state distribution of their different conformers (**Chart 3.1**) are studied theoretically by DFT method.

3.3.1. Population Ratio of Enol Conformers

The energies of *cis*, *trans* and open conformers of enol isomer were obtained for fully optimized geometries in different solvents at different temperatures using the integral equation formalism-polarizable continuum (IEF-PCM) model.[233,234] The dielectric constants

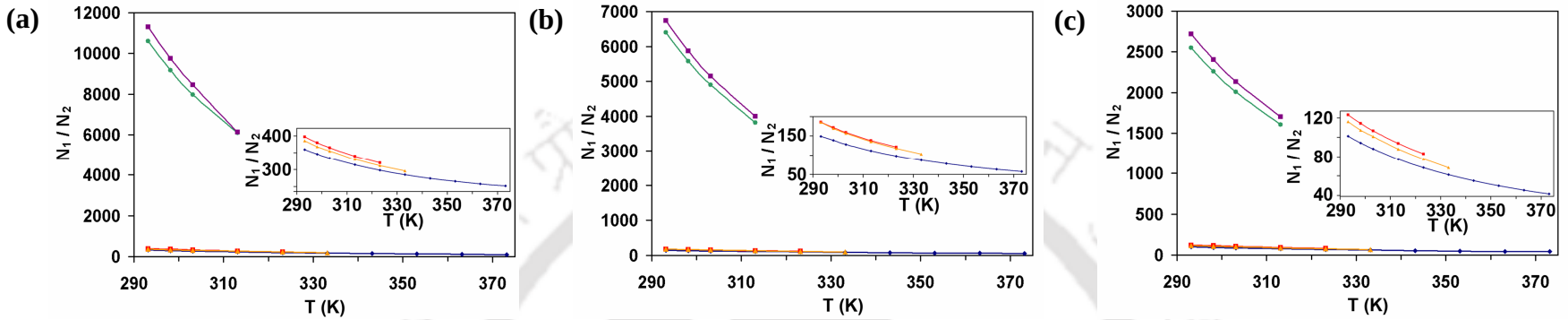

Figure 3.10. Population ratio of *cis*-enol to *trans*-enol of (a) HPBI, (b) HPIP-b, and (c) HPIP-c in cyclohexane (-■-), dioxane (-●-), acetonitrile (-▲-), methanol (-■-), and ethylene glycol (-♦-) at different temperatures. The inset in each figure is the enlarged plot for acetonitrile, methanol, and ethylene gylcol.

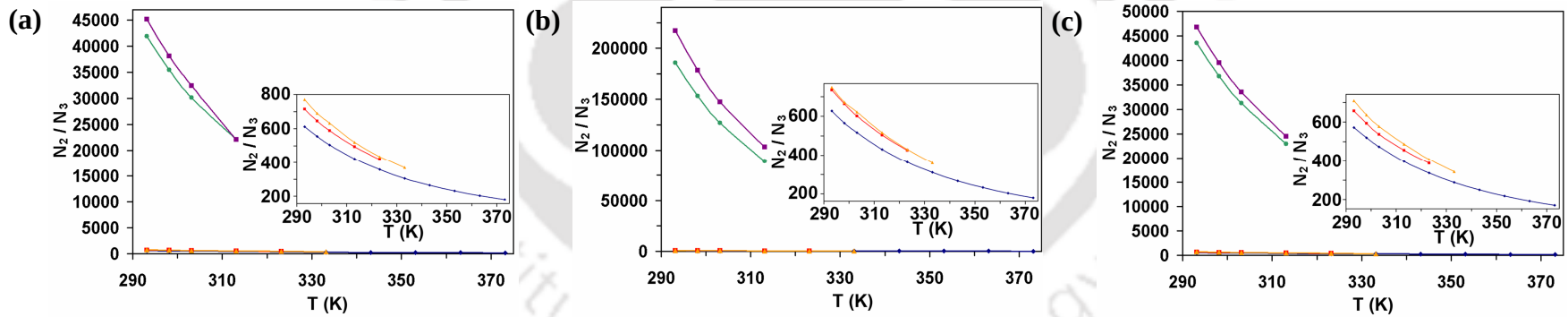

Figure 3.11. Population ratio of *trans*-enol to open enol of (a) HPBI, (b) HPIP-b, and (c) HPIP-c in cyclohexane (-■-), dioxane (-●-), acetonitrile (-▲-), methanol (-■-), and ethylene glycol (-♦-) at different temperatures. The inset in each figure is the enlarged plot for acetonitrile, methanol, and ethylene gylcol.

available from the literature,[191] were used for these calculations. Using the energies thus obtained and the Boltzmann distribution equation (**Eq. 3.1**),

$$\frac{N_{cis}}{N_{trans}} = e^{-\frac{\Delta E}{kT}} \qquad 3.1$$

the relative population for *cis*-enol to *trans*-enol at different temperature are plotted in **Figures 3.10**. The population ratios of *trans*-enol to open enol at different temperature obtained by following the same procedure are given in **Figures 3.11**. The relative population of open-enol is negligible and at a given temperature and solvent, the ratio of *cis*-enol to *trans*-enol decreases in the order HPBI > HPIP-b > HPIP-c. For all of the molecules, in a particular solvent the ratio decreases with an increase in temperature which indicates that the population of *trans*-enol relative to *cis*-enol increases. In other words, increase in temperature favors the *trans*-enol form.

3.3.2. Absorption Spectra

Table 3.13 summarizes the absorption maxima and their corresponding molar extinction coefficient in different solvents measured at 293 K. The absorption spectra in few selected solvent and at different temperatures are shown in **Figure 3.12**. The absorption spectra of HPBI and HPIP-b have resolved structure and the resolution decreases in HPIP-c. The absorption spectra of HPBI, HPIP-b and HPIP-c in all the solvents consist mainly of three vibronic bands at around 285-300 nm, 315-325 nm and 330-340 nm. In a given solvent and temperature the absorption peaks are red-shifted in HPIP-b compared to HPIP-c which are red-shifted compared to HPBI.

Table 3.13. Absorption band maxima and Log(ε_{max}) of HPBI, HPIP-b and HPIP-c in different solvents at 293 Kelvin.[a]

Solvent	HPBI	HPIP-b	HPIP-c
Ethylene glycol	292 (4.14), 317 (4.29), 331 (4.25)	299 (4.22), 325 (4.36) , 337 (4.334)	288 (4.22), 318 (4.18, broad)
Methanol	291 (4.10), 316 (4.28), 329 (4.24)	297 (4.24), 324 (4.35), 334 (4.33)	286 (4.27), 317 (4.20, broad)
Acetonitrile	291 (4.16), 317 (4.35), 330 (4.32)	296 (4.28), 322 (4.39), 335 (4.38)	286 (4.27), 316 (4.25), 326 (4.24)
1,4-Dioxane	292 (4.17), 319 (4.37), 333 (4.338)	297 (4.27), 323 (4.37), 337 (4.36)	287 (4.13), 318 (4.17), 329 (4.15)
Cyclohexane	285 (4.03), 293 (3.95), 321 (4.15), 336 (4.11)	287 (3.42), 297 (3.70), 327 (3.78), 341 (3.78)	-

[a]The band maxima are given in nm and the values in parentheses are the corresponding Log ε_{max}.

The absorption spectra of HPBI, HPIP-b and HPIP-c in all the solvents show hypochromic effect with the increase in temperature with the exception of HPIP-b in

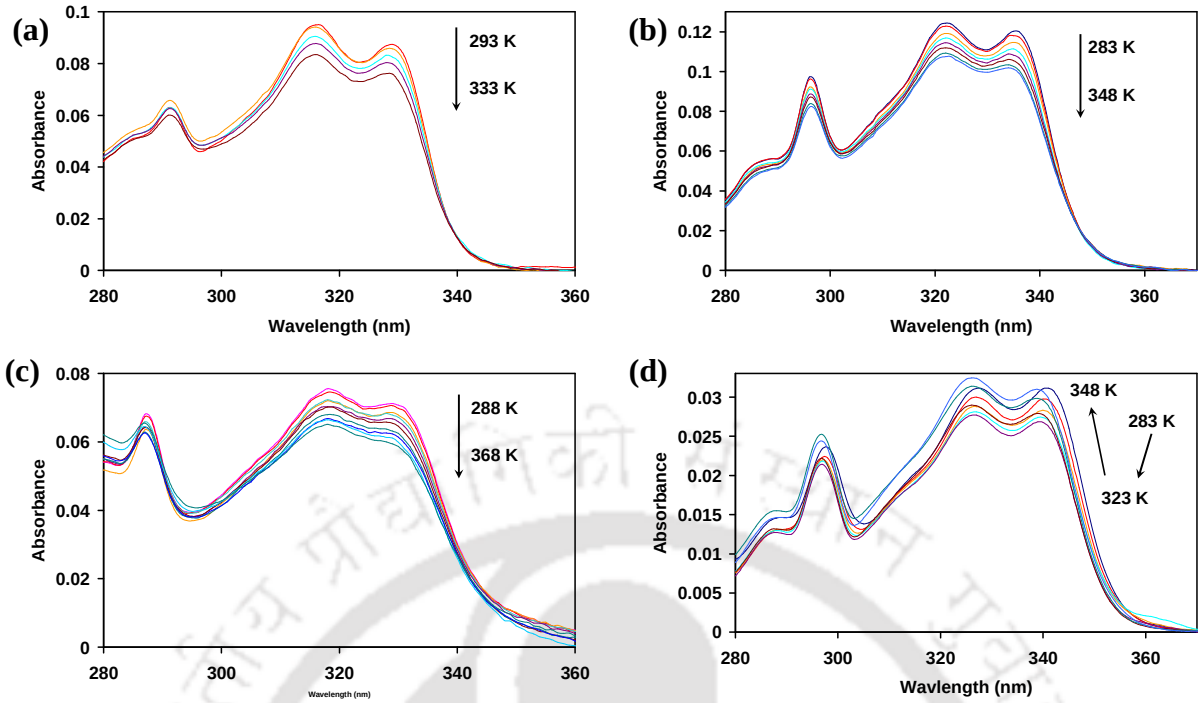

Figure 3.12. UV-Visible absorption spectra of (a) HPBI in methanol, (b) HPIP-b in acetonitrile, and (c) HPIP-c in dioxane, and (d) HPIP-b in cyclohexane at different temperatures.

cyclohexane (**Figure 3.12d**). Peculiar behaviour is observed for the absorption spectra of HPIP-b in cyclohexane, the absorbance decrease with a blue shift for initial increase in temperature from 283 K to 323 K. However, upon further increases of temperature from 323 K to 348 K the absorbance increases. In general the absorption maxima remain is insensitive to the change in temperature. But alike HPIP-b in cyclohexane a small blue shift is observed for HPBI and HPIP-b in ethylene glycol.

3.3.3. Fluorescence Emission Spectra

At room temperature, all three molecules HPBI, HPIP-b and HPIP-c emit dual fluorescence in most of the solvents (**Table 3.13**). The shorter wavelength emission band that exhibits vibrational structure is the emission (normal) due to the excited enol form that exists in ground state. The red shifted and more intense emission band is due to the emission from keto, formed after ESIPT, which is characterized by its large Stokes' shift from the absorption band.[6,95,99,174,175,255-258] The fluorescence intensity of both the bands depends on the wavelength of excitation. This was illustrated by the representative 3D emission spectra of HPIP-c in methanol at room temperature and the corresponding contour diagram (**Figures 3.13a** and **3.13b**). Clear dual fluorescence is obtained in protic solvents for all of the three

Table 3.14. Fluorescence band maxima of HPBI, HPIP-b and HPIP-c in different solvents at different temperatures.[a]

Normal band

T		HPBI					HPIP-b					HPIP-c		
(Kelvin)	EG	MeOH	ACN	Dx	Cy	EG	MeOH	ACN	Dx	Cy	EG	MeOH	Acn	Dx
283	338, 353, 371	333, 349, 367	334, 343, 365		371	363	360	335, 351, 373		370	355	352	327, 342, 359	
293	338, 353, 371	333, 349, 367	334, 343, 365	332, 343, 363	370	363	358	335, 351, 373	335, 342, 352, 367	370	355	352	327, 342, 359	326, 342, 360
303	338, 353, 371	333, 349, 367	334, 343, 365	332, 343, 363	369	363	357	335, 351, 373	335, 342, 352, 367	370	355	350	327, 342, 359	326, 342, 360
313	338, 353, 371	333, 349, 367	334, 343, 365	332, 343, 363	369	363	357	335, 351, 373	335, 342, 352, 367	370	354	350	327, 342, 359	326, 342, 360
323	338, 353, 371	333, 349, 367	334, 343, 365	332, 343, 363	369	363	356	335, 351, 373	335, 342, 352, 367	370	352	350	327, 342, 359	326, 342, 360
333	338, 353, 371	333, 349, 367	334, 343, 365	332, 343, 363	368	363	355	335, 351, 373	335, 342, 352, 367	370	351	349	327, 342, 359	326, 342, 360
343	338, 353, 371		334, 343, 365	332, 343, 363	365	363		335, 351, 373	335, 342, 352, 367	370	351		327, 342, 359	326, 342, 360
353	338, 353, 371			332, 343, 363		363			335, 342, 352, 367		350			326, 342, 360
363	338, 353, 371			332, 343, 363		363			335, 342, 352, 367		350			326, 342, 360
373	338, 353, 371					363					350			

Keto band

T		HPBI					HPIP-b					HPIP-c		
(Kelvin)	EG	MeOH	ACN	Dx	Cy	EG	MeOH	ACN	Dx	Cy	EG	MeOH	Acn	Dx
283	454	455	461		473	492	490	488		490	475	474	476	
293	454	455	461	465	473	492	490	488	489	490	475	474	476	478
303	454	455	461	465	473	492	490	488	489	490	475	474	476	478
313	454	455	462	465	473	491	490	488	489	490	475	474	476	478
323	454	455	462	466	473	491	490	488	489	490	475	474	476	478
333	454	455	462	466	473	491	490	488	489	490	475	474	476	478
343	455		263	467	473	491		488	489	490	475		476	478
353				468		491			489		475			478
363	456			469		491			489		475			478
373	457					491					475			

[a] λ_{Exc} = 310 nm. EG, MeOH, Acn, Dx and Cy stand for ethylene glycol, methanol, 1,4-dioxane and cyclohexane respectively.

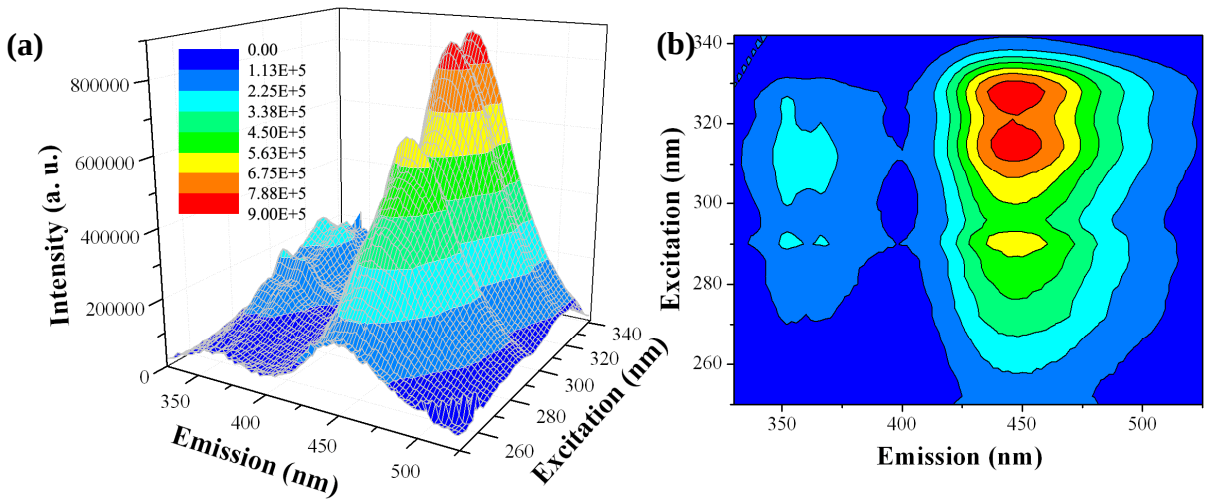

Figure 3.13. (a) 3-D Emission spectra of HPIP-c in methanol at room temperature, and (b) its corresponding contour diagram.

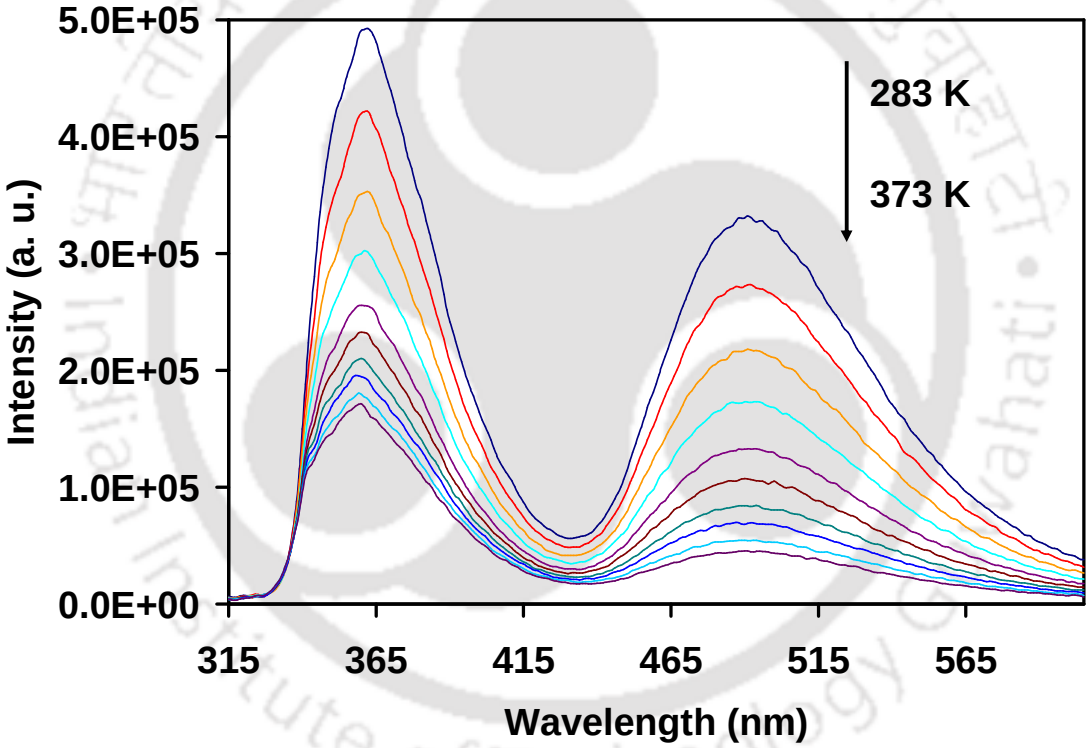

Figure 3.14. Emission spectra of HPIP-b in ethylene glycol at different temperatures (λ_{exc} = 310 nm).

molecules. For HPIP-b and HPIP-c in both methanol and ethylene glycol, the normal emissions are more intense than tautomer emissions (HPIP-b in ethylene glycol is shown as representative plot, **Figure 3.14**). On the other hand, the tautomer emissions dominate over the normal emissions in aprotic solvents. HPBI in cyclohexane shows almost a single emission band from keto with negligible normal emission (**Figure 3.15**). Upon increasing the polarity and hydrogen bond formation capacity of the solvents, the normal band is red shifted

for all of the molecules while the keto band is blue shifted in the case of HPBI and HPIP-c but is insensitive in the case of HPIP-b. All of these results are consistent with the earlier literature reports.[6,95,174,175]

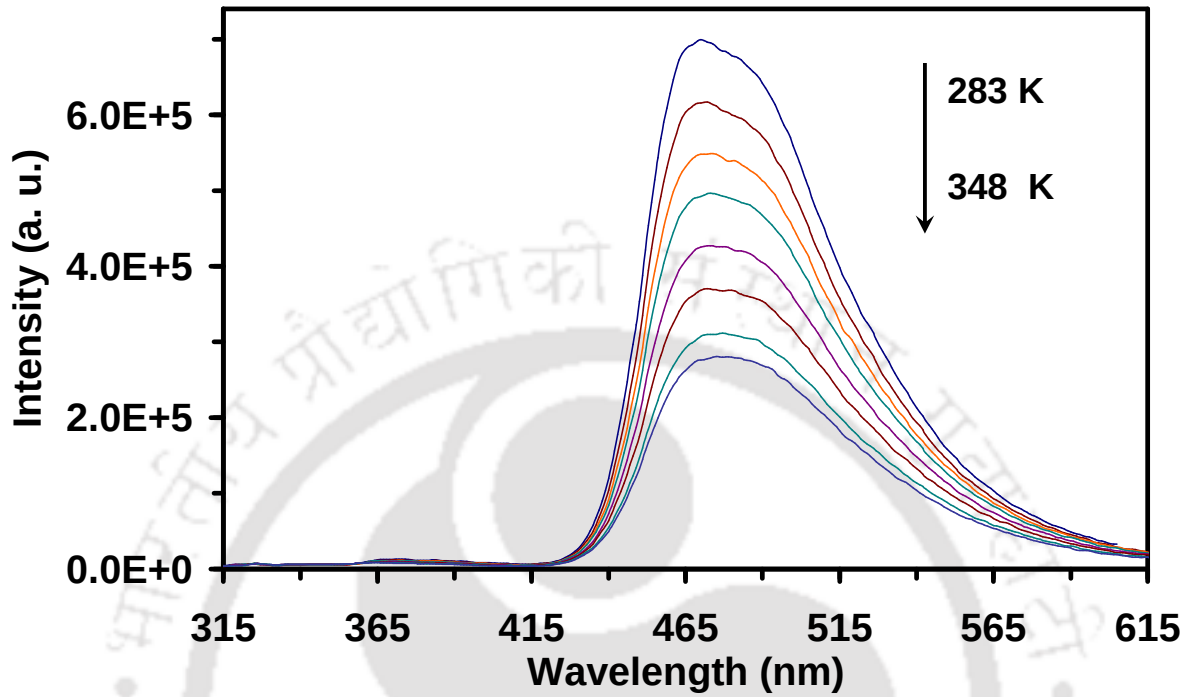

Figure 3.15. Emission spectra of HPBI in cyclohexane at different temperatures (λ_{exc} = 310 nm).

As shown for the emission spectra of HPIP-b in acetonitrile at different temperatures (**Figures 3.16a** and **3.16b**) in all other solvents also (not shown) the emission band maxima of both normal and tautomer emission are independent of excitation wavelength. This shows that emissions occur from excited state structures of completely relaxed states at these range temperatures. The variation in temperature hardly affects the emission band position (**Table 3.14**). However, the effect of temperature on fluorescence intensities depends on the nature of the solvent. The fluorescence spectra of HPIP-b in acetonitrile (**Figure 3.16a**) and HPIP-b in ethylene glycol (**Figure 3.14**) shown as a representative demonstrates the effect of temperature in aprotic and protic solvents, respectively. In aprotic solvents where the normal emissions are weak, the temperature effects on their spectral intensities are relatively smaller, but the strong tautomer emission intensity decreases significantly with rise in temperature. However, in protic solvents where the normal emission is also significant, both tautomer and normal emission decreases substantially with increase in temperature. The same behaviors are observed in all aprotic and protic solvents for all three molecules.

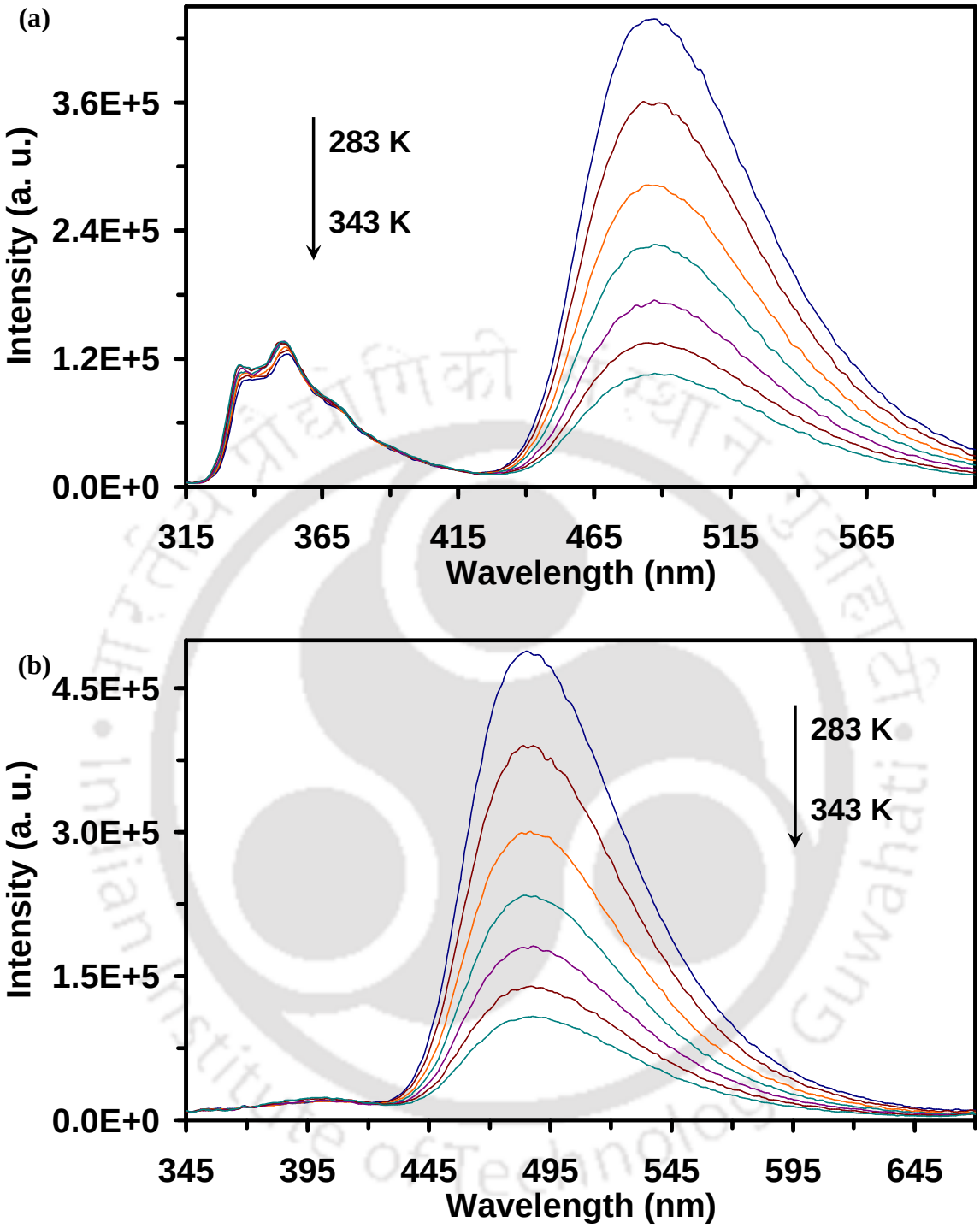

Figure 3.16. Emission spectra of HPIP-b in acetonitrile at different temperatures (a) λ_{exc} = 310 nm, and (b) λ_{exc} = 340 nm.

3.3.4. Fluorescence Quantum Yield

The quantum yield of the normal band of both HPBI and HPIP-b in acetonitrile and dioxan increases with increase in temperature (**Figures 3.17**). Since the ESIPT process is faster the emission from *cis*-enol is not observed in these systems. It is well

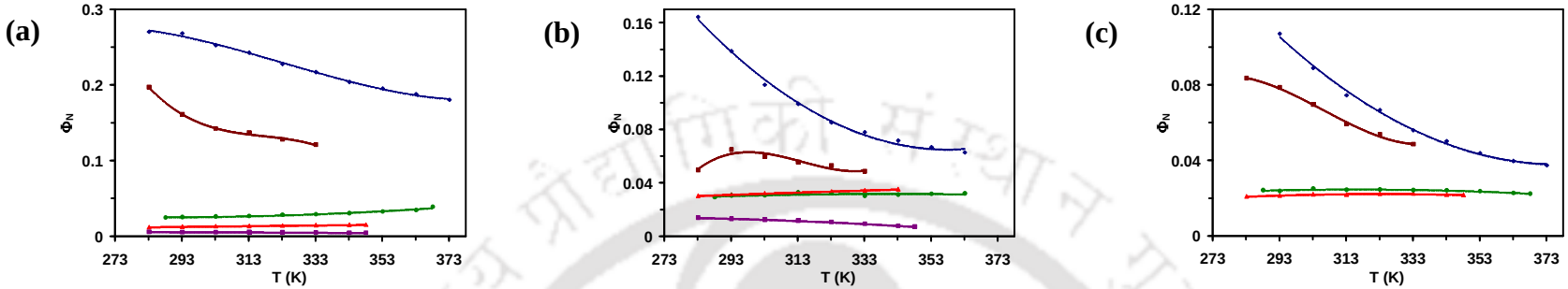

Figure 3.17. Plot of quantum yield of normal band against temperature for (a) HPBI, (b) HPIP-b, and (c) HPIP-c in cyclohexane (purple), dioxane (green), acetonitrile (red), methanol (brown), and ethylene glycol (blue) at different temperatures.

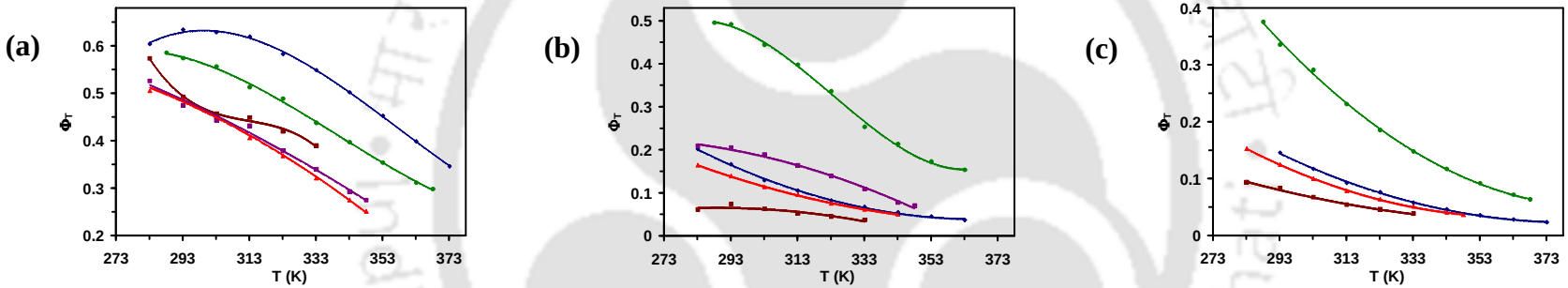

Figure 3.18. Plot of quantum yield of tautomer band against temperature for (a) HPBI, (b) HPIP-b, and (c) HPIP-c in cyclohexane (purple), dioxane (green), acetonitrile (red), methanol (brown), and ethylene glycol (blue) at different temperatures.

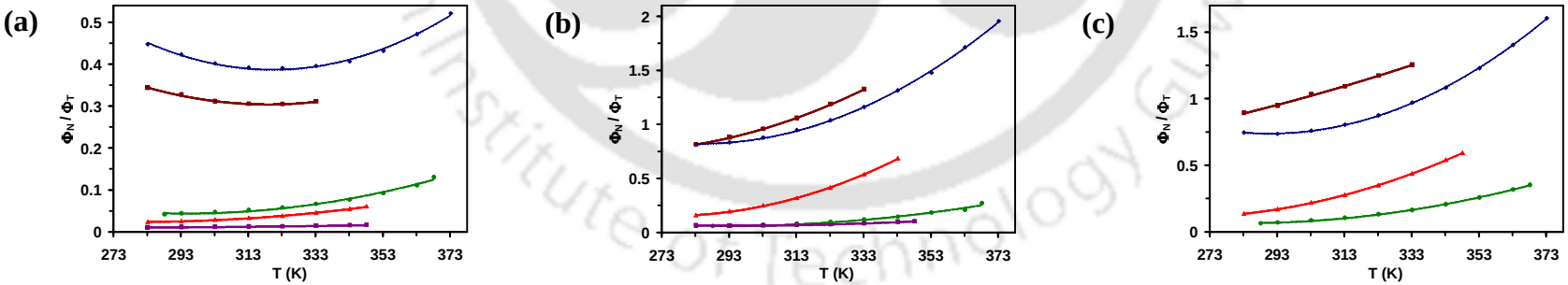

Figure 3.19. Quantum yield ratio of normal to tautomer bands of (a) HPBI, (b) HPIP-b, and (c) HPIP-c in cyclohexane (purple), dioxane (green), acetonitrile (red), methanol (brown), and ethylene glycol (blue) at different temperatures.

established that *cis*-enol, which forms an intramolecular hydrogen bonded cyclic ring, is the species responsible for ESIPT and *trans*-enol is responsible for the normal emission.[6,95,174,175] Therefore the increase in quantum yield of normal emission with rise in temperature is due to the increase in population of *trans*-enol in the ground state (**Section 3.3.2**). For HPIP-c in acetonitrile, the quantum yield remains almost constant while in dioxane there is an insignificant decrease in the quantum yield of the normal emission. This difference in behaviour of HPIP-c can be explained by the fact that the relative population of *trans*-enol to *cis*-enol decreases in the order HPBI > HPIP-b > HPIP-c. For both HPBI and HPIP-b in cyclohexane, and for all of the three molecules in protic solvents methanol and ethylene glycol, the quantum yield of the normal band decreases. This shows that the increase in nonradiative decay of *trans* or solvated enol dominates over the increase in their population with increase in temperature. Though a negative slope is displayed in the plot of quantum yield of the normal band to temperature for HPBI in methanol, and for both HPIP-b and HPIP-c in ethylene glycol, the plots are curved upward at higher temperature. On the other hand, the quantum yield of the tautomer band decreases with temperature for all the three molecules in all the solvents (**Figures 3.18**) due to decrease in the relative population of *cis*-enol and enhanced nonradiative decay of keto-tautomer with increase in temperature. Rodríguez et al. found that the methylated derivative of HPIP-b at pyridine nitrogen is non-fluorescent due to the formation of a nonemissive ICT state after ESIPT.[280] The methylation enhances the electron withdrawing ability of the azole moiety and hence the ICT from the phenolic moiety to the heterocyclic ring is more favored.

The quantum yield ratios of normal to tautomer bands of HPBI, HPIP-b and HPIP-c in different solvents at different temperatures are shown in **Figures 3.19**. For HPIP-b and HPIP-c at a given temperature, the ratio is in the order methanol > ethylene glycol > acetonitrile > dioxane. For HPBI it follows the order ethylene glycol > methanol > dioxane > acetonitrile > cyclohexane. There is an increase in the quantum yield ratio of the normal to tautomer band of all the molecules in all the solvents studied except for HPBI in methanol and ethylene glycol, where normal emission dominates over the tautomer emission (**Figure 3.19**). The ratios of HPBI in methanol and ethylene glycol indicates that the nonradiative decay from solvated enol dominates till 323 K above that the ratios show upward curvature.

3.3.5. Fluorescence Excitation Spectra

As expected, the excitation spectra recorded at the normal band (~350 to 370 nm) is blue shifted from those recorded at the keto tautomer band (~450 to 495 nm) in all three

molecules in all solvents. This is consistent with the fact that the normal and keto emissions originate from two distinct ground state species viz. *trans*-enol and *cis*-enol respectively. The two spectra differ considerably in aprotic solvents but the differences in spectra are small in protic solvents due to solvation of *trans*-enol in protic salvation to form solvated enol.

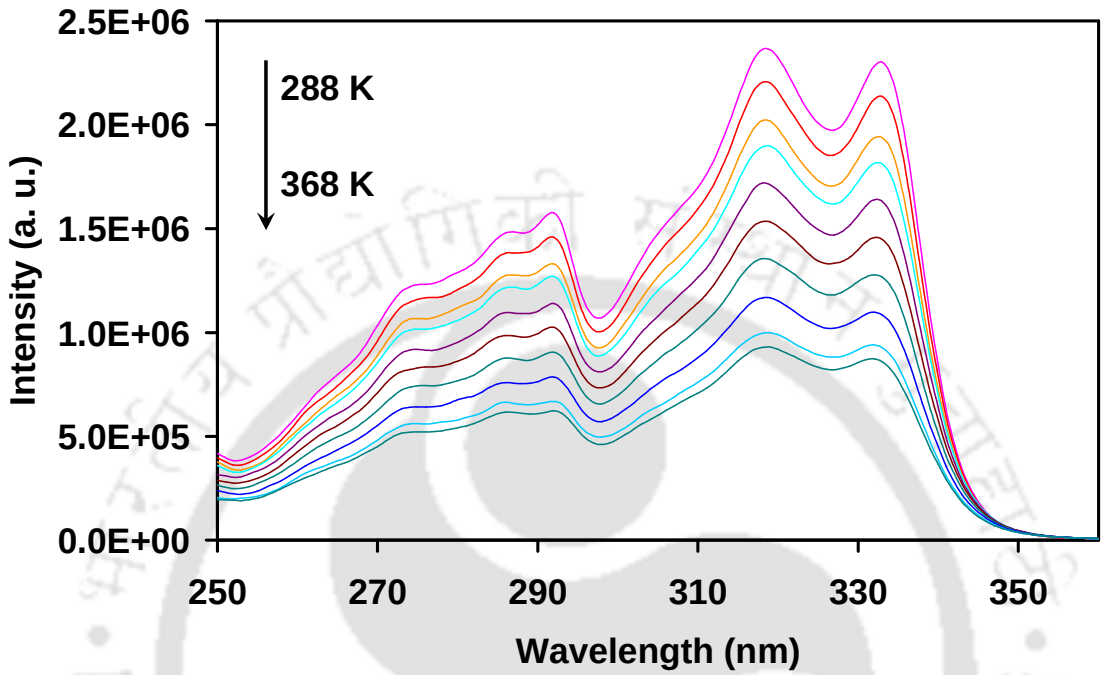

Figure 3.20. Fluorescence excitation spectra of HPBI in 1,4-dioxane at different temperatures (λ_{em} = 480 nm).

The general features of the temperature dependent fluorescence excitation spectra of all three molecules recorded at tautomer band are the same in all the solvents. Those of HPBI in dioxane are shown as representative plot in **Figure 3.20**. The spectra monitored at the tautomer band match better with the corresponding absorption spectra indicating that the species responsible for the tautomer band i.e. the *cis*-enol is the prominent structure in the ground state. The spectral intensity decreases with increase in temperature. This is due to a decrease in relative population of *cis*-enol and increases in the nonradiative decay of the keto-tautomer after ESIPT. As discussed earlier in **Sections 3.1.4** and **3.2.5**, the torsional rotation of keto-tautomer to a twisted structure is one of the nonradiative decay pathways.

The effect of temperature on the spectral intensities of the excitation spectra observed at the normal band varies for all three molecules in different solvents. Based on the effect of temperature on the spectral intensities excitation spectra observed at the normal band, they may be classified into three different types. For all of the molecules in protic polar solvents ethylene glycol and methanol, and HPIP-b in cyclohexane; the fluorescence excitation spectra

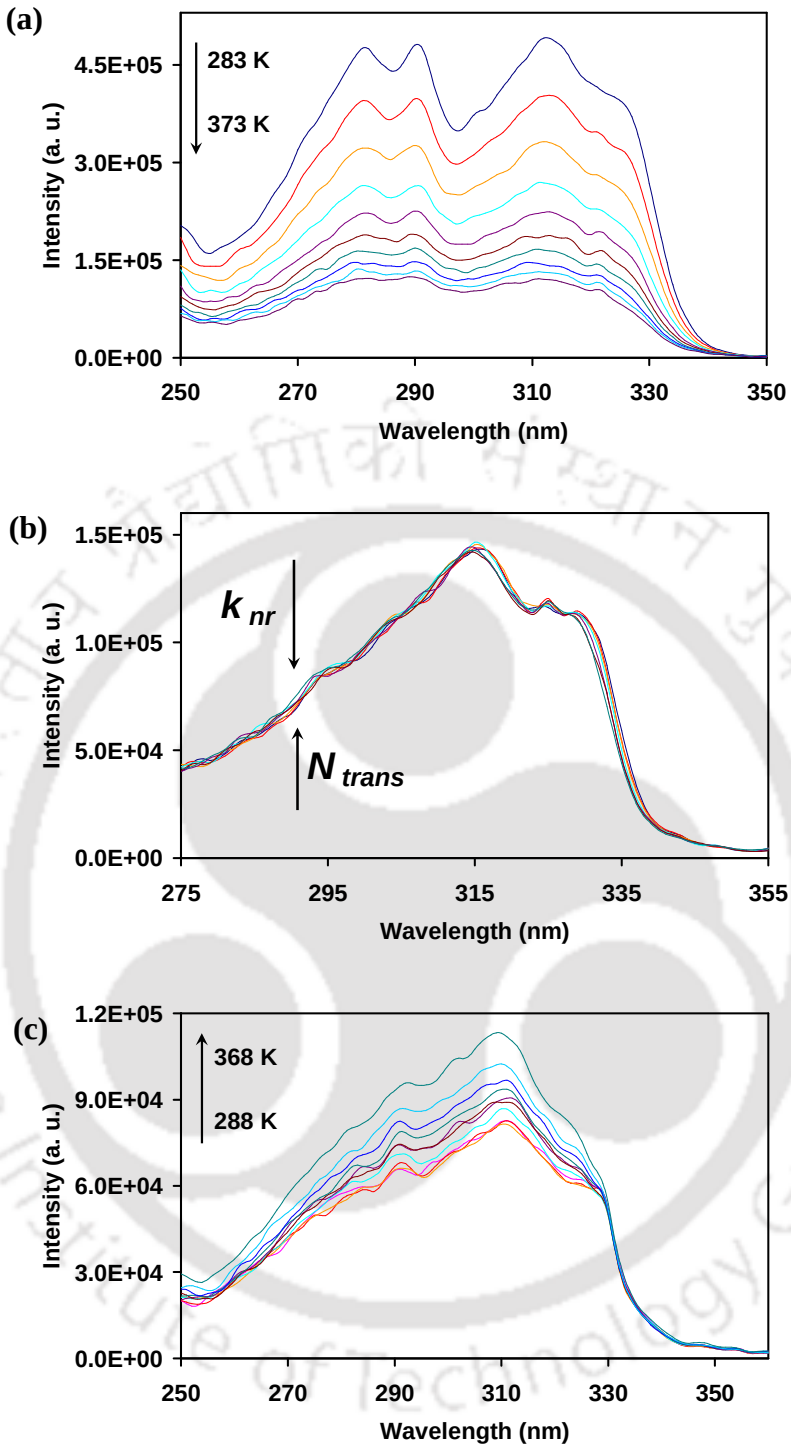

Figure 3.21. Fluorescence excitation spectra of (a) HPIP-c in ethylene glycol (λ_{em} = 355 nm), (b) HPIP-b in acetonitrile (λ_{em} = 360 nm), and (c) HPBI in 1,4-dioxane (λ_{em} = 365 nm) at different temperatures.

recorded at the normal band decrease with a rise in temperature. As a representation the excitation spectra of HPIP-c in ethylene glycol are shown in **Figure 3.21a**. This indicates that the nonradiative transition from the normal emission dominates over the increase in relative population of its ground state precursor with increase in temperature. In the second type, as

shown in **Figure 3.21b** the spectral intensities of the excitation band remain invariant in the studied temperature range. The behavior was observed by HPIP-b and HPIP-c in acetonitrile and dioxane, and HPBI in cyclohexane. This indicates that the increase in the rate of nonradiative decay was compensated by the increase in relative population of *trans*-enol with increase in temperature. In the third type, the increase in relative population of *trans*-enol with rise in temperature is higher than the increase in the nonradiative decay with rise in temperature (**Figure 3.21c**). The behavior is observed in the excitation spectra of HPBI in acetonitrile and dioxane where the spectral intensity decreases with increases in temperature.

3.3.6. Time Resolved Fluorescence

The lifetime values of all the three molecules in different solvents at different temperatures are given in **Tables 3.15-3.17**. Small differences are observed between the present measurements of lifetime values and the earlier literature values.[6,174,281] These differences may be due to the difference in the temperature, the wavelength of excitation and the wavelength used for monitoring the decay.

As a representation, the decay profile of HPIP-b in methanol at different temperatures monitored at the normal and tautomer bands is shown in **Figure 3.22**. With rise in temperature, a small decrease in lifetimes of the normal emission of HPBI is observed in cyclohexane, dioxane and ethylene glycol, whereas a small increase is observed in acetonitrile and methanol. However, the lifetimes of the keto tautomer of HPBI gradually decrease with increase in temperature in all the solvents. The temperature has greater effect on the lifetimes of the tautomer than on that of normal species.

The normal and the tautomer emission of HPIP-b and HPIP-c are single exponential in aprotic solvents whereas, they are biexpoential in methanol. In ethylene glycol, the tautomer emission is single exponential, but the normal emission is monoexpoential in HPIP-c and biexponential in HPIP-b. This suggests that due presence of pyridine nitrogen the local environment around pyridine nitrogen substituted analogues have different solvation in protic solvents and thus different lifetime. Such behaviour was also observed in 2-(2'-aminophenyl)benzimidazole.[103] The observation of two lifetime decays could be due to superimposition of many such exponential decays.[282] As in HPBI, in nitrogen analogues also the lifetime of the tautomer decreases strongly with increase in temperature and the effect is marginal for the lifetime of the normal species.

Table 3.15. Lifetime data of HPBI in different solvents at different temperatures.[1]

Temperature	Cyclohexane		1,4-Dioxane		Acetonitrile		Methanol		Ethylene Glycol	
(K)	τ^N	τ^T	τ^N	τ^T	τ^N	τ^T	τ^N	τ^T	τ^N	τ^T
293	1.74	3.76	1.41	4.32	1.58	3.83	1.59	3.93	1.62	4.48
303	1.71	3.52	1.33	4.15	1.59	3.62	1.58	3.82	1.61	4.31
313	1.71	3.29	1.34	3.96	1.65	3.39	1.56	3.72	1.60	4.12
323	1.68	3.06	1.38	3.72	1.68	3.14	1.60	3.63	1.60	3.89
333	1.62	2.80	1.38	3.58	1.71	2.92	1.63	3.48	1.59	3.67
343	1.60	2.51	1.37	3.35	1.78	2.65			1.59	3.39

[1]Lifetimes are given in nanosecond.

Table 3.16. Lifetime data of HPIP-b in different solvents at different temperatures.[1,2]

Temperature	Cyclohexane[3]	1,4-Dioxane		Acetonitrile		Methanol				Ethylene Glycol		
(K)	τ^T	τ^N	τ^T	τ^N	τ^T	τ_1^N (f_1)	τ_2^N (f_2)	τ_1^T (f_1)	τ_2^T (f_2)	τ_1^N (f_1)	τ_2^N (f_2)	τ^T (f_1)
293	3.41	1.02	3.66	1.14	1.59	0.55 (32)	1.65 (68)	0.84 (80)	4.47 (20)	0.64 (89)	2.35 (11)	2.00
303	3.02	1.00	3.28	1.10	1.33	0.76 (41)	1.69 (59)	0.70 (81)	4.35 (19)	0.55 (86)	2.28 (14)	1.52
313	2.62	0.99	2.82	1.09	1.00	0.71 (43)	1.69 (57)	0.58 (78)	4.34 (22)	0.53 (86)	2.31 (14)	1.24
323	2.26	0.96	2.46	1.07	0.82	0.52 (34)	1.63 (66)	0.45 (74)	4.24 (26)	0.42 (79)	1.88 (21)	0.97
333	1.89	0.96	2.12	1.04	0.67	0.51 (34)	1.68 (66)	0.39 (72)	4.14 (28)	0.42 (79)	1.91 (21)	0.78
343	1.56	0.95	1.66	1.04	0.58					0.39 (75)	1.77 (25)	0.64

[1]Lifetimes are given in nanosecond. [2]Values within parentheses are the relative percentage component. [3]The lifetime of the normal species could not be measured due to weak fluorescence of the normal species.

Table 3.17. Lifetime data of HPIP-c in different solvents at different temperatures.[1,2]

Temperature	1,4-Dioxane		Acetonitrile		Methanol				Ethylene Glycol	
(K)	τ^N	τ^T	τ^N	τ^T	τ_1^N (f_1)	τ_2^N (f_2)	τ_1^T (f_1)	τ_2^T (f_2)	τ^N	τ^T
293	1.10	2.85	1.28	1.45	0.32 (84)	1.84 (16)	0.98 (86)	3.10 (14)	0.79	2.36
303	1.06	2.36	1.26	1.12	0.29 (84)	1.87 (16)	0.77 (86)	3.24 (14)	0.68	1.81
313	1.04	2.16	1.24	0.88	0.32 (85)	2.12 (16)	0.62 (86)	3.42 (14)	0.60	1.39
323	1.03	1.69	1.22	0.71	0.26 (84)	2.34 (16)	0.49 (84)	3.46 (16)	0.50	1.13
333	1.01	1.50	1.21	0.62	0.29 (84)	2.91 (16)	0.44 (83)	3.54 (17)	0.45	0.88
343	0.97	1.44	1.20	0.49					0.41	0.60

[1]Lifetimes are given in nanosecond. [2]Values within parentheses are the relative percentage component.

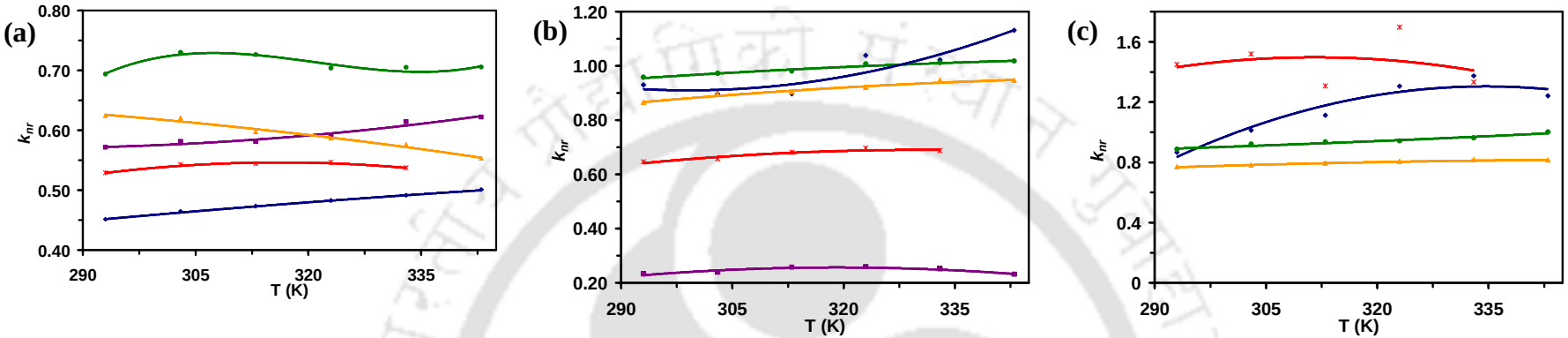

Figure 3.23. Nonradiative decay plots of normal band against temperature for (a) HPBI, (b) HPIP-b, and (c) HPIP-c in cyclohexane (-■-), dioxane (-●-), acetonitrile (-▲-), methanol (-*-), and ethylene glycol (-♦-).

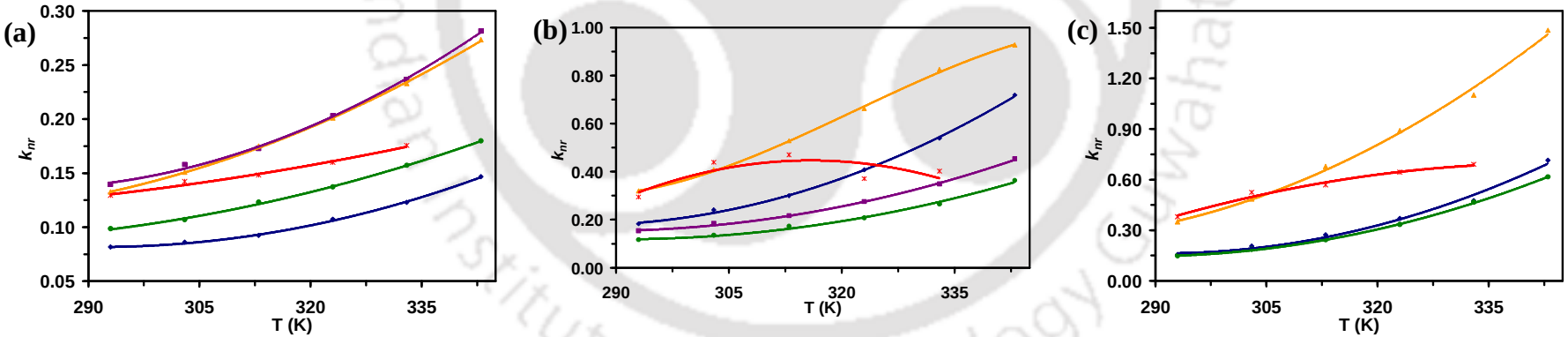

Figure 3.24. Nonradiative decay plots of tautomer band against temperature for (a) HPBI, (b) HPIP-b, and (c) HPIP-c in cyclohexane (-■-), dioxane (-●-), acetonitrile (-▲-), methanol (-*-), and ethylene glycol (-♦-).

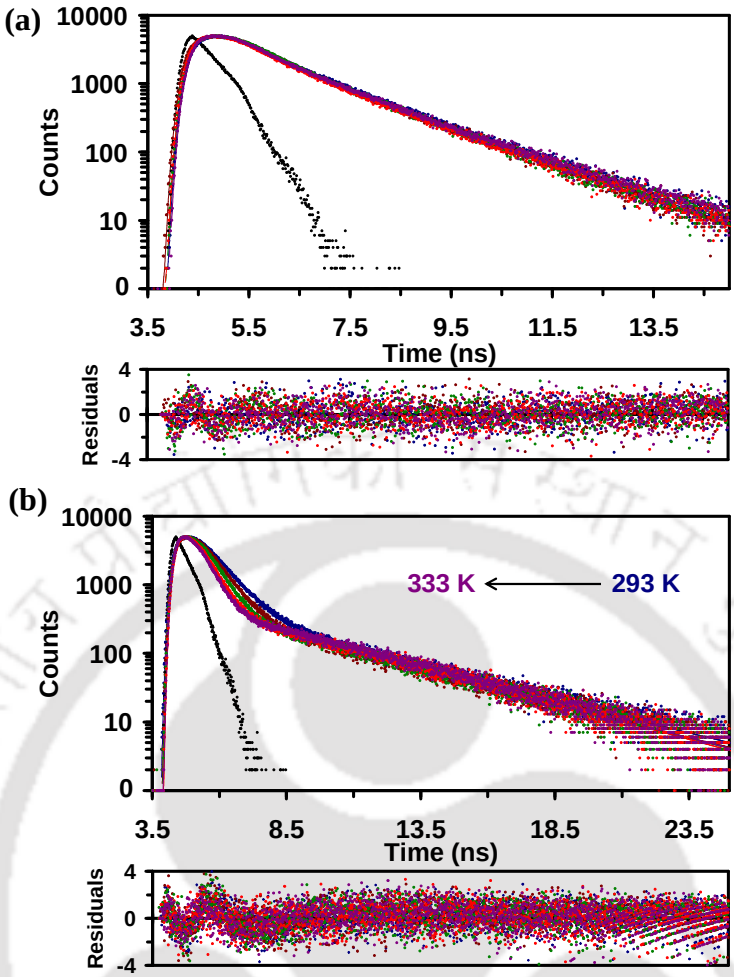

Figure 3.22. Decay profile of HPIP-b in methanol at different temperatures from 293 K to 333 K with interval of 10 K monitored at the (a) normal band (~ 355 nm), (b) tautomer band (~ 490 nm) and λ_{exc} = 308 nm.

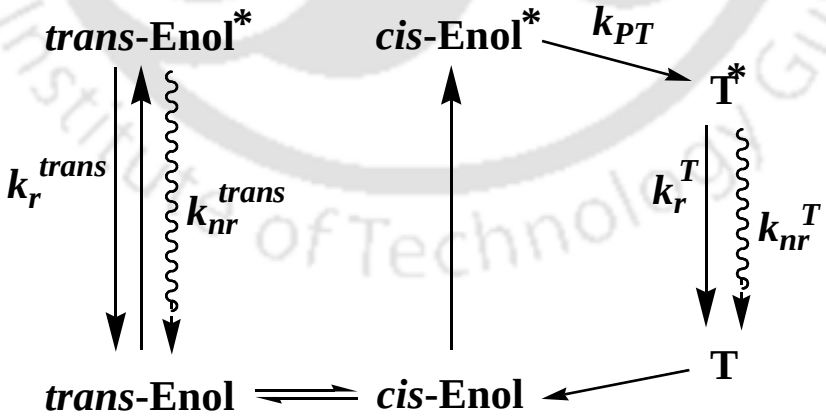

Scheme 3.2. Kinetics schemes for the decay of *trans*-enol and ESIPT process in nitrogen substituted HPBI analogues.

The results can be explained by the commonly accepted kinetics scheme for ESIPT molecules (**Scheme 3.2)** i.e. in the excited *cis*-enol undergoes the ESIPT process while the excited *trans*-enol gives the normal emission. Increase in temperature affects the relative

population of ground state conformers and also increases the nonradiative decay which in turn affects the fluorescence of both enol and tautomer forms. Since the rise in temperature decreases population of *cis*-enol and also increases the nonradiative decay, the decrease in emission and lifetime are more for tautomer emission than those for normal emission.

3.3.7. Conclusion

The effects of temperature on the dual fluorescence of HPBI, HPIP-b and HPIP-c due to ESIPT were studied in different solvents of different polarity and hydrogen bonding capacity. The quantum yield ratio of the normal to tautomer band increases with increase in temperature except for HPBI in methanol and ethylene glycol. This shows that the rate of decrease in quantum yield with increase in temperature is greater in the tautomer band than in the normal band. The change in the fluorescence with increase in temperature is influenced by two factors: (i) the increase in relative population of *trans*-enol with respect to that of *cis*-enol, and (ii) the increase in nonradiative decay from the excited states. As with the rise in temperature, the population of *cis*-enol decreases and the nonradiative decay of tautomer increases, temperature affects the tautomer emission more than the normal emission. With rise in temperature, the increase in nonradiative decay of the normal emission competes with the increase in relative population of *trans*-enol. Nitrogen substitution in the benzene ring of HPBI increases the nonradiative deactivation to the ground state. The changes in the fluorescence emission are also reflected in the lifetime of the normal and tautomer emissions. In general, the lifetime decreases with rise in temperature indicating the increase in the rate of nonradiative decay.

Chapter 4

Study of Fluorescence Sensing Ability of 2-(2'-Hydroxyphenyl)benzimidazole and its Nitrogen Substituted Analogues Toward Metal Ions

4.0. Introduction

Fluorescence sensors and probes are one of the common analytical tools for the detection and measurements of various kinds of analytes due to their high sensitivity.[27,28,163,283-291] Moreover, the techniques applied in the analyses, based on fluorescence sensors are easy to handle and less expensive. Most of the fluorescence chemosensors are based on a turn on/off mechanism where the fluorescence is enhanced or quenched upon binding with the analyte.[289,290] Since the intensity of the fluorescence is dependent on the concentrations of both analyte and sensor molecule, measurements at only one emission wavelength face practical limitations specially for use in biological systems due to the difficulty in determination of the fluorophore concentration. One possible solution to the problem is to use a fluorophore that exhibits spectral shift in the emission or excitation spectra upon binding with the analyte.[292-296] This provides a ratiometric measurement of the emission intensities at two excitation or emission wavelengths. The ratiometric measurments eliminate the artifacts due to concentration variation, photobleaching, or any instrument related parameters.[297,298]

ESIPT exhibiting molecules find suitable application as fluorescence sensors for solvent polarity,[291,299,300] viscosity,[300] pH,[287] anions,[141,301-306] and cations[170,298,307-312] because of their photophysical properties such as high fluorescence, large Stokes' shifts and photostability.[27,28,163] In most of the cases, fluorescence sensing by ESIPT is based on ratiometric measurements due to their dual fluorescence.[141,170,287,298-313] A limited number of works have been done on the investigations on cation sensing based on derivatives of HPBO.[298,309,313]

Fahrni et al. have studied the complexation of carboxylic acid derivatives of HPBI, HPBO, and HPBT with Zn^{2+} ion in water.[27,298] They found that deprotonation of the hydroxyl proton occurs upon coordination with Zn^{2+} ion. This results in the formation of the corresponding phenolate ions of the benzazoles. They also found that while the fluorescence of oxazole and thiazole derivatives increase upon complexation with Zn^{2+}, the imidazole derivative does not show significant change in the quantum yield but it exhibits ratiometric response toward Zn-complexation. Jen et al. developed one-photon and two-photon-absorbing sensors containing one and two HPBO groups that act as binding sites for metal ions.[311] These sensor molecules have unique response for Zn^{2+} ion and their properties are dramatically affected by base. While the sensor molecule with one binding site has more sensitivity to Zn^{2+} ion at low concentration, the molecule with two binding sites exhibits a larger enhancement in fluorescence. O'Halloran et al. also designed HPBO based fluorescent

sensor Zimbo-5 that has a variety of chelating groups in the molecular structure.[309] They showed that Zn^{2+} and Cd^{2+} induce an emission shift while other heavy metal ions quench the fluorescence of Zimbo-5.

However, interaction of HPBI, the imidazole analogue of HPBO, with metal ions has not been studied yet to the best of my knowledge. In this chapter, we report the photophysical study of HPBI and its nitrogen substituted analogues viz. HPIP-b and HPIP-c upon interaction with alkali, alkaline and transition metal ions. The ratiometric response of the fluorophores toward complexation with different metal ions and the influence of nitrogen substitution in the benzene ring of HPBI upon complexation are the main theme of the study.

4.1. Absorption Spectra

4.1.1. Alkali and Alkaline Metal Ions

HPBI shows in increase in absorbance on increasing concentrations of Na^+, Mg^{2+} and Ca^{2+} ions, but shows a decrease in the case of Ba^{2+}. However, no shift is observed and the changes in the spectral shape are also not significant. As a representation, **Figure 4.1** shows the increase in absorbance of HPBI in increasing concentration of Na^+. HPIP-b in presence of Mg^{2+}, Ca^{2+} and Ba^{2+} ions and HPIP-c in presence of Na^+, Ca^{2+} and Ba^{2+} ions also show similar trend in the absorption spectra.

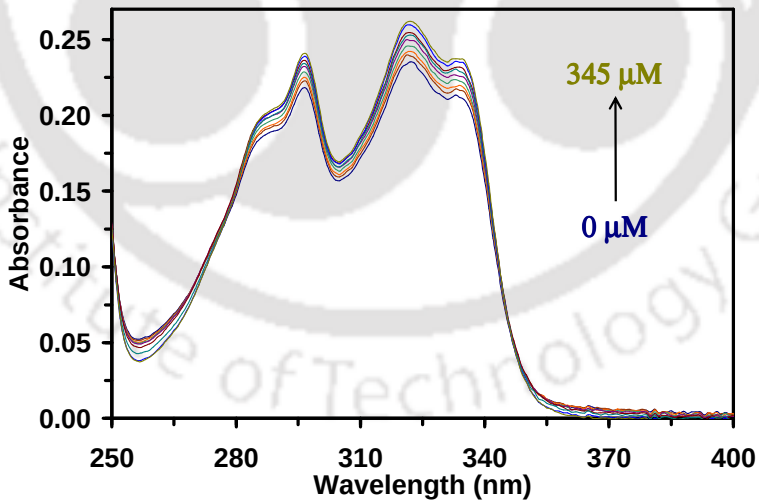

Figure 4.1. Absorption spectra of HPBI in presence of Na^+.

However, in the presence of Na^+ ion, HPIP-b shows a stepwise change in the absorption spectra as the concentration of Na^+ is increased from 0 to 9.7 µM as is shown in **Figure 4.2**. For initial addition of Na^+ ion to HPIP-b solution, the absorbance increases until the concentration of Na^+ reaches 5.2 µM (1:1 molar ratio, **Figure 4.2a**). Above this

concentration ([Na^+ > 5.2 μM), a new band appears at 354 nm while the band maximum at 322 nm decreases and an isosbestic point is observed at 338 nm (**Figure 4.2b**). The new band reaches the maximum when [Na^+] = 6.0 μM. Further increase in concentration from 6.0 μM to 7.1 μM decreases the absorbance of 354 nm band and increases that of 322 nm band with an isosbestic point at 338 nm (**Figure 4.2c**). Beyond 7.1 μM, the 354 nm band increases again while the 322 nm band decreases (**Figure 4.2d**). Above 9.7 μM of Na^+, no significant change in the spectra is observed.

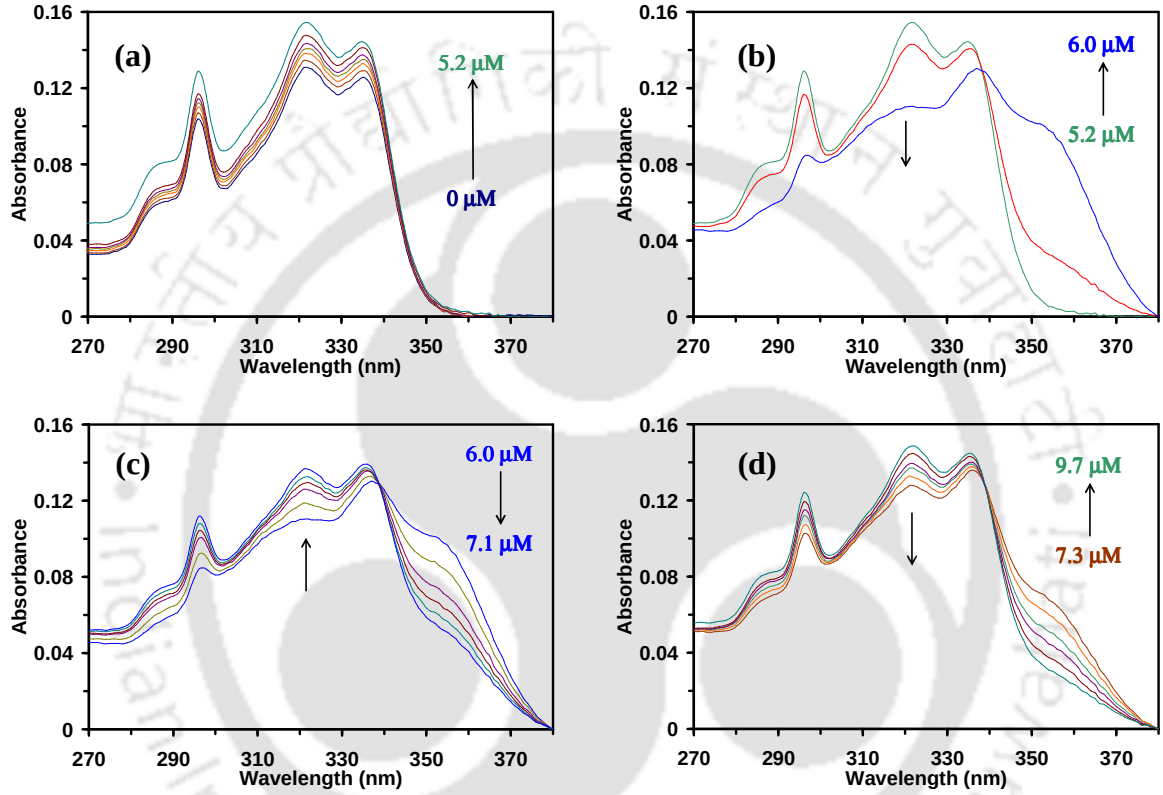

Figure 4.2. Stepwise change in the absorption spectra of HPIP-b at (a) 0-5.2 μM, (b) 5.2-6.0 μM, (c) 6.0-7.3 μM, and (d) 7.3-9.7 μM of Na^+.

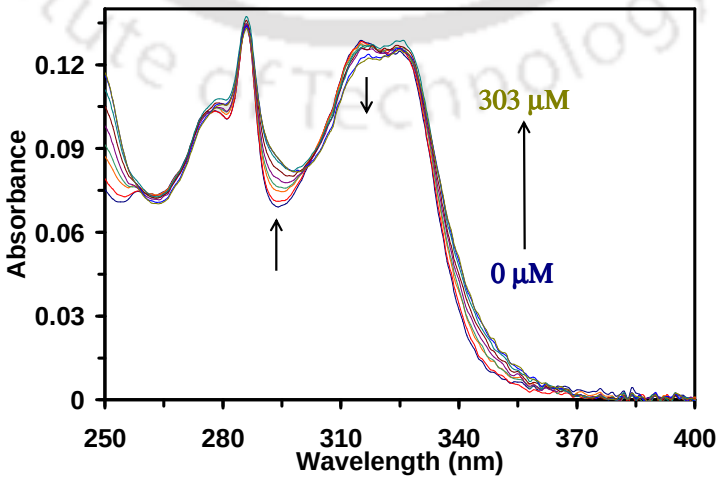

Figure 4.3. Absorption spectra of HPIP-c in presence of Mg^{2+}.

Figure 4.3 shows the effect of Mg^{2+} ion on HPIP-c. On increasing the concentration of Mg^{2+}, the absorbance at onset increases while that of the main band at 315 decreases. However, unlike in the earlier case (interaction of Na^{+} ion with HPIP-b) the spectral changes are not significant.

4.1.2. Ni^{2+}, Cu^{2+} and Zn^{2+} Metal Ions

Figure 4.4 depicts the absorption spectra of HPIP-b at different concentrations of Zn^{2+} ion. The absorbance of the main band decreases and a new band starts to appear at the red side of the absorption spectra (~ 360 nm) and the spectral changes reach saturation at higher concentrations and a quasi isosbestic point is also observed. Similar behaviour is also observed in the other two molecules (Figures not shown), but the saturation point for the interaction of Zn^{2+} with HPBI and HPIP-b is reached at 500 μM and 460 μM, respectively. However, for HPIP-c the saturation point is reached at 8 μM which is ~ 1.5 equivalent. This shows the sensitivity of HPIP-c toward Zn^{2+} is nearly 60 times higher than that of its analogues.

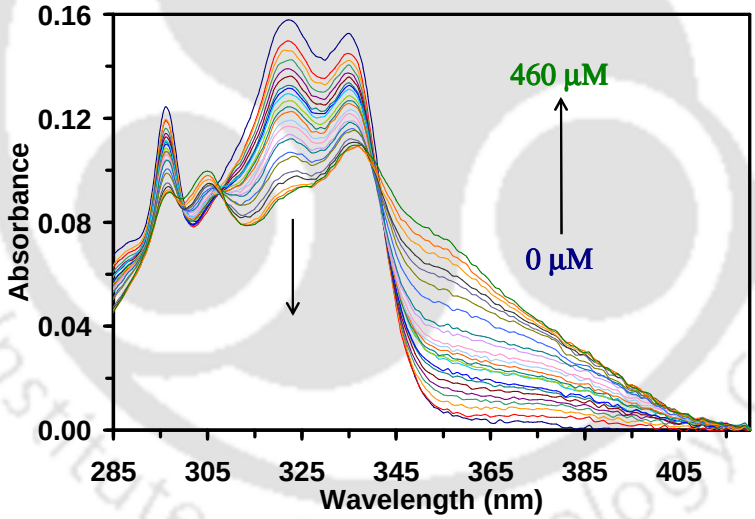

Figure 4.4. UV-Visible spectra of HPIP-b in presence of Zn^{2+}.

The effect of Cu^{2+} ions on the absorption spectra of all three fluorophores is nearly similar to that of Zn^{2+} up to ~ 10 μM (i.e. ~ 2 equivalents). That is, a decrease in absorbance of the main band with a formation of new band on the red side band. The isosbestic points are observed at 334 nm, 342 nm and 334 nm in the absorption spectra of HPBI, HPIP-b and HPIP-c, respectively. **Figure 4.5** shows the absorption spectra of HPBI in presence of Cu^{2+} ion as representative plot. On increasing the concentration until 13 μM, the absorbance of the shoulder at 355-370 nm increases (**Figure 4.5a**). On the other side of the isosbestic point, the

absorbances of the vibronic bands at 315-323 nm decrease. Above this concentration of Cu^{2+} ion the isosbestic points disappear and the absorbances increase with increasing concentration of Cu^{2+} ion, but the increases in small and it is saturated at ~ 350 μM (**Figure 4.5b**).

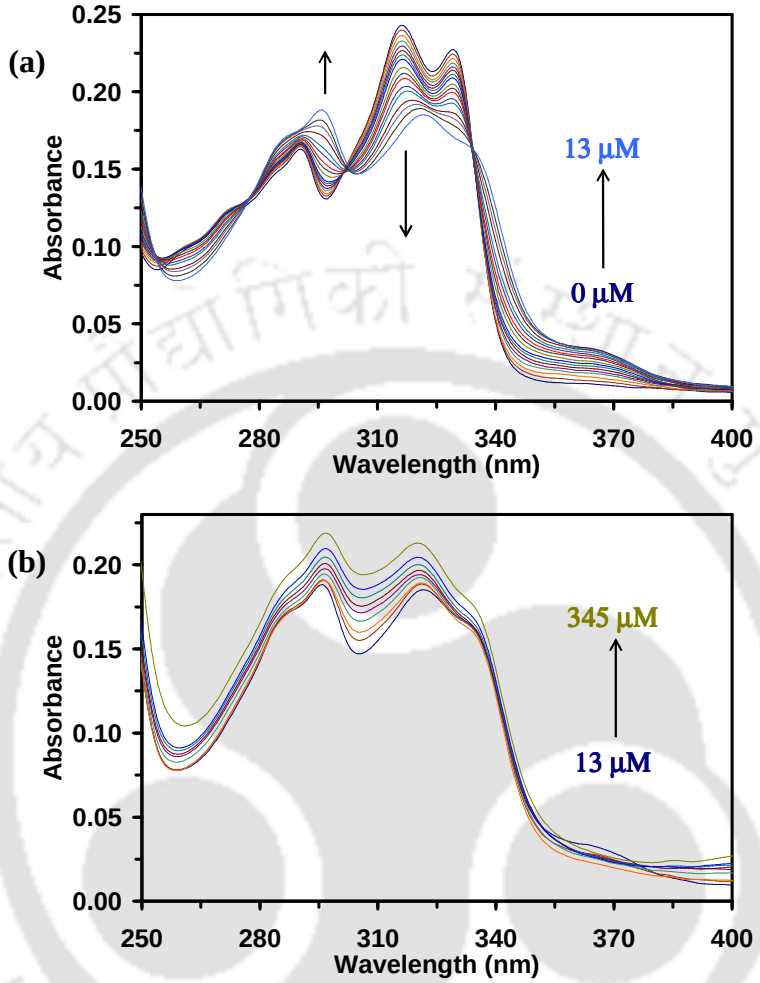

Figure 4.5. UV-Visible spectra of HPBI in presence of Cu^{2+} (a) from 0 μM to 13 μM, and (b) ≥ 13 μM.

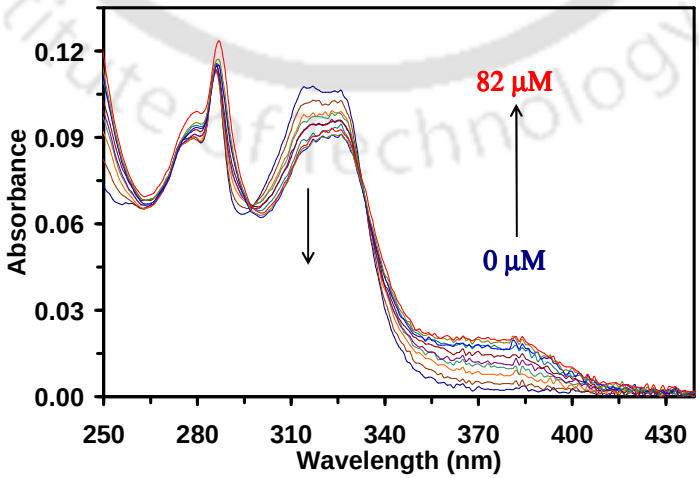

Figure 4.6. Absorption spectra of HPIP-c in presence of Ni^{2+}.

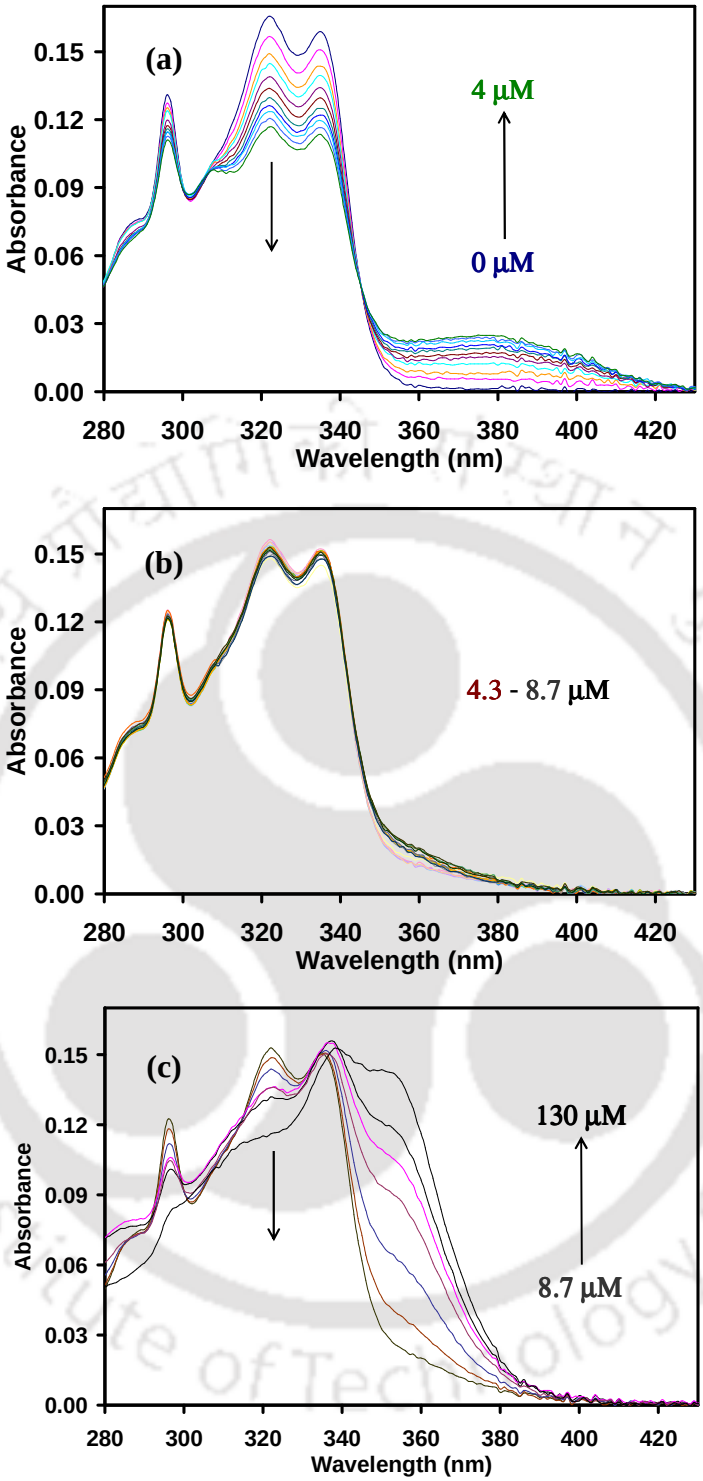

Figure 4.7. Stepwise change in absorbance of HPIP-b in presence of Ni^{2+} in the range (a) 0 - 4 μM, (b) 4.3 - 8.7 μM, and (c) 8.7 - 130 μM.

The effect of Ni^{2+} on the absorption spectra of HPBI and HPIP-c is also similar to that of Zn^{2+} ion. **Figure 4.6** shows the representative spectra of HPIP-c in presence of Ni^{2+} ion. With increase in Ni^{2+} ion concentration, the absorbances of the vibronic bands at 315-330 nm decrease. On the red side, a new red band appears at 360-370 nm whose absorbance increases

with Ni^{2+} ion concentration. The spectra of HPBI and HPIP-c reach the saturation point at 55 μM and 82 μM, respectively.

However, HPIP-b shows stepwise change in the absorption spectra upon interaction with Ni^{2+} ion (**Figures 4.7**). The effect is quite similar to that of Na^{+} ion on HPIP-b. A new band appears at 380 nm and its absorbance increases while those of vibronic bands at blue side decrease with increase in Ni^{2+} ion concentration up to 4 μM (~ 1 equivalent) and an isosbestic point is observed at ~ 345 nm (**Figure 4.7a**). From 4 μM to 4.3 μM, the band at 380 nm disappears rapidly and the spectra remain constant till 8.7 μM (**Figure 4.7b**). With further increase in Ni^{2+} ion amount, a new band starts to appear at ~ 360 nm and the absorbances of the vibronic bands at 296 nm and 321 nm decrease. The changes continue till the saturation point (130 μM). A quasi-isosbestic point is observed at ~ 334 nm (**Figure 4.7c**).

4.2. Fluorescence Spectra

4.2.1. Alkali and Alkaline Metal Ions

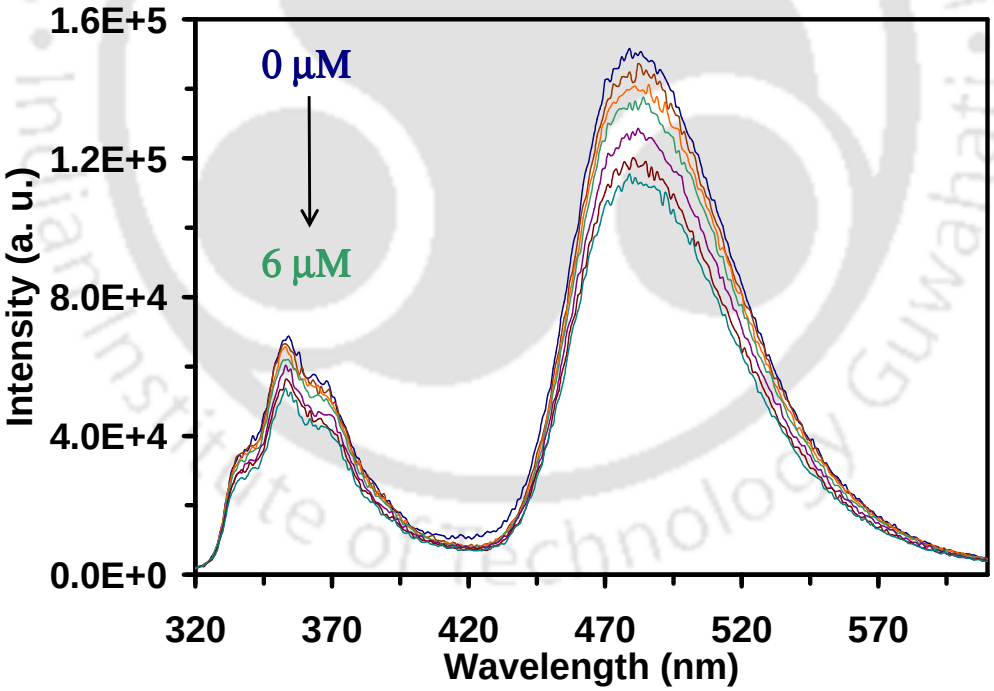

Figure 4.8. Fluorescence spectra of HPIP-b in presence of Ca^{2+} (λ_{exc} = 308 nm).

Except for a small decrease in normal and tautomer emissions, no significant change is observed in the fluorescence spectra of HPBI and its analogue in presence of Na^{+} and Ba^{2+} ions. Similar behaviour is observed for the fluorescence spectra of HPBI and HPIP-b in presence of Ca^{2+} ion and that of HPIP-b in presence of Mg^{2+} ion. As a representation, **Figure**

4.8 shows the fluorescence of HPIP-b in presence of Ca^{2+} ion where both normal and tautomer emissions decrease with increasing concentration of Ca^{2+} ion and reaches saturation on reaching 6 μM.

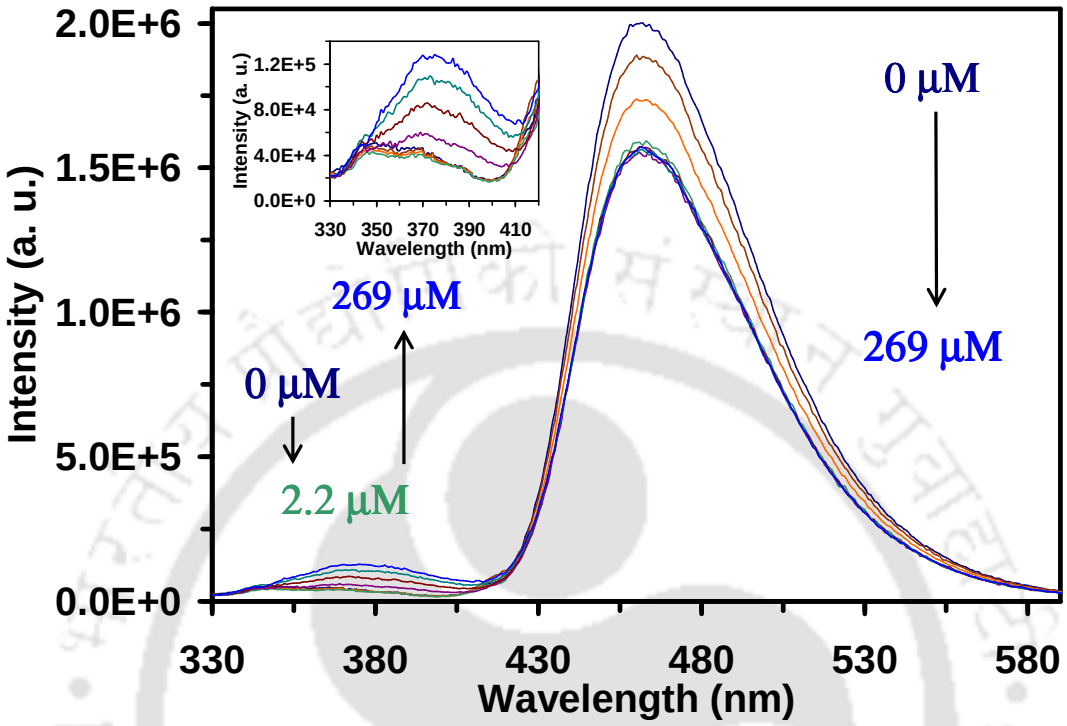

Figure 4.9. Fluorescence spectra of HPBI in presence of Mg^{2+} (λ_{exc} = 300 nm). The inset shows the expanded spectra of normal band region.

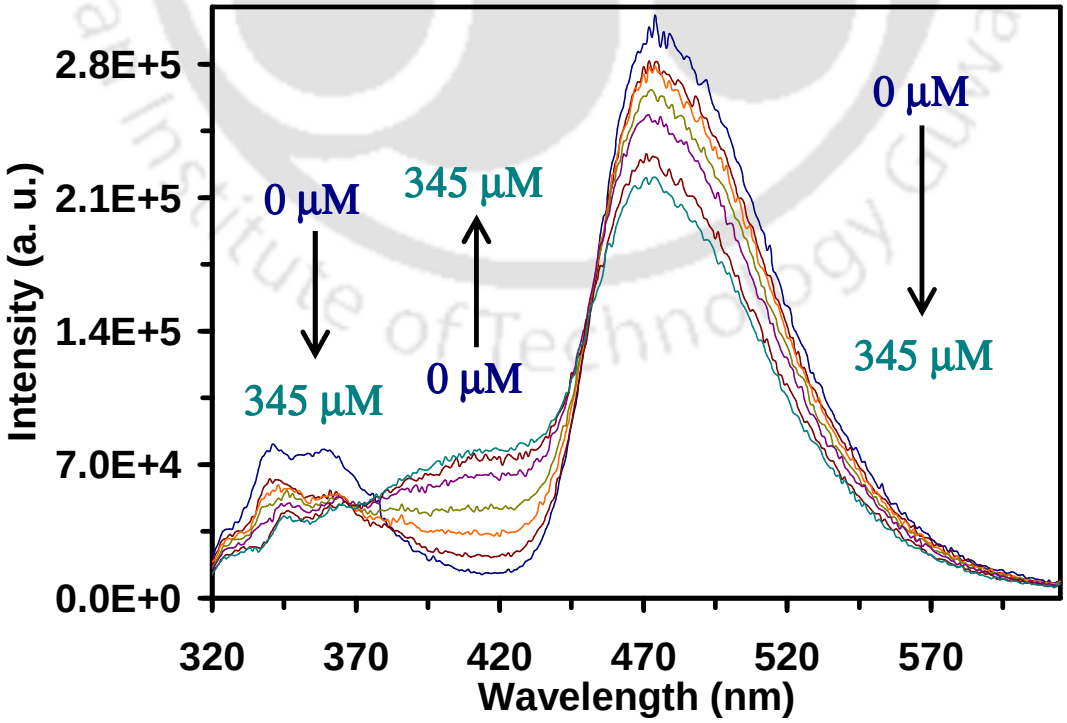

Figure 4.10. Fluorescence spectra of HPIP-c in presence of Mg^{2+} (λ_{exc} = 308 nm).

It is interesting to note that in presence of Na^+ unlike in the absorption spectra no significant effect is observed in the fluorescence spectra of HPIP-b (not shown). This indicates that the Na^+ complex of HPIP-b is unstable in the excited state and the metal ion has only weaker interaction with HPIP-b in the excited state. The tautomer band of HPBI decreases with increases in Mg^{2+} concentration, but the normal emission of HPBI initially decreases till 2.22 μM, then it is red shifted to 375 nm (**Figure 4.9**). The 375 nm band enhances with increase in concentration of Mg^{2+} and the saturation point was reached at 269 μM.

However, in case of HPIP-c a new emission band is generated at 405-415 nm in presence of Mg^{2+} and Ca^{2+} ions. As a representation, **Figure 4.10** shows the fluorescence spectra of HPIP-c in presence of Mg^{2+} ions. As the concentration of Mg^{2+} ions increases, both normal and tautomer emissions decrease and a new emission band is generated at 413 nm which increases with Mg^{2+} concentration. An isoemissive point is also observed at 451 nm.

4.2.2. Ni^{2+}, Cu^{2+} and Zn^{2+} Metal Ions

As in absorption spectra, the effects of transition metals ions Ni^{2+}, Cu^{2+} and Zn^{2+} on the fluorescence of the fluorophores are more pronounced than that in presence of alkali and alkaline earth metal ions.

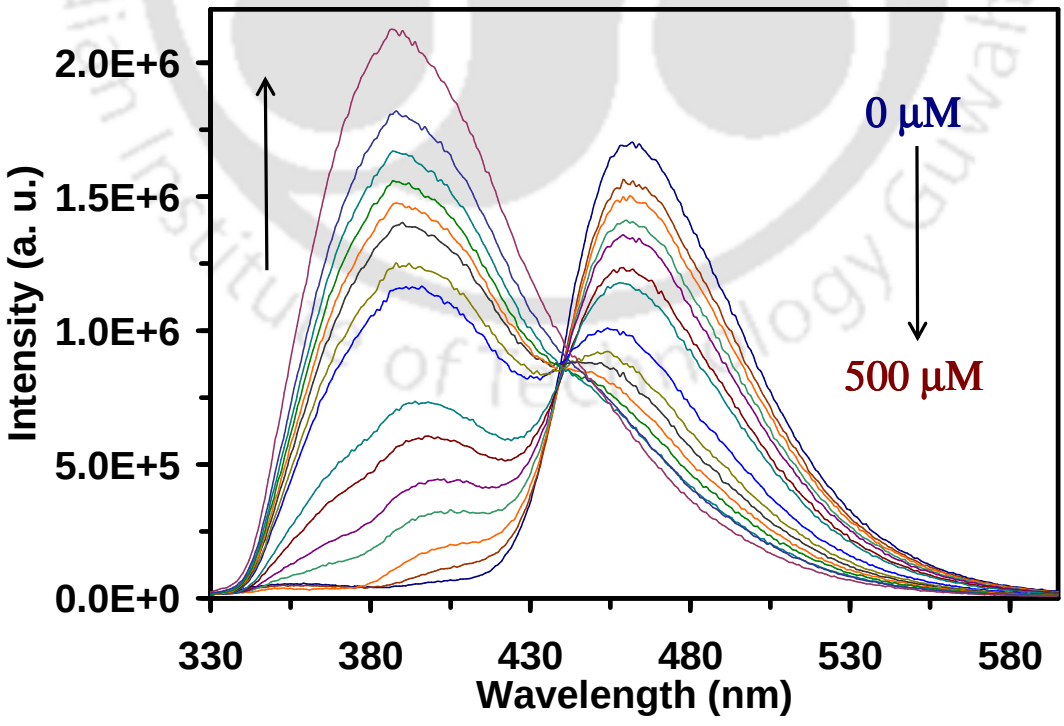

Figure 4.11. Fluorescence spectra of HPBI in presence of Zn^{2+} (λ_{exc} = 300 nm).

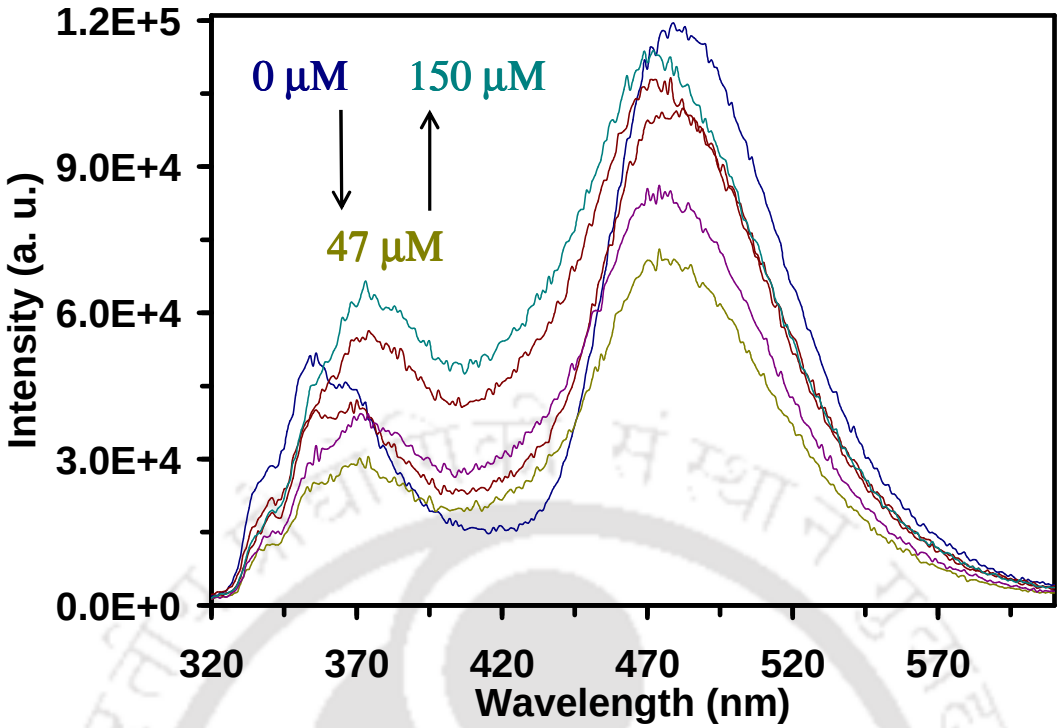

Figure 4.12. Fluorescence spectra of HPIP-b in presence of Zn^{2+} (λ_{exc} = 308 nm).

Addition of Zn^{2+} ion decreases the fluorescence intensities of both normal and tautomer emissions and a new band appears in all the three molecules (**Figures 4.11** to **4.13**). The new band is red shifted relative to normal band and blue shifted relative to tautomer band. In HPBI and HPIP-c, the dual emissions of the ligands are placed by a single emission in presence of Zn^{2+} ion. A quasi-isoemissive point is observed at 440 nm in the fluorescence spectra of HPBI in presence of Zn^{2+} ion (**Figure 4.11**). Two quasi-isoemissive points are observed at 373 nm and 446 nm in the fluorescence of HPIP-c on increasing concentration of Zn^{2+} ion (**Figure 4.13**). But in case of HPIP-b, even at saturation limit (500 µM) the emission spectrum is not single emission and no quasi-isoemissive point is also observed. The excitation spectra recorded at normal and tautomer emission matches with that of the pure ligand and the additional band was observed when monitored at 440 nm only in presence of metal ion. The new excitation band agrees well with new red band of the absorption spectrum in presence of Zn^{2+} (**Figure 4.14**) These results indicate that like Na^{+} ion complex of HPIP-b, its Zn^{2+} complex is also unstable. However, Zn^{2+} complexes of HPBI and HPIP-c are quite stable.

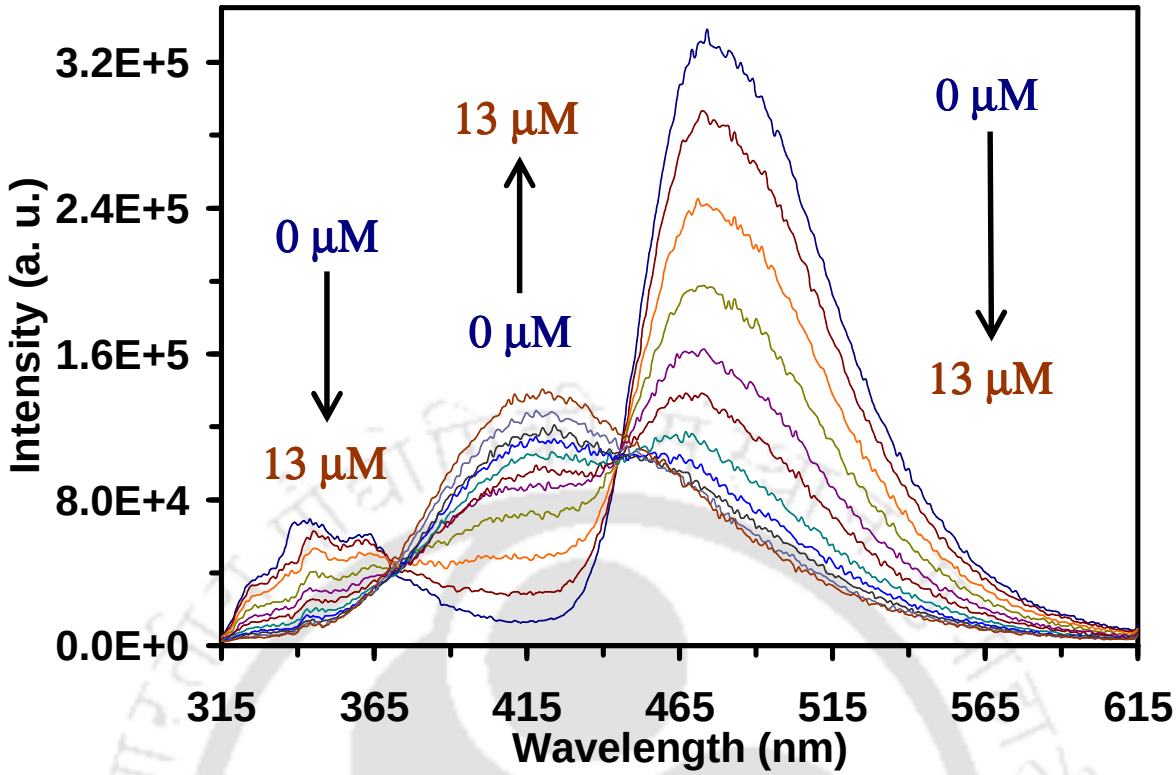

Figure 4.13. Fluorescence spectra of HPIP-c in presence of Zn^{2+} (λ_{exc} = 310 nm).

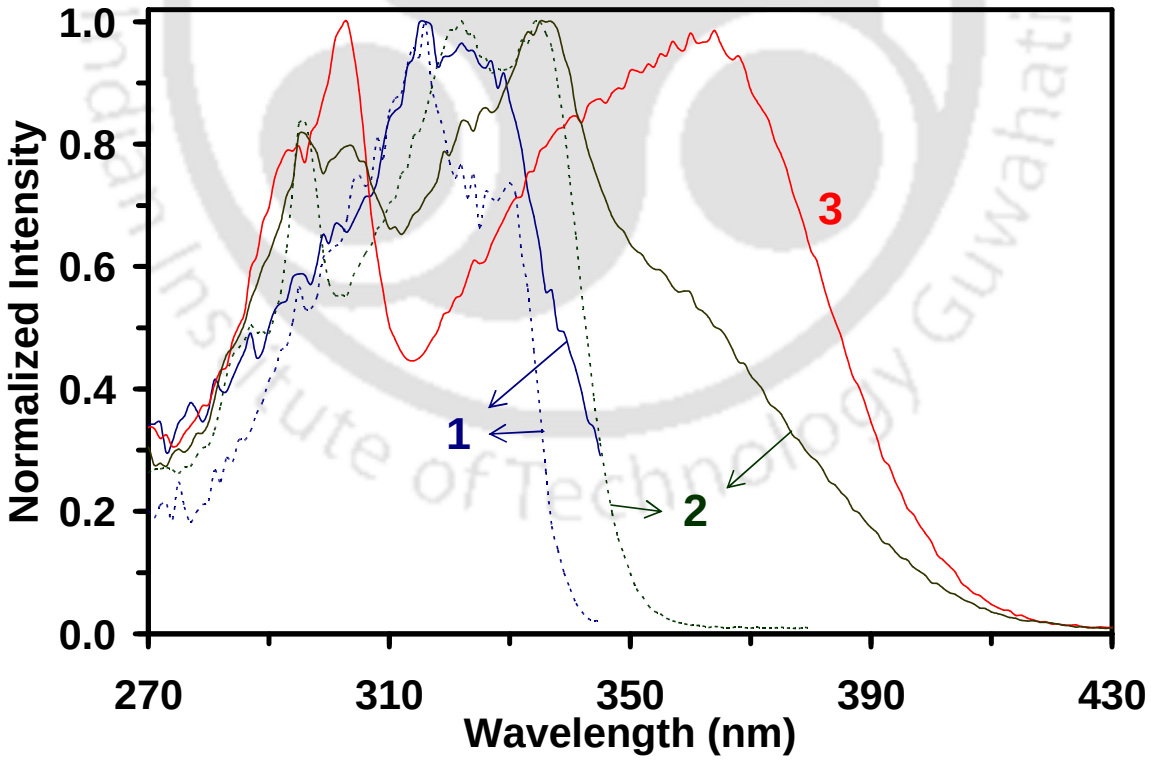

Figure 4.14. Normalized fluorescence excitation spectra of HPIP-b in presence (solid lines) and absence (dotted lines) of Zn^{2+} (500 μM) monitored at (1) λ_{em} = 350 nm (blue), (2) λ_{em} = 440 nm (red), and (3) λ_{em} = 480 nm (green).

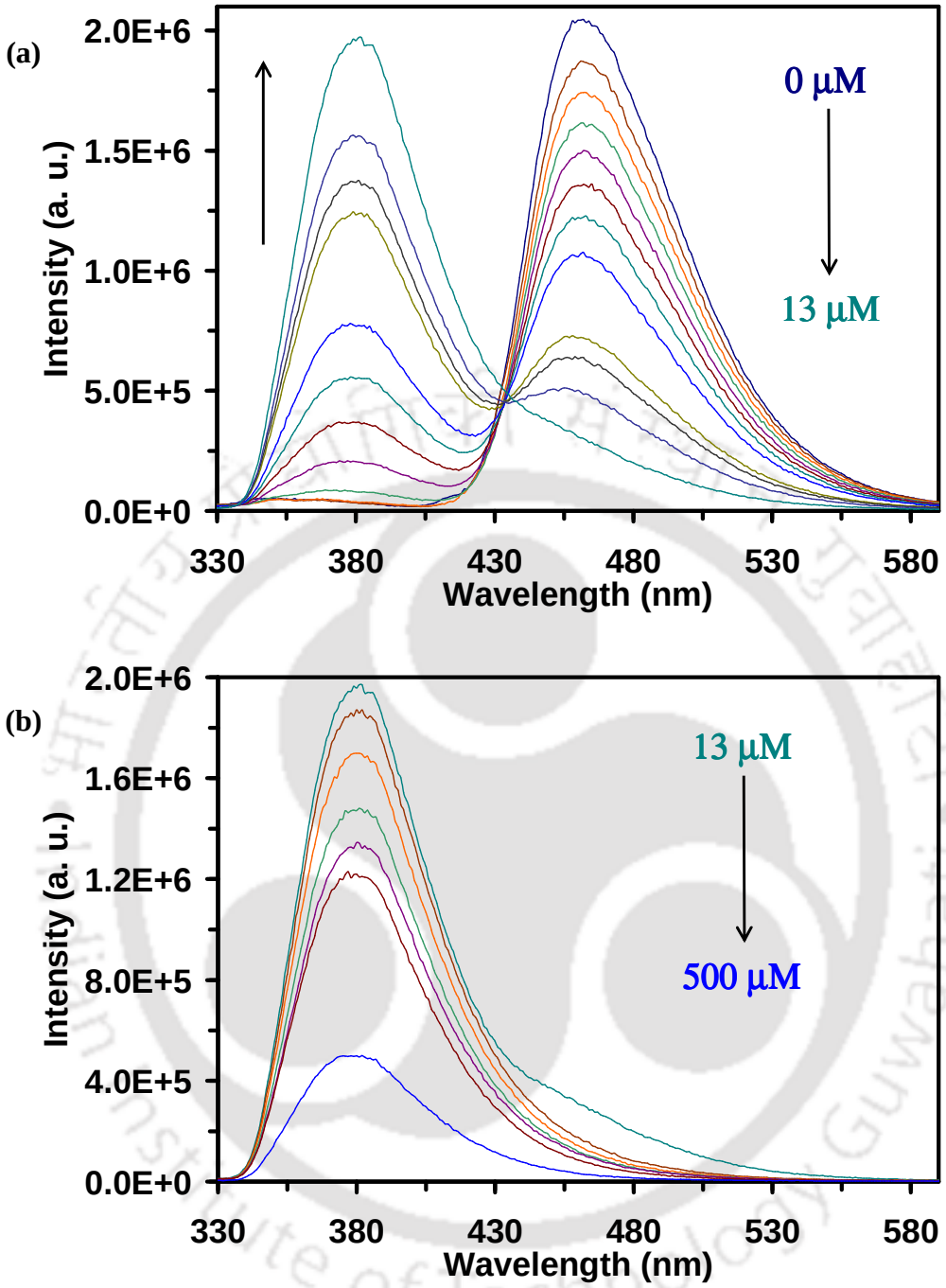

Figure 4.15. Fluorescence spectra of HPBI in presence of (a) 0-13 μM, and (b) above 13 μM of Cu^{2+} (λ_{exc} = 302 nm).

The effect of Cu^{2+} at lower concentrations (up to ~ 10 μM) is similar as that of Zn^{2+}. That is decreases in fluorescence of both emissions with an appearance of new band in between those bands. **Figure 4.15** shows the stepwise change observed in the fluorescence of HPBI on addition of Cu^{2+} ion. On initial addition of Cu^{2+} solution to HPBI till 13 μM, the tautomer emission decreases and the normal emission also decreases with the emergence of

red shift band at 380 nm. Beyond 13 μM, 380 nm band is quenched with increase in concentration.

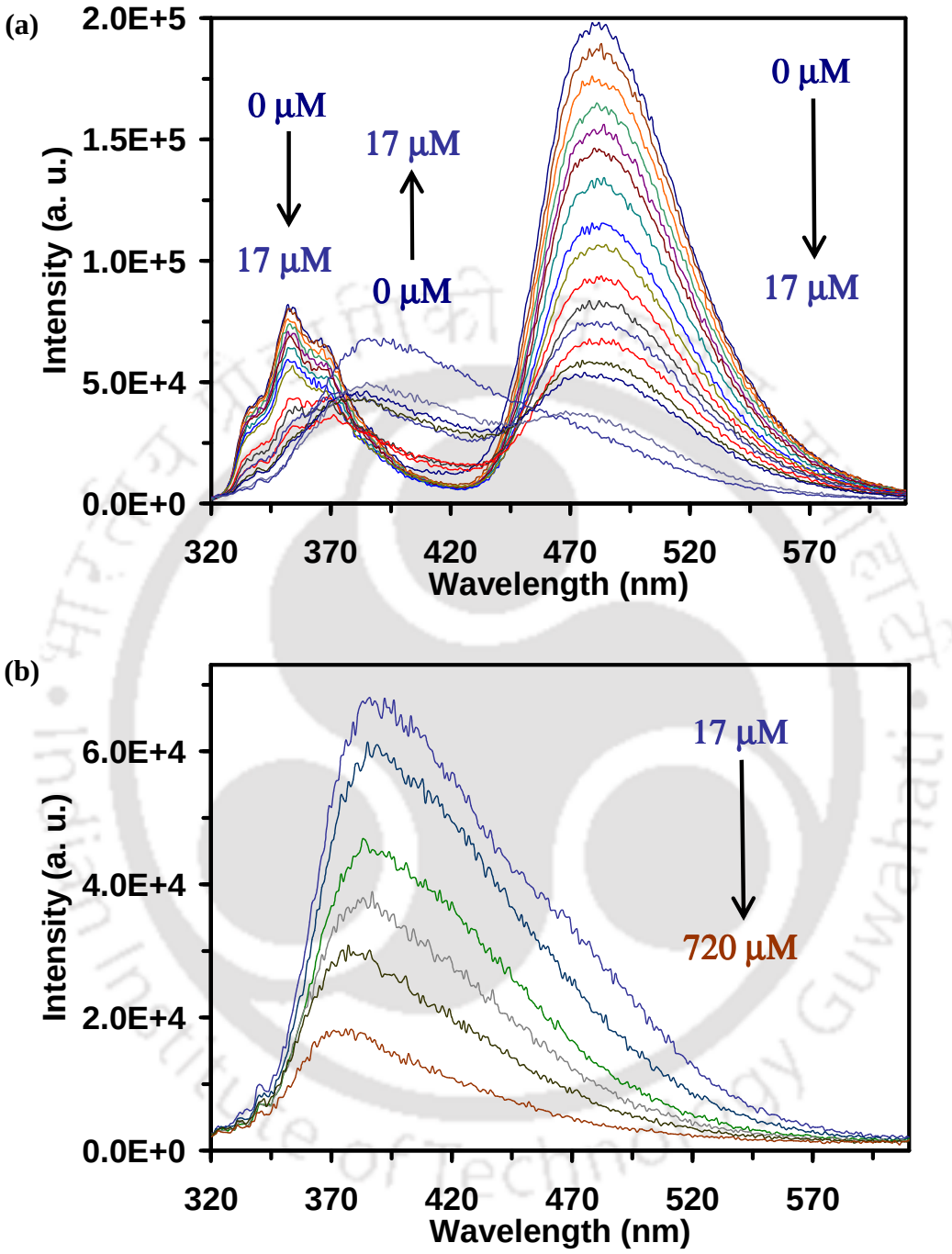

Figure 4.16. Fluorescence spectra of HPIP-b in presence of (a) 0-17 μM, and (b) above 17 μM of Cu^{2+} (λ_{exc} = 308 nm).

Figures 4.16 and **Figures 4.17** show the effect of Cu^{2+} ion of HPIP-b and HPIP-c. Although the general features of both HPIP-b and HPIP-c are similar to those of HPBI, but the magnitudes of the changes are different in these molecules. The new band of Cu^{2+}-HPBI at lower concentration is strong, but those of nitrogen substituted analogues are weak. The

excitation spectra recorded for the new fluorescence bands in presence of Cu^{2+} ions (not shown) indicate that the corresponding red shifted absorption bands are their ground state precursor in all three molecules.

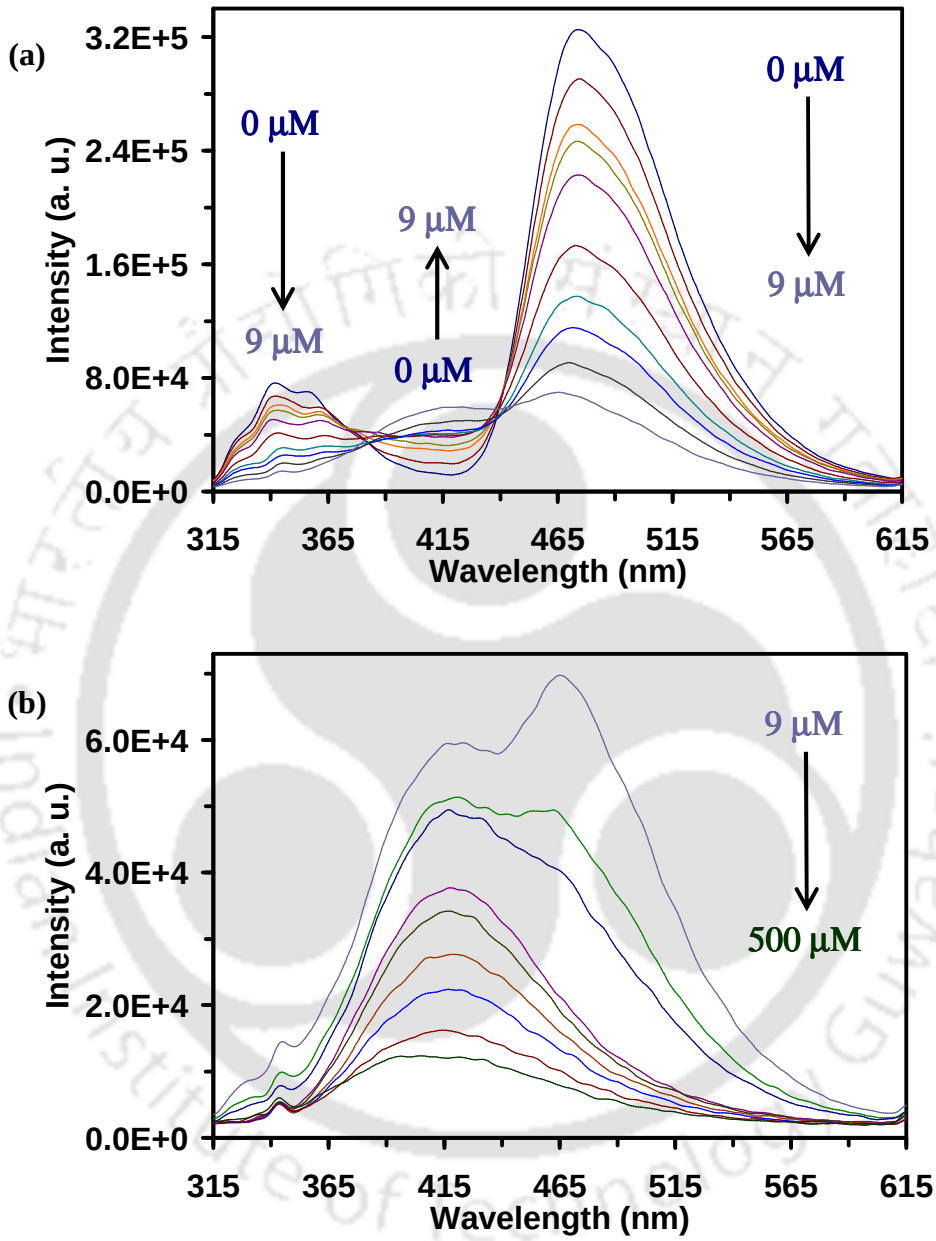

Figure 4.17. Fluorescence spectra of HPIP-c in presence of (a) 0-9 μM, and (b) above 9 μM of Cu^{2+} (λ_{exc} = 310 nm).

The effect of Ni^{2+} ion on the fluorescence spectra of HPBI resembles that of Mg^{2+}. **Figure 4.18** shows the fluorescence spectra of HPBI excited at 299 nm in presence of Ni^{2+} ion. The normal emission of HPBI initially decreases until the concentration of Ni^{2+} is 16 μM with a red shift from 352 nm in the absence of ion to 368 nm in 16 μM of Ni^{2+}. On further increase beyond 16 μM, the normal emission increases with further red shift to 378 nm at 350

μM (saturation limit). The shifting is due to emergence of a new band at the red side of the normal emission. However, the tautomer emission gradually decreases with an increase in metal ion concentration. The fluorescence excitation spectrum of the 378 nm fluorescence band matches with the absorption spectrum of the new red shifted band (not shown). On the other hand, Ni^{2+} quenches both normal and tautomer emissions of pyridine nitrogen substituted molecules and no new fluorescence band is detected at any concentration of metal ion (**Figure 4.19)**. The concentration required for complete quenching of fluorescence of HPIP-b (350 μM) is less than that required for that of HPIP-c (830 μM).

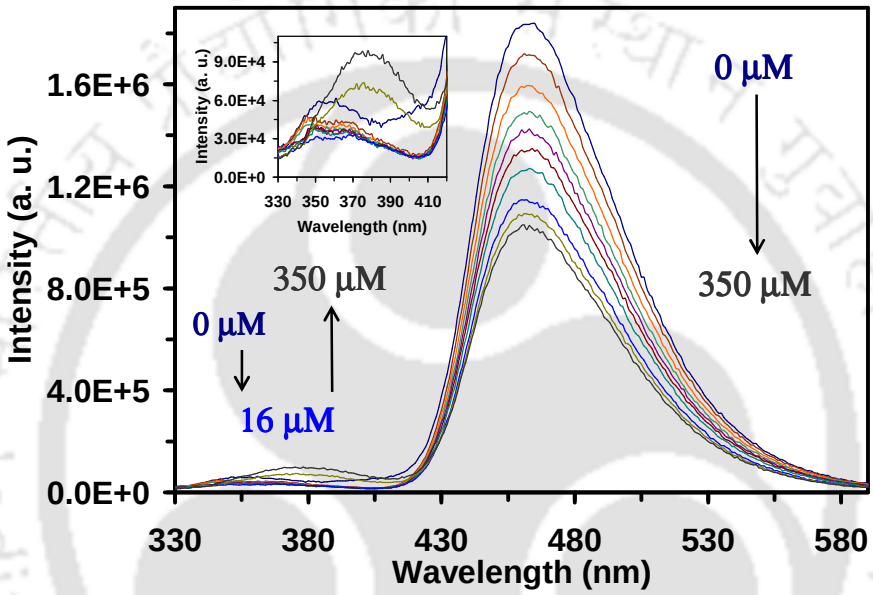

Figure 4.18. Fluorescence spectra of HPBI in presence of Ni^{2+} (λ_{exc} = 299 nm). Inset shows the enlarged spectra of normal band region.

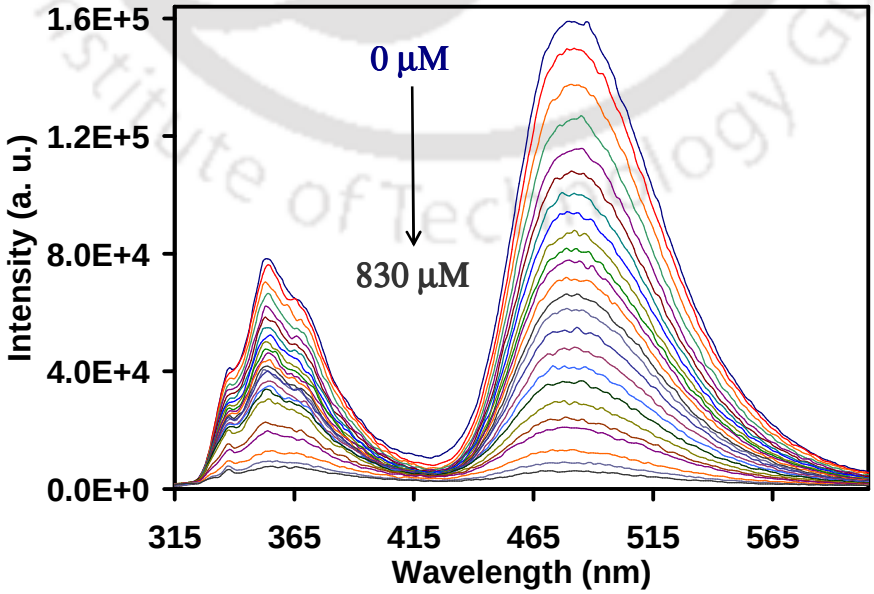

Figure 4.19. Fluorescence spectra of HPIP-b in presence of Ni^{2+} (λ_{exc} = 306 nm).

4.3. Fluorescence Intensity Ratio

From the absorption and fluorescence spectra it is seen that the alkali and alkaline earth metal ions have lower binding affinity toward the fluorophores than transition metal ions Ni^{2+}, Cu^{2+} and Zn^{2+}. The intensity ratios of normal to tautomer emission of HPBI, HPIP-b and HPIP-c are plotted against concentration of metal ions in **Figures 4.20**, **4.21** and **4.22**, respectively. In most of the cases, metal coordination hinders the ESIPT process. In particular Ni^{2+}, Cu^{2+} and Zn^{2+} ions produce substantial change in intensity ratios. The histogram plot (**Figure 4.23**) shows that HPBI has high sensitivity towards Cu^{2+} and Zn^{2+} ions. The sensitivity of the intensity ratio is highest towards Cu^{2+}. It is 143 times higher in presence of Cu^{2+} than in the absence of metal ion and it is 14 times higher than that in presence of Zn^{2+}. Intensity ratio of HPIP-b is more sensitive towards Ni^{2+} and Cu^{2+} ions and the intensity ratios at I_{355}/I_{480} are 2.1 and 2.8 times higher than that of pure ligand (**Figure 4.21**). On the other hand, despite being highly sensitive towards metal ion like Zn^{2+}, the intensity ratio of HPIP-c is relatively less sensitive toward metal ions, the highest value is obtained for Cu^{2+} ion which is 1.9 higher than that of pure ligand at I_{342}/I_{476} (**Figure 4.22**).

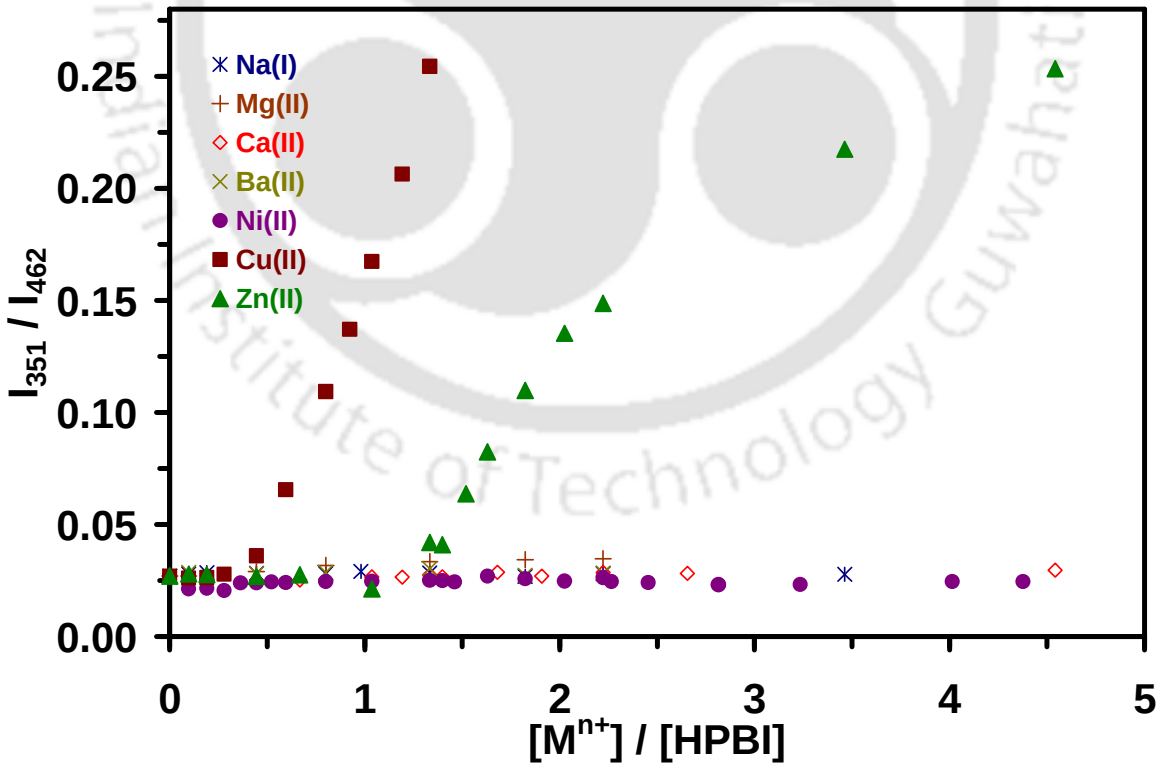

Figure 4.20. Fluorescence intensity ratio of normal (351 nm) to tautomer (462 nm) bands of HPBI at different concentration of metal ions.

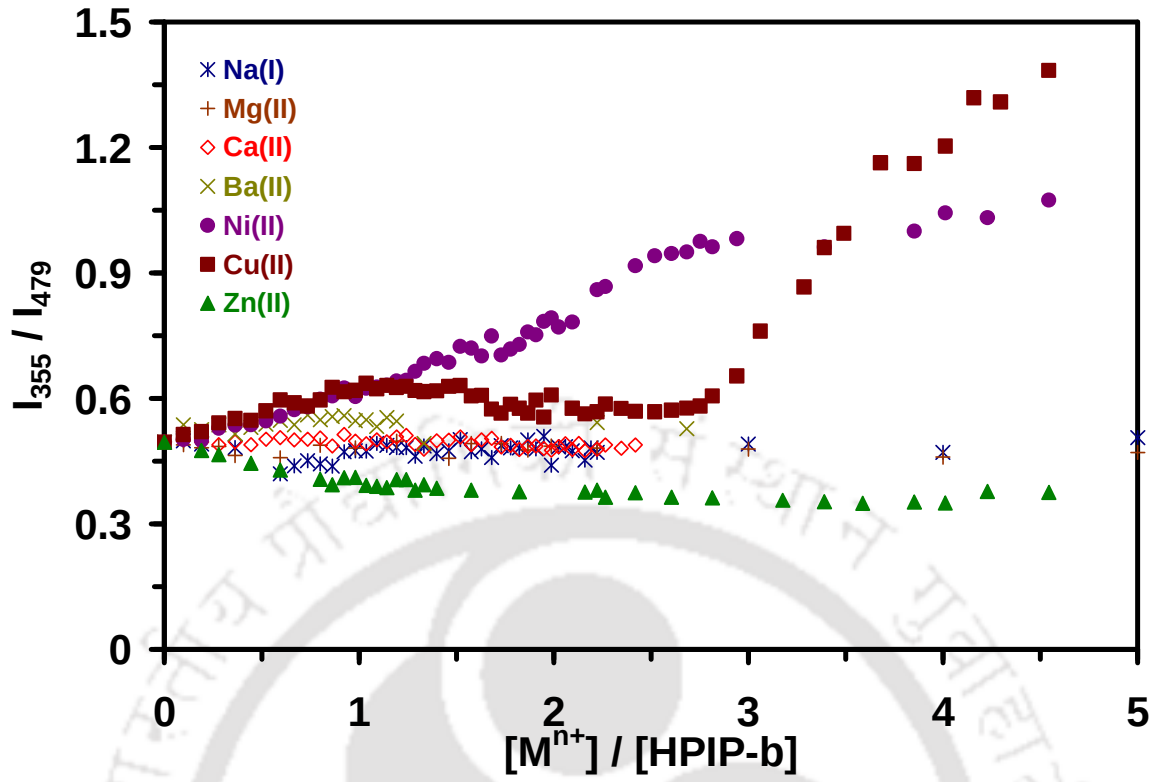

Figure 4.21. Fluorescence intensity ratio of normal (355 nm) to tautomer (479 nm) bands of HPIP-b at different concentration of metal ions.

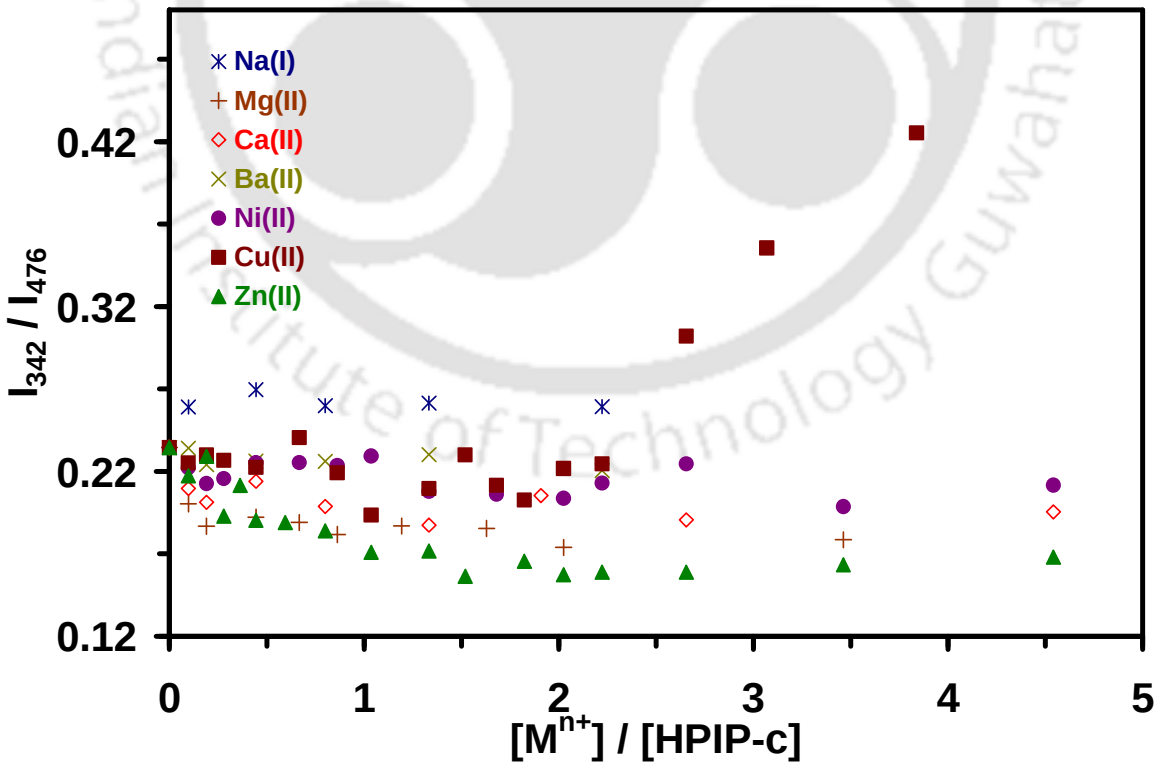

Figure 4.22. Fluorescence intensity ratio of normal (342 nm) to tautomer (476 nm) bands of HPIP-c at different concentration of metal ions.

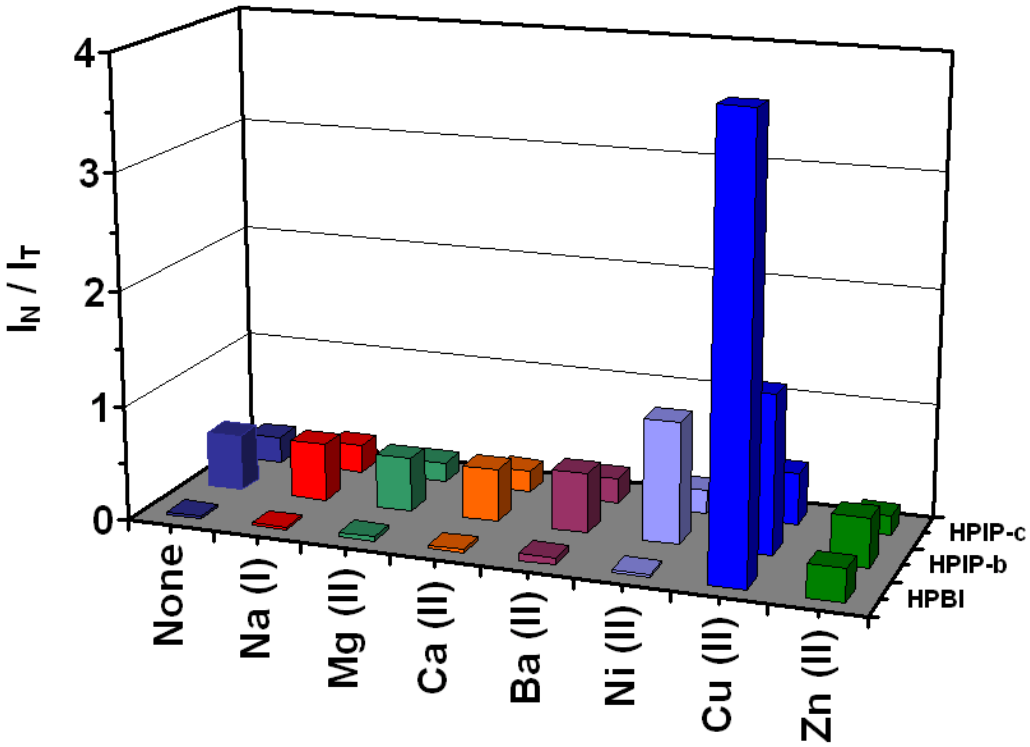

Figure 4.23. Histogram plot of normal to tautomer band ratio at fluorophore to metal concentration ratio of 1:5.

The results suggest that nitrogen substitution on the benzene ring of HPBI decreases the fluorescence sensitivity of the fluorophore towards metal ions. This may be due to reduced fluorescence quantum yield of the nitrogen substituted analogues. In addition, the presence of extra nitrogen increases the weaker interaction between the metal ions and the pyridine nitrogen by coordination (similar to hydrogen bonding). This interaction increases the ICT from the phenolic moiety to the aromatic moiety. The ICT increases the nonradiative decay due to increased vibrational overlap between the ground and excited states.

4.4. Metal Complexes

Since the spectral characteristics of the molecules are more sensitive towards Ni^{2+}, Cu^{2+} and Zn^{2+}, the spectral maxima of the three molecules in presence of these metals are complied in **Table 4.1**. As seen earlier, The results reveal that all three molecules form complexes with Ni^{2+}, Cu^{2+} and Zn^{2+}. Imidazole nitrogen and phenolic oxygen are available for metal coordination in HPBI. In addition pyridine nitrogen is available for coordination in HPIP-b and HPIP-c. Fahrni et al. investigated the interaction of Zn^{2+} ion with derivatives of HPBI, HPBO and HPBT and found that the shoulder of the excitation spectra of the metal complex matches with the excitation spectrum of the deprotonated form.[298] From this they hypothesized that the coordination of metal resulted in the deprotonation of phenolic group.

Table 4.1. Absorption maxima (λ_{max}^{abs}, nm) and fluorescence maxima (λ_{max}^{flu}, nm) of ligands and transition metal complexes of the HPBI, HPIP-b and HPIP-c.

Solution	λ_{max}^{abs}	λ_{max}^{flu}		
		Normal	Complex	Tautomer
HPBI				
No metal ion	330, 316, 291	352	-	462
Ni^{2+} (350 μM)	369, 330, 316, 291	-	378	-
Cu^{2+} (13 μM)	364, 334, 321, 295	-	382	-
Zn^{2+} (500 μM)	358, 333, 321, 297, 288	-	414	-
HPIP-b				
No metal ion	335, 322, 296	338, 355, 368	-	479
Ni^{2+} (130 μM)	353, 339, 314, 297	338, 355, 368	-	479
Cu^{2+} (17 μM)	357, 337, 305	-	386	-
Zn^{2+} (47 μM)	356, 335, 321, 305, 297	341, 356, 371	382	474
HPIP-c				
No metal ion	326, 314, 285	325, 340, 359		474
Ni^{2+} (23 μM)	370, 326, 314, 287	328, 346, 368	409	473
Cu^{2+} (10 μM)	380, 321, 291	-	412	-
Zn^{2+} (13 μM)	362, 326, 290	-	418	-

The absorption spectra of the metal complexes are red shifted compared to the ligand. However, not only the deprotonation of –OH group, but also the protonation at the ring nitrogen(s) can contribute to this red shift.[6,95] Therefore, it is difficult to verify the hypothesis. The extent of red shift differs with the nature of the metal ions. This clearly indicates that metal binding has significant role in the bathochromic shift and therefore it is not merely due to deprotonation. It is well established,[314,315] that binding of cations with ring nitrogens produces a bathochromic shift in the absorption and fluorescence spectra, and that the shift is more pronounced upon binding with the pyridine nitrogen than that with the imidazole nitrogen. Therefore, in HPBI the imidazole nitrogen is involved in coordination with the metal ions and the oxygen of the phenolic group might also be involved in the coordination. The red shift observed in the absorption and the fluorescence spectra of the metal complex of nitrogen substituted analogues are comparable to those of HPBI. From this it may be inferred that the coordination sites of the metal ions are same in all three molecules. The attempts to crystallize the metal complexes were successful only in case Ni^{2+} complex of HPIP-b. The solved crystal structure of Ni^{2+}-HPIP-b 1:2 complex is shown in **Figure 4.24**. The parameters of the complex are provided in **Appendix A4**. The ligand binds with Ni^{2+} ion in a bidentate binding mode through its imidazole nitrogen and phenolic oxygen. The cyclic intramolecular hydrogen bonded ring is broken upon binding with the metal ions. This prevents the ESIPT reaction thereby reducing the tautomer emission, only normal emissions are observed in metal complexes. Due to paramagnetic nature of the metal ions Ni^{2+} and Cu^{2+} the

fluorescence is quenched in presence of Ni^{2+} and Cu^{2+} (at higher concentration). Since, Zn^{2+} is diamagetic no such quenching is observed in the fluorescence spectra of Zn^{2+} complexes even at saturation limits.

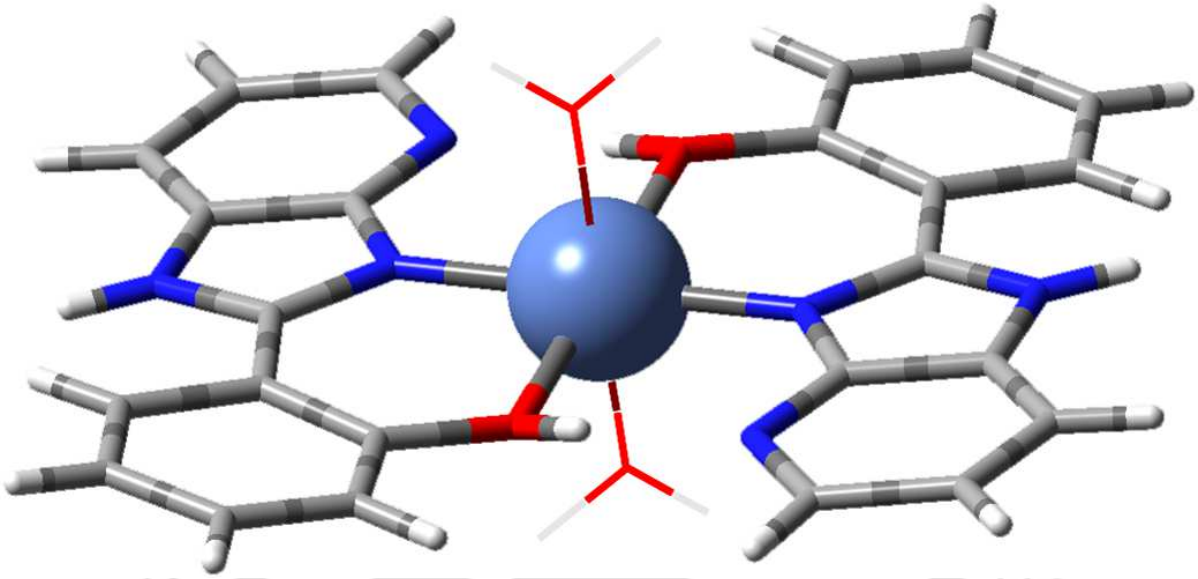

Figure 4.24. Crystal structure of HPIP-b-Ni^{2+} complex.

4.5. Conclusion

In summary, the effects of metal ions on the dual fluorescence of HPBI and its pyridine nitrogen substituted analogues toward metal ions are investigated. The photophysical perturbations induced by alkali and alkaline earth metal ions are small. However, significant changes are observed upon binding with transition metal ions Ni^{2+}, Cu^{2+} and Zn^{2+}. Although the fluorescence intensity ratios change in all three molecules, HPBI, HPIP-b and HPIP-c, the changes are higher in HPBI than in its nitrogen substituted analogues. The normal to tautomer fluorescence intensity ratio of HPBI increases by 143 and 10.4 fold in the presence (5 equivalents) of Cu^{2+} and Zn^{2+}, respectively, compared to that in neat solution. The fluorescence ratio of HPIP-b changes by 2.1 and 2.8 fold in presence of Ni^{2+} and Cu^{2+}, respectively, Cu^{2+} ion enhances the fluorescence ratio of HPIP-c by 1.9 folds. This shows that nitrogen substitution on the benzene ring of HPBI decreases the fluorescence emission ratio. The increases in shorter wavelength intensities are attributed to the disruption of ESIPT process due to the binding of metal ions by coordination through imidazole nitrogen and phenolic oxygen of the ligands. The mode of binding is confirmed by the single crystal structure of Ni^{2+} complex with HPIP-b with stoichiometric ratio [Ni^{2+}]:[HPIP-b] of 1:2 where the ligand coordinates with the metal centre through its phenolic oxygen and imidazole nitrogen.

Chapter 5

Photophysical Properties of 2-(2'-Hydroxyphenyl)benzimidazole and its Nitrogen Substituted Analogues in Microheterogeneous Media

5.0. Introduction

Studies on organized microheterogeneous assemblies have been growing rapidly during the past few decades as these serve as good miniature models for studying and mimicking important phenomena in biosystems.[316-318] Among the studies on microheterogeneous media, inclusion complexes are one of the interesting subjects for many researchers. Inclusion complexes provide valuable information about noncovalent intermolecular interactions between the host and guest molecules where the guest component is residing within the cavity of the host molecule without forming any covalent bond.[316] Apart from biomimicking,[317,319] inclusion complexes find applications in drug delivery,[318] nano-sized molecular devices,[320] and energy storage devices.[321]

Cyclodextrins (CDs)[316-318,320] are the most sought host systems for studying such inclusion complexes. CDs are cyclic oligosaccharides composed of glucopyranose units linked by α-(1,4) bonds with hydrophilic external walls and interior hydrophobic nano-sized cavity of different size and shape.[316-318,322,323] In nature, CDs are formed by the action of bacteria such as *Bacillus macerans* and *Paenibacillus macerans* on starch.[324-326] The shape of the cyclic ring is like a conical cylinder and is frequently characterized as a doughnut or wreathshaped truncated cone. The secondary hydroxyl groups of the glucopyranose unit are situated on one rim of the ring whereas the primary hydroxyl groups are situated on the other rim. The most commonly used CDs are α-, β-, and γ-CD which have six, seven, and eight glucopyranose units, respectively. Though larger CDs are available, they have lesser value in terms of applications.[322]

Reverse micelles are another kind of organized microheterogeneous assemblies that are widely studied. Reverse micelles are formed by the aggregation of surfactant molecules, which consist of hydrophobic side chain and polar head group, in nonpolar solvents in the presence of water molecules.[327-329] The polar head groups in the reverse micellar system are collected together in an inner core toward the polar water pool and the hydrocarbon chains are directed outward to the nonpolar oil phase. A distinguishing feature of these reverse micelles is their ability to solubilize fairly large amounts of water in the polar core. The size of a reverse micelle is measured in terms of the molar ratio, w_0, of polar solvent to surfactant. As an example, for AOT/*n*-heptane/water reverse micellar system, the radius of the water pool is roughly $2w_0$ Å.[330,331] Two layers are found in the confined water pool viz. the bound water and free water. The bound water layer is located at the interfacial region between the polar head group and water molecules while the free water layer resides inside the core of the water pool. Reverse micelles have been extensively used as interesting models for biological

membranes[332] and water molecules confined in biological systems.[333] Structure, equilibrium and dynamics of molecules in confined environments and at various interfaces play a crucial role in various biological and natural processes.[334,335] The water pool in the reverse micelle is also employed as a reaction medium for enzomolysis.[336]

In nature organized assemblies are also found in numerous systems, for example proteins. Proteins are biopolymer molecules made up of several amino acid residues and are the main target of all the medicines.[337,338] Proteins are important for structure, function, and regulation of cells, tissues, and organs; and every protein has a unique function in maintaining life.[337,338] The structure of a protein gives rise to its biological function of great selectivity and variety. Its structure depends on hydrophobic, electronic, and steric parameters.

Serum albumins are the most abundant proteins found in blood plasma in the circulatory system and have been the most extensively studied proteins for many years.[339] Serum albumin functions as transport proteins for various exogenous and endogenous substances in the body by hydrophobic, hydrophilic, and ionic interactions. Many researchers have studied the structures, functions and properties of serum albumins to understand their interactions with other external substances. Some of albumins widely studied are human serum albumin, bovine serum albumin (BSA), equine serum albumin and rat serum albumin. The external substances that have been studied for interaction with serum albumins are fatty acids, metal ions, pigments, and numerous drugs.[340] For elucidating information regarding environment of the binding sites protein-bound fluorescent probes are often used.

Despite the fact that the utility of HPBI as fluorescent probe has been well established,[70,77,100,341] the utility of its nitrogen substituted analogues HPIP-b and HPIP-c are not yet investigated. Chattopadhyay pointed out that although the ESIPT process is affected by the microheterogeneous media, it also strongly depends on the nature of the molecule.[342] As already discussed in **Sections 3.1** and **3.2**, substitution of N-heteroatom in the benzene ring of HPBI reduces the quantum yield,[6,174,175] and on the other hand nitrogen substitution on the phenolic ring increases the quantum yield.[177,178] Theoretical calculations predicted that the proton coupled charge transfer state may act as the major nonradiative decay channel for the proton transferred tautomer.[96,264,265,343] The ESIPT is accompanied by a torsional rotation of the two aromatic rings which lead to an ICT state from where the nonradiative decay occurs. This should increase environmental sensitivity of the nitrogen substituted analogues more than that of HPBI.

This chapter discusses the effect of the presence and position of N-heteroatom in benzene ring of HPBI on the photophysical properties in different microheterogeneous environments. In this study the potential implications of HPBI, HPIP-b and HPIP-c as probes and sensors are also explored based on ratiometric fluorescence emission[139,295,340,344] which has better advantages over measurement on single emission. The ratio eliminates the errors generated due to concentration variation, photobleaching, or any instrument related parameters.[299,300] The chapter is divided into three sections. The first section is the study of photophysical properties of HPBI, HPIP-b and HPIP-c in presence of β-CD. The second section is the discussion on ESIPT behavior of these molecules in AOT reverse micelle and in the third section; study on interactions of the molecules with BSA is discussed.

5.1.0. HPBI, HPIP-b and HPIP-c in β-Cyclodextrin

The hydrophobicity of the β-CD cavity enhances the solubility[345] and fluorescence of the encapsulated guest molecule.[346] Therefore, CDs have been used as a microenvironment to study excited state processes such as proton transfer,[346-348] charge transfer[349-351] and energy transfer.[352,353] Douhal et al. reviewed the dynamics and structural aspects of host guest interactions in CD.[354,355] The inclusion complexes of a fluorophore in aqueous host molecules including CDs were recently reviewed by Nau et al.[356] Wagner more recently reviewed the hydrogen bonding of excited states in supramolecular inclusion complexes including CDs.[357]

Unlike ICT and intermolecular proton transfer, the effect of β-CD on ESIPT processes is still relatively less studied.[77,100,281,358,359] Douhal et al. investigated the effect of β-CD on the dynamics of ESIPT molecule.[354] Warner et al. studied the dual fluorescence of HPBI and the corresponding benzoxazole and benzothiazole in presence of β-CD.[100] They showed the existence of weak intramolecular hydrogen bonding in HPBI and the formation of strong intermolecular hydrogen bonds with the hydroxyl groups of CD. They further showed that the phototautomers exist as zwitterions. More recently Guchhait et al. studied the ESIPT process of 1-hydroxy-2-napthaldehyde in CDs.[359]

In this section, we extended the study of the effect of β-CD on ESIPT in HPBI using DMSO as the solvent. The nitrogen substituted analogues of HPBI viz. HPIP-b and HPIP-c are also studied. This study is an attempt to explore the efficiency of these fluorophores as potential fluorescence probes by investigating the properties of these inclusion complex assemblies utilizing ESIPT reaction.

5.1.1. Absorption Spectra

HPIP-b and HPIP-c have low solubility in water but their solubility enhances in the presence of β-CD. This enhancement in solubility is an indication of inclusion complex formation by the encapsulation of the fluorophores in the hydrophobic cavity of β-CD. The effect of β-CD on the absorption spectra of HPIP-b and HPIP-c in water are depicted in **Figure 5.1**. Though absorbance maxima of both HPIP-b and HPIP-c are nearly unaffected with increase in concentration of β-CD, a small hyperchromic effect is observed. These increases in absorbance are attributed to the detergent action of the host molecule β-CD on the guest molecule which also confirms the formation of the host-guest inclusion complex.[360,361]

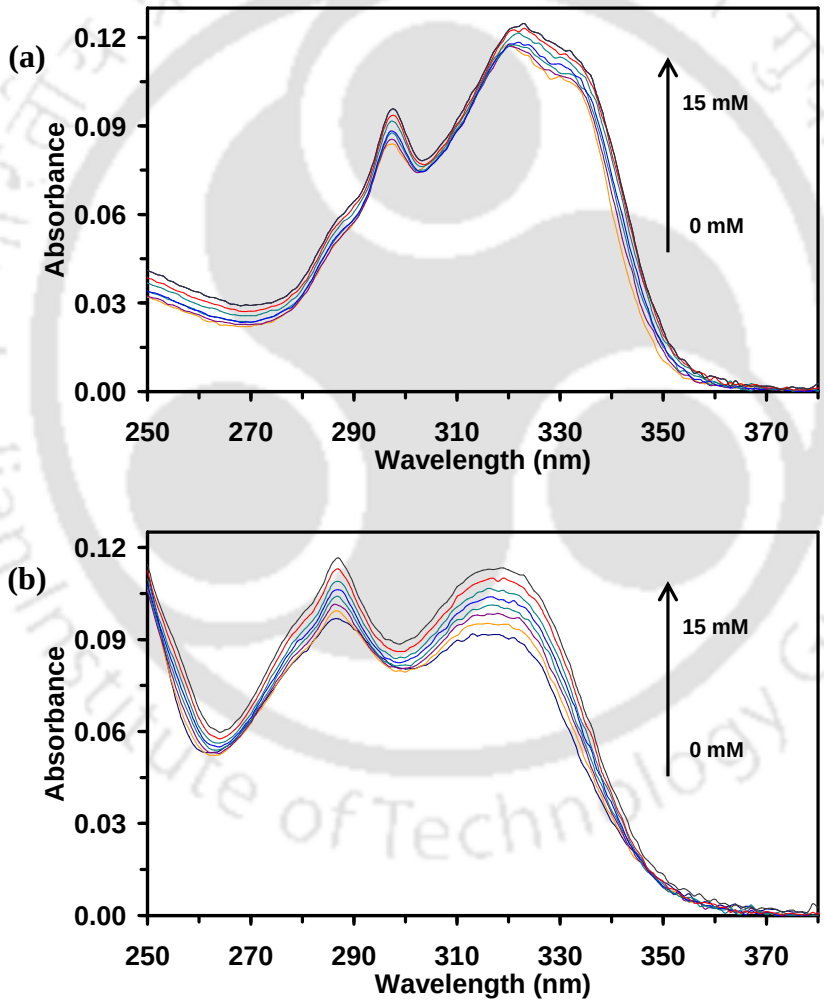

Figure 5.1. Absorption spectra of (a) HPIP-b, and (b) HPIP-c at different concentrations of β-CD in water.

The effect of β-CD on the absorption spectra of HPBI and its analogues in DMSO are presented in **Figure 5.2**. Same as in aqueous solution, there is a hyperchromic effect in the absorption spectra of HPBI and HPIP-c upon addition of β-CD (**Figure 5.2a** and **5.2c**). The

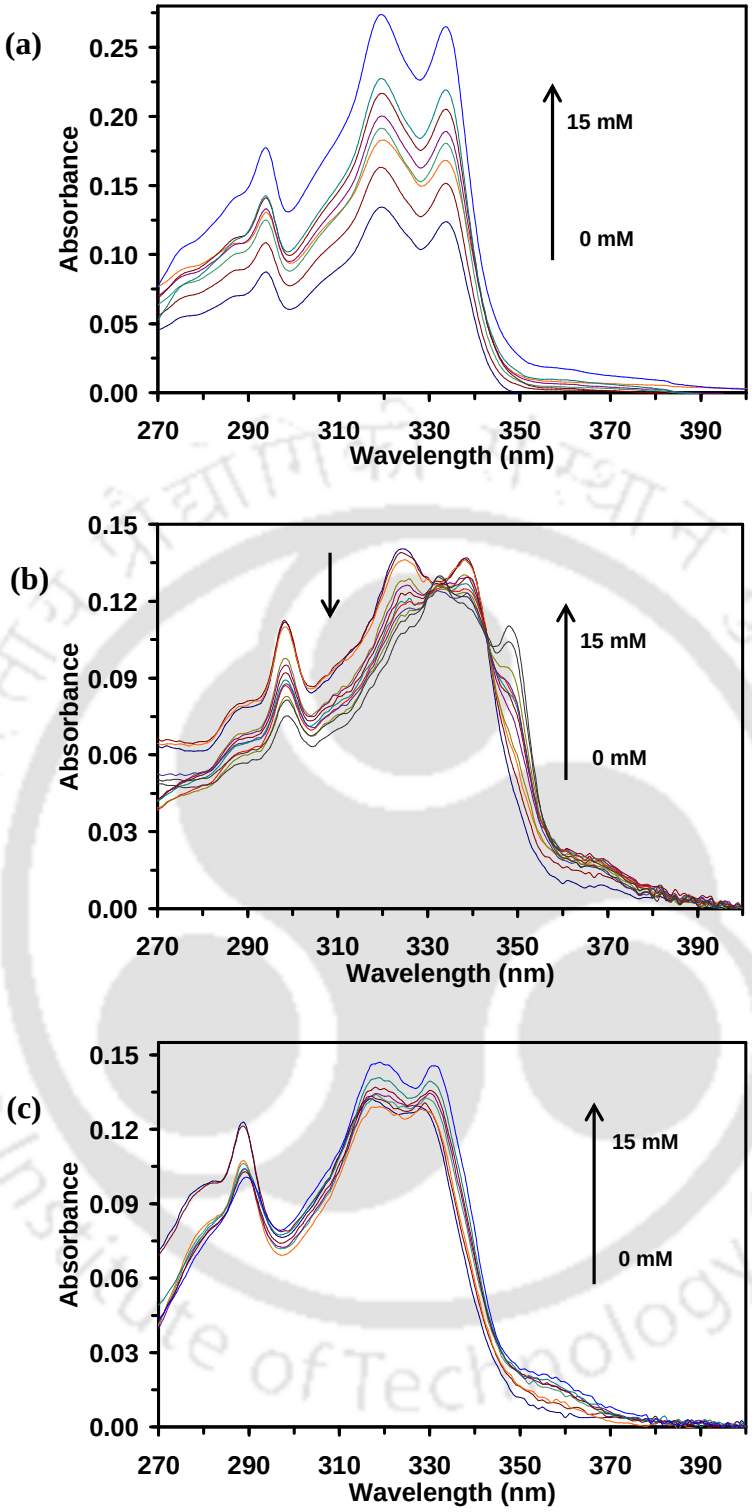

Figure 5.2. Absorption spectra of (a) HPBI, (b) HPIP-b, and (c) HPIP-c in increasing concentration of β-CD in DMSO.

changes in absorption spectra of HPIP-b in DMSO are different in the sense that isosbestic points are observed (**Figure 5.2b**). However, the most striking difference between DMSO and aqueous solution is the appearance of a weak new band at ~ 365 nm in HPIP-b and

HPIP-c. The band's absorption is very weak in DMSO, but increases with increase in concentration of β-CD in DMSO. In HPBI although the red shifted band is absent in the absence of β-CD in DMSO, it appears in DMSO at higher concentrations of β-CD.

5.1.2. Fluorescence Emission Spectra

Figure 5.3 depicts the fluorescence of HPIP-b and HPIP-c in aqueous solution upon excitation at 310 nm. Upon addition of β-CD, a small enhancement is observed in the intensity of the normal emission of HPIP-b (**Figure 5.3a**). However, there is a significant

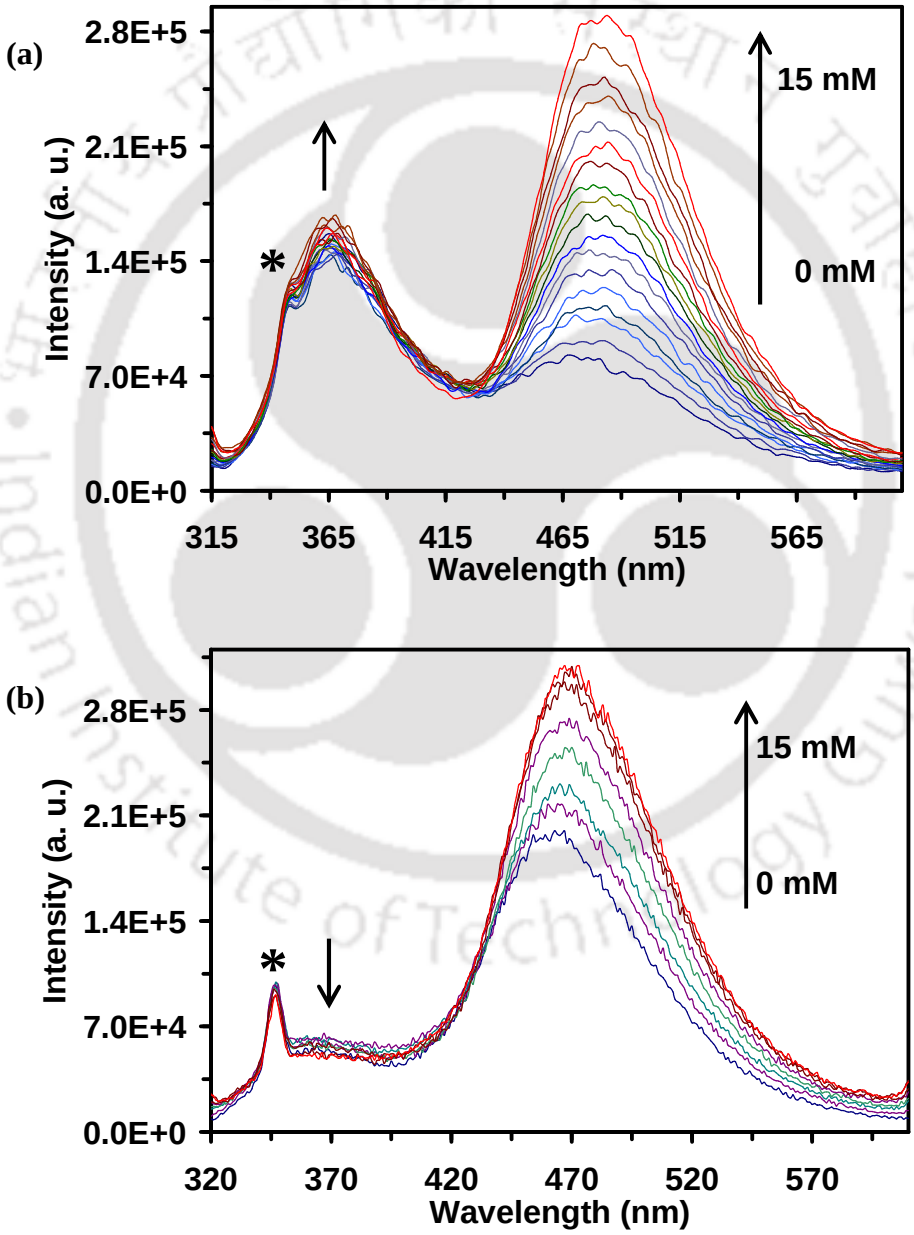

Figure 5.3. Fluorescence spectra of (a) HPIP-b, and (b) HPIP-c at different concentrations of β-CD in water (λ_{exc} = 310 nm). Water Raman band is denoted by *.

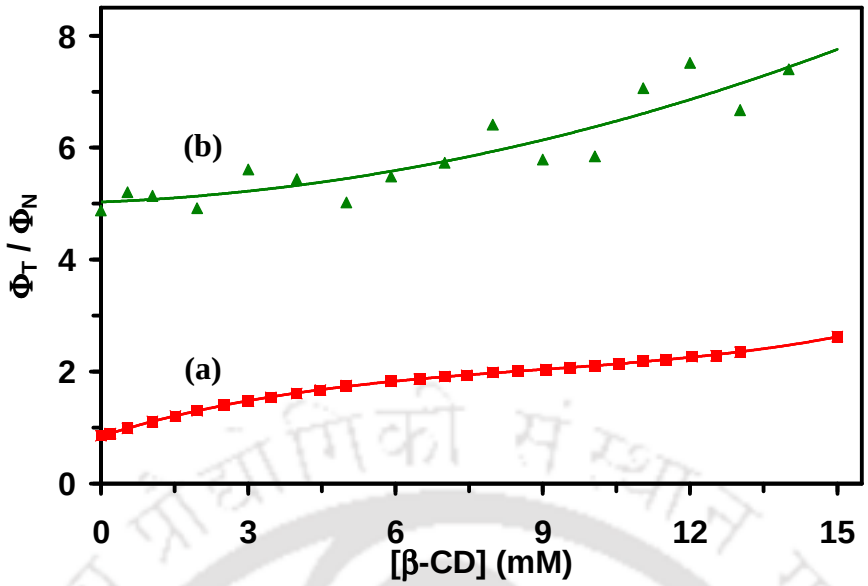

Figure 5.4. Plot of quantum yield ratio of tautomer to normal bands of (a) HPIP-b, and (b) HPIP-c against [β-CD] in water (λ_{exc} = 310 nm).

change in the tautomer fluorescence of HPIP-b in aqueous solution with increasing β-CD concentration. While the emission maximum of the normal band at 365 nm is nearly unaffected, that of tautomer band is red-shifted by 16 nm from 468 nm in aqueous medium to 484 nm at 15 mM of β-CD with substantial enhancement in fluorescence. The full width at half-maximum (FWHM) of normal band also remains nearly constant (61 ± 4 nm), but that of tautomer band decreases from 5635 cm^{-1} in absence of β-CD to 3170 cm^{-1} at 15 mM of β-CD. The quantum yield ratio of tautomer to normal emission (Φ_T/Φ_N) increases from 0.9 (in absence of β-CD) to 2.6 (at 15 mM concentration of β-CD, **Figure 5.4**).

The effects of β-CD on fluorescence characteristics of HPIP-c in aqueous media are little different from that of HPIP-b (**Figure 5.3b**). The intensity of the normal emission is reduced upon increase in tautomer emission with a quasi isoemissive point. But the increase in tautomer emission is relatively smaller in magnitude to that of HPIP-b. The tautomer band is red-shifted from 464 nm at 0 mM to 469 nm at 15 mM of β-CD. The FWHM of tautomer band decreases from 3715 cm^{-1} in absence to 3400 cm^{-1} at 15 mM of β-CD. The Φ_T/Φ_N ratio increases from 4.9 at 0 mM to 7.4 at 15 mM concentration of β-CD (**Figure 5.4**).

Red shifts are observed in tautomer bands of HPIP-b and HPIP-c upon decreasing the polarity of the environment.[6,174] Therefore, the red shift suggests the inclusion of the guest molecule into the hydrophobic cavity of the host β-CD. This is further substantiated by the decrease in FWHM of tautomer band due to reduction in solvated structures. The

enhancement of tautomer emission in β-CD complex can be explained as follows. HPBI and its analogues are present in both *cis* and *trans*-enol forms.[6,98,174] It was already shown in **Section 3.1** that *cis*-enol is less polar than *trans*-enol. The closed *cis*-enol upon excitation exclusively undergoes ESIPT to form the tautomer and the *trans*-enol upon excitation gives normal emission. The assignment of the fluorescence band is already discussed in **Section 3.3**. Protic solvent breaks the intramolecular hydrogen bond and forms more solvated *trans*-enol that lead to an increase in normal emission. Complex formation shifts the *cis*- and *trans*-enol equilibrium toward *cis*-enol due to reduced polarity of the interior of β-CD and by reduction in the intermolecular hydrogen bond with external water. The increase in relative population of *cis*-enol results in the enhancement of the tautomer emission. However, the increase in the relative population of *cis*-enol is not the sole factor that leads to increase in the tautomer emission. The other factor that is responsible for the increase in the tautomer fluorescence is the decrease in the nonradiative decay in inclusion complex. It should be noted here that torsional induced rotational relaxation of the phototautomer to non-emissive ICT acts as nonradiative channel for the deactivation of excited tautomer (**Section 3.1.4**).[96,265,343] Douhal et al. also reported that the twisting motion of 2-(2′-hydroxyphenyl)-4-methyloxazole after ESIPT is restricted by β-CD nanocavity.[362]

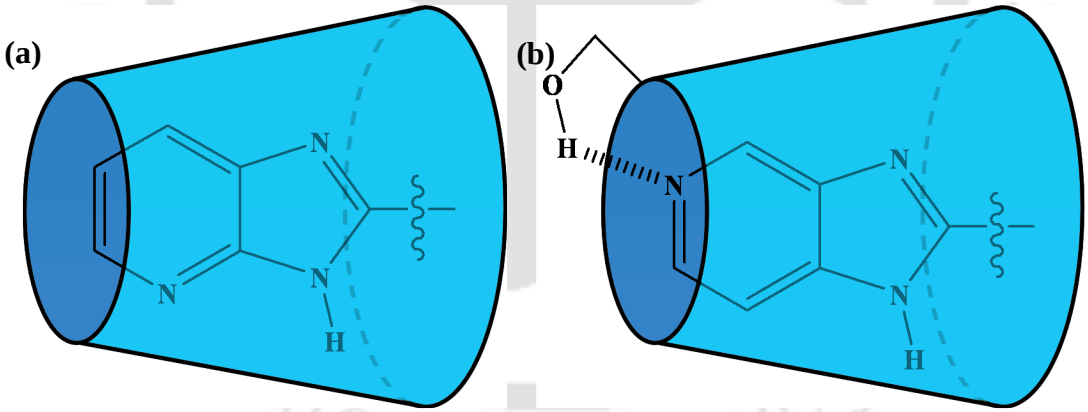

Figure 5.5. Sites of hydrogen bond formation with the imidazopyridyl moiety of (a) HPIP-b, and (b) HPIP-c in β-CD nanocavity.

Warner et al. reported that the fluorescence spectrum of HPBI in aqueous β-CD remains unaffected except small red shift in the longer wavelength emission.[100] However, unlike HPBI, significant changes are observed in the tautomer emission of nitrogen substituted analogues upon encapsulation in aqueous β-CD cavity. The tremendous increase is also observed in the tautomer to normal emission ratio. All these suggest that the nitrogen substitution makes HPIP-b and HPIP-c more sensitive to environment and can be better ratiometric probe than HPBI. Our earlier theoretical studies on HPBI and its analogues

suggested that nitrogen substitution increases the torsional induced formation of non-emissive ICT state (**Section 3.1**). This is due to higher electron accepting capability of imidazopyridyl moiety over benzimidazolyl moiety. In addition hydrogen bonding of the solvent with pyridine nitrogen increases the electron withdrawing ability of the imidazopyridine ring that increases the ICT. In 2-(4'-*N*,*N*-dimethylaminophenyl)imidazopyridines also it is reported that the hydrogen bonding of the solvent with pyridine nitrogen induces the ICT.[363,364] Rodríguez et al. also found that the pyridine nitrogen methylated derivative of HPIP-b is non-fluorescent due to the formation of a non-emissive ICT state after ESIPT.[280] The electron withdrawing ability of the azole moiety increases with methylation and hence the ICT from the phenolic moiety to the heterocyclic ring is favored more. Complex formation reduces the interaction of water molecule with pyridine nitrogen such as reduction in hydrogen bonding should reduce the electron withdrawing ability of the azole moiety. The difference in behavior of HPIP-b and HPIP-c is due to the position of the pyridine nitrogen atom. As shown in **Figure 5.5** (see later for the orientation), the hydrogen bonding of the rim hydroxyl group/ water molecule with pyridine nitrogen is less feasible in HPIP-b complex than HPIP-c complex. Therefore, the decrease in the nonradiative decay by torsional rotation is more in HPIP-b than HPIP-c due to higher reduction in hydrogen bonding with pyridine nitrogen.

Figure 5.6 depicts the fluorescence spectra of HPBI, HPIP-b and HPIP-c in DMSO at different concentration of β-CD. As in aqueous medium, in DMSO also HPBI exhibits dual emission due to normal and tautomer fluorescence (**Figure 5.6a**). The intensities of both the bands increase with β-CD concentration up to 4 mM. With further increase in β-CD concentration, the intensity of the tautomer emission increases with increase in β-CD concentration. But that of normal emission decreases above 4 mM and a new band starts to appear at 415 nm. The intensity of the band increases with β-CD concentration. On the other hand in both HPIP-b and HPIP-c the additional band appears as a shoulder in between the normal and tautomer bands even in the absence of β-CD. With increase in β-CD the tautomer emission undergoes a blue shift with increase in intensity and the new band buried underneath the tautomer band. The normal emission intensity decreases and a quasi isoemissive points are observed. These changes suggest that in DMSO also the ESIPT process is favored more upon formation of inclusion complex.

To confirm the origin of the emitting species, the fluorescence excitation spectra of all three molecules were recorded in DMSO at different concentrations of β-CD (**Figures 5.7**, **5.8** and **5.9**). The excitation spectra monitored at the normal emission (**Figures 5.7a**, **5.8a** and **5.9a**) are blue-shifted from the excitation spectra monitored at the tautomer emission

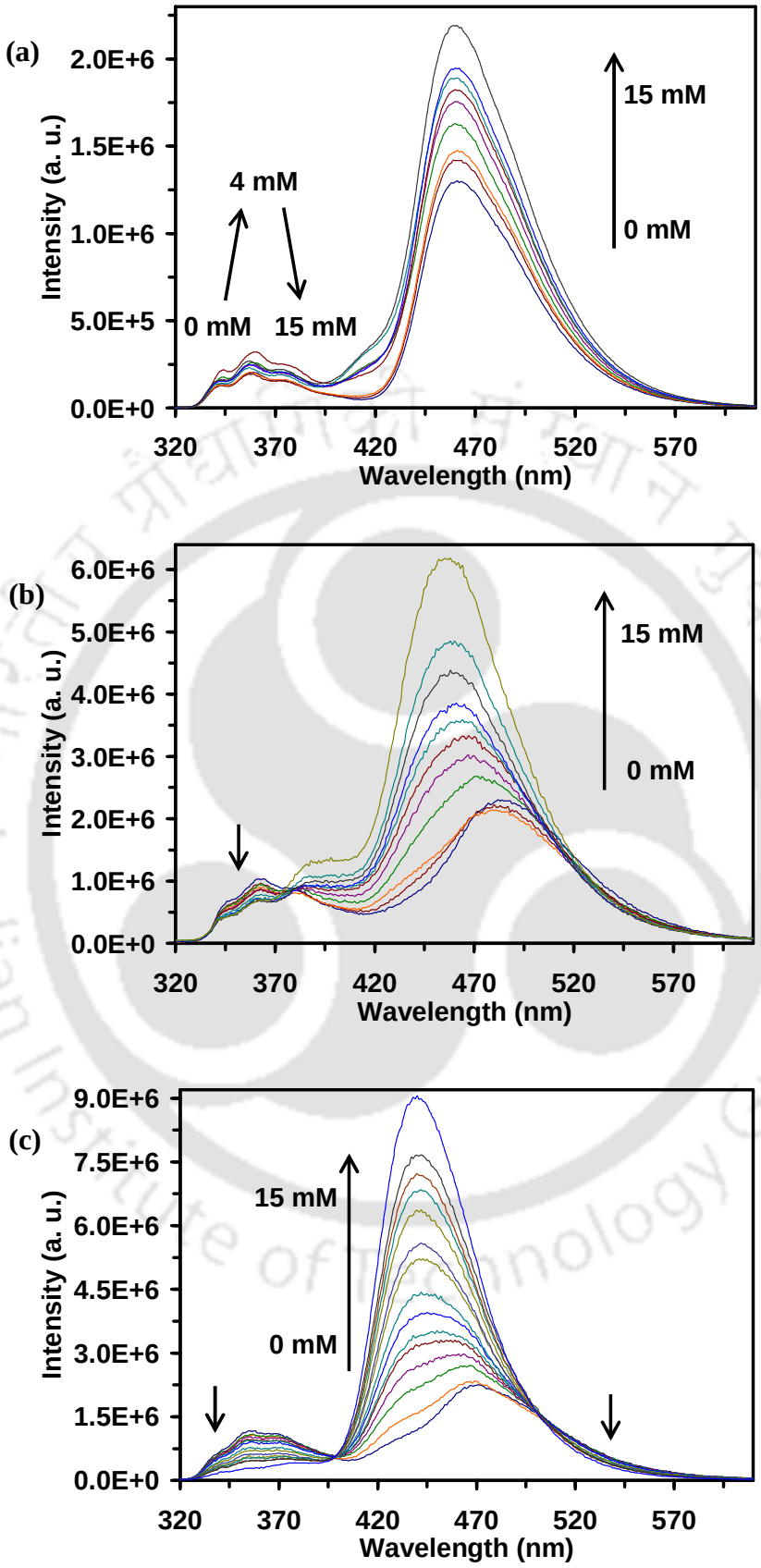

Figure 5.6. Fluorescence spectra of (a) HPBI, (b) HPIP-b, and (c) HPIP-c in DMSO as a function of [β-CD].

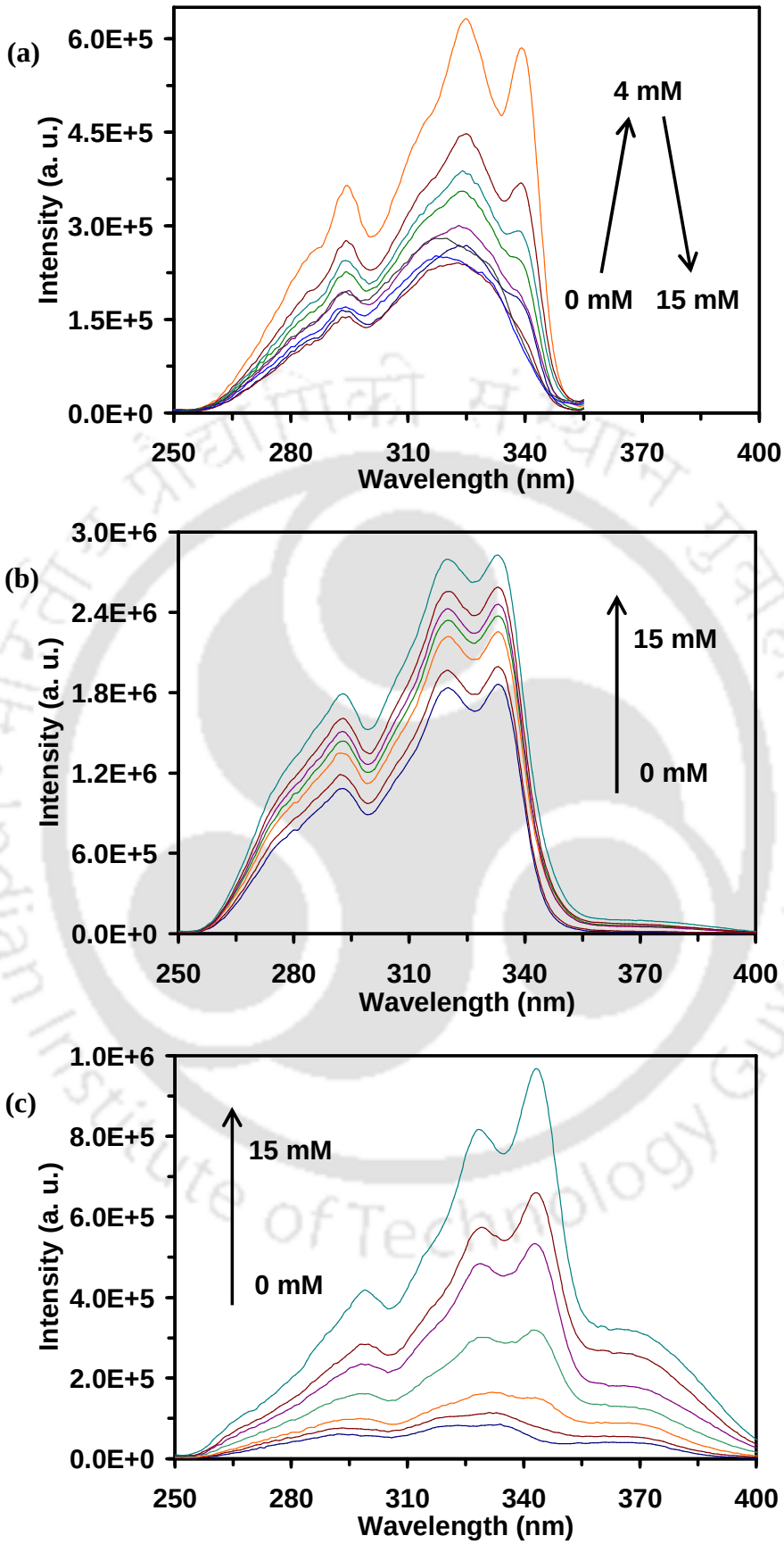

Figure 5.7. Fluorescence excitation spectra of HPBI in DMSO with increasing concentration of β-CD at (a) λ_{em} = 365 nm, (b) λ_{em} = 420 nm, and (c) λ_{em} = 465 nm.

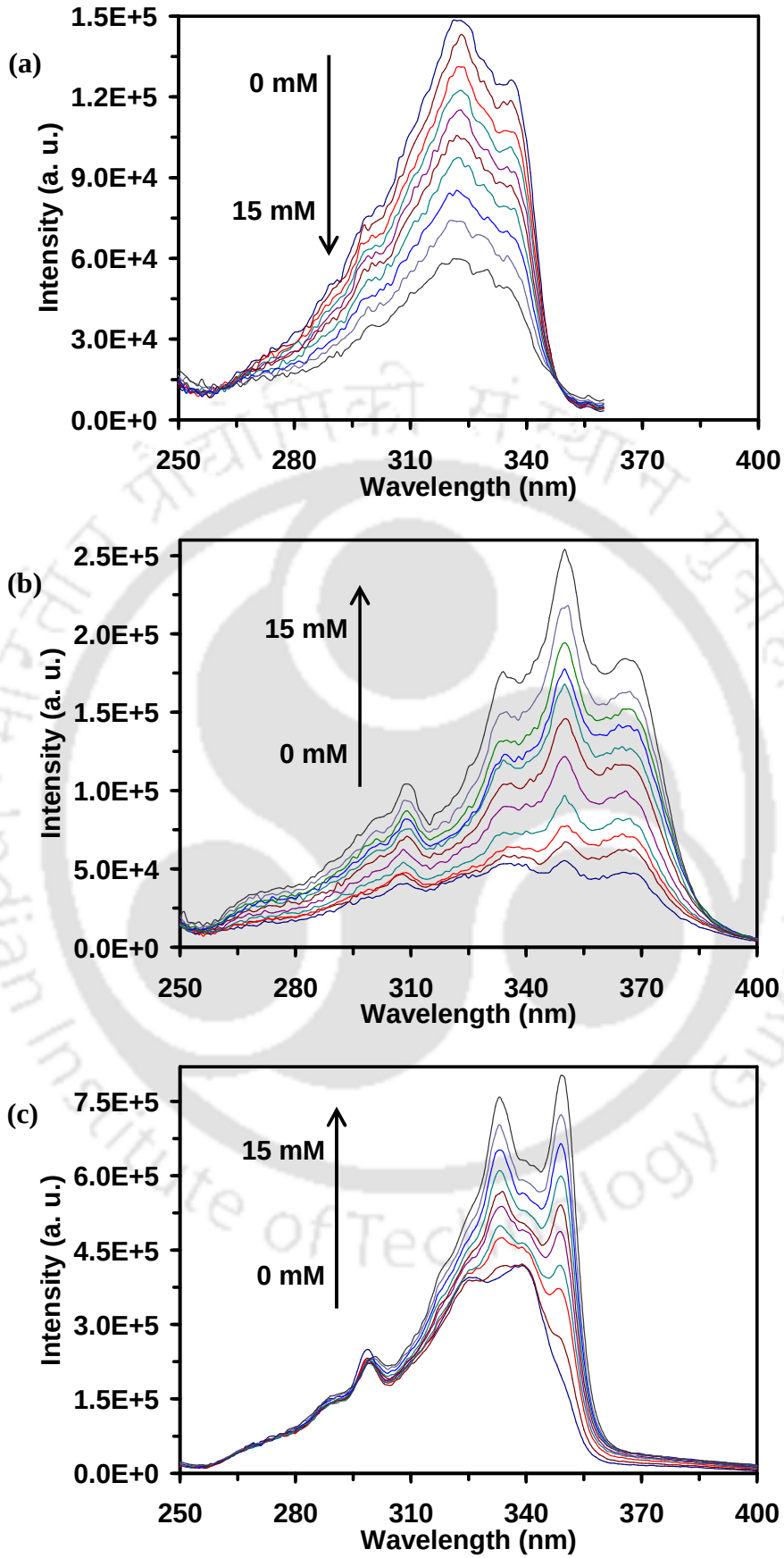

Figure 5.8. Fluorescence excitation spectra of HPIP-b in DMSO with increasing concentration of β-CD at (a) λ_{em} = 365 nm, (b) λ_{em} = 415 nm, and (c) λ_{em} = 485 nm.

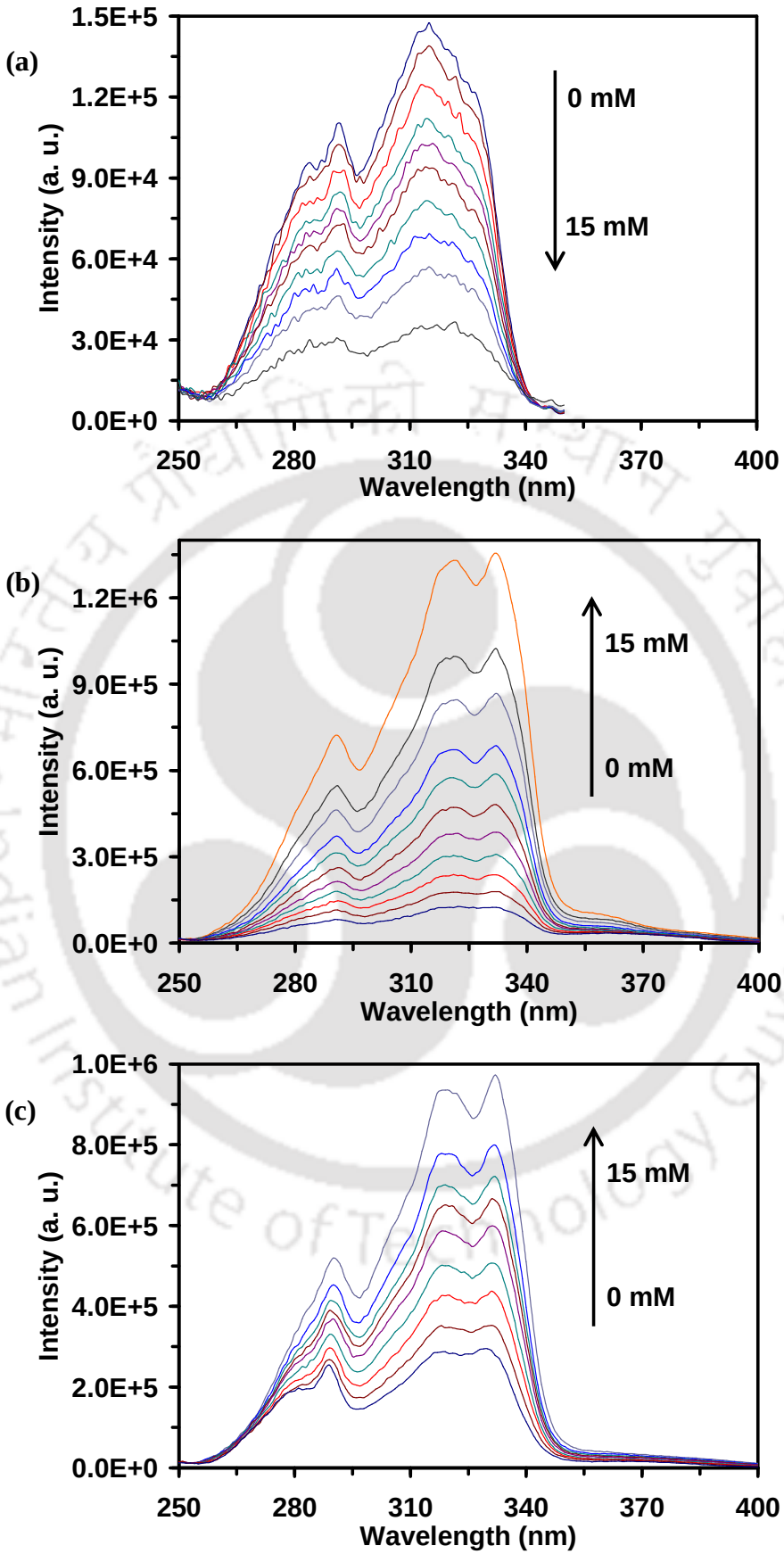

Figure 5.9. Fluorescence excitation spectra of HPIP-c in DMSO with increasing concentration of β-CD at (a) λ_{em} = 355 nm, (b) λ_{em} = 430 nm, and (c) λ_{em} = 465 nm.

(**Figures 5.7c**, **5.8c** and **5.9c**). This indicates that the normal and tautomer emissions originate from two distinct ground state species, *trans*- and *cis*-enols respectively. The red shifted absorption band at around 365 nm is present only in the excitation spectra monitored at 420 nm (**Figure 5.7b**), 415 nm (**Figure 5.8b**) and 430 nm (**Figure 5.9b**). These show that the new band is due to a different species. It can be assigned to the monoanion formed by the deprotonation of phenolic proton. This is supported by the following facts: (i) a red shift is observed in the absorption and the excitation spectra upon deprotonation in HPBI and its analogues HPIP-b and HPIP-c, and the new band absorption spectrum is close to that of monoanion absorption spectrum (see later) (ii) and the positions of the bands are consistent with the fact that the monoanion fluorescence spectrum is red shifted with respected to normal emission and blue shifted compared to tautomer emission.

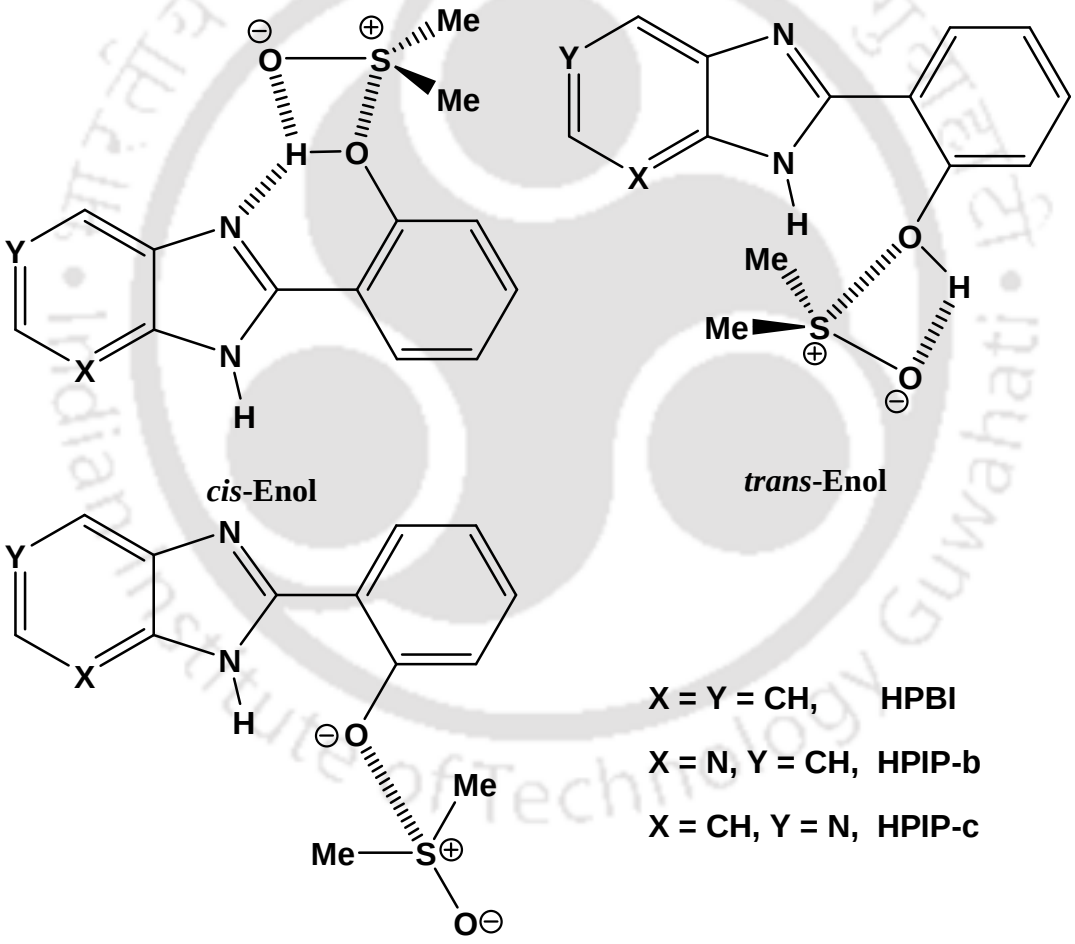

Chart 5.1. Solvated structures.

DMSO acts as proton acceptor and it can abstract the proton from hydrogen bond donor depending upon the acidity of the donor. The resulting anion is stabilized by solvation (**Chart 5.1**). The monoanion is formed in nitrogen substituted analogue even in the absence

of β-CD but not in HPBI due to greater stabilization of monoanionic form of HPIP-b and HPIP-c than the monoanionic form of HPBI due to presence of pyridine nitrogen. This was substantiated by the lower p*K*a of HPIP-b and HPIP-c than that of HPBI.[6,95,175] The pK_a value of HPBI decreases inside the β-CD due to stabilization of monoanion by β-CD nanocavity, therefore addition of β-CD leads to formation of monoanion in HPBI.[281] Mukherjee et al. also observed the formation of monoanion in 4-methyl-2,6-diformylphenol in DMSO.[365] They also reported that the monoanion is more stabilized in DMSO than in water due to higher dipole moment of DMSO.

Table 5.1. Lifetimes of HPBI, HPIP-b and HPIP-c in absence and presence of β-CD (15 mM) in DMSO.

Sample	Normal Emission[1]		Tautomer Emission[1]		Anion Emission[2]	
	τ_1^N (ns)	χ^2	τ_1^T (ns)	χ^2	τ_1^A (ns)	χ^2
			HPBI			
DMSO	1.5	1.0	4.4	1.0		
DMSO + β-CD	1.5	1.0	4.4	1.0	3.2	1.0
			HPIP-b			
DMSO	1.2	1.0	3.2	1.1	4.0	1.1
DMSO + β-CD	1.2	1.1	3.5	1.2	4.1	1.0
			HPIP-c			
DMSO	1.2	1.0	3.4	1.1	3.7	1.0
DMSO + β-CD	1.2	1.0	3.9	1.0	3.9	1.0

[1]λ_{exc} = 308 nm [2]λ_{exc} = 375 nm.

The formation of monoanion was further substantiated by fluorescence decay measurements. The lifetime data of HPBI, HPIP-b and HPIP-c in DMSO in presence and absence of β-CD are tabulated in **Table 5.1**. The lifetimes of the normal emission of the fluorophores is not affected by the presence of β-CD. Although the lifetime of tautomer emission of HPBI is not affected by β-CD, there is slight increase in the lifetime of tautomer emission of HPIP-b and HPIP-c. Using 375 nm laser diode as the excitation source, the decay was monitored at 420 nm, 435 nm and 438 nm for HPBI, HPIP-b and HPIP-c, respectively. The lifetime values thus obtained are different from those of the normal and tautomer emissions. This confirms the formation of monoanion.

5.1.3. Binding Constants

To determine the stoichiometry and the binding constant of the inclusion complexes, the fluorescence intensities of the tautomer emissions at different β-CD concentration in water as well as DMSO were analyzed using Benesi-Hildebrand equations[366,367] (**Equation 5.1**) for 1:1 complex formation.

$$\frac{1}{I - I_0} = \frac{1}{I_\alpha - I_0} + \frac{1}{(I_\alpha - I_0)K[CD]} \qquad (\mathbf{5.1})$$

where I_0, I and I_∞ are emission intensities in the absence of β-CD, at an intermediate β-CD concentration and when the molecule is completely encapsulated in β-CD, respectively, and K being the association constant.

The plot of $1/(I\text{-}I_0)$ against $[\beta\text{-CD}]^{-1}$ obtained (**Appendix A5**) shows linear variation justifying the validity of equation 1 and thus showing the formation of a 1:1 complex between the fluorophores and β-CD both in water and DMSO. The plots of $1/(I\text{-}I_0)$ against $[\beta\text{-CD}]^{-2}$ could not be fitted linearly (not shown) for all the solutions which rules out the 1:2 complex formation with β-CD. The association constants obtained from the Benesi-Hildebrand plot for HPIP-b and HPIP-c with β-CD in water are 200 M^{-1} and 95 M^{-1}, respectively. Warner and his group calculated the binding constant for HPBI:β-CD inclusion complex formation to be 131 M^{-1} in water.[358] In DMSO, association constants for HPBI, HPIP-b and HPIP-c are 193 M^{-1}, 78 M^{-1} and 70 M^{-1}, respectively.

5.1.4. pH Titration

The prototropic equilibrium of the fluorophores are affected by complexation and the calculation of acidity constants (pK_a) which gives useful information about guest orientation inside the inclusion complex.[100,368,369] Hence, the acidity constants (pK_a) of HPIP-b and HPIP-c in the presence of β-CD (15 mM) was determined spectrophotometrically with the help of UV-Visible absorption measurements at different pH in aqueous β-CD solutions (**Figure 5.10**).

In presence of β-CD, HPIP-b is completely in neutral form at pH 6.3 while HPIP-c is neutral at pH 5.3. The pK_a value for the neutral-monoanion equilibrium of HPIP-b was found to be 8.3 which is little lower than 8.6 in the absence of β-CD reported by Dogra *et. al.*[6] In case of HPIP-c also the pK_a value for the neutral-monoanion equilibrium (8.6) is lower than that in aqueous solution (9.3).[175]

The fluorophores have two acidic centers viz. the phenolic OH and the imidazole NH. Phenol has pK_a ~ 10 while imidazole has pK_a ~ 14.5. Hence, since observed pK_a is closer to that of phenol the monoanion formed is due to the deprotonation of phenolic OH. The lower pK_a value observed here compared to phenol (~10) may be due to polarisation of phenolic OH bond as a result of presence of electron withdrawing imidazopyridine moiety. Since the pK_a of the imidazole >NH group is higher than hydroxyl proton of the β-CD,[370] we did not attempt to calculate the pK_a of the imidazole >NH group.

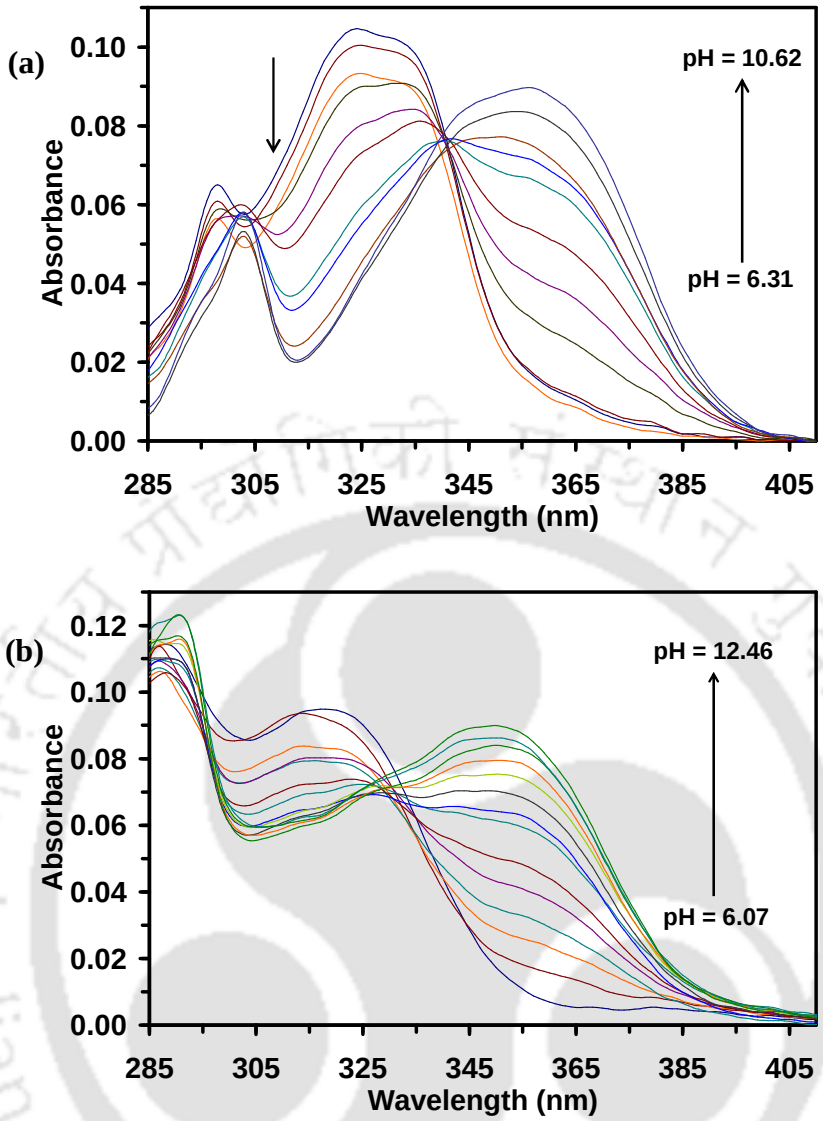

Figure 5.10. Absorption spectra of (a) HPIP-b, and (b) HPIP-c in 15 mM aqueous β-CD at different pH.

Similar decrease in pK_a values were observed for 2-(2'-hydrophenyl)benzazoles,[22] and other aromatic alcohols.[370] The lowering of pK_a value for the neutral-monoanion in presence of β-CD is ascribed to the formation of intermolecular hydrogen bond between the phenolic oxygen and the alcoholic OH groups of β-CD, the alcoholic OH groups acting as the H-bond donor. This facilitates the stabilization of the monoanion formed by deprotonation. The difference in the pK_a values in presence and absence of β-CD is a measure of strength of intramolecular hydrogen bond, through which the ESIPT occurs. It appears that the strength of intramolecular hydrogen bond depends on the position of pyridine nitrogen and is stronger in HPIP-c than HPIP-b. This was consistent with the fact that Φ_T/Φ_N is higher in HPIP-c than HPIP-b (**Figure 5.4**).

5.1.5. Orientations of the Guests in Inclusion Complex and NMR Studies

The length and interior diameter of β-CD cavity are 7.9 Å and 7.8 Å, respectively.[323] The dimension of the DFT optimized structure HPIP-b already calculated in **Section 3.1** is shown in **Figure 5.11**. The dimensions of HPBI and HPIP-c are nearly same as those of HPIP-b. Based on the dimensions of the host and guest molecules, it can inferred that the guest can be encapsulated only partially and the guest molecule can enter the cavity of β-CD in two possible ways as shown schematically in **Figure 5.12**. If the guests were oriented as shown in **Figure 5.12a**, the –OH group of the guest molecules will be present near the rim. On the other hand, if the guests were present in the reverse way as shown in **Figure 5.12b**, the –OH group of the guest molecules will be present inside the cavity. Since the interior of the CD nanocavity is hydrophobic the formation of monoanion is possible only if the solvent molecule interacts with guest molecules. The formation of monoanion clearly suggests that the phenyl ring of the molecule is present outside the cavity (**Figure 5.12a**). Such an orientation allows restricted hydrogen bonding with solvent molecules. It is also feasible for intermolecular H-bonding with the -OH group of β-CD.

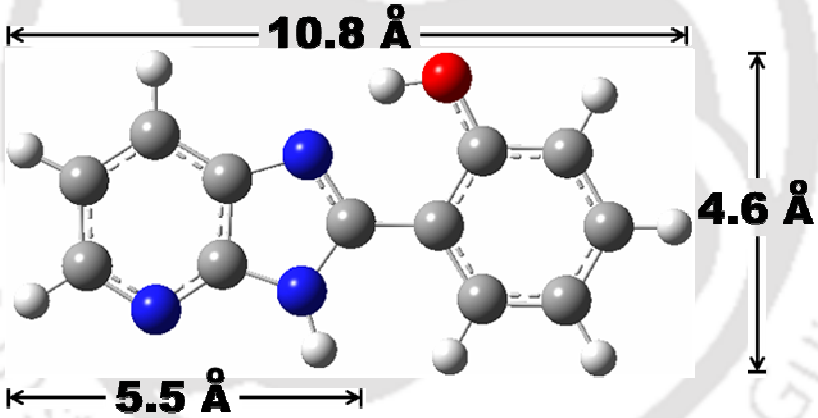

Figure 5.11. Optimized geometry of HPIP-b obtained from DFT calculations.

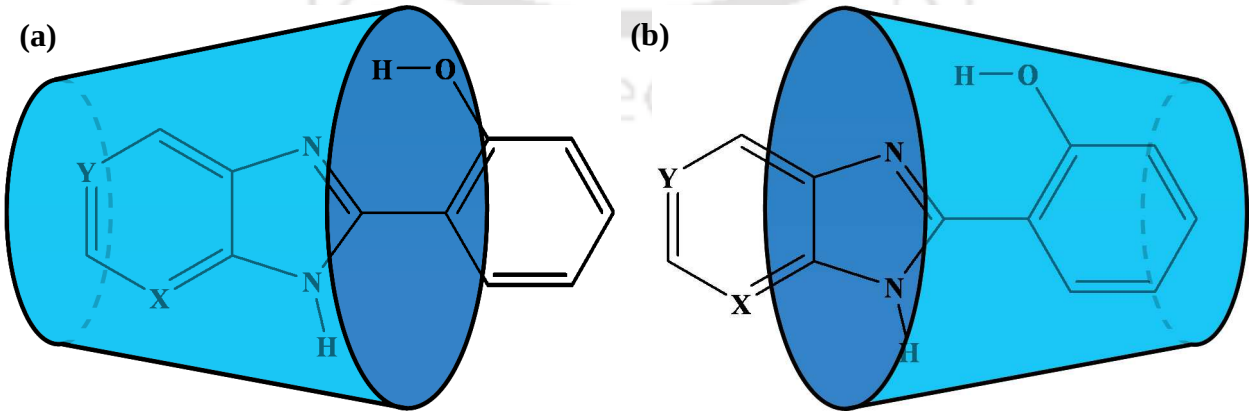

Figure 5.12. Mode of 1:1 complexation of HPIP-b with β-CD with the heterocyclic imidazopyridine moiety (a) inside, and (b) outside the β-CD nanocavity.

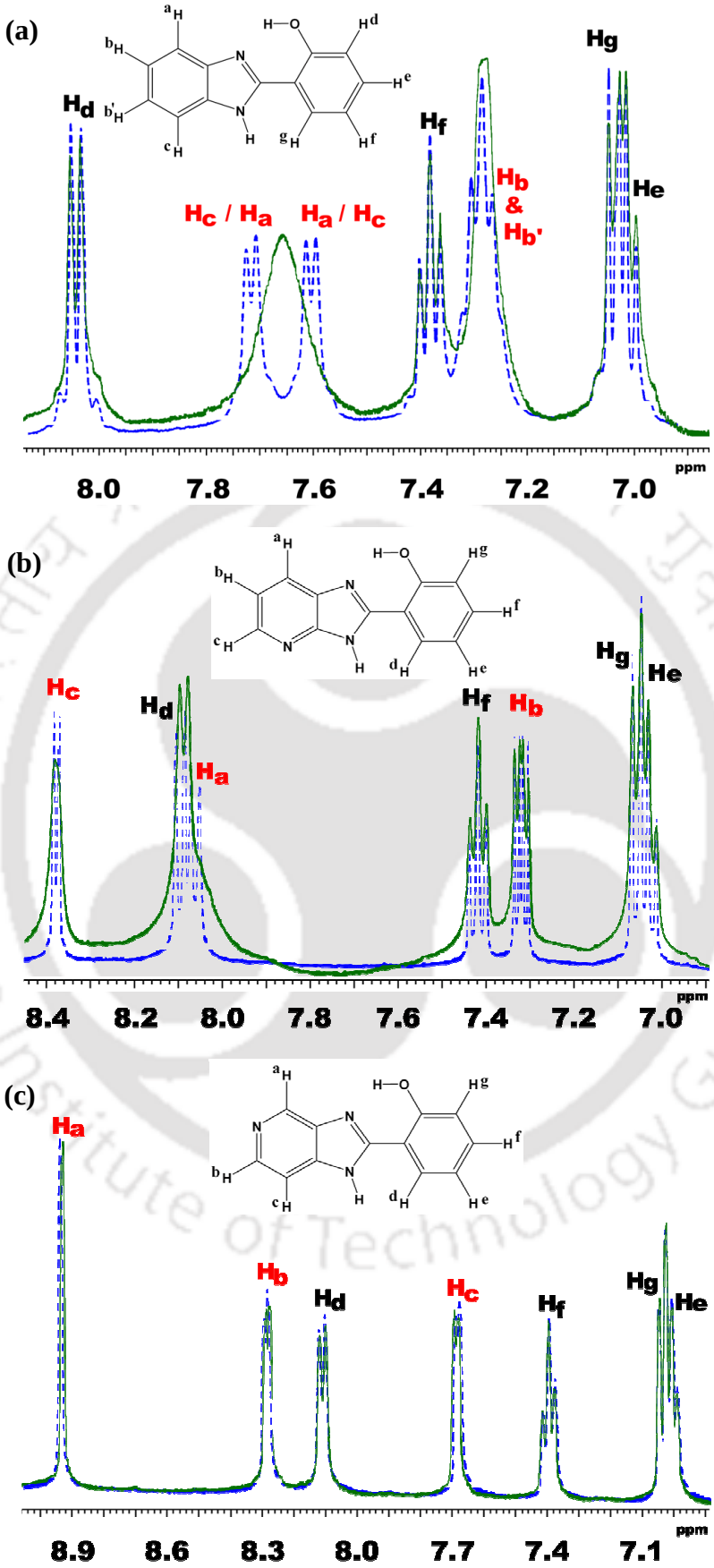

Figure 5.13. ^{1}H NMR spectra of (a) HPBI, (b) HPIP-b, and (c) HPIP-c in the presence (solid line) and absence (dotted line) of β-CD in DMSO-d_6.

Formation of monoanion indicates that HPIP-b and HPIP-c partially penetrate the β-CD cavity through the imidazopyridine moiety. The phenolic group resides outside the upper rim and exposed to the solvent environment and its -OH group presents near the rim. HPBI was also reported to have the same orientation in aqueous β-CD.[100]

The NMR spectra of the guest in the presence and the absence of β-CD should give a clear picture of the orientation of the molecules inside the β-CD cavity.[349] Due to poor solubility the NMR spectra in heavy water could not be recorded. But ^{1}H NMR spectra were recorded in DMSO and the aromatic region of the spectra is depicted in **Figure 5.13**. NMR decoupling experiments were performed for proton assignments. The proton assignments from decoupling experiments are described in **Appendices A1**, **A2** and **A3**.

In all of three molecules, as expected, the complexation with β-CD affects protons of the benzimidazole/pyridoimidazole more than the protons of the hydroxyphenyl ring. The chemical shift values for HPIP-b are in the order $H_e < H_g < H_b < H_f < H_a < H_d < H_c$. In the absence of β-CD, H_a proton peak appears as doublet at 8.04 ppm and H_d proton peak appears as doublet at 8.10 ppm. In the presence of β-CD, H_d proton is affected less, but H_a proton peaks are shifted down field and merged with H_d proton to appears as a broad shoulder. The H_c proton appears as doublet in the absence of β-CD and the doublet merged to appear as broad single peak in presence of β-CD. The well resolved peaks of H_b proton in the absence of β-CD become less resolved in presence of β-CD. However, the effect of β-CD complexation is negligible for protons of the phenyl ring. Similarly in case of HPIP-c, the chemical shift values of H_a, H_b and H_c are affected more than that of phenyl ring protons. The chemical shift values for HPIP-c are in the order $H_e < H_g < H_f < H_c < H_d < H_b < H_a$ where the H_d proton is shifted up-field and the protons of the heterocyclic moiety are in the downfield region. In HPBI the peaks of benzene ring protons are blurred even in absence of β-CD, but clear splitting are appeared in those of phenolic ring proton. The splitting of phenolic ring proton is unaffected but the peaks of benzene ring protons are affected in presence of β-CD (**Figure 5.13a**).

The mode of encapsulation of HPBI and its analogues are different from corresponding (4'-*N*,*N*-dimethylamino) substituted analogues where the 2-(4'-*N*,*N*-dimethylamino)phenyl is encapsulated and the benzimidazole/imidazopyridine ring is present outside the cavity.[349,371,372] On the other hand, Douhal et al. demonstrated that ESIPT exhibiting milrinone also enters the CD cavity through pyridine ring.[373] It appears that substitution influences the orientation of the molecules inside the cavity.

5.1.6. Conclusion

HPBI, HPIP-b and HPIP-c enter the β-CD cavity through benzimidazole/ imidazopyridine moiety. NMR confirms the proposed orientation of the molecules. Encapsulation of HPIP-b and HPIP-c by β-CD enhanced the ESIPT reaction. Although all of the three molecules form 1:1 inclusion complexes with β-CD, the effects of β-CD on HPIP-b and HPIP-c are much significant compared to HPBI. Remarkable enhancement in fluorescence and red shift are observed in tautomer emission of HPIP-b and HPIP-c than that of HPBI. The tautomer emission is increased by both ESIPT favorable environment of β-CD cavity and reduction in the torsional induced nonradiative decay through twisted ICT state. The pK_a for the neutral-monoanion equilibrium of the molecules decreases due to greater stabilization of monoanion inside the nanocavity. All three molecules donate the proton to DMSO to form monoanion in DMSO. However, the monoanion of HPBI is formed in DMSO solution only when [β-CD] > 4 mM. The presence of extra nitrogen stabilizes the monoanion and HPIP-b and HPIP-c. Therefore, they are present as both neutral and monoanion in presence as well as absence of β-CD in DMSO. The presence of extra nitrogen makes HPIP-b and HPIP-c more sensitive to environment than HPBI and therefore they can be a better environment probe than HPBI.

5.2.0. Effect of AOT Reverse Micelle

Many important biological processes happen in small pockets of confined water surrounded by biological systems, such as water in proteins, biomembranes, vicinity of DNA, etc.[374-377] However, these processes do not occur in bulk water. The difference is probably because of the presence of localized charged boundaries surrounding the confined biological water. Studies of such biological processes in such environment have been of research interest for years and still clear cut knowledge of these systems is not attained. The water molecules in the water pool of reverse micelle have properties quite similar to those bound to biological systems in terms of less mobility and less polarity compared to that of ordinary bulk water. Therefore, reverse micelles are one of the attractive biomimicking models for biological systems.[378-381]

Reverse micelles have three different regions viz. the confined water pool, the interfacial region formed by a monolayer of the surfactant molecules surrounding the pool and the external hydrophobic oily region. The confined water pool has atleast two types of water populations present: bound water molecules which are strongly associated with the polar head group of the surfactants, and free water molecules which lie deep inside the core

of the water pool.[331,375] The properties of free and bound water molecules differ markedly with each other.[379,380,382,383] Fayer *et. al.* demonstrated that the water in the interfacial region has different structure from that of the water present inside the core of the water pool.[382,383] The two types of water are coupled by hydrogen bonding network which slower the dynamics compared to that in bulk water. On increasing the size of reverse micelle, which is usually expressed in terms of water to surfactant molar ratio (w_0 = [H_2O]/[Surfactant]),[336,384,385] the extent of free water increases over the bound water that coexist and exchange rapidly with each other.

Information about the environment of different regions in reverse micelle are obtained by inserting a probe molecule into this structure in different locations. Thus local polarity,[386,387] viscosity[388] and dynamics[389] of different regions of reverse micelle can be provided by the probe molecule. Hydrogen bond/proton transfer probe molecules are effective in studying such systems.[379,390-397] As the different regions of water nanopool are interconnected by hydrogen bonds researchers introduced hydrogen bond/proton transfer sensitive probes to obtain the properties and structural insights of the water nanopool in reverse micelle.[379,390-397] ESIPT exhibiting molecules have also been used as the probe molecules for the study.[341,378,391,398] Earlier Bhattacharyya et al have studied the ESIPT phenomenon of HPBI in AOT/*n*-heptane/water reverse micelle.[341] They found that both the normal and tautomer emissions are enhanced in the water pool of reverse micelle. In this section, we extended the study on the effects of AOT/*n*-heptane/water reverse micelle on the photophysics of nitrogen substituted analogues of HPBI viz. HPIP-b and HPIP-c. The results obtained for HPBI in this study are also compared with those obtained by Bhattacharyya et al.

5.2.1. Solubility and Absorption Spectra

The solubility of HPBI, HPIP-b and HPIP-c in *n*-heptane is quite low but when AOT is present in *n*-heptane, their solubility is enhanced significantly. It can be inferred from this that these molecules interact with the polar headgroup region of the AOT in the solution. Except small decrease in absorbance the absorption spectra (**Figure 5.14**) of HPBI and HPIP-b are less sensitive to the change in water content. Same results were reported for HPBI earlier.[341] On the other hand with increase in water amount a small increase in absorbance is observed in the spectrum of HPIP-c. As no spectral shifts or occurrence of new band was observed in the absorption spectra, it can be inferred that the fluorophores exist only as neutral molecule in the ground state.

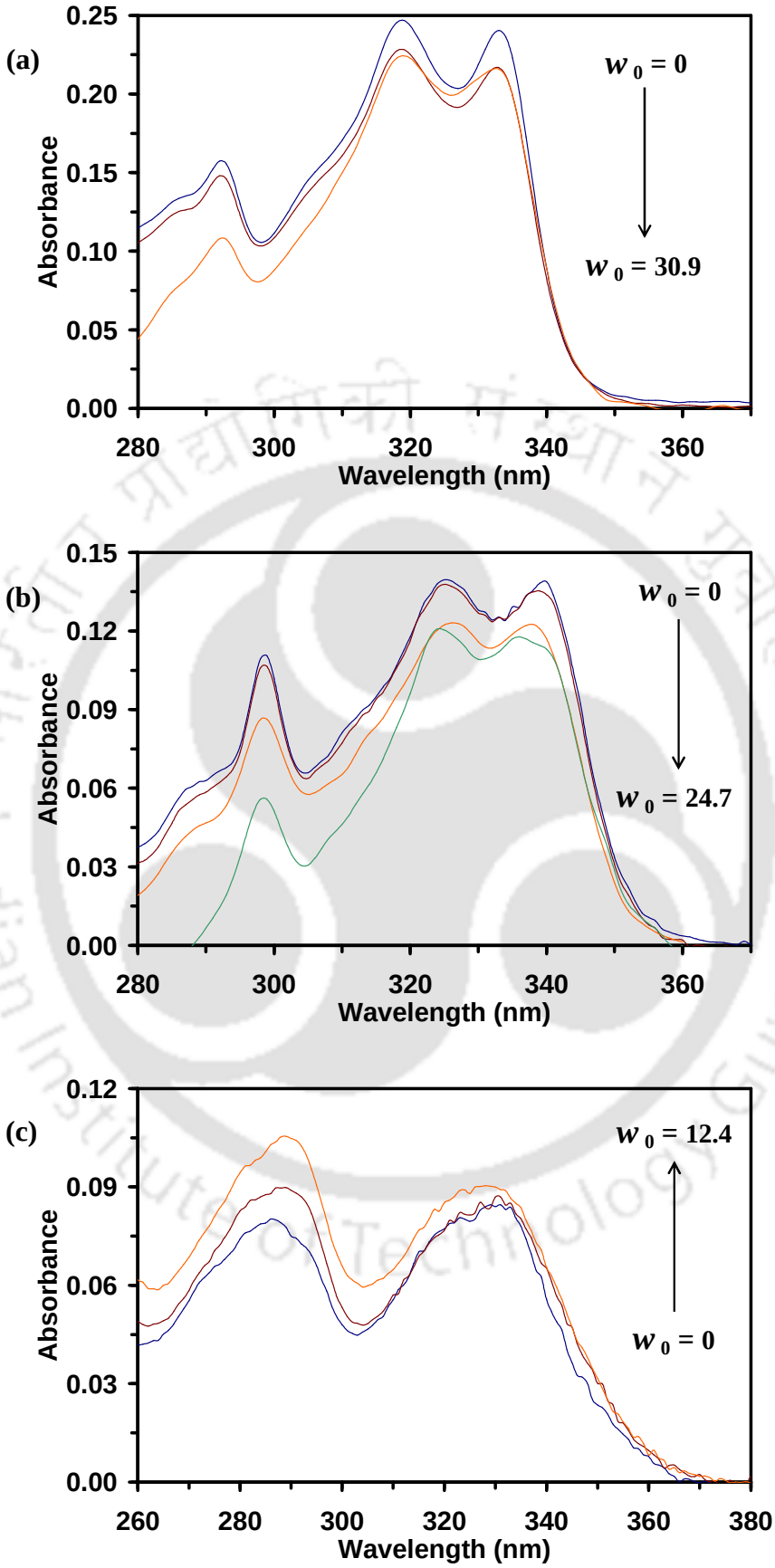

Figure 5.14. UV-Visible spectra of (a) HPBI, (b) HPIP-b, and (c) HPIP-c as a function of w_0.

5.2.2. Fluorescence Emission Spectra

The fluorescence spectrum of HPBI (**Figure 5.15**) in dry AOT solution (w_0 = 0) is nearly a single emission peak. The intensity of the normal band is negligible and the Stokes shifted tautomer band is highly intense. Until w_0 = 12.4 the intensity of the tautomer band remains almost same, but a small blue shift from 463 nm at w_0 = 0 to 459 nm at w_0 = 12.4 is observed. Upon further increase in w_0 (= 30.9), the intensity is markedly increased and blue shifted to 457 nm. The normal band is also slightly enhanced and structured with red shift of 2 nm on varying from w_0 = 0 to 30.9. The structure of the normal band becomes more prominent on increasing w_0. The blue shift of the tautomer band and the red shift of the normal band indicate that the environment surrounding the HPBI molecule becomes more polar on subsequent addition of water to the AOT reverse micelle. This is further substantiated by the fluorescence emission of HPBI in neat non-polar *n*-heptane. In heptane only the tautomer band with emission maximum is at 478 nm which is red shifted than that in AOT reverse micelle. Our observed fluorescence results agree well with the results obtained by Bhattacharyya et al.[341]

The fluorescence of HPIP-b and HPIP-c in neat non-polar n-heptane also only has the tautomer band with emission maxima at 495 and 490 nm, respectively. The emission maxima of tautomer bands in dry AOT are 496 and 474 nm, respectively. However, both HPIP-b and HPIP-c show dual emission in dry AOT solution (**Figure 5.15**). Upon increase in w_0 value, the intensities of both normal and tautomer bands decrease in both HPIP-b and HPIP-c. The reduction in the intensity of the tautomer bands of both molecules decrease with increase in w_0. In HPIP-b, the intensity of tautomer decreases till w_0 = 9.3 and with further increase in w_0 (> 9.3), the tautomer band remains constant. In case of HPIP-c, the intensity of the tautomer band decreases till w_0 = 18.5 while that of the normal band decreases till 3.1. Overall a small blue shift in tautomer band and a red shift in normal band of both HPIP-b and HPIP-c are observed with increase in size of the water nanopool. These shifts indicate the HPIP-b and HPIP-c molecules enter the more polar water pool.

In AOT/*n*-heptane solution, the rotational mobility of the surfactant molecules is less restricted.[399,400] On addition of water, the surfactants align together to form reverse micelles and water is solubilized inside the core of the reverse micelles. On further increase in amount of added water, the size of the water pool swells and the polarity of the system increases. Three factors can contribute to the decrease in intensity of the tautomer band with increase in w_0. The first is nonradiative de-excitation of the tautomer formed by torsion rotation (as discussed in **Section 3.1**) to ICT state. The ICT is favored more with increase in w_0 due to

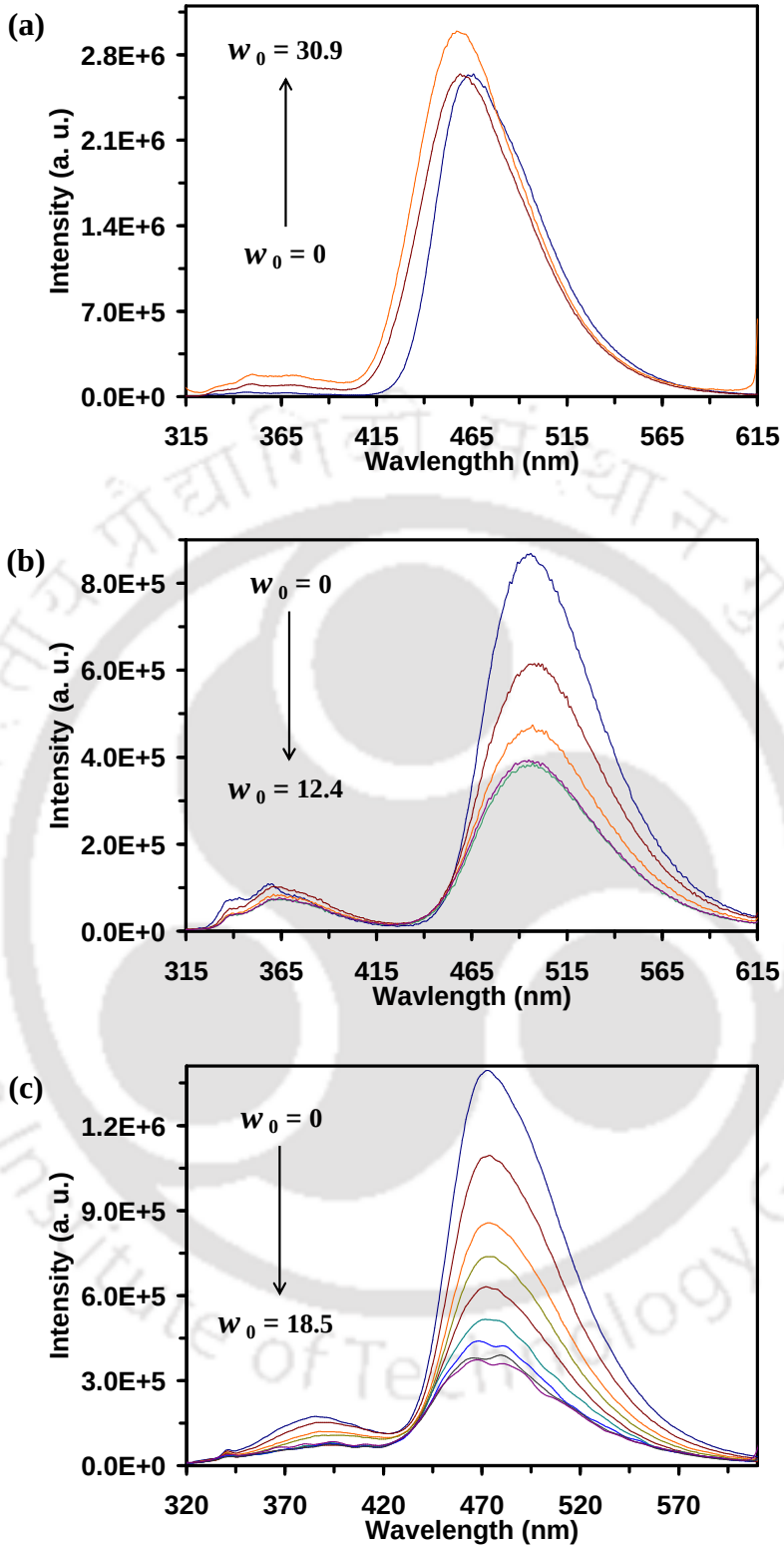

Figure 5.15. Fluorescence emission spectra of (a) HPBI, (b) HPIP-b and (c) HPIP-c as a funtion of w_o, λ_{exc} = 310 nm.

increase in polarity. The second is shifting of *cis*-enol to *trans*-enol equilibrium toward the *trans*-enol due to perturbation from external water molecules by breaking the cyclic

intramolecular hydrogen bonded ring in *cis*-enol and favoring the formation of *trans*-enol. The third is the formation of solvated open enol form as discussed below:

More than half of the total reduction in the tautomer band in HPIP-c is observed to be completed at w_0 = 1.44 while in HPIP-b it is till 3.1. Douhal and his group proposed that the water nanopool consists of three regions viz. bulk-like water core and two shells surrounding the core.[379] The outer shell is strongly attached to the polar head group of the surfactant. As the size of water pool increases till w_0 = 2, the first region which is the shell of bound water molecules attached to the polar head group is formed. In this region, the confinement effects dominate over the relaxation dynamics of these water molecules. On further increase in size to $w_0 \approx 5$, the core of the water pool begins to grow gradually as a result of which the water content in the core increases and relaxation dynamics of these water molecules also change. Beyond $w_0 > 5$, the third region, no more significant change in the relaxation dynamics occurs. But there is an appreciable decrease in the fluorescence of HPIP-b and HPIP-c at $w_0 >$ 5 also. It appears that the length and nature of the probes also play a role in the determination of relaxation limit.

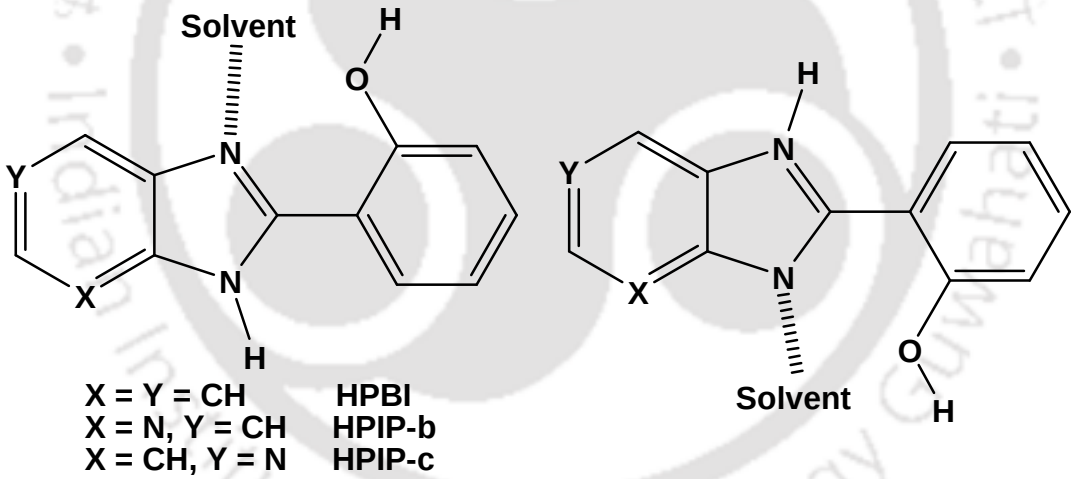

Chart 5.2. Solvated open enol conformers.

The results also suggest that HPIP-b and HPIP-c preferentially reside at the interfacial region between the water pool and the polar head groups. Further lowering of the tautomer band of both HPIP-b and HPIP-c shows that the environment surrounding the molecules continues to change. The change in environment is because of the drifting away of the molecules from the interfacial region toward the core of the nanopool. The movement away from the interfacial region is influenced by the solvent water molecules by forming hydrogen bond with the enol forms. These hydrogen bonds break the intramolecular hydrogen bonded cyclic ring in *cis*-enol and result in formation of solvated open enol conformer (**Chart**

5.2).[95,174,175] Guchhait *et. al.* had also reported similar solvated structure of proton transfer probe 1-hydroxy-2-naphthaldehyde in micelles.[359] Bhattacharyya *et al*. explained the increase in the normal emission of HPBI in AOT reverse micelle upon addition of water is due to formation of polyhydrated open enol conformer.[341]

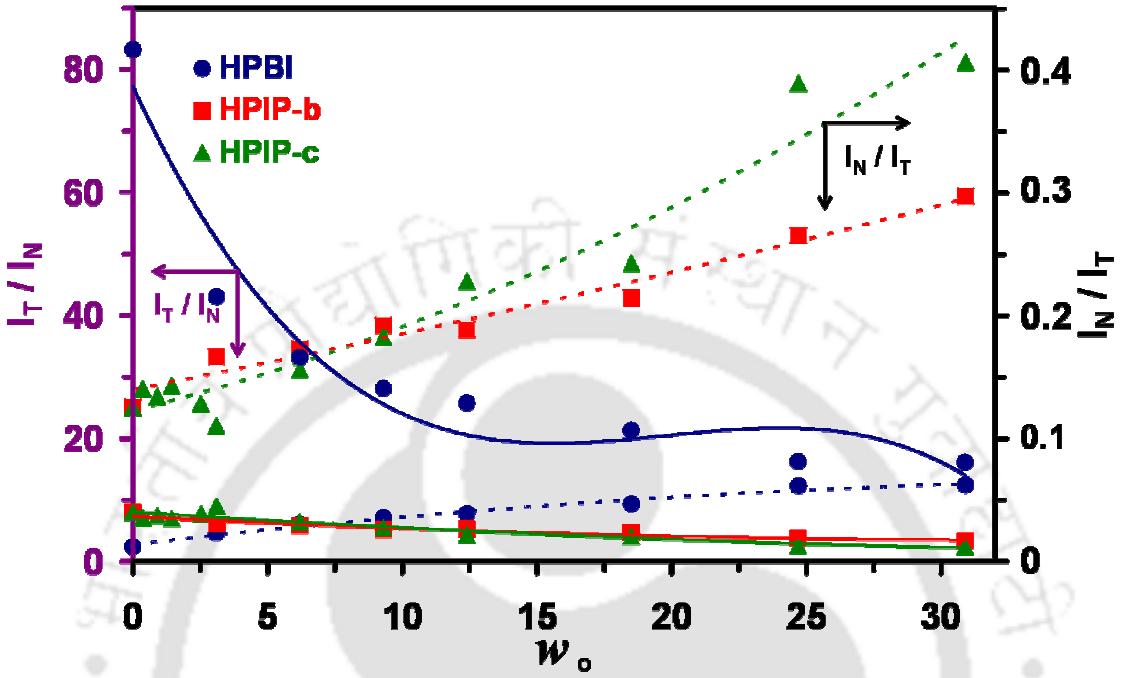

Figure 5.16. Fluorescence emisson ratio of tautomer to normal emissions (solid curve) for HPBI, HPIP-b and HPIP-c excited at 310 nm as a function of w_o values. The dotted curves represent the normal to tautomer emission ratio.

As mentioned earlier the formation of solvated open enol conformers also increases the normal to tautomer ratio (**Figure 5.16**). The decrease in tautomer to normal ratio is highest in HPBI. The ratio in HPBI at w_0= 30.9 is 5.2 times less than that at w_0 = 0. While the decreases in ratio (from w_0 = 0 to 30.9) in HPIP-b and HPIP-c are 2.4 and 3.2 times, respectively. This indicates the cyclic intramolecular hydrogen bonded cyclic ring is strongest in HPBI and is least perturbed by the surrounding protic water molecules. As a result there is no significant change in the intensity of the tautomer band.

5.2.3. Fluorescence Excitation Spectra

Pal et al. observed that in dry AOT solution, 7-hydroxy-4-methylcoumarin exists only in the neutral form in the ground state as well as in the excited state.[386,387] But at higher w_0 values, apart from the neutral form, the anionic form of the molecule is also observed in the excited state though only the neutral form is present in the ground state. On the other hand, Valeur et. al. found that the photoacid 2-naphthol is localized at the interfacial region and no

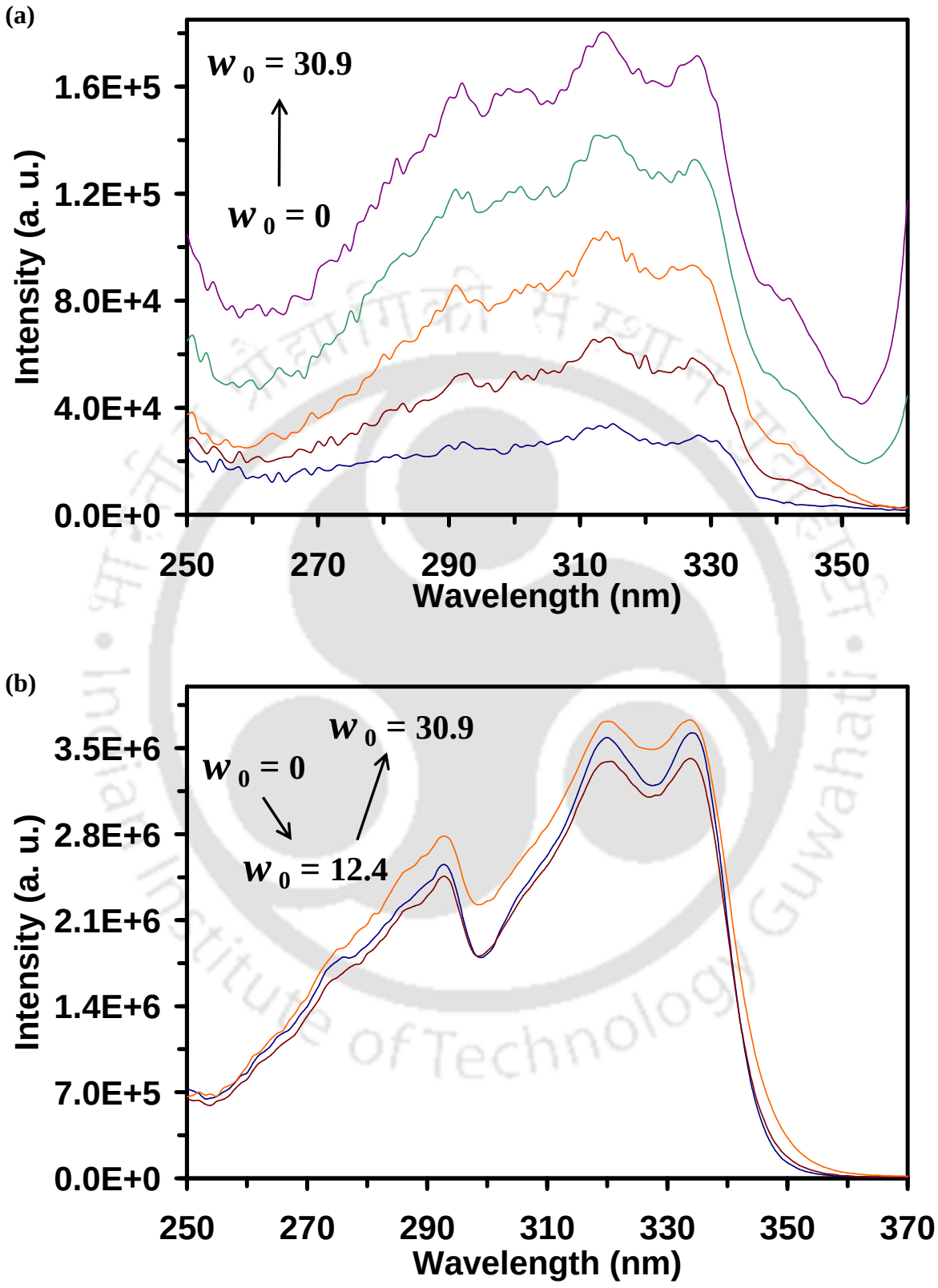

Figure 5.17. Fluorescence excitation spectra of HPBI monitored at the (a) normal (λ_{em} = 365 nm), and (b) tautomer (λ_{em} = 465 nm) bands.

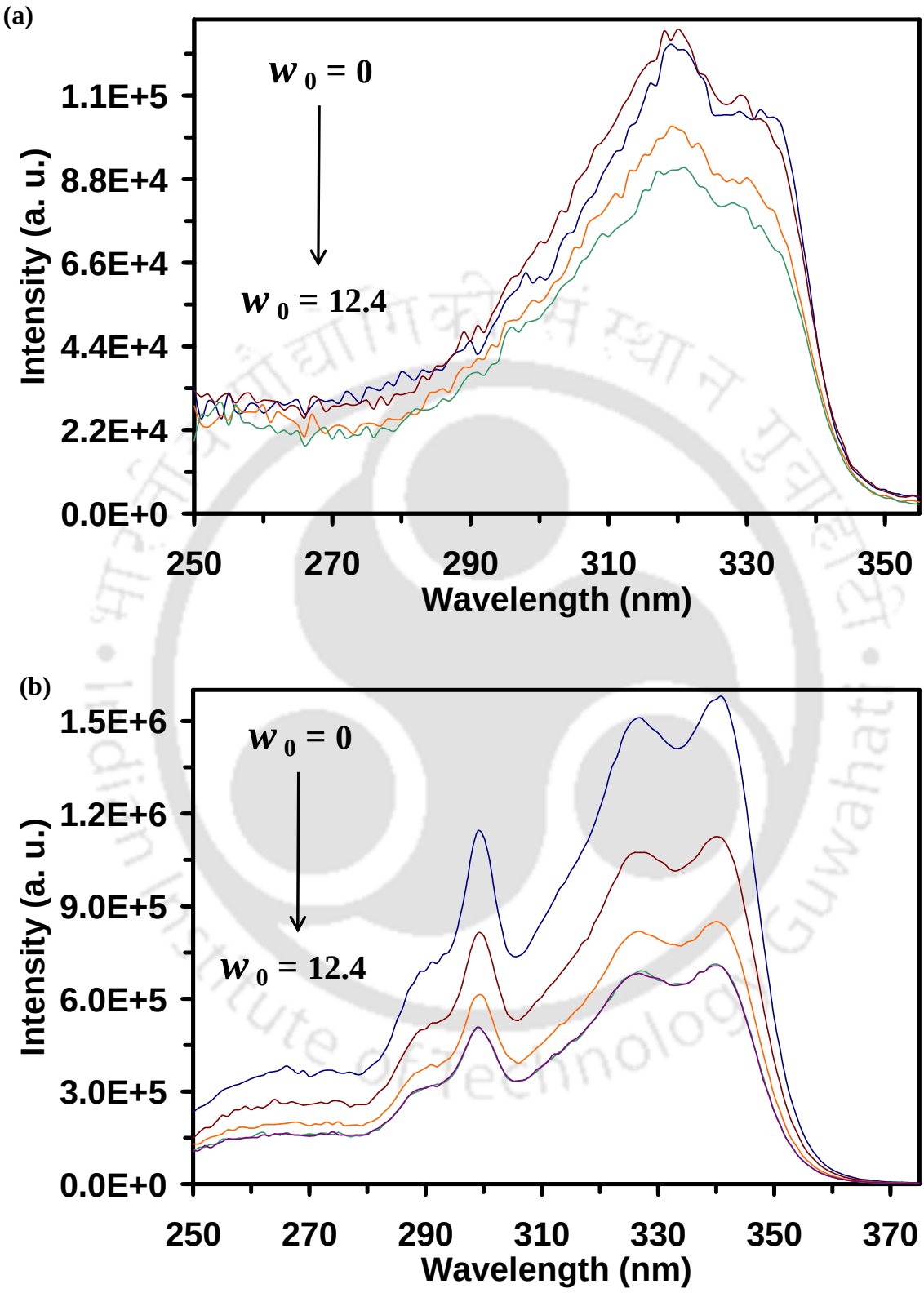

Figure 5.18. Fluorescence excitation spectra of HPIP-b monitored at the (a) normal (λ_{em} = 390 nm), and (b) tautomer (λ_{em} = 495 nm) bands.

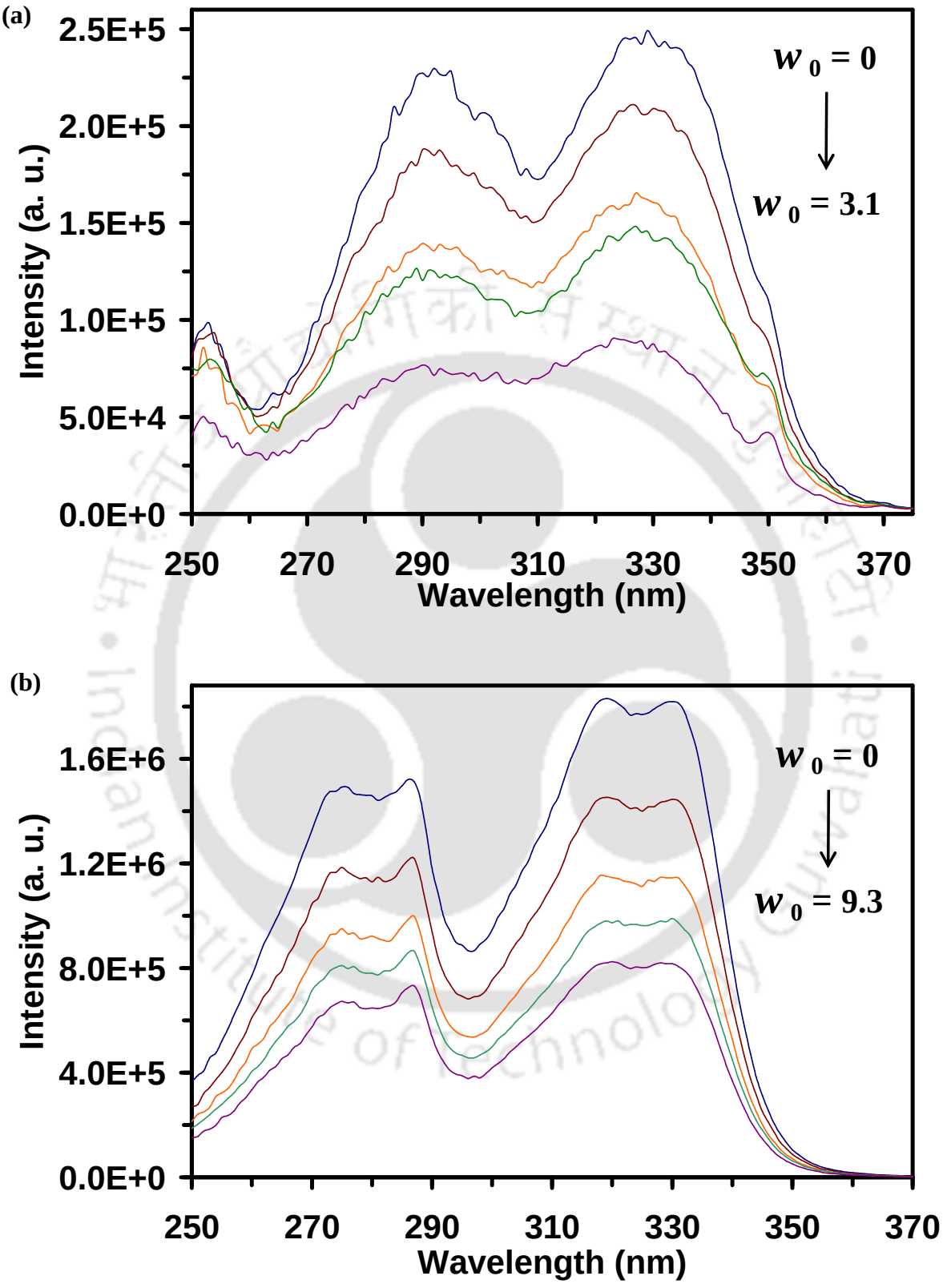

Figure 5.19. Fluorescence excitation spectra of HPIP-c monitored at the (a) normal (λ_{em} = 360 nm), and (b) tautomer bands (λ_{em} = 475 nm).

deprotonation occurs in the excited state irrespective of w_0 value, whereas the charged photoacid sulfonato derivatives of 2-naphthol are localized around the center of the water pool and show significant proton transfer activity.[391,392] In the previous section, we have seen that in DMSO, HPBI in presence of β-CD and nitrogen substituted analogues even in absence of β-CD form anion even in the ground state. Since the excitation spectra give a better picture, the excitation spectra were recorded for all three molecules monitored at both bands.

The fluorescence excitation spectra of HPBI (**Figure 5.17)** show quite differently from those of HPIP-b (**Figure 5.18**) and HPIP-c (**Figure 5.19**). The excitation spectra of HPBI monitored at the normal band show an increase in intensity (**Figure 5.17a**). This indicates that not only the increase in the nonradiative decay of the tautomer but also the rise in relative population of enol conformers is responsible for the enhancement in the normal band rather than increase in the nonradiative decay. But the spectra monitored at the tautomer band initially decreases till w_0 = 12.4 (**Figure 5.17b**) then increases on increase in size of the nanopool following the similar trend as observed in the tautomer band of emission spectra of HPBI (**Figure 5.15b**). However, in case of HPIP-b and HPIP-c, same as emission spectra the intensities of the excitation spectra monitored at both normal and tautomer bands decrease. While the excitation spectra monitored at normal band of HPIP-b reach saturation point at w_0 = 12.4, the spectra monitored at tautomer band reach saturation point at w_0 = 9.3. On the other hand, both excitation spectra of HPIP-c get saturated at w_0 = 9.3. However the excitation spectra do not indicate the formation of any additional band due to deprotonation. Thus, ruling out the existence of anionic species.

5.2.4. Fluorescence Lifetime

Time resolved fluorescence is a useful technique to explore the location of fluorescence probe in a multi component environment.[242,246,401-404] Independent of the size of the nanopool, biexponential decay is observed in the normal emissions and the tautomer emissions exhibit monoexponential decay (**Table 5.2**). However, the lifetimes of both normal and tautomer bands decrease with increase in water content. This is due to the increase in polarity and hydrogen bonding experienced by the fluorophores. Though the present lifetimes data for HPBI are a bit shorter than those obtained by Bhattacharyya et al.[341] In the case of HPBI when w_0 = 0, one of the decays with 9.2 % composition monitored at the normal band matches with that of tautomer emission. This is due to the overlap of the tautomer band and the normal band of HPBI at w_0 = 0. Dogra et al. had assigned the normal band of HPBI due to emission from *trans*-enol rotamer.[95] This further indicates that there is only one species and

that is the *trans*-enol rotamer which is responsible for the normal band of HPBI in AOT reverse micelle at $w_0 = 0$. On increasing the size of the water nanopool, the contribution from the tautomer of HPBI is not observed in the decay profile of the normal band. Instead apart from the *trans*-enol, a new species is observed in the biexponential decay of the normal band. The new species has lifetime different from that of the tautomer and *trans*-enol and can be assigned to solvated enol.[95] At $w_0 = 12.4$, the solvated enol form has the major contribution of 53.2% with lifetime of 1.81 ns while the trans-enol form has a contribution of 46.8% with 1.14 ns lifetime. The decrease in lifetimes of both normal and tautomer bands is not so significant in HPBI.

Table 5.2. Fluorescence lifetime of HPBI, HPIP-b and HPIP-c in AOT reverse micelles monitored at normal and tautomer band maxima.

w_o	Normal Band				Tautomer Band		
	λ_{Em} (nm)	τ_1^N (f_1)	τ_2^N (f_2)	χ^2	λ_{Em} (nm)	τ_1^T (f_1)	χ^2
			HPBI				
0	350	1.47 (90.8)	4.20 (9.2)	1.08	470	4.30 (100)	1.14
12.4	355	1.14 (46.8)	1.81 (53.2)	1.00	465	4.12 (100)	1.18
			HPIP-b				
0	355	1.10 (85.4)	2.20 (14.6)	1.00	500	4.84 (100)	1.25
3.1	355	0.95 (85.4)	1.97 (14.6)	1.01	500	3.80 (100)	1.17
6.2	355	0.80 (78.0)	1.65 (22.1)	1.00	500	3.19 (100)	1.16
9.3	355	0.70 (68.8)	1.44 (31.2)	1.03	500	2.91 (100)	1.26
			HPIP-c				
0	390	0.97 (17.5)	2.73 (82.5)	0.98	485	4.83 (100)	1.04
0.36	385	0.76 (23.9)	2.44 (76.1)	1.00	485	4.68 (100)	1.02
0.9	390	0.71 (29.2)	2.21 (70.8)	1.00	480	4.41 (100)	1.00
3.1	390	0.65 (48.3)	1.85 (51.8)	1.00	485	3.66 (100)	1.00
9.3	385	0.58 (69.0)	1.88 (31.0)	1.01	485	2.86 (100)	1.04

[1] λ_{exc} = 308 nm.

In the case of HPIP-b and HPIP-c, both the components in the normal emission have different lifetimes than that of the tautomer band even at $w_0 = 0$. This shows that the normal band has contribution from two different excited species – one is the *trans*-enol and the other is the solvated open enol form. The presence of extra nitrogen might have lead to this solvated enol, where the fluorophores should have formed hydrogen bonding with surfactant. The relative population between the *trans*-enol and the solvated open enol also changes to a great extent. The *trans*-enol has lifetime of 1.10 ns with contribution of 85.4 % in dry AOT while the solvated open enol form has 2.20 ns lifetime with contribution of 14.6 %. *trans*-Enol has lifetime of 0.27 ns in water (pH 7.0). The lifetimes of *trans*-enol in acetonitrile and ethanol are 0.65 and 0.76 ns, respectively.[174] At $w_0 = 9.3$, the lifetimes of *trans*-enol and solvated enol form are 0.70 ns and 1.44 ns, respectively. The relative contribution of *trans*-enol reduces to 68.8 % and that of solvated enol rises to 31.2%. *trans*-Enol of HPIP-c in dry

AOT has lifetime of 2.73 ns with relative contribution of 82.5 % and the solvated enol form has 0.97 with contribution of 17.5 %. *trans*-Enol of HPIP-c has lifetime of 0.05 ns in water (pH 7.1). The lifetimes of *trans*-enol of HPIP-c in acetonitrile and methanol are 1.0 ns and 0.34 ns, respectively.[175] At w_0 = 9.3, the lifetimes of *trans*-enol and solvated enol form are 1.88 ns and 0.58 ns, respectively. The solvated enol form becomes a major contributor with relative contribution of 69.0 %. All these show the shifting of equilibrium to towards solvated enol.

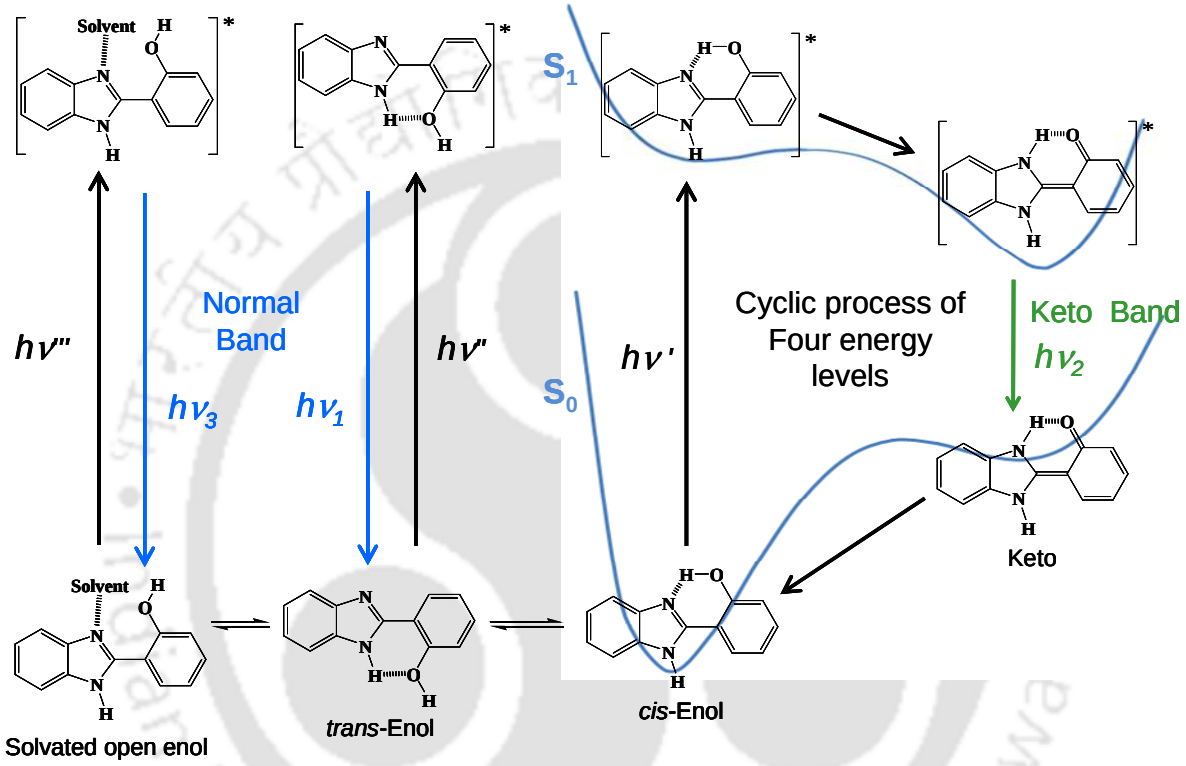

Figure 5.20. Schematic diagram of the photophysical processes of HPBI occurring in AOT reverse micelle.

Based on the experimental results a scheme was formulated for the photophysical processes of the fluorophores occurring in AOT reverse micelle and is depicted in **Figure 5.20**. *cis*-Enol is the main component present in dry AOT with some population of *trans*-enol and small contribution from solvated enol (in pyridine nitrogen substituted analogues) and all are in equilibrium. Addition of water increases the formation of *trans*-enol and solvated enol from *cis*-enol. Initially, the molecules reside at the interfacial region between the polar head group and water nanopool. With further addition of water, formation of solvated enol conformers indicates that the molecules drift away from the interfacial region and reside between the interfacial region and the center of the bulk water nanopool. When the fluorophore molecules are photoexcited, the *cis*-enol conformers undergo the ESIPT process

and give the tautomer band while the *trans*-enol and open enol emit the normal band.

5.2.5. Conclusion

The ESIPT behavior of HPBI, HPIP-b and HPIP-c in AOT reverse micelle is reported. The tautomer to normal band ratio of these fluorophores decrease with increasing value of w_0. The extent of decrease in the ratio is 5 times in HPBI from w_0 = 0 to 30. In addition there is a blue shift of tautomer band of HPBI with increasing volume of bulk water in reverse micelle. However, there is no appreciable shift in the tautomer band of HPIP-b and HPIP-c; and the decrease in ratio is ~ 2 times. This shows that initially these molecules preferentially reside in the interfacial region between the oil and water surface. On further increase in w_0, the molecules drift away toward the bulk of the nanopool that increases the relative population of solvated open enol conformers. The decrease in tautomer to normal band ratio is due to nonradiative de-excitation of the tautomer formed by torsion rotation and shifting of *cis*-enol, *trans*-enol, solvated enol equilibrium toward solvated enol.

5.3.0. Effect of Bovine Serum Albumin

Serum albumin is the most abundant protein found in blood plasma in the circulatory system. It has the ability to bind with extremely different types of compounds and this makes it important in separation and drug delivery methods.[405-407] Serum albumins function as transport proteins for various exogenous and endogenous molecules in the body by hydrophobic, hydrophilic, and ionic interactions. BSA is a globular water-soluble protein which is used as a model in many physical and chemical studies since it exhibits high conformational adaptability to a number of ligands.[408,409] Besides, BSA is readily available and is easy to be extracted. Because of its stability and reproducibility, it is ideal for use in the calibration of many biological assays.[410]

The tertiary structure of BSA is composed of three domains I, II, and III and each of which is composed of subdomains A and B. Domains II and III share a common interface and because of which the binding of an external molecule, termed as ligand, to domain III associates with conformational change of domain II and hence the binding affinities. The primary binding sites are located in the hydrophobic cavities of subdomains IIA and IIIA which are sometimes referred to as site I and site II, respectively.[242,406,411,412] The binding site I is sometime referred to as Sudlow's site I or warfarin binding site while the binding site II is also known as Sudlow's site II or binding site of ibuprofen. The BSA molecule contains two tryptophan residues – Trp-134 and Trp-213. The former tryptophan residue is located in the

hydrophilic subdomain IB near the surface of the albumin molecule. Being at the surface of BSA, subdomain IB is exposed to solvent environment. Trp-213 is located deep in a hydrophobic microenvironment in subdomain IIA.

In solution, a molecule of known structure and properties so called probe/ligand is used to interact with proteins. The information that is obtained from the interaction helps to create inferences as to the forces involved and the topography of the binding sites of the protein analyzed. This has been the main method applied in modern days for structural elucidation of protein molecules in solution. The molecular interactions are often monitored using optical techniques mainly the fluorescence spectroscopic techniques as these methods are relatively easy to use, highly sensitive and they display a variety of measurable properties.[413] Protein-bound fluorescent probes have been used extensively for elucidating information regarding environment of their binding sites.[242,343,414-418] Besides, proton transfer probes are important in identifying proton or acceptor at the binding site. The prototropic transformation of the proton transfer exhibiting probes can decipher the binding interaction with biological receptors and the environmental factors affecting the transformation.[290,419]

In this section, the interaction of HPBI, HPIP-b and HPIP-c with BSA is studied. The effect of interaction with BSA on the photophysics of these molecules is reported. The main objective of the work is to study how the interaction with the host BSA molecule is reflected by nitrogen substitution at different position of the benzene ring of HPBI.

5.3.1. Absorption Spectra

The absorption spectra of HPBI, HPIP-b and HPIP-c at different BSA concentrations are presented in **Figures 5.21**. Gradual addition of BSA to the aqueous HPBI and HPIP-c solutions lead to increase in the absorbance of the fluorophores. However, on addition of BSA to aqueous HPIP-b solution, the absorbance is decreased. BSA induced spectral changes are evidence for the interaction between the ligands and BSA. The different trend observed in HPIP-b than in HPBI and HPIP-c shows that the binding mode/binding site of HPIP-b is different from those of HPBI and HPIP-c.

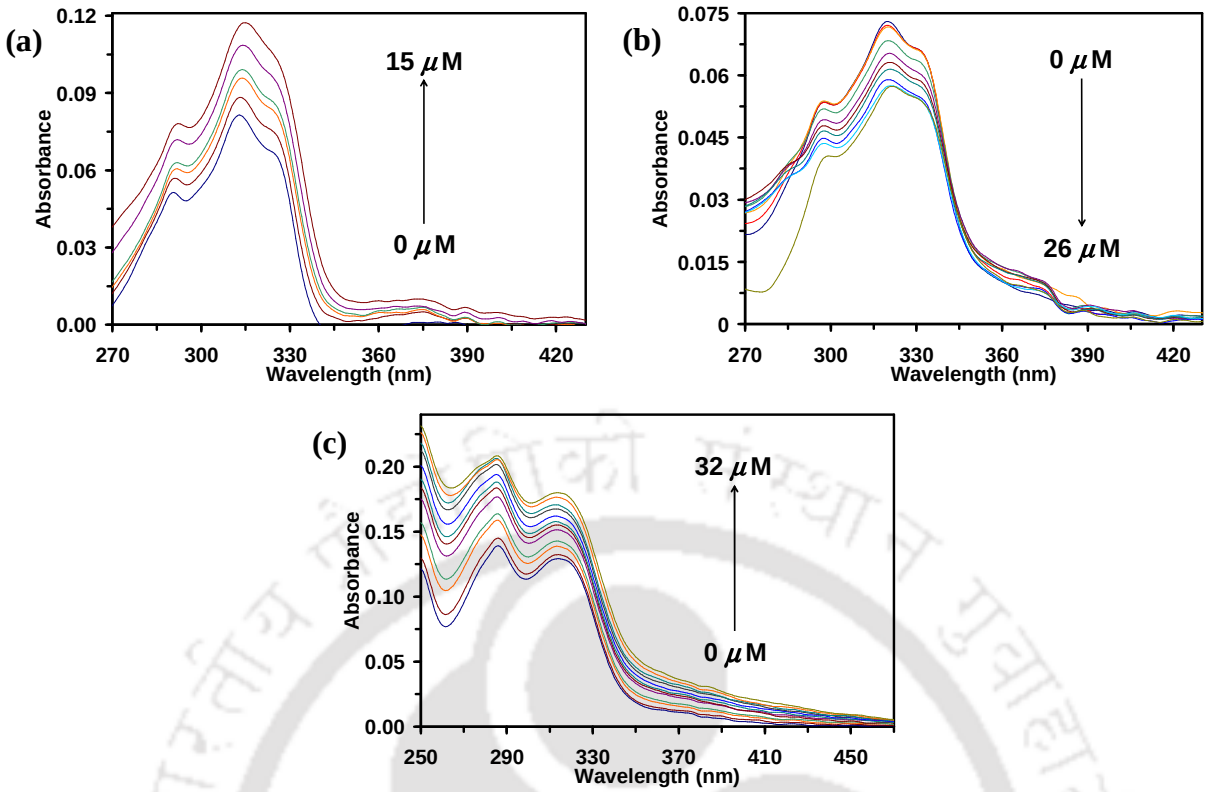

Figure 5.21. Absorption spectra of (a) HPBI, (b) HPIP-b, and (c) HPIP-c in presence of BSA.

5.3.2. Fluorescence Spectra

In aqueous buffer solution (pH 7.0-7.1), HPBI, HPIP-b, and HPIP-c display fluorescence consisting of the normal and tautomer emissions (**Figure 5.22**). The emissions observed are in agreement with the data available in the literature.[6,95,175] The tautomer emissions of HPBI and HPIP-c are more prominent than the normal emission and the intensity ratio of normal to tautomer emission of 0.19 and 0.17, respectively. But in case of HPIP-b both normal and tautomer bands are nearly equal intense and the intensity ratio is 1.17.

Upon gradual addition of BSA, initially the intensities of both normal and tautomer emissions of HPBI decrease with red shifts till 4 μM of BSA (**Figure 5.23a**). The bathochromic shift shows that HPBI enters into a less polar environment from a polar environment. With further addition of BSA, both emissions begin to increase, but the bathochromic shift continues. The saturation limit is observed at 48 μM of BSA. Though it is not very clear for the reason of initial decrease in fluorescence of HPBI, this indicates the interaction of electronic excited states of HPBI and the BSA.

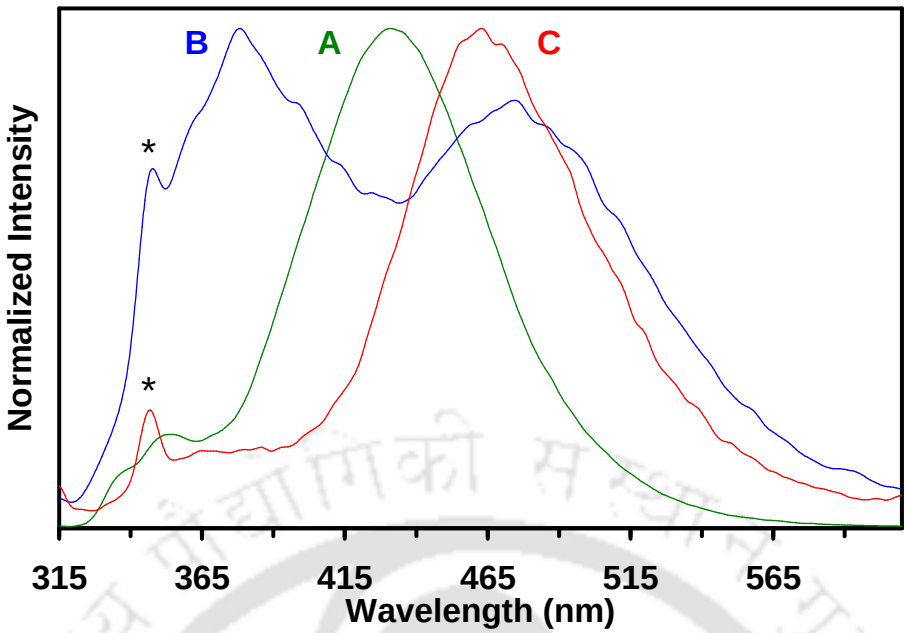

Figure 5.22. Normalized fluorescence spectra of HPBI (A), HPIP-b (B) and HPIP-c (C) at pH ~ 7.1. Water Raman band is denoted by *.

Initially, the normal band of HPIP-b with a maximum at 378 nm is more prominent than the tautomer band but as the concentration of BSA increases the tautomer band becomes more prominent (**Figure 5.23b**). Upto 3.3 μM BSA, the intensity of the normal band is slightly decreased and the emission maximum is blue shifted, but increases with further addition of BSA. Although the emission spectrum of BSA overlaps with that of normal emission, the increase in intensity is not simply due to emission from BSA. This can be inferred from **Figure 5.23a**, where upto 46 μM of BSA, no significant enhancement in the normal emission of HPBI. The normal band of HPIP-b is blue shifted from 378 nm in absence of BSA to 360 nm at 200 μM of BSA. Since the dipole moment decreases in the excited state (**Table 3.1**), the emission is expected to be blue shifted in polar environment. The initial decrease in intensity of the normal band suggests the shifting of equilibrium towards *cis*-enol. At higher concentration, the decrease in the nonradiative rate is responsible for the increase in intensity. The blue shift in the normal band upon increasing the concentration of BSA shows that the *trans*-enol of HPIP-b molecule binds at the hydrophilic pocket of the host BSA. On the other hand, no shift is observed in the tautomer band, this suggested that the *cis*-enol is exposed to solvent molecule. In other words, *cis*-enol also binds at the hydrophilic site of BSA. Since the major hydrophilic binding site of BSA is the subdomain IB which contains Trp-134 residue, it could be that the molecule HPIP-b binds at the subdomain IB. Further docking study might give a clear picture.

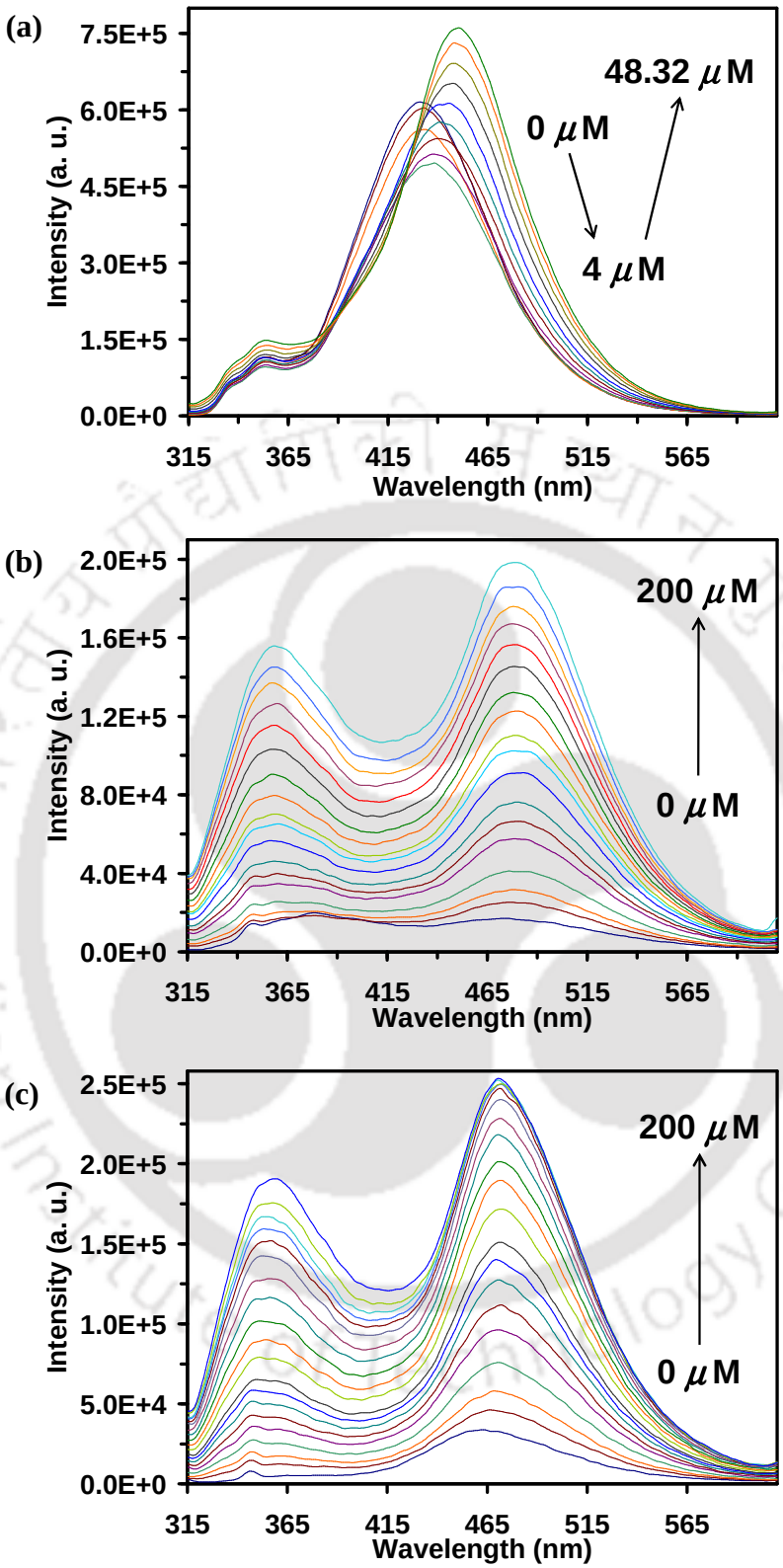

Figure 5.23. Emission Spectra of (a) HPBI, (b) HPIP-b, and (c) HPIP-c in presence of BSA (λ_{exc} = 310 nm).

In case of HPIP-c, both normal and tautomer emissions increase with increasing concentration of BSA (**Figure 5.23c**). There is no change in the position of the normal band

of HPIP-c in presence of BSA, but the tautomer band is red-shifted from 463 nm in absence of BSA to 471 nm at 200 μM of BSA. The red shift indicates the HPIP-c molecule moves toward the hydrophobic binding site of BSA.

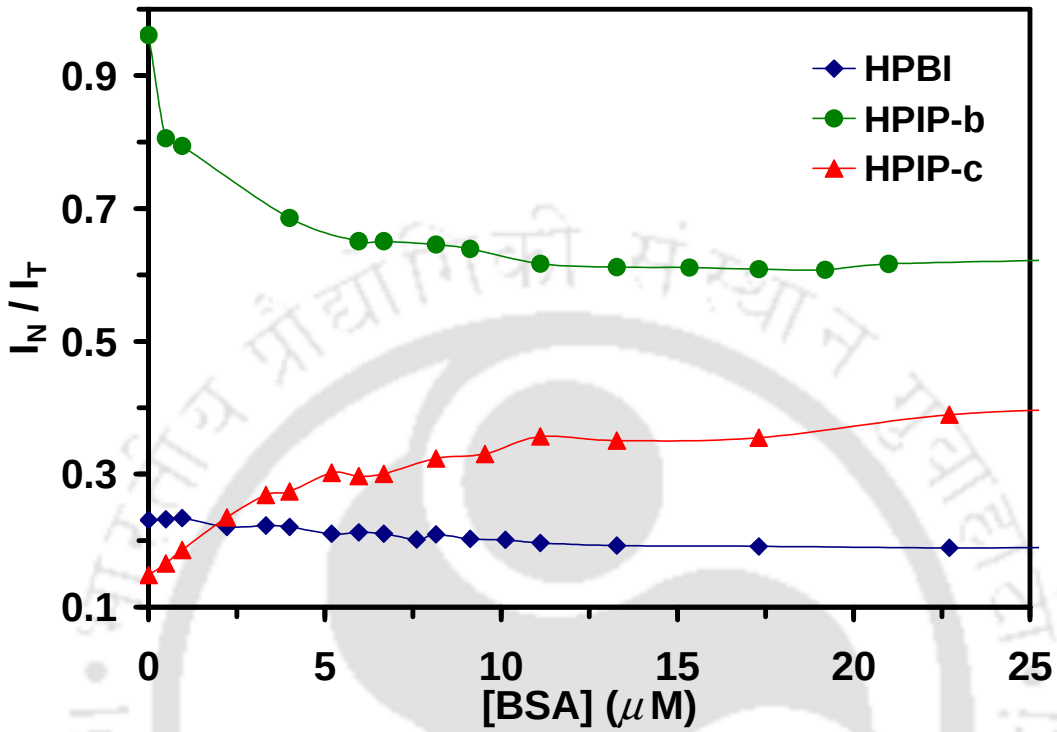

Figure 5.24. Fluorescence intensity ratio plot of normal to tautomer bands of HPBI (square), HPIP-b (circle) and HPIP-c (triangle) against concentration of BSA.

The intensity ratios of normal to tautomer bands follow different trend in all three molecules (**Figure 5.24**). It may be mentioned here the contribution of BSA to normal emission is minimum in these concentration range ([BSA] ≤ 25 μM). The emission intensities of the normal emission were also corrected for the contribution of BSA, but it hardly has an impact. HPBI shows a small gradual decrease in the intensity ratio with increase in concentration of BSA. The decrease in the intensity ratio is relatively more in HPIP-b upto 1:1 ratio. In HPIP-b, beyond 1:1 concentration ratio, the decrease in the intensity ratio of normal to tautomer bands becomes less. This decrease in the ratio in HPBI and HPIP-b shows that the tautomer emission becomes more prominent with increase in concentration of BSA. The increase in the tautomer emission may be due to two main factors: (i) decrease in nonradiative deactivation of the phototautomer through the formation of ICT by torsional rotation of the two aromatic rings (**Sections 3.1** and **3.2)**. (ii) Shifting of equilibrium in BSA towards *cis*-enol conformer of HPBI and HPIP-b which is the ground state precursor of the phototautomer.

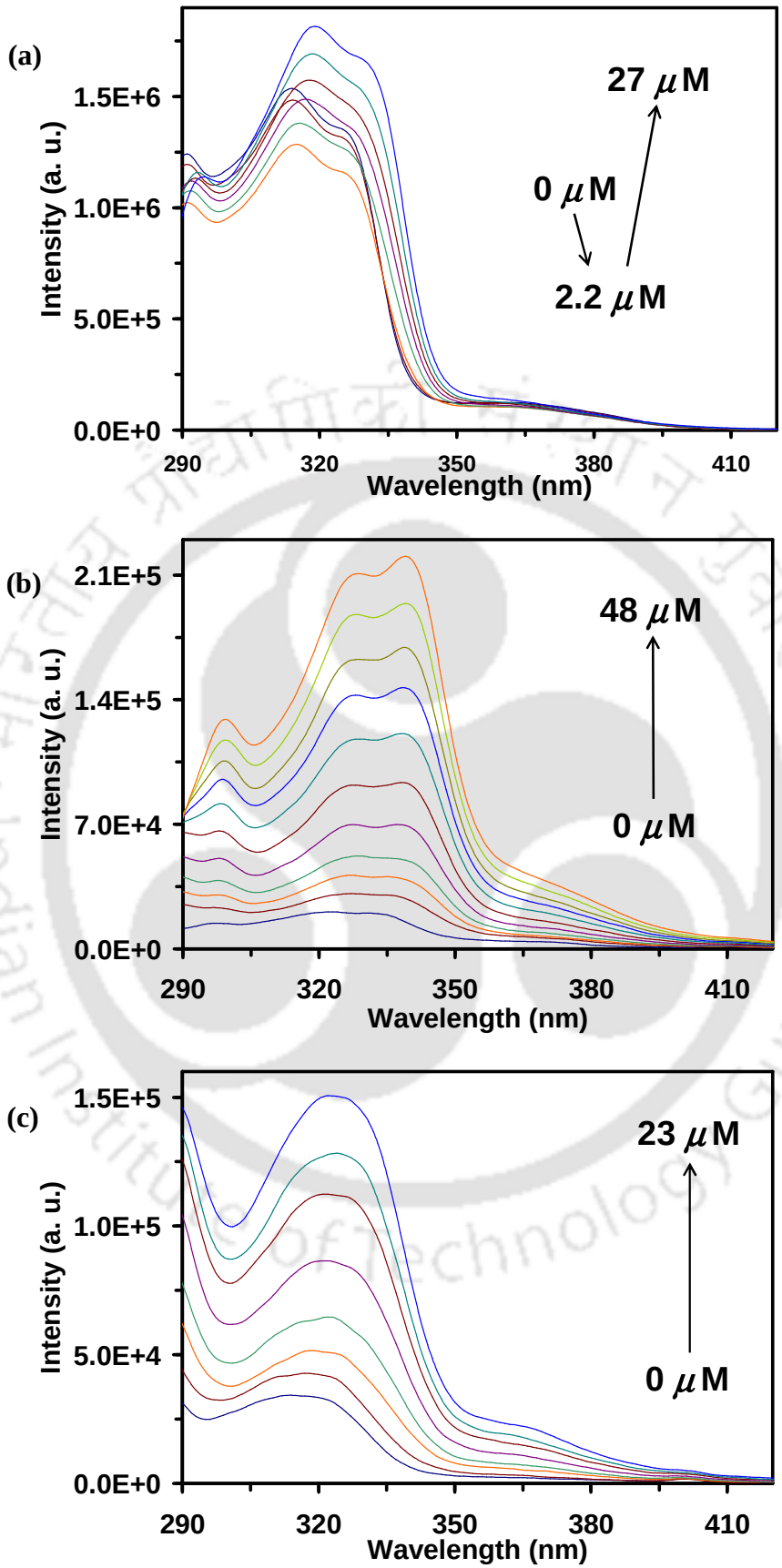

Figure 5.25. Fluorescence excitation spectra of (a) HPBI, (b) HPIP-b, and (c) HPIP-c monitored at the tautomer bands in presence of BSA.

However, in case of HPIP-c the ratio increases with a positive slope upon increase in concentration of BSA. This shows that with increase in concentration of BSA the normal emission becomes more prominent than the tautomer emission. This increase in intensity ratio of HPIP-c indicates that the breaking of cyclic intramolecular hydrogen bonded ring to form *trans*-enol in HPIP-c is facilitated in BSA. This may be due to hydrogen bonding of the guest molecule with the amino acid residues of BSA where a proton donor or acceptor is available for hydrogen bonding. In other words, the site of BSA at which the molecule HPIP-c binds favors the formation of *trans*-enol of HPIP-c. Further more, this shows that the hydrophobic sites of BSA at which the molecules HPBI and HPIP-c bind are different. It may be noted that in the former case, *cis*-enol is the favored conformer.

The fluorescence excitation spectra of the fluorophores monitored at the tautomer emission as the function of BSA concentration is more interesting (**Figures 5.25**) than that of normal emission (not shown). The excitation spectra of HPBI monitored at the tautomer band are different from those of HPIP-b and HPIP-c in the sense for initial addition of BSA up to 2.2 μM, the intensity of the band in HPBI decreases (**Figures 5.25a**). For further addition of BSA, the intensity increases with increase in BSA concentration. However, the fluorescence excitation spectral intensities of HPIP-b and HPIP-c gradually increase with increase in BSA concentration (**Figures 5.25b** and **5.25c**). Even in the absence of BSA the excitation spectra of HPBI has a shoulder at ~ 360 nm and its intensity increases with increase in BSA concentration. On the other hand, in the excitation spectra of HPIP-b and HPIP-c no such shoulder are observed in absence of BSA, but a shoulder emerges on red side of the spectrum in both HPIP-b and HPIP-c with addition of BSA. The new band gains intensity with addition of BSA.

As the main excitation band is due to *cis*-enol, to understand the red end shoulder, the fluorescence spectra were obtained by excitation at the red end shoulder (**Figure 5.26**). HPBI has a new emission band at 440 nm in water and the intensity of the band increases with increase in BSA concentration. Addition of BSA shifts the emission maximum of HPIP-b to red side and new band appears at 443 nm and its intensity enhances with increase in BSA quantity. In HPIP-c, no band is observed in absence of BSA and a band emerges with addition of BSA and its intensity increases with further addition of BSA.

The red side excitation bands and the corresponding fluorescence bands in HPBI can be assigned to zwitterions and in HPIP-b and HPIP-c, they can be assigned to corresponding monoanions. These assignments are based on the following facts: (i) The red side

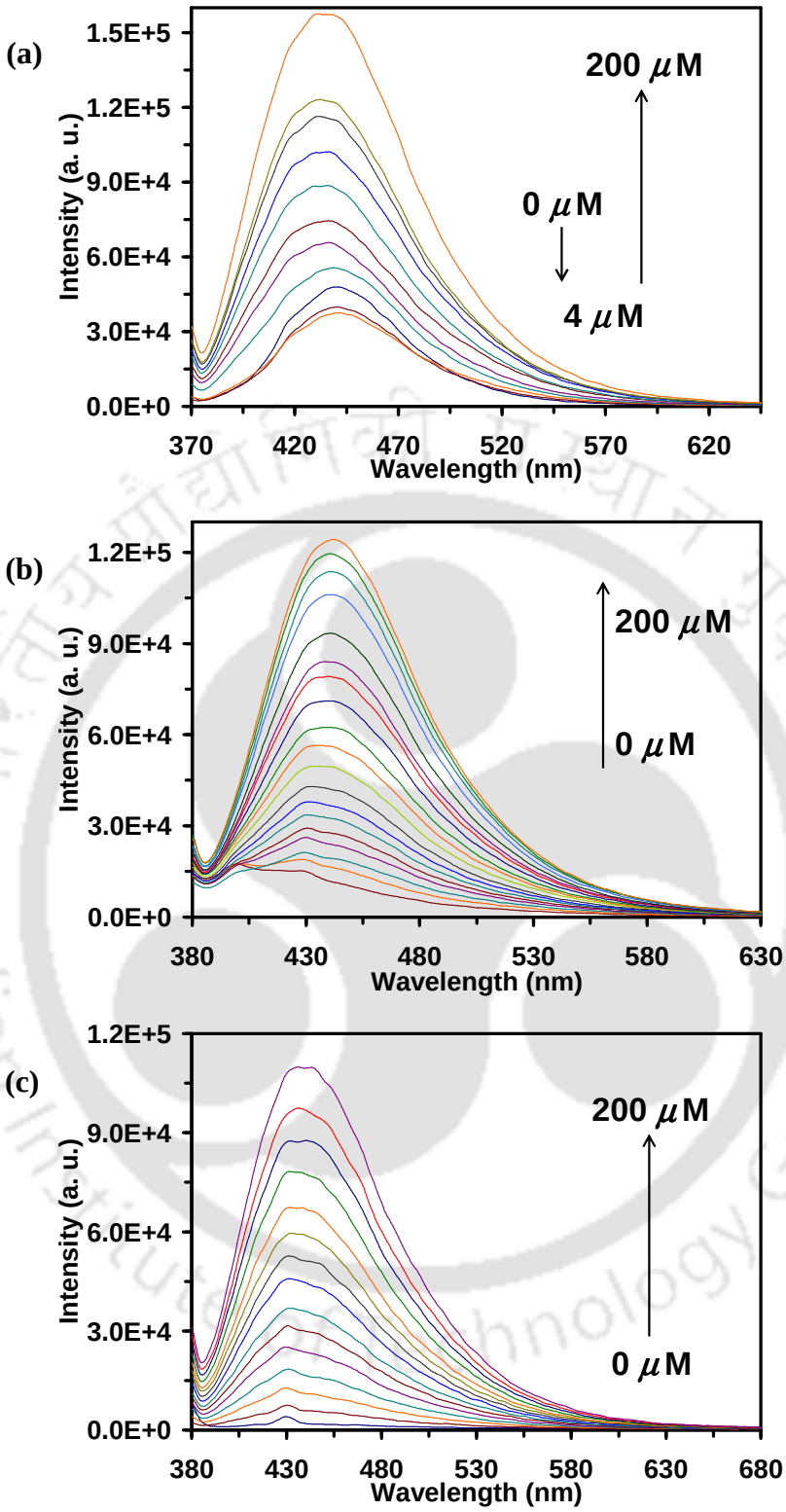

Figure 5.26. Fluorescence spectra of (a) HPBI (λ_{exc} = 365 nm), (b) HPIP-b (λ_{exc} = 375 nm), and (c) HPIP-c (λ_{exc} = 375 nm) in presence of BSA.

fluorescence spectral band maximum (440 nm) is red shifted compared to monoanion of HPBI. (ii) Sinha and Dogra reported the formation of zwitterions in aqueous medium at pH 6,[95] and the fluorescence maximum of the observed zwitterions agree well with that of

Table 5.3. Fluorescence excitation (λ_{max}^{exc} nm) and emission (λ_{max}^{fl} nm) band maxima of the red shifted band.

Solution	λ_{max}^{exc}	λ_{max}^{fl}
HPBI		
0 μM	362	441
27 μM	360	440
Monoanion in water[95]	304, 228	410
Zwitterion[95]		440
HPIP-b		
0 μM	-	-
48 μM	~ 365	443
Monoanion in water[6]	360	461
Monoanion in DMSO	369	421
HPIP-c		
0 μM	-	-
23 μM	366	439
Monoanion in water	351	438
Monoanion in DMSO	363	433

fluorescence spectrum obtained by excitation at 365 nm in case of HPBI and 375 nm in case of HPIP-b and HPIP-c (**Table 5.3**). (iii) However, formation of zwitterions was not observed for pyridine nitrogen substituted analogues in any environment.[6,174,175] (iv) The pK_a value for neutral-monoanion equilibrium of HPBI is very high (~ 10), whereas those of HPIP-b (8.6) and HPIP-c (9.3) are relatively small. The pK_a value is expected to decrease inside the protein, due to interaction of phenolic –OH group with amino acid residues of proteins, as found in β-CD (**Section 5.1**). (v) The fluorescence excitation and emission spectral maxima of the new red side band of HPIP-b and HPIP-c also in reasonable agreement with those of corresponding monoanions (**Table 5.3**). Small discrepancy in the excitation and emission spectral maxima may be due to effect from the environment.

5.3.3. Binding Constants

The association constants for the binding of the ligands with BSA protein were determined from the fluorescence emission data by using the Benesi-Hildebrand equation (**Equation 5.1**).[366,367] The emission intensities of the tautomer emission at 455 nm, 484 nm and 472 nm are used for the Benesi-Hildebrand plot of HPBI, HPIP-b and HPIP-c, respectively. The Benesi-Hildebrand plots (**Figure 5.27**) obtained with good linear correlations of R^2 = 0.99 confirm the formation of 1:1 inclusion complexes between the fluorophores and BSA protein. The binding constants of HPBI, HPIP-b and HPIP-c with BSA protein are 14.3 x 10^3 M^{-1}, 14.9 x 10^3 M^{-1} and 4.0 x 10^3 M^{-1}, respectively. It is difficult to explain the trend in the binding constant values due to the complicacy of the complexes.

However, the possible reason could be that HPBI is more hydrophobic than HPIP-c; and the hydrophobicity plays greater role than hydrogen bonding at the hydrophobic binding sites at which HPBI and HPIP-c bind. On the other hand, HPIP-b binds strongly with the binding site through hydrogen bonding which has greater impact than hydrophobicity.

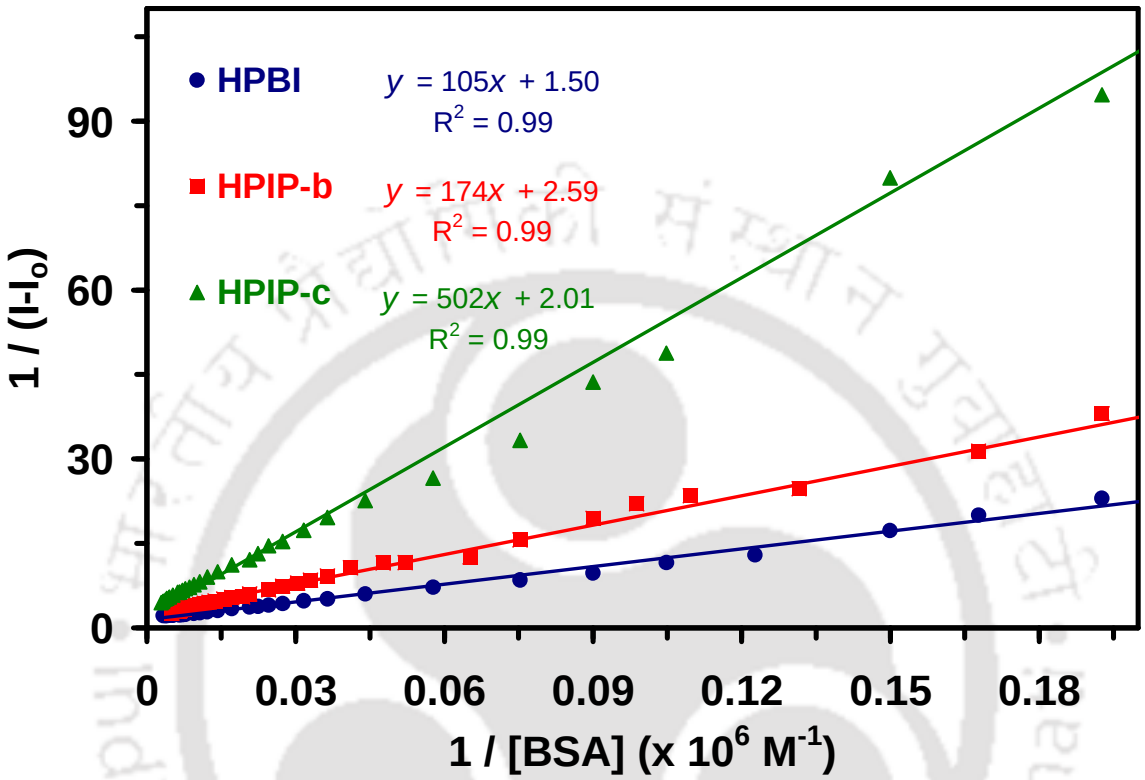

Figure 5.27. Benesi-Hildebrand plot for the HPBI (●), HPIP-b (■), and HPIP-c (▲).

5.3.4. Conclusion

Study on interaction of the fluorophores with BSA is reported. All three fluorophores form 1:1 complexes with BSA. The fluorescence of both normal and tautomer bands increase substantially in BSA. However, the intensity ratios of normal to tautomer bands of HPBI and HPIP-b decrease, but that of in HPIP-c increases in BSA. HPBI and HPIP-c bind in the hydrophobic site of BSA. On the other hand, HPIP-b binds at the hydrophilic site of BSA. Although both HPBI and HPIP-c bind at hydrophobic sites, their binding pockets and interaction with BSA are different. Further docking studies are required to identify the exact location of the fluorophores. In addition to *cis*- and *trans*-enolic forms, HPBI is present in the zwitterionic form, whereas HPIP-b and HPIP-c are present as monoanion in addition to *cis*- and *trans*-enols in the ground state. In the excited state also along with tautomer and enol forms, HPBI and its pyridine nitrogen analogues are present in the zwitterionic form and the monoanionic form, respectively.

Chapter 6

Excited State Intramolecular Proton Transfer and Rotamerism in 2-(2'-Hydroxyphenyl)-3*H*-oxazo[4,5-*b*]pyridine

6.0. Introduction

o-Hydroxyphenylbenzazoles[50,52,67,95,98,99,102,123,256,257,259,261,269-274,276-278,281,420-442] HPBI, HPBO and HPBT have been studied extensively due to ESIPT exhibited by them and their high fluorescence and large Stokes shift of the ESIPT products. This class of compounds have wide applications as lasers, probes, sensors and electronic devices.[95,123,269,444,445] These *o*-hydroxyphenylbenzazoles have similarities in terms of molecular structures and the ESIPT processes they undergo. However, they have markedly difference in some of their photophysical characteristics such as quantum yields and lifetimes, and amongst the three molecules HPBI has the highest yield.[98,123,269]

As mentioned earlier, these molecules exist in the ground state in two rotameric forms *cis*-enol and *trans*-enol.[52,123] In HPBO, the *trans*-keto rotamer, which is the *trans* conformer of the proton transferred tautomer formed by torsion rotation of 180° is also detected in the ground state.[102] Formation of open enol is also suggested in protic solvents.[1,123] As discussed earlier, different rotameric and isomeric forms are also possible for HPBI (**Sections 3.1.2** and **3.2.2**). In recent years, studies on the pyridine nitrogen sustituted analog of HPBI have gained momentum.[279] The role of nitrogen substitution in HPBI on ESIPT and rotamerism was discussed theoretically and experimentally in detail earlier sections. As discussed, these compounds have low quantum yield due to enhanced nonradiative decay through proton coupled charge transfer. Some of the photophysical properties of HPIP-b are similar to those of HPBI and HPBO (**Section 3.1.2**).

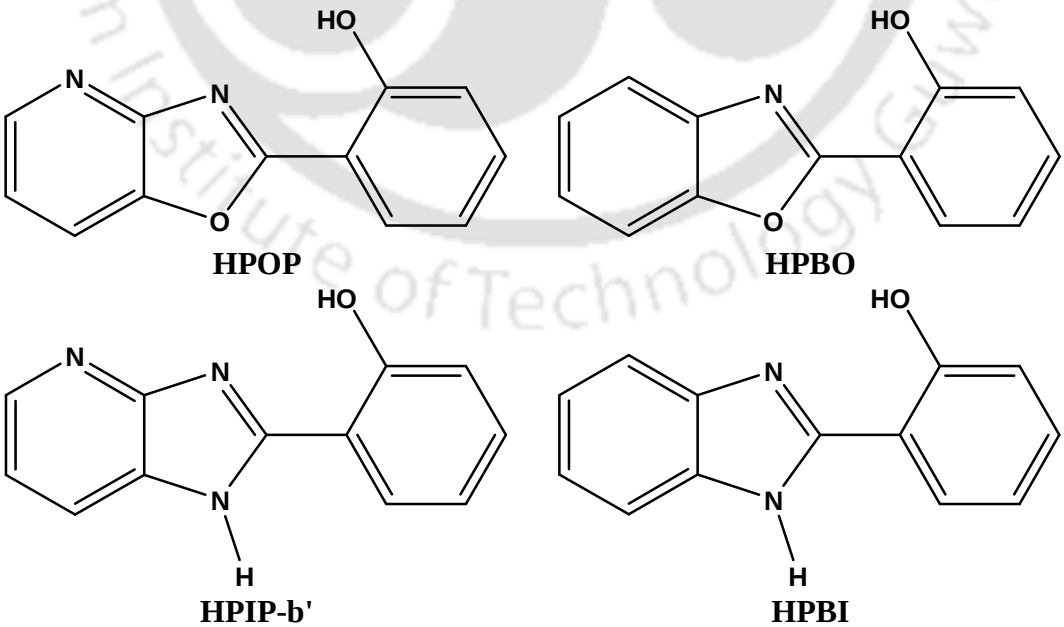

Chart 6.1. Nitrogen Substituted Analogues of HPBI and HPBO.

To the best of the author's knowledge, studies on pyridine nitrogen substitution on HPBO are not reported yet. Thus, the nitrogen subsituted analogue of HPBO, 2-(2'-hydroxyphenyl)-3*H*-oxazo[4,5-*b*]pyridine (HPOP, **Chart 6.1**) was synthesized and its photophysical characteristics were studied in different solvents, pH and temperatures. HPOP is a nitrogen substituted analogue of HPBO and the structure of HPOP resembles that of HPIP-b' (**Chart 6.1**), where in the present molecule the nitrogen in position 3 is replaced by oxygen.

The chapter is divided into three sections. The first section deals with the study of photophysical properties of HPOP in different solvents. Temperature effect on photophysical properties of HPOP are presented in the second section. The effect of pH on the absorption and fluorescence spectra is discussed in the third section.

6.1.0. Effect of Solvents

6.1.1. Absorption Spectra

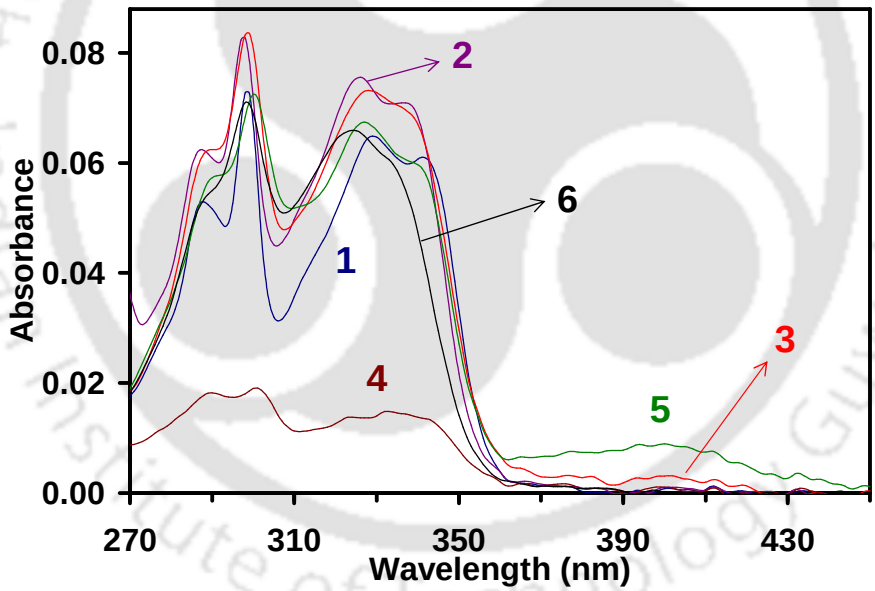

Figure 6.1. UV-visible absorption spectra of HPOP in (1) cyclohexane, (2) ethyl acetate, (3) methanol, (4) glycerol, (5) dimethylsulfoxide, and (6) water (pH ~ 7.2).

Figure 6.1 shows the representative UV-visible absorption spectra of HPOP in selected solvents. The absorption peaks and their molar absorption coefficient in different solvents are summarized in **Table 6.1.** In general, HPOP has four vibronic absorption peaks at 287-289 nm, 297-301 nm, 324-329 nm and 334-342 nm regions in all solvents. The well resolved vibronic structures indicate coplanarity of the phenolic and oxazopyridine rings and the rigidity of the molecular structure. The two shorter wavelength peaks of HPOP are similar

to those found in benzimidazole,[447,448] 2-phenylbenzimidazole[308,449] and benzoxazole.[450] The two longer wavelength bands in HPOP are red shifted compared to benzimidazole and benzoxazole and are observed in all the solvents studied. The bathochromic shift is due to intramolecular hydrogen bond formation which increases the conjugation between the phenolic and oxazopyridine rings.

Table 6.1. UV-Visible absorption band maxima (λ_{max}[ab], nm) and molar absorption coefficient in Log ε_{max} of HPOP in different solvents.

Solvent	Dielectric Constant	λ_{max} (Log ε_{max})
Cyclohexane[a]	2.02	288 (3.70), 299 (3.86), 329 (3.81), 342 (3.79)
1,4-Dioxane	2.21	288 (3.80), 299 (3.93), 327 (3.90), 338 (3.88)
Toluene	2.48	287 (4.10), 299 (3.99), 329 (3.86), 341 (4.82)
Chloroform	4.81	289 (3.79), 299 (3.92), 329 (3.89), 341 (4.85)
Ethyl Acetate	6.02	287 (3.79), 298 (3.92), 326 (3.88), 338 (4.85)
Tetrahydrofuran	7.6	287 (3.80), 298 (3.92), 326 (3.88), 340 (3.85)
1-Butanol	17.8	289 (3.75), 298 (3.89), 329 (3.82), 342 (3.79)
1-Propanol	20.1	289 (3.75), 298 (3.89), 329 (3.82), 342 (3.79)
Ethanol	24.6	288 (3.79), 297 (3.90), 328 (3.83), 340 (3.81)
Methanol	32.63	289 (3.79), 299 (3.93), 328 (3.87), 338 (3.84)
N,*N*-Dimethylformamide (DMF)	36.7	289 (3.76), 298 (3.89), 326 (3.88), 339 (3.84)
Acetonitrile	37.5	287 (3.76), 297 (3.89), 324 (3.85), 335 (3.83)
Glycerol	42.5	289 (3.26), 301 (3.28), 327 (3.15), 342 (3.15)
DMSO	47	289 (3.76), 300 (3.86), 327 (3.83), 341 (3.77), 400 (2.95)
Water (pH ~ 7.2)	78.54	288 (3.73), 299 (3.85), 324 (3.84), 334 (3.78)

[a]The solution in cyclohexane is saturated.

HPOP in DMSO has an additional broad absorption band at 400 nm. The existence of tautomer or monoanionic species in the ground state may account for the occurrence of this extra band in DMSO (see later). The 400 nm broad absorption band is also observed in protic solvents but the absorbance is very weak (absorbance less than 0.005 at 10 μM HPOP).

6.1.2. Fluorescence Emission Spectra

HPOP exhibits dual fluorescence in all the solvents (studied). The fluorescence characteristics of HPOP are similar to those observed in HPBI, HPBO, and HPIP-b the isomeric form of HPIP-b'.[6,50,52,67,95,97-99,102,123,174,259,261,279-281] The shorter wavelength emission (normal emission) is due to the excited *trans*-enol that exists already in the ground state. The red-shifted emission band is due to the emission from keto structure that formed after ESIPT, which is characterized by its large Stokes' shift from the absorption band of the molecule.[6,95,99,174,175,255-258] The fluorescence emission maxima and quantum yields of normal and tautomer bands of HPOP are compiled in **Table 6.2** and representative normalized fluorescence emission spectra of HPOP in selected solvents are shown in **Figure 6.2**. The

Table 6.2. Fluorescence maxima (λ_{flu}, nm) and quantum yields of normal and tautomer emissions of HPOP in different solvents, λ_{exc} = 300 nm.

Solvent	λ_{em}^{N}	Φ_N	λ_{em}^{T}	Φ_T	Φ_T / Φ_N
Cyclohexane	340, 358, 373	0.0035	516	0.0077	2.2
1,4-Dioxane	364, 377	0.0093	497	0.0033	0.35
Chloroform	370	0.0028	498	0.0091	3.18
Ethyl acetate	363, 374	0.0035	508	0.0028	0.8
1-Butanol	385	0.0073	467	0.0236	3.23
1-Propanol	386	0.0066	465	0.0254	3.85
Ethanol	386	0.0061	462	0.0229	3.75
Methanol	390	0.0032	464	0.0209	6.53
DMF	385	0.0255	473	0.0131	0.52
Acetonitrile	380	0.0051	452	0.0145	2.84
Glycerol	389	0.0901	499	0.0803	0.89
DMSO	386	0.0461	472	0.0852	1.85
Water	389	0.0007	491	0.0014	1.97

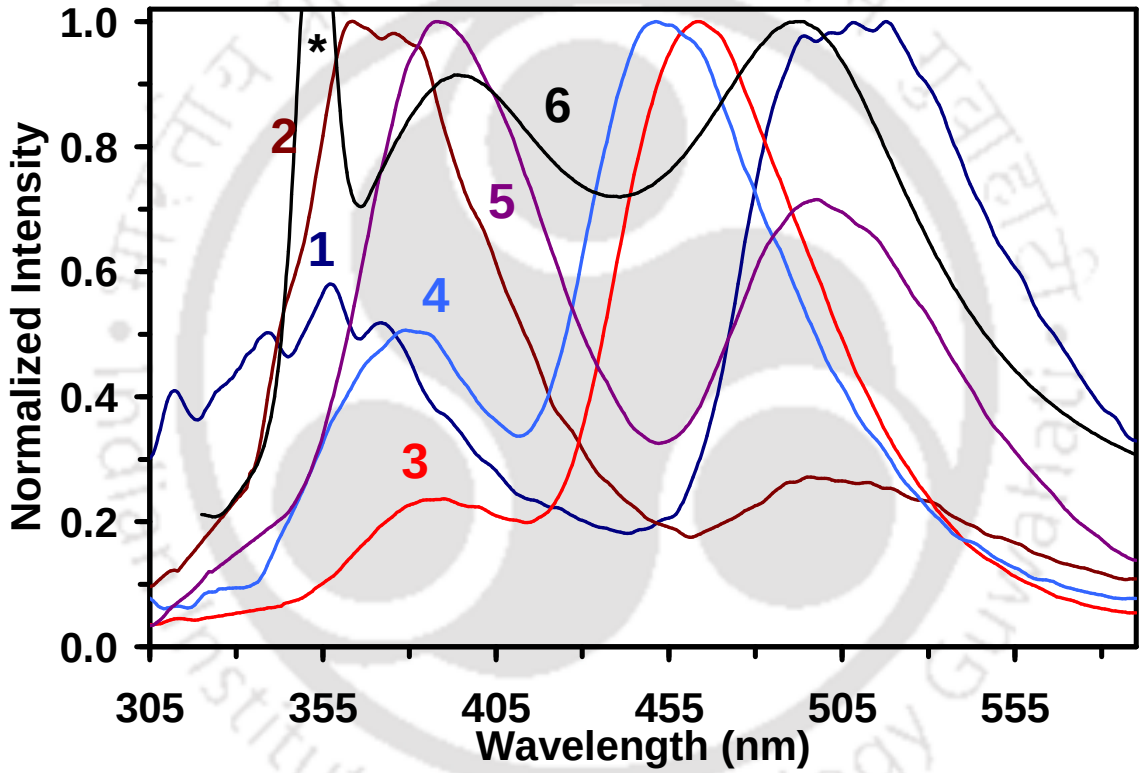

Figure 6.2. Normalized fluorescence spectra of HPOP excited at 300 nm in (1) cyclohexane, (2) 1,4-dioxane, (3) methanol, (4) acetonitrile, (5) glycerol, and (6) neutral (pH = 6.43). λ_{exc} = 300 nm (λ_{exc} = 315 nm for neutral solution). Water Raman band is denoted by *.

normal band of HPOP is structured in non-polar solvents cyclohexane, dioxane and ethyl acetate. Compared to HPBI,[95] HPBO,[433] and HPIP-b[174] the normal band of HPOP is more red-shifted in polar solvents although the tautomer emissions of the fluorophores fall almost in the same region. The red shift in the normal band is because of the greater conjugation between the phenolic and oxazopyridine rings due to increase in electronegativity of the oxazopyridine ring. **Figure 6.3** shows the effect of excitation wavelength in acetonitrile as

representative plot. The relative intensity of the tautomer band increases with λ_{exc}.

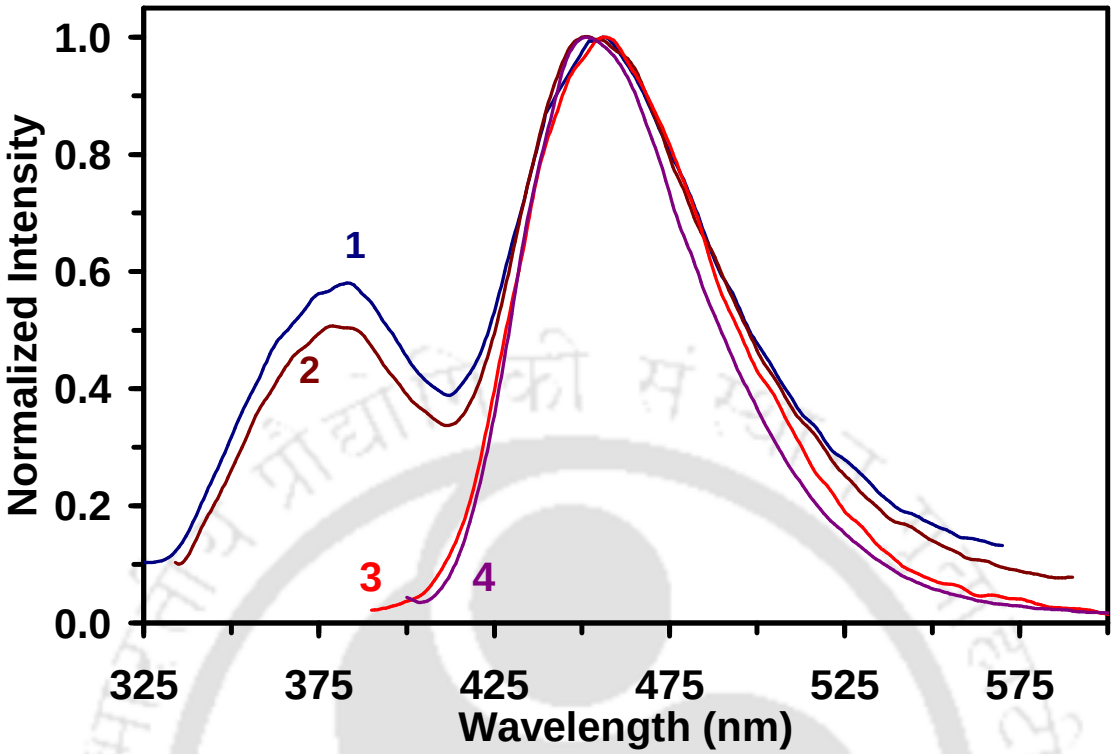

Figure 6.3. Normalized fluorescence spectra of HPOP in acetonitrile (1) λ_{exc} = 290 nm, (2) λ_{exc} = 300 nm, (3) λ_{exc} = 375 nm, and (4) λ_{exc} = 395 nm.

Compared to HPBO and HPIP-b, HPOP has lower quantum yield.[6,123,174,450] In HPBO[123] and HPIP-b (**Section 3.1**), formation of ICT state by torsion rotation of the phototautomer acts as the major nonradiative decay pathway that leads to decrease in the fluorescence quantum yield. Substitution with the electronegative atom in the aromatic ring generally favors the ICT from the phenolic ring to the aromatic ring.[174,175] Therefore, formation of ICT state could have been favored more in HPOP due to substitution by more electronegative atoms. This is consistent with the fact that the quantum yield of the tautomer follows the order HPBO > HPIP-b > HPOP.

6.1.3. Fluorescence Excitation Spectra

The excitation spectrum of HPOP in all the solvents monitored at the normal band is different from the one recorded at the tautomer band. The difference is well observed in non-polar solvents. The excitation spectra monitored at the normal bands are blue shifted with respect to those recorded at the tautomer bands. This indicates the normal and tautomer bands originate from two distinct ground state species and they can be assigned to *trans*-enol and *cis*-enol, respectively.

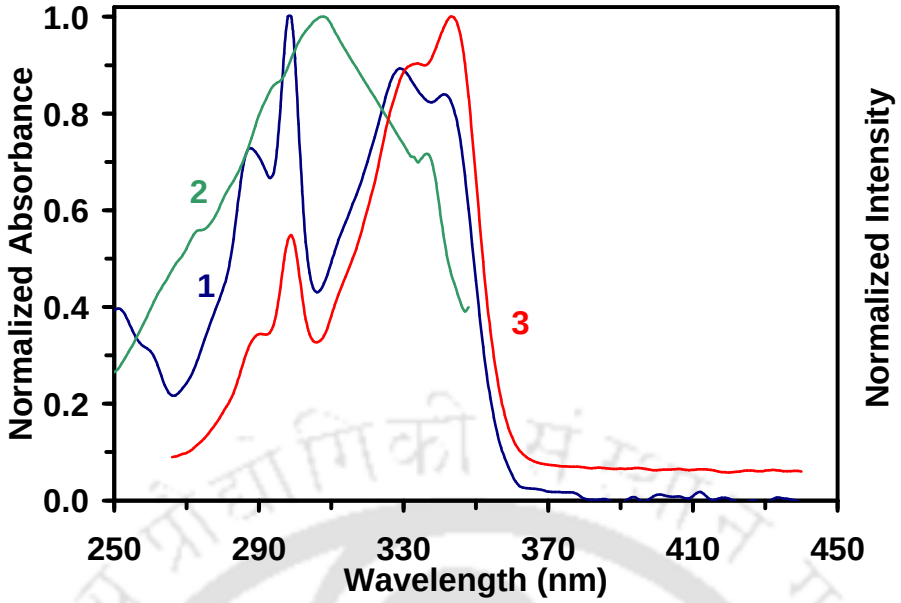

Figure 6.4. Normalized (1) absorbance, and fluorescence excitation spectra of HPOP in cyclohexane monitored at (2) normal (355 nm), and (3) tautomer (517 nm) bands.

Figure 6.4 shows the normalized absorbance and the excitation spectra of HPOP in non-polar cyclohexane. In non-polar solvents, the spectra recorded at tautomer band resembles better with the corresponding absorption spectra indicating that the species responsible for the tautomer band, which is the *cis*-enol, is the major component present in the ground state.

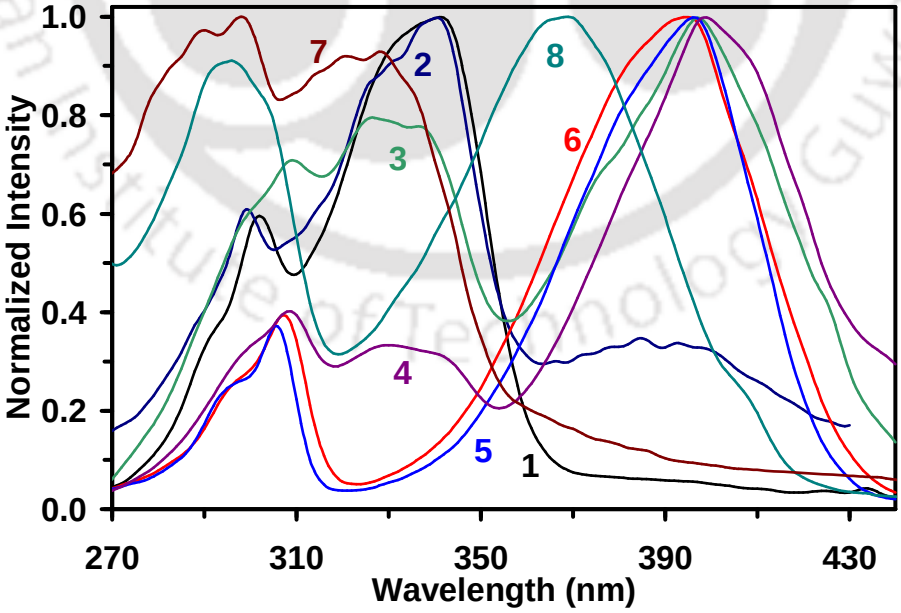

Figure 6.5. Normalized fluorescence excitation spectra of HPOP in (1) glycerol, (2) 1,4-dioxane, (3) DMF, (4) DMSO, (5) acetonitrile, (6) methanol, (7) in water (pH ~ 6.43) monitored at the tautomer band, and (8) in water (pH ~12.93) monitored at the monoanion emission.

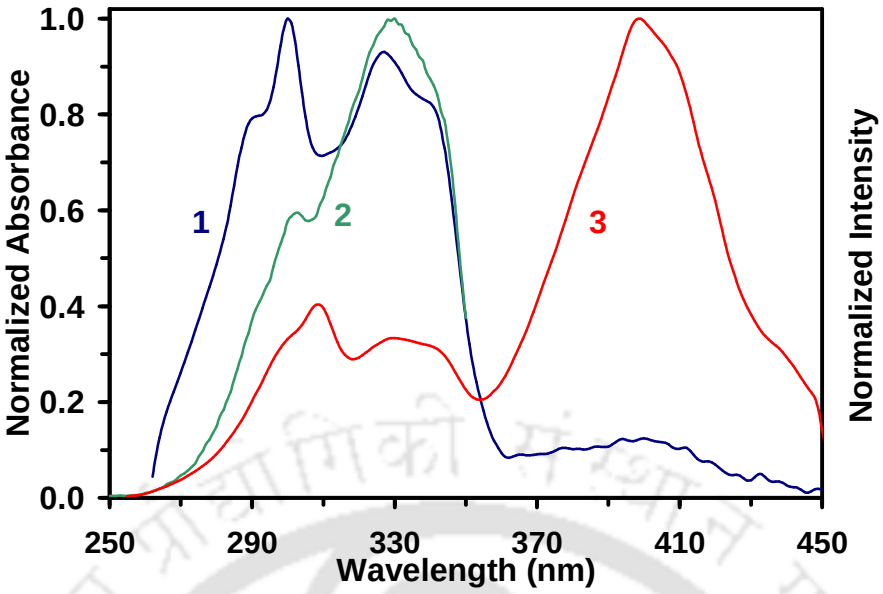

Figure 6.6. Normalized (1) absorbance and fluorescence excitation spectra of HPOP in DMSO monitored at (2) normal (387 nm), and (3) tautomer (480 nm) band.

The normalized fluorescence excitation spectra of HPOP in dioxane and polar solvents monitored at the tautomer band are shown in **Figure 6.5**. In DMF, DMSO as well as in dioxane (along with the band in the other solvent) a new longer wavelength band appeared (maxima in the range 385-400 nm). The maxima of the new band of the excitation spectra match with the tail band (400 nm) observed in the absorption spectrum of HPOP in DMSO (**Figure 6.6**). These observations indicate that in DMF, DMSO and dioxane apart from *cis*- and *trans*-enols, one more distinct species is present in the ground state. Although no clear band was observed in the absorption spectra in acetonitrile and alcohols, the excitation spectra clearly establish that in these solvents also, two ground state species are responsible for the long wavelength emission (**Figure 6.6)**. The relative population of these two species varies with solvents.

6.1.4. Binary Solvent Mixtures

To get further insights on the two species and three species equilibria and the photophysical properties, the absorption and the fluorescence characteristics of HPOP were also studied in binary solutions, water/glycerol and acetonitrile/DMSO mixtures where two and three ground state species, respectively, are present. A hypochromic effect is observed in the absorption spectra of HPOP in water with increase in composition of glycerol in the binary mixture (**Figure 6.7)**. The absorption band is red shifted from 324 nm in pure water to 327 nm in 100% of glycerol.

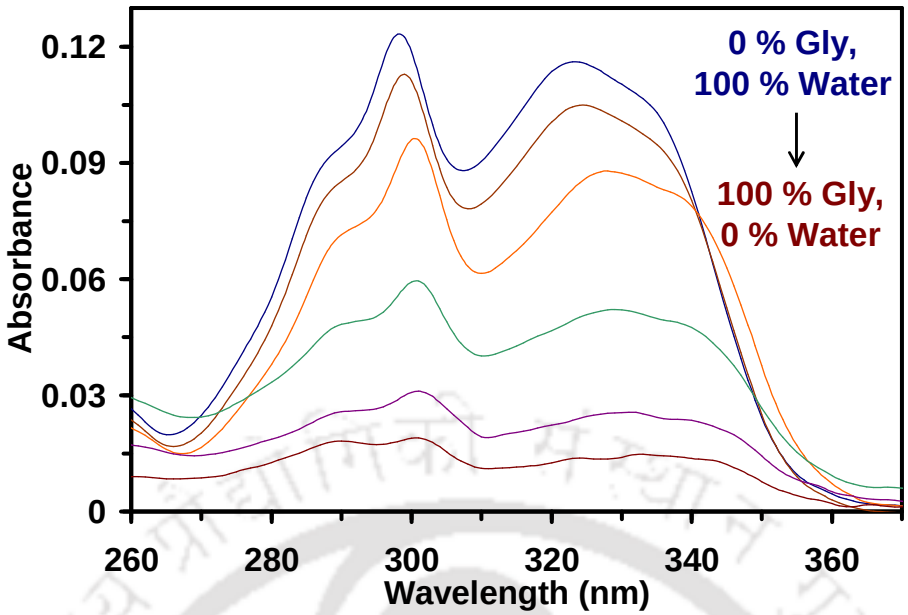

Figure 6.7. UV-Visible absorption spectra of HPOP in water/glycerol binary solutions.

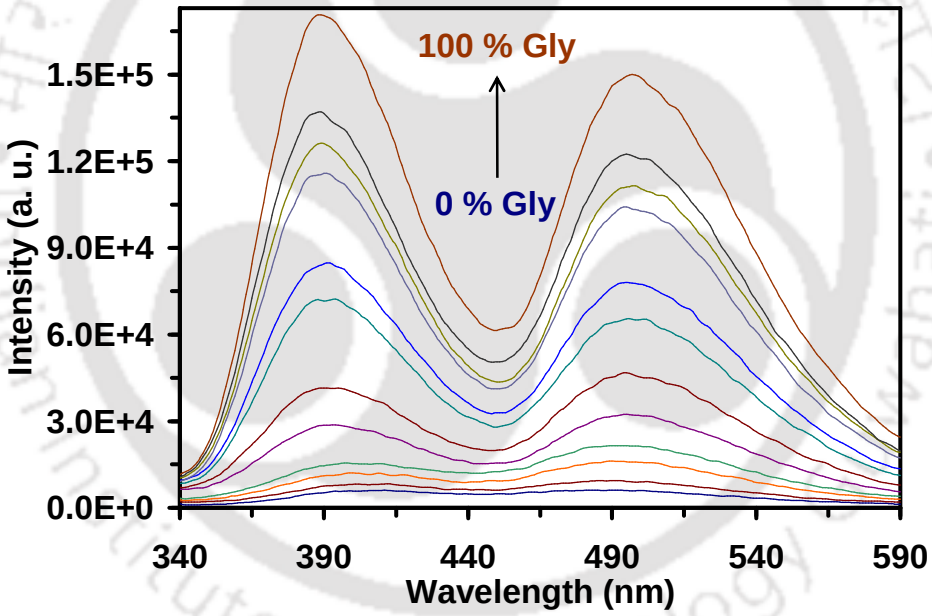

Figure 6.8. Fluorescence spectra of HPOP in water/glycerol binary solutions.

In water/glycerol binary solution, both the normal and tautomer emissions of HPOP increase with increase in concentration of glycerol in water (**Figure 6.8**). The emission maxima of the normal emission is gradually blue shifted on increasing the composition of glycerol from 398 nm (in water) to 391 nm (in 100 % glycerol) while that of tautomer emission is red shifted from 492 nm to 497 nm. The shifts are due to decrease in the polarity of the surrounding environment around HPOP molecule. Such shifts with increase in polarity are often observed in ESIPT molecules.[25]

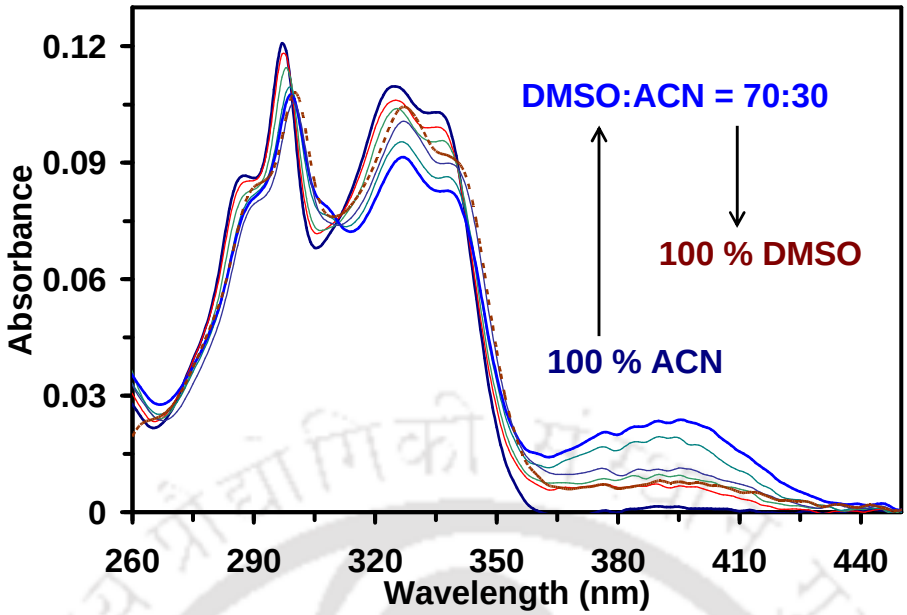

Figure 6.9. UV-Visible absorption spectra of HPOP in acetonitrile/DMSO binary solutions.

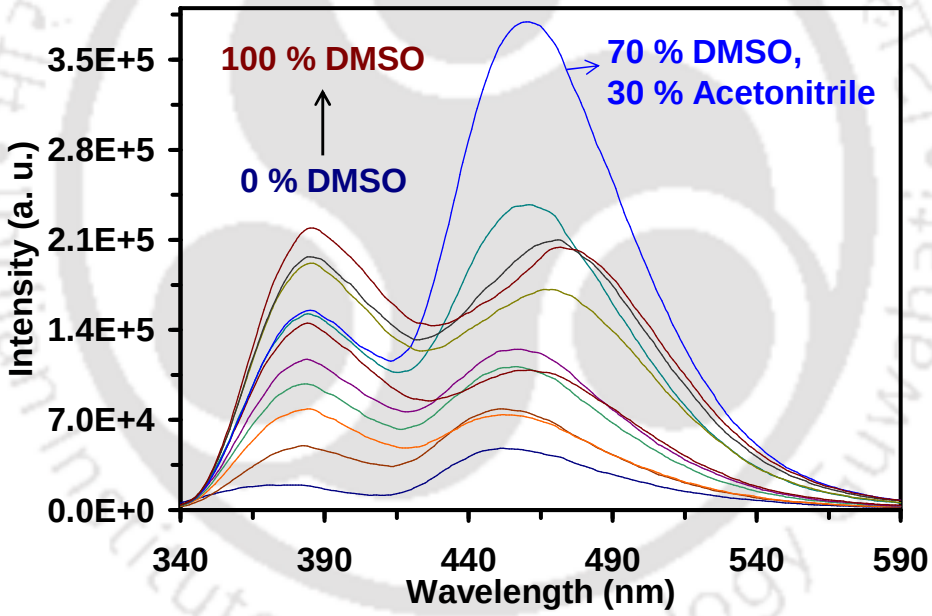

Figure 6.10. Fluorescence spectra of HPOP in acetonitrile/DMSO binary solutions. λ_{exc} = 300 nm.

With increase in concentration of DMSO in acetonitrile/DMSO mixture, there is a red shift in the absorption spectrum (297, 324 and 335 nm) of HPOP in acetonitrile with a decrease in absorbance. In addition, a new broad band emerges at 396 nm with gradual increase in composition of DMSO. A quasi-isosbestic point is also found at 343 nm till the composition of DMSO reaches 70 % in the binary solvent mixture (**Figure 6.9)**. At 70 % of DMSO, the band at 396 nm reaches the maximum. On further increase in composition of

DMSO the absorbance of 396 nm band decreases and that of structured shorter wavelength band increases.

In acetonitrile/DMSO binary solution, although the intensity of the normal emission increases with increase in composition of DMSO (**Figure 6.10**), the increase in intensity of the tautomer emission is more until it reaches the maximum at 70 % DMSO. Same as the absorption band at 396 nm, the fluorescence intensity of the tautomer also decreases with further increase in amount of DMSO. This suggests that the 70 % DMSO is the most favorable composition for red shifted ground state species. This also indicates that the species responsible for the 396 nm band is preferentially more solvated in DMSO. It appears that at higher concentration this preferential solvation cluster is disturbed.

6.1.5. Ground State Tautomer

As reported earlier (**Section 5.1.2**)**,** HPIP-b and HPIP-c form monoanion in DMSO. DMSO acts as proton acceptor and the resulting monoanion formed is stabilized by solvation. However in HPOP, the longer wavelength excitation band at 396 nm may be assigned to the tautomer that is formed in the ground state rather than to the monoanion. The proposition that the ground state species is the tautomer form is based on the following observations. (i) The tautomer emits at 491 nm in water while the monoanion emits at 471 nm (see later). The fluorescence maximum in acetonitrile when excited at 395 nm matches with that of the tautomer emission rather than the monoanion (**Figure 6.3**). (ii) The relative intensity of the tautomer increases until the absorbance of the 396 nm band increases (i.e. 70 % of DMSO in DMSO/acetonitrile mixture) and decreases with decrease in absorbance of the 396 nm band. (iii) The excitation spectrum of the monoanionic form of HPOP in basic methanol does not coincide with the longer wavelength excitation band (396 nm) of HPOP in methanol (**Figure 6.11**).

The enolic forms in a number of hydroxyarylbenzimidazoles are reported to be in equilibrium with the tautomeric form in the ground state.[54,451,452] The enolic and tautomeric forms of 2-(3'-hydroxy-2'-pyridyl)benzimidazole have almost the same energy and are in equilibrium in water although it exists only as the enol in nonaqueous solution.[54] Although in aprotic solvents, 2-(4'-amino-2'-hydroxyphenyl)benzimidazole and its alkyl substituted derivatives exist in planar *cis*-enol form, they are found to be present in enol and tautomer forms in protic solvents.[451] 2-(1'-hydroxy-2'- naphthyl)benzimidazole exists as cis-enol form in apolar solvents, but an equilibrium between *cis*- and *trans*-enolic forms and tautomer is

observed in ethylene glycol, glycerol and 40 % ethanol in water.[452] In glycerol, just as in non-polar solvents, *cis*- and *trans*-enols are the species found in the ground state with *cis*-enol as the major component. Ground state tautomer species are not observed in glycerol. Recently, Sekiya et al. observed tautomer form in the ground state of HPBI in two of its polymorphic crystalline forms.[279]

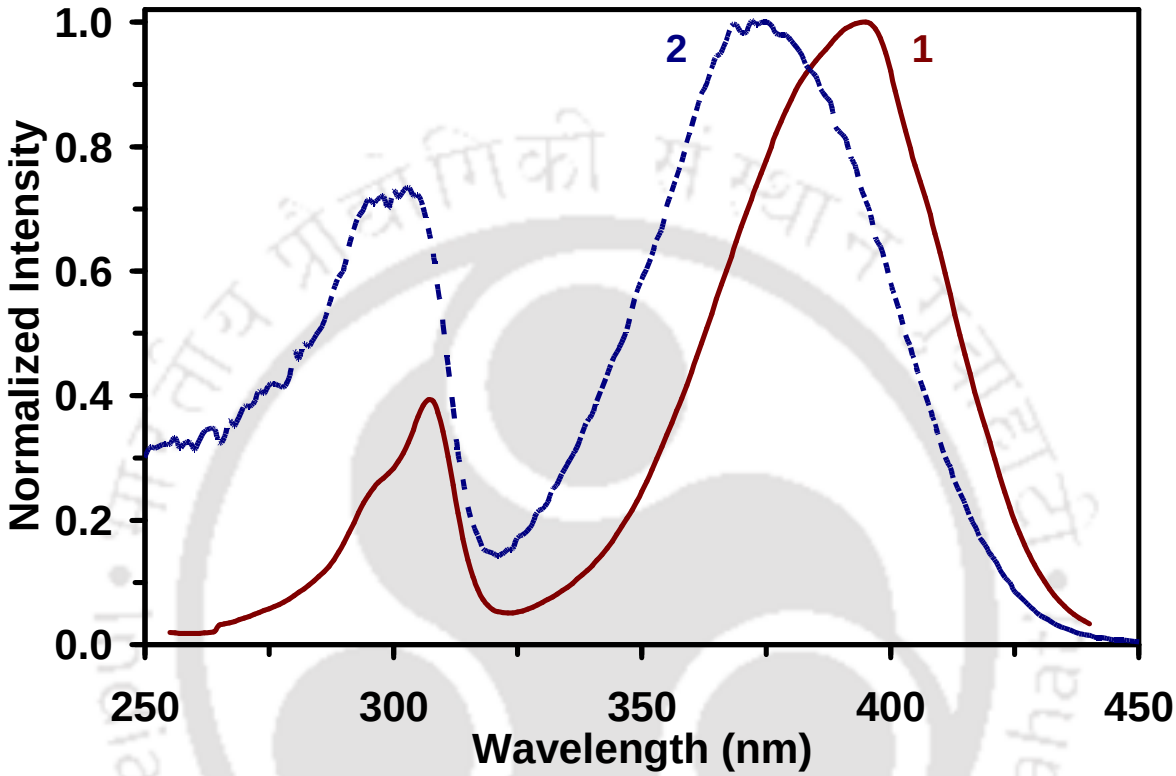

Figure 6.11. Normalized fluorescence excitation spectra of (1) neutral (λ_{em} = 464 nm), and (2) monoanionic (λ_{em} = 481 nm) forms of HPOP in methanol.

6.1.6. Time Resolved Fluorescence Measurements

Using the LED 308 nm and Laser Diode 375 nm as light sources, the lifetimes of the normal and tautomer bands are measured (**Table 6.3)**. Due to weak fluorescence, the lifetime could not be measured in a few solvents. In dioxane and propanol monoexponential decays are observed when monitored at the normal band emission maxima with a slit width of 20 nm. In other solvents, when monitored at the normal band emission maxima with same slit width, biexponential decays are observed. However, the longer lifetime values match with those lifetime of the values of tautomer. Therefore, it can be inferred the observed bi-exponential decay is due to overlap of the normal and tautomer emissions. In the case of tautomer emission single exponential is observed in all the solvents except glycerol. In glycerol, biexponential is observed where the shorter lifetime value matches with the shorter

lifetime value when monitored at the normal emission band. The single exponential decay of the longer wavelength emission further substantiates our assignment that the third ground state species is the tautomer. If it would have been the monoanion, one should expect a biexponential decay with two different lifetimes one for the tautomer and other for the monoanion.

Table 6.3. Lifetime values for the normal and tautomer bands of HPOP in different solvents.[a,b]

Solvent	Monitored at λ_{em}^{N}				Monitored at λ_{em}^{T}			
	λ_{em} (nm)	τ_1 (f_1)	τ_2 (f_2)	χ^2	λ_{em} (nm)	τ_1 (f_1)	τ_2 (f_2)	χ^2
Cyclohexane					515	0.17 (100)		1.00
1,4-Dioxane	370	1.90 (100)		1.34	500	2.77 (100)		1.00
1-Butanol	390	1.23 (77.1)	4.8 (22.9)	1.03	475	5.0 (100)		1.15
					470[c]	4.8 (100)		1.36
1-Propanol	380	1.64 (100)		1.19	470	5.0 (100)		1.07
					468[c]	5.1 (100)		1.08
Ethanol	380	0.68 (78.4)	4.6 (21.6)	1.00	470	5.0 (100)		1.09
					470[c]	5.2 (100)		1.03
Methanol	395	0.48 (46.0)	5.0 (54.0)	1.00	465	4.5 (100)		1.03
					470[c]	5.1 (100)		1.00
DMF	385	1.41 (82.3)	3.4 (17.7)	1.00	465	3.6 (100)		1.30
DMSO	385	1.19 (94.8)	4.9 (5.2)	1.09	470	4.7 (100)		1.04
					470[c]	4.9 (100)		1.02
Glycerol	385	1.16 (64)	3.9 (36)		500	3.5 (10)	1.22 (90)	1.00
DMSO/ACN (70/30)					465[c]	5.0 (100)		1.02

[a]Values within parentheses are the relative percentage of the component. [b]λ_{exc} = 308 nm unless otherwise mentioned. [c]λ_{exc} = 375 nm.

The radiative (k_r) and nonradiative (k_{nr}) rate constants calculated from fluorescence quantum yields and lifetime values of HPOP in different solvents are tabulated in **Table 6.4** to understand the effect of solvation on the dynamics of the excited state. The nonradiative decay of the tautomer emission in cyclohexane happens to be very high which is ~ 20 times that in alcohols. The nonradiative decay is higher than the radiative decay in all solvents and is responsible for the low quantum yield nature of the fluorophore.

Table 6.4. Radiative rate (k_r, 10^7 s^{-1}) and nonradiative decay rate (k_{nr}, 10^7 s^{-1}) for the normal and tautomer bands of HPOP in different solvents.

Solvent	Normal Band		Tautomer Band	
	k_r^N	k_{nr}^N	k_r^T	k_{nr}^T
Cyclohexane			4.6	587.2
1,4-Dioxane	0.5	52.1	0.1	36.1
1-Butanol	0.4	48.6	0.5	19.4
1-Propanol	0.4	60.6	0.5	19.5
Ethanol	0.5	76.3	0.5	19.2
Methanol	0.1	34.9	0.5	21.9
DMF	1.5	56.5	0.4	27.3
DMSO	3.4	69.4	1.8	19.5
Glycerol	4.3	43.7	5.6	63.6

6.2.0. Effect of Temperature

6.2.1. Absorption and Emission Spectra

Hypochromic effect is observed in the absorption spectra of HPOP in all the solvents with increase in temperature. **Figure 6.12** shows the representative absorption spectra of HPOP in DMSO at different temperatures. In DMSO, the tautomer absorption peak also decreases with rise in temperature.

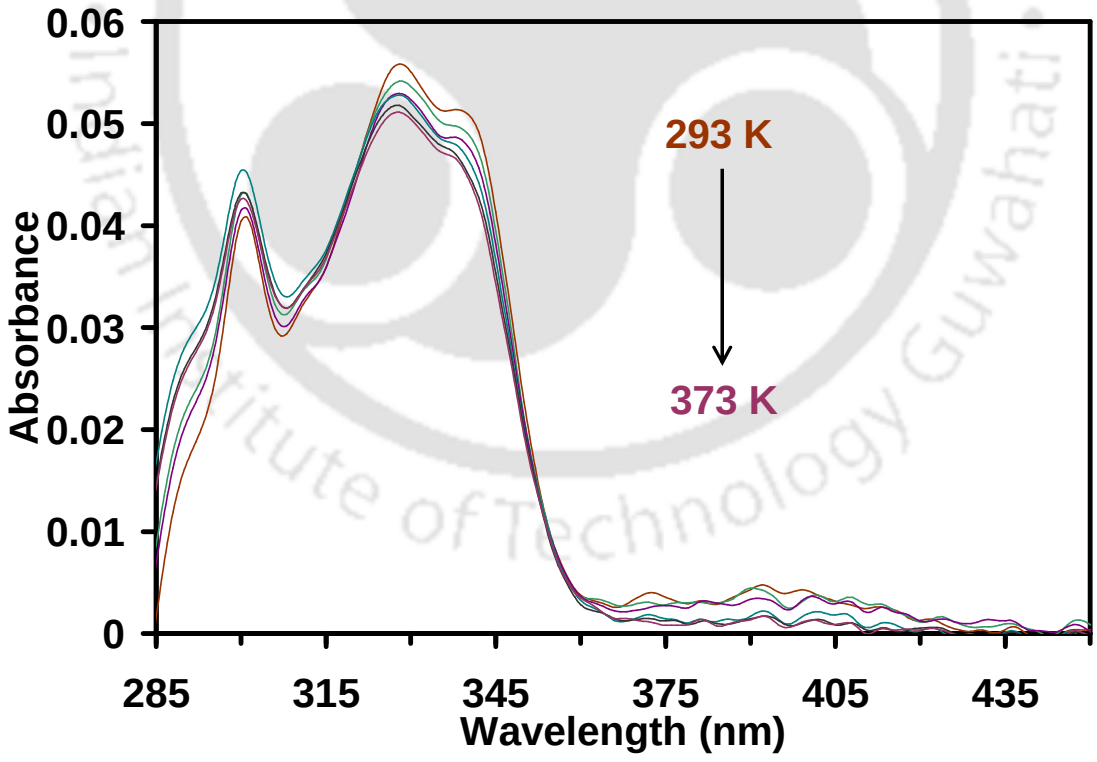

Figure 6.12. Absorption spectra of HPOP in DMSO at different temperatures.

The variation of fluorescence characteristics of HPOP in acetonitrile is different from those in DMF, DMSO and glycerol. **Figure 6.13** shows the fluorescence spectra of HPOP in

acetonitrile at different temperatures. With increase in temperature, the normal emission increases with a blue shift from 383 nm to 375 nm while the tautomer emission decreases with a small blue shift from 456 nm to 451 nm. A quasi isoemissive point is observed at 400 nm indicating a possible existence of equilibrium. The enhancement of the normal emission indicates that the equilibrium shifts towards the *trans*-enol with rise in temperature. The behavior is same as that of HPBI and other analogues (**Section 3.3**).

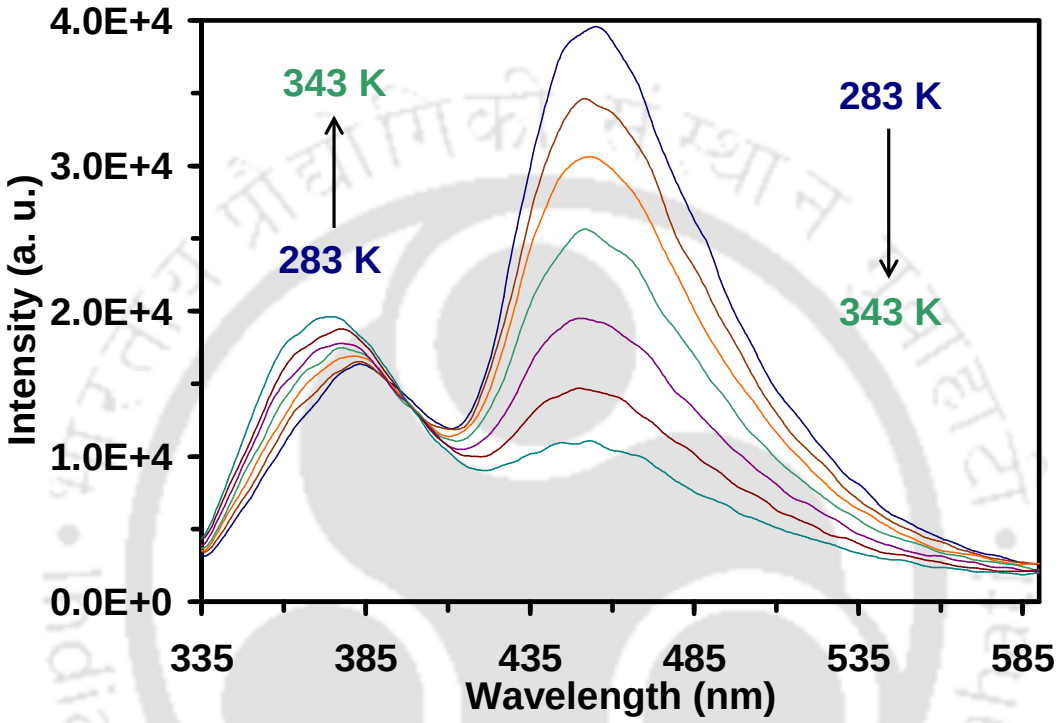

Figure 6.13. Fluorescence spectra of HPOP in acetonitrile at different temperatures, λ_{exc} = 300 nm.

Figures 6.14, **6.15**, and **6.16** show the change in dual fluorescence of HPOP at different temperatures in DMF, DMSO and glycerol, respectively. In DMF, DMSO and glycerol, although the relative intensities of the normal and tautomer emissions are solvent dependent, both normal and tautomer bands decrease with increasing temperature irrespective of the solvent. The normal emission in DMF is blue shifted from 386 nm to 381 nm, but the tautomer emission is red shifted from 469 nm to 484 nm (**Figure 6.14**). In DMSO, the normal emission maxima remain constant at 387 nm in all the temperatures while the tautomer emission is red shifted from 471 nm to 482 nm (**Figure 6.15**). On the other hand, in glycerol, both the normal and tautomer emission maxima remain constant at 386 nm and 500 nm, respectively in all the temperatures (**Figure 6.16**). The rate of change in intensity is highest in most viscous glycerol and least in least viscous acetonitrile and it also decreases with rise in temperature.

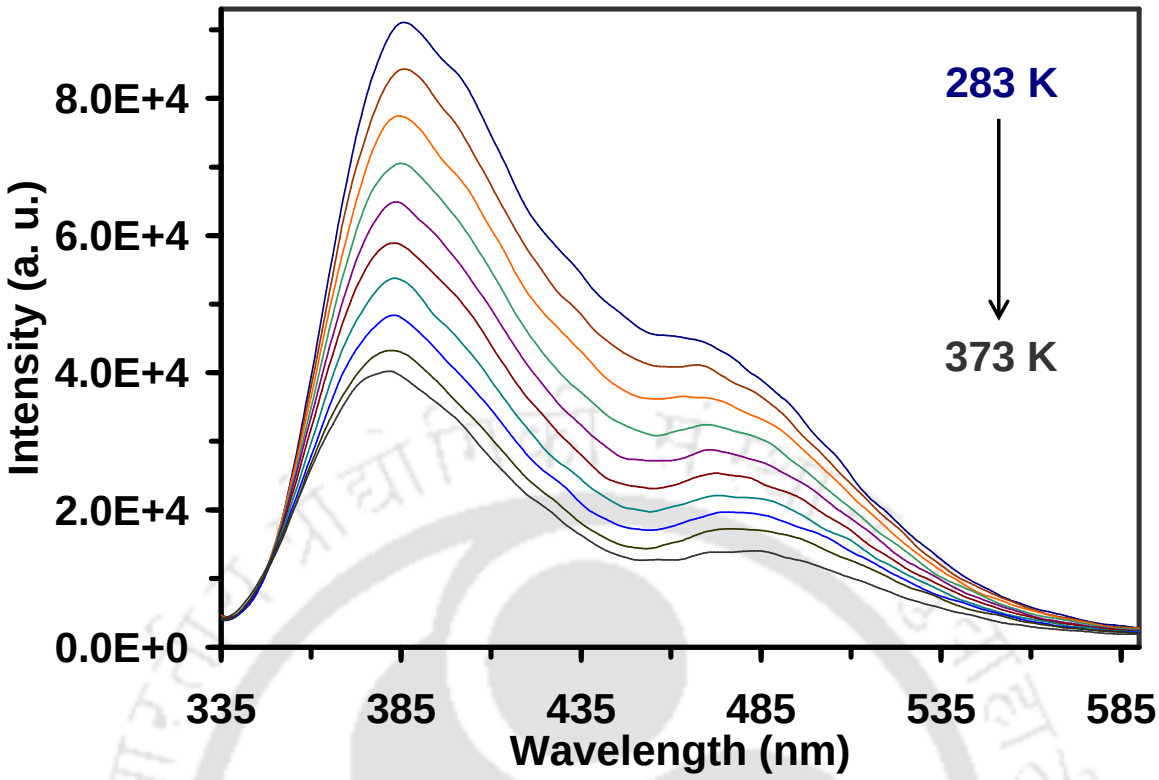

Figure 6.14. Fluorescence spectra of HPOP in DMF at different temperatures, λ_{exc} = 300 nm.

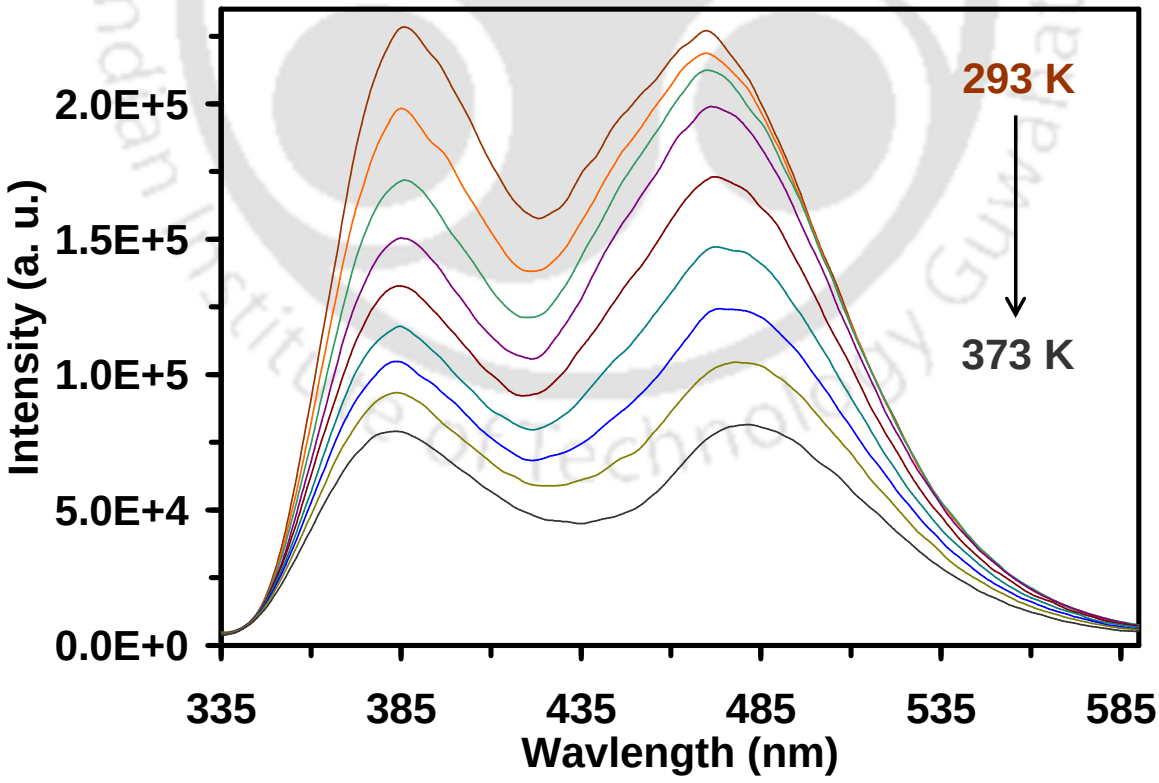

Figure 6.15. Fluorescence spectra of HPOP in DMSO at different temperatures, λ_{exc} = 300 nm.

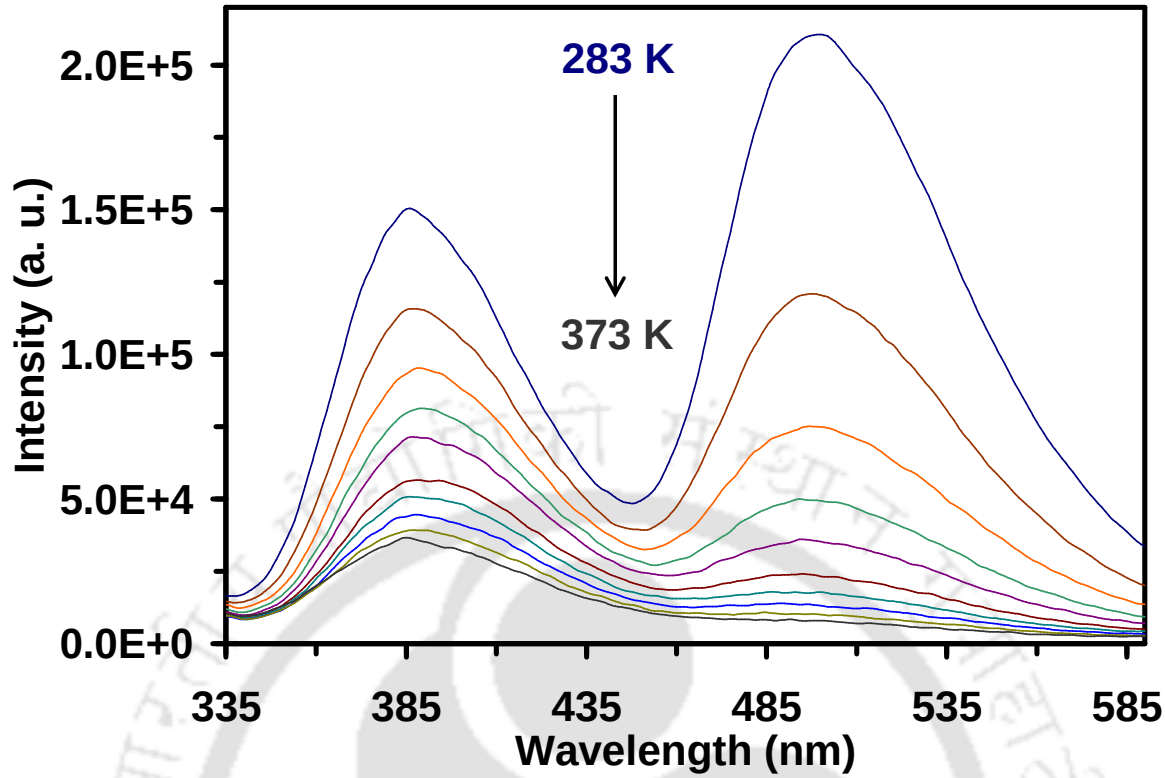

Figure 6.16. Fluorescence spectra of HPOP in glycerol at different temperatures, λ_{exc} = 300 nm.

6.2.2. Quantum Yield

The quantum yield of the normal emission of HPOP in acetonitrile increases with increase in temperature (**Figures 6.17**). The quantum yield of the normal emission of HPBI and HPIP-b in acetonitrile and dioxane also increase with increase in temperature (**Sections 3.3.2** and **3.3.5)**. The rise in temperature is expected to increase the nonradiative decay. As discussed earlier, *cis*-enol which has intramolecular hydrogen bonded cyclic ring, is the species responsible for ESIPT and *trans*-enol gives the normal emission. With increase in temperature the intramolecular hydrogen bond breaks in *cis*-enol which leads to formation of *trans*-enol. Therefore, the increase in quantum yield of normal emission in acetonitrile with rise in temperature indicates the increase in relative population of *trans*-enol more than the increase in the nonradiative decay. However, in DMF, DMSO and glycerol the quantum yield of normal emission decreases with increase in temperature (**Figures 6.17**). This suggests that the enhancement in the nonradiative decay is more significant than the rise in relative population of *trans*-enol in these solvents. The same behavior is observed by HPBI and its analogues in protic solvents (**Section 3.3.5**).

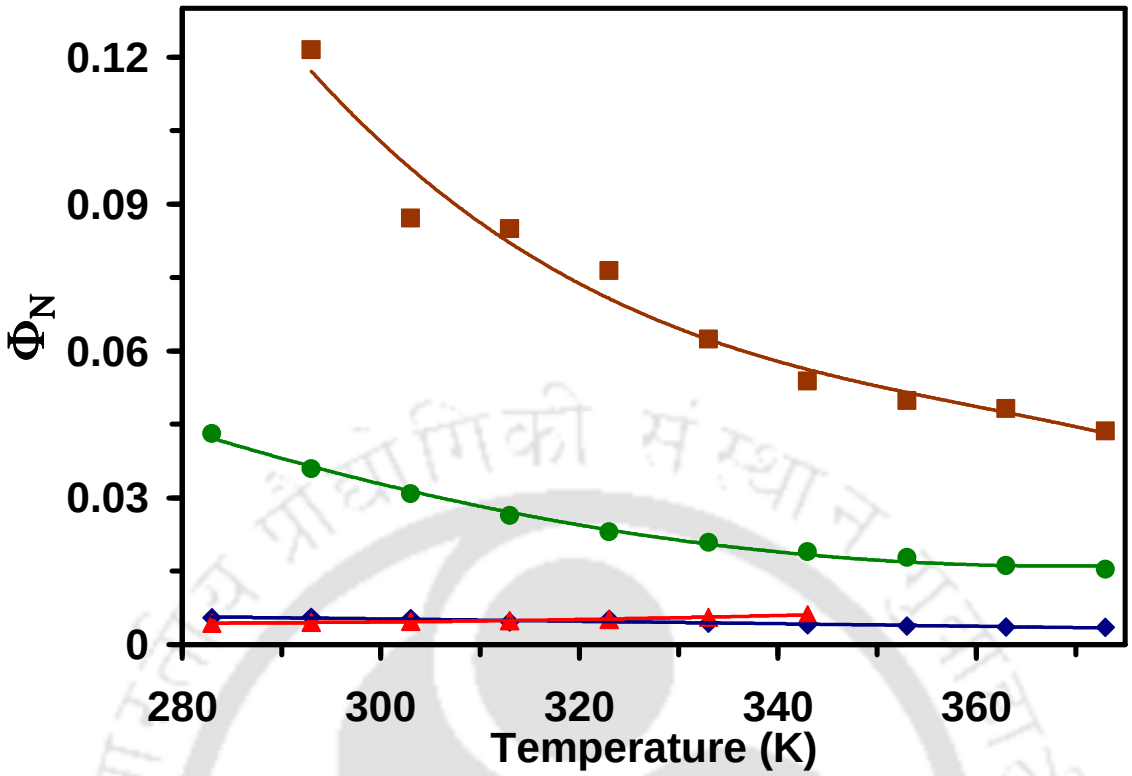

Figure 6.17. Quantum yield of normal emission of HPOP in acetonitrile (-▲-), DMF (-♦-), DMSO (-■-), and glycerol (-●-) at different temperatures.

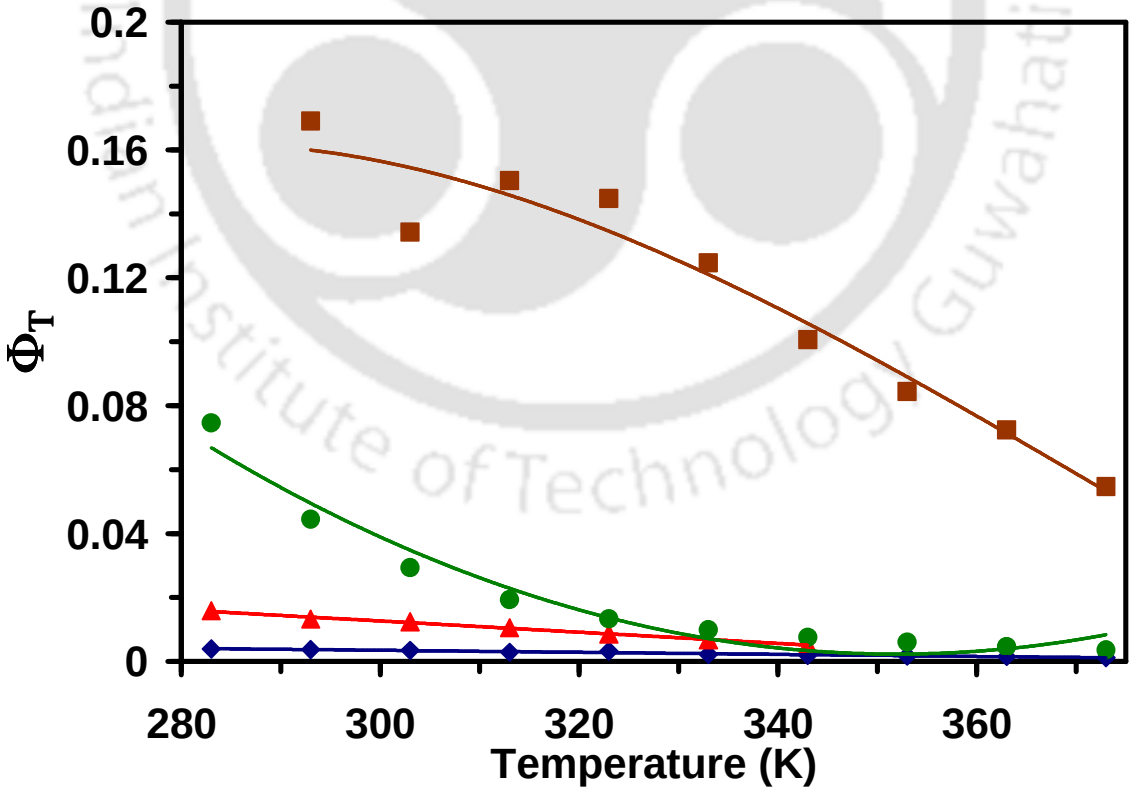

Figure 6.18. Quantum yield of tautomer emission of HPOP in acetonitrile (-▲-), DMF (-♦-), DMSO (-■-), and glycerol (-●-) at different temperatures.

In case of tautomer emission, the quantum yield decreases with temperature in all the solvents (**Figure 6.18**). The change in the quantum yield is highest in DMSO and least in DMF. In glycerol, the plot shows a slight upward curve which is indicative that the decrease in quantum yield become less as the temperature rises. This is probably because of the breaking of solvated structure with increase in temperature. Two factors play a role on the decrease in the quantum yield: (i) decrease in the relative population of *cis*-enol and, (ii) enhanced nonradiative decay of keto-tautomer with increase in temperature. Such decrease in the quantum yield of the tautomer band with temperature is already discussed in detail in **Section 3.3.5** for HPBI and analogues. The plot of quantum yield ratios of normal to tautomer bands Φ_N/Φ_T of HPOP against temperature show positive slop in acetonitrile, DMF and glycerol (**Figure 6.19**). However, in DMSO the plot is less sensitive to temperature.

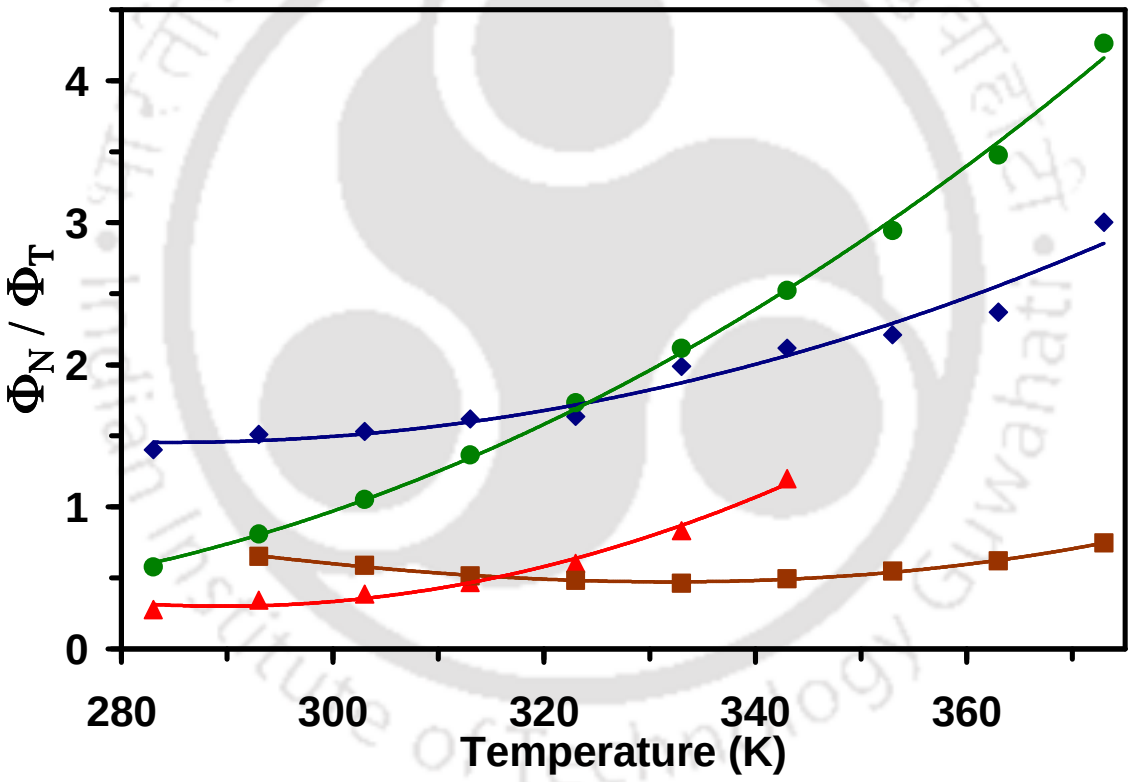

Figure 6.19. Quantum yield ratio Φ_N/Φ_T of HPOP in acetonitrile (-▲-), DMF (-♦-), DMSO (-■-), and glycerol (-●-) at different temperatures.

6.2.3. Fluorescence Excitation Spectra

In acetonitrile, the spectral intensities of the excitation spectra increase with temperature when monitored at the normal emission band (**Figure 6.20**). As mentioned earlier this is due to the fact that increase in relative population of *trans*-enol with rise in temperature dominates over the increase in the nonradiative decay with rise in temperature.

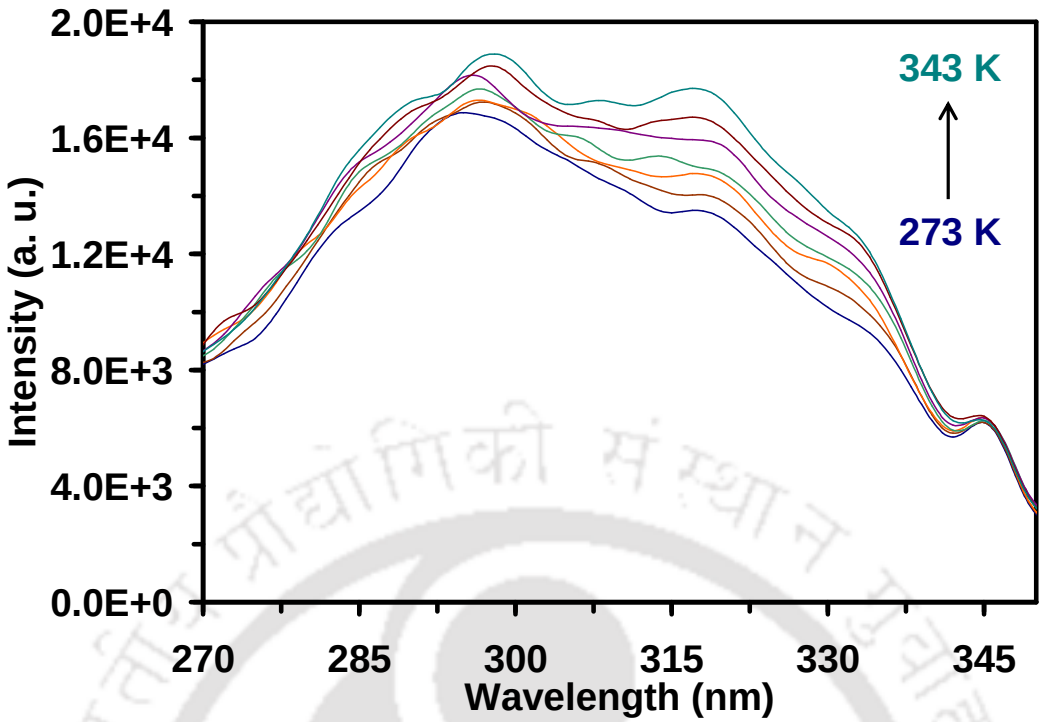

Figure 6.20. Excitation spectra of HPOP in acetonitrile monitored at normal band (385 nm).

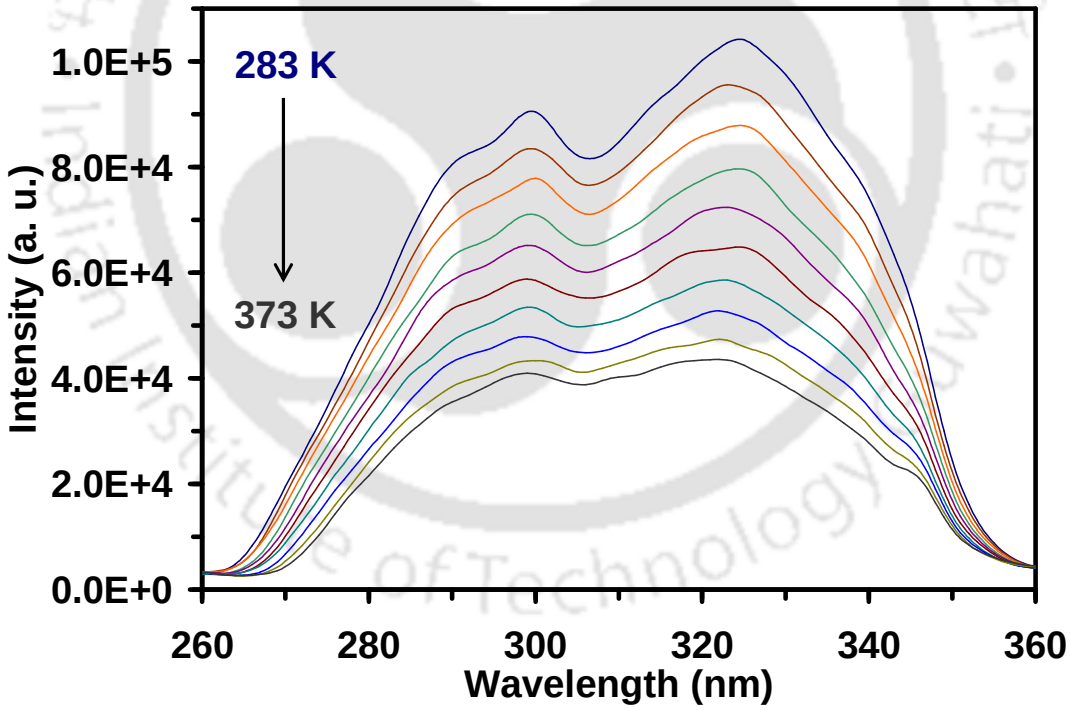

Figure 6.21. Excitation spectra of HPOP in DMF monitored at normal band (385 nm).

However, in DMF, DMSO and glycerol the intensities decrease when monitored at the nomal emission band. As a representation the excitation spectra of HPOP in DMF are shown in **Figure 6.21**. Therefore, it may be concluded the increase in nonradiative transition

in the normal emission with increase in temperature dominates over the increase in relative population of *trans*-enol.

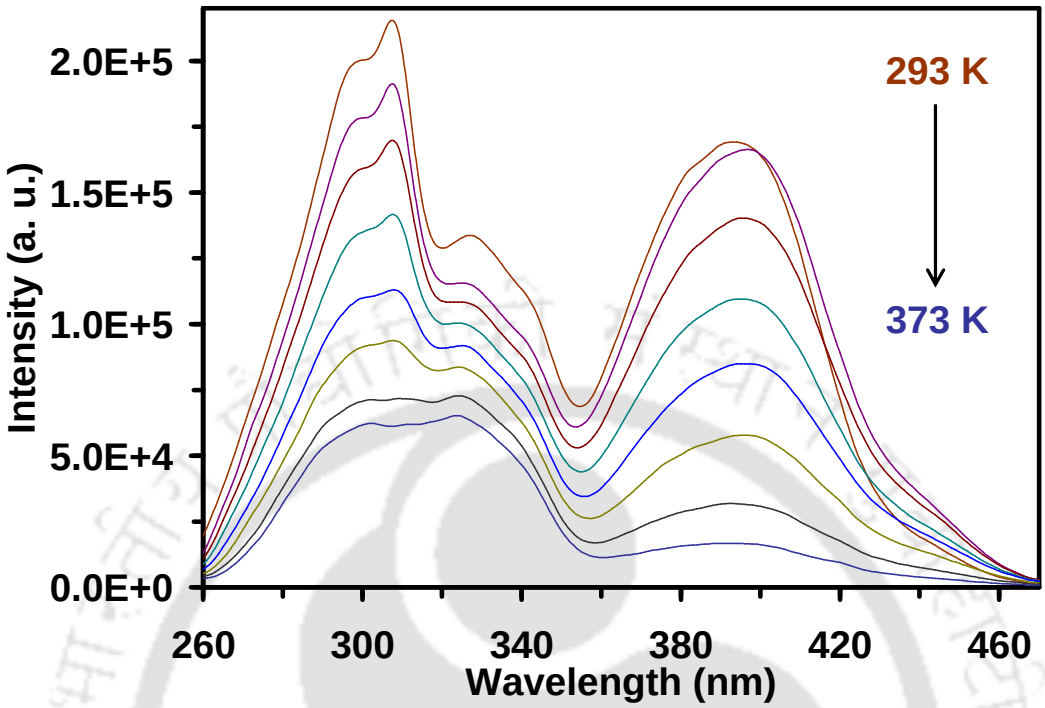

Figure 6.22. Excitation spectra of HPOP in DMSO monitored at tautomer band (480 nm).

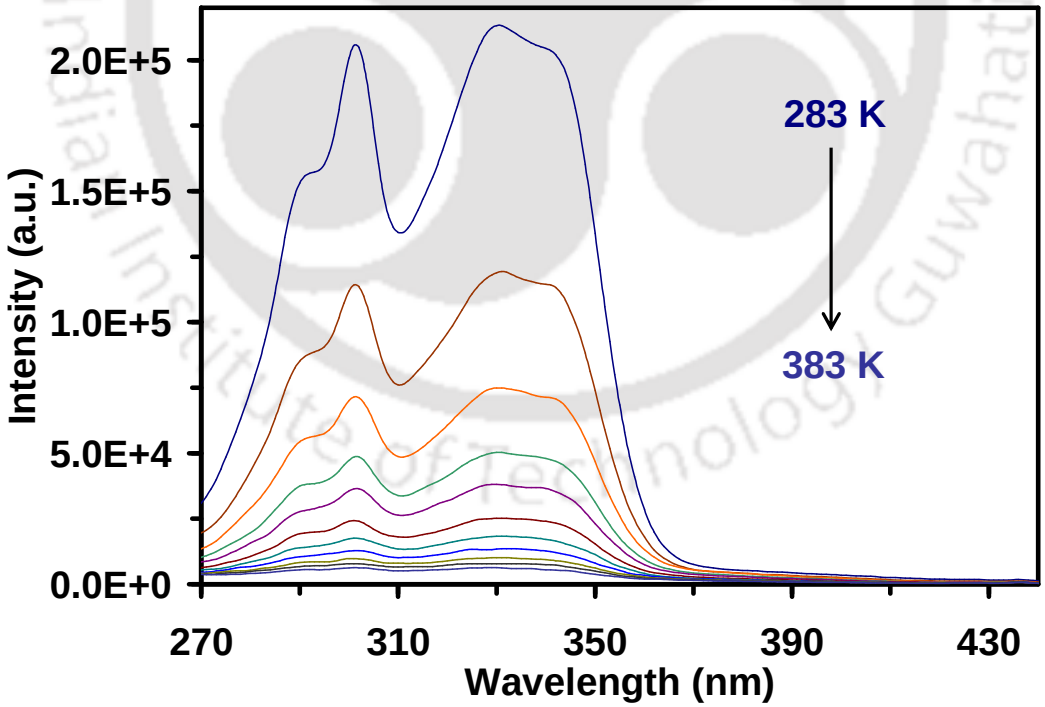

Figure 6.23. Excitation spectra of HPOP in glycerol monitored at tautomer band (500 nm).

The general features of the effect of temperature on the fluorescence excitation spectra recorded at tautomer band all the studied solvents are the same. As a representation,

Figure 6.22 shows the excitation spectra of HPOP in DMSO recorded at tautomer band. In case of HPOP in glycerol, excitation of ground state tautomer is not observed (**Figure 6.23**).

As is discussed earlier in **Section 6.1.2**, in acetonitrile, DMF and DMSO the tautomer is observed in the ground state also. The excitation intensity ratio of the tautomer to *cis*-enol (I_T/I_E) decreases with increases in temperature (**Figure 6.24**). The effect is more pronounced in DMSO at higher temperature. This indicates that the enol and tautomer (keto) equilibrium shifts toward the enol with rise in temperature. The increase in temperature favors *trans*-enol over other species. Due to this in acetonitrile, DMSO and DMF, despite the fact the relative population of *cis*-enol over the tautomer increases in the ground state the fluorescence intensity of the tautomer decreases. The decrease in relative population of *cis*-enol and increase in nonradiative decay of the phototautomer are the contributing factors which lead to the decrease in spectral intensity of tautomer band. The decrease in the fluorescence with temperature is more prominent is glycerol.

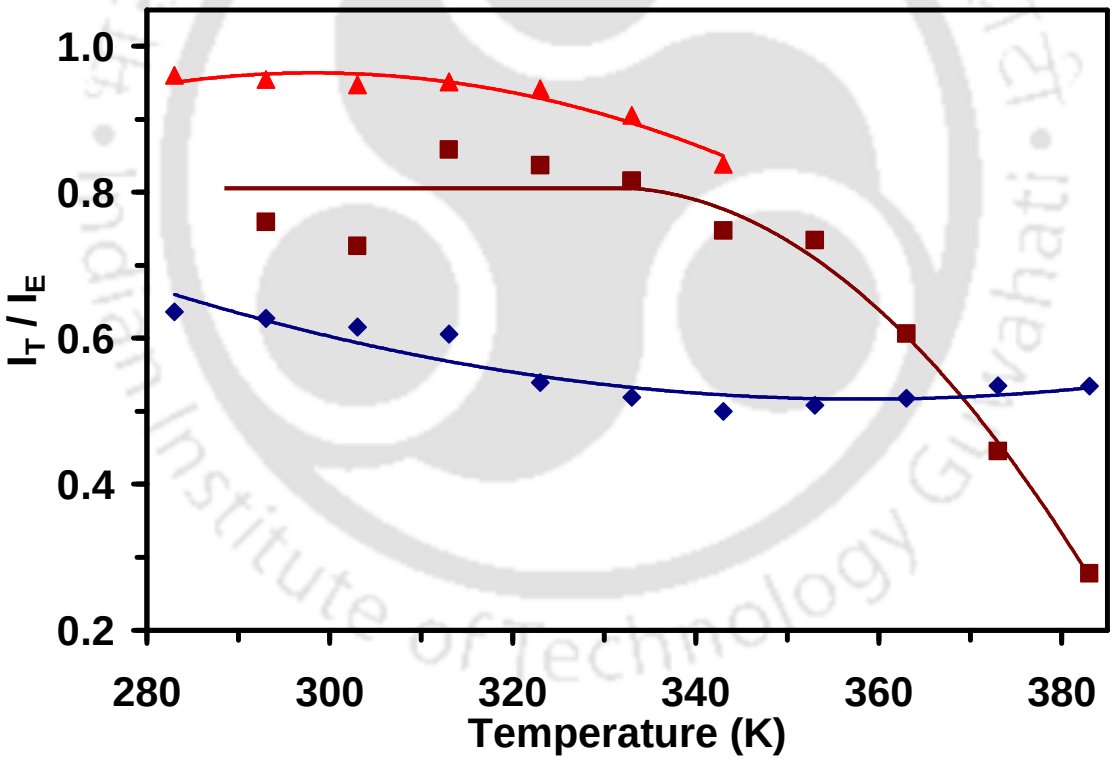

Figure 6.24. Intensity ratio of the ground state *cis*-enol and tautomer structures obtained from the excitation spectra recorded at the tautomer emission of HPOP in acetonitrile (triangle), DMF (diamond), and DMSO (square) at different temperatures.

6.3.0. Neutral-Monoanion Equilibrium

HPOP has only one acidic center i.e. phenolic –OH, the deprotonation of this leads to formation of monoanion.

6.3.1. Absorption Spectra

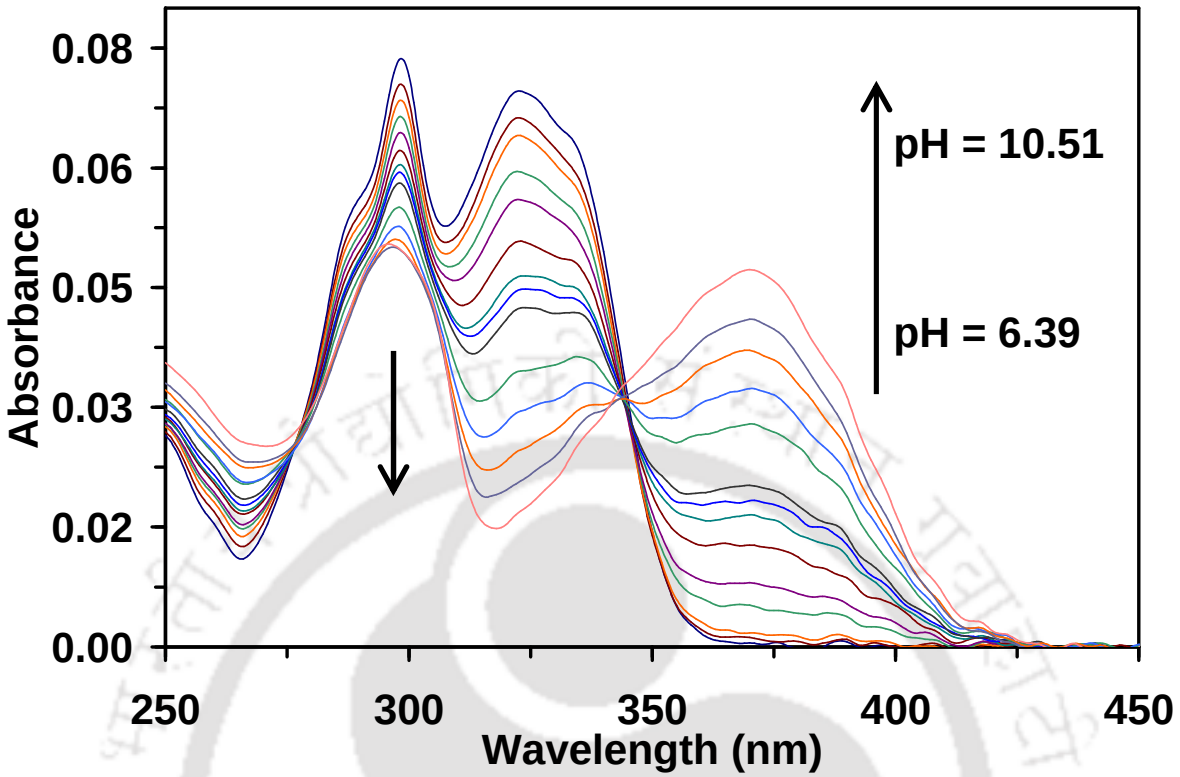

Figure 6.25. UV-Visible absorption spectra of HPOP at from pH = 6.39 to pH 10.51.

The molecule is neutral at pH 6.39. Upon increasing the pH from pH 6.39, a new band appears at the red side 370 nm in the absorption spectra (**Figure 6.25**). The absorbance of the neutral molecule decreases on increasing the pH of the solution and reaches the minimum at pH ~ 10.51. On the other hand, the absorbance of the new band increases and reaches the maximum at pH ~ 10.51. Beyond pH ~ 10.51, no appreciable change in the absorption spectra is observed. This indicates that at this pH the molecule is fully deprotonated to form the monoanion. A quasi-isosbestic point is observed at 345 nm which shows the neutral molecule is in equilibrium with monoanion. From the Henderson plot for the neutral-monoanion equilibrium, the pK_a for the equilibrium is found to be 9.36; in HPBO, the pK_a is 10.4.[54] Substitution with nitrogen decreases the pK_a with respect to HPBO. However, in HPIP-b, the pK_a for the neutral-monoanion equilibrium is 8.6.[6] Based on the general concept, substitution with more electronegative atom (oxygen) in the heterocyclic ring is expected to decrease the pK_a of HPOP with respect to that of HPIP-b. However, it should be noted here, oxygen replaces not merely the nitrogen atom, but the "NH" group. The hydrogen of the "NH" group is involved in hydrogen bonding with monoanion and it plays a crucial role in the stabilization of the monoanion.[95] Due to less stabilization of the monoanion in

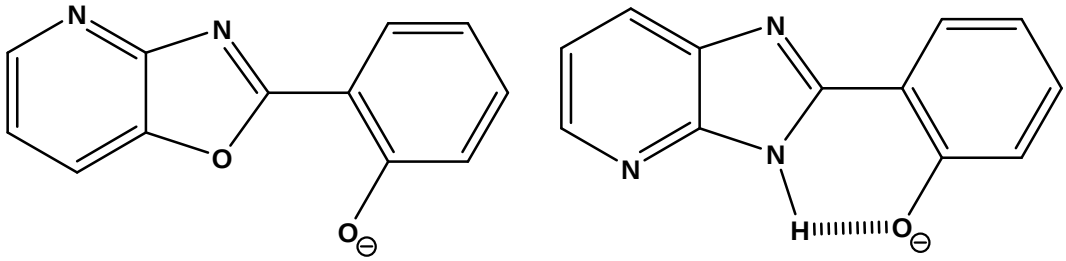

Chart 6.2. Monoanionic Forms of HPOP and HPIP-b.

HPOP in comparison to HPIP-b (**Chart 6.2**), the pK_a of the HPOP is higher than that of HPIP-b. Higher pK_a of HPBO than HPBI substantiates the argument.

6.3.2. Fluorescence Spectra

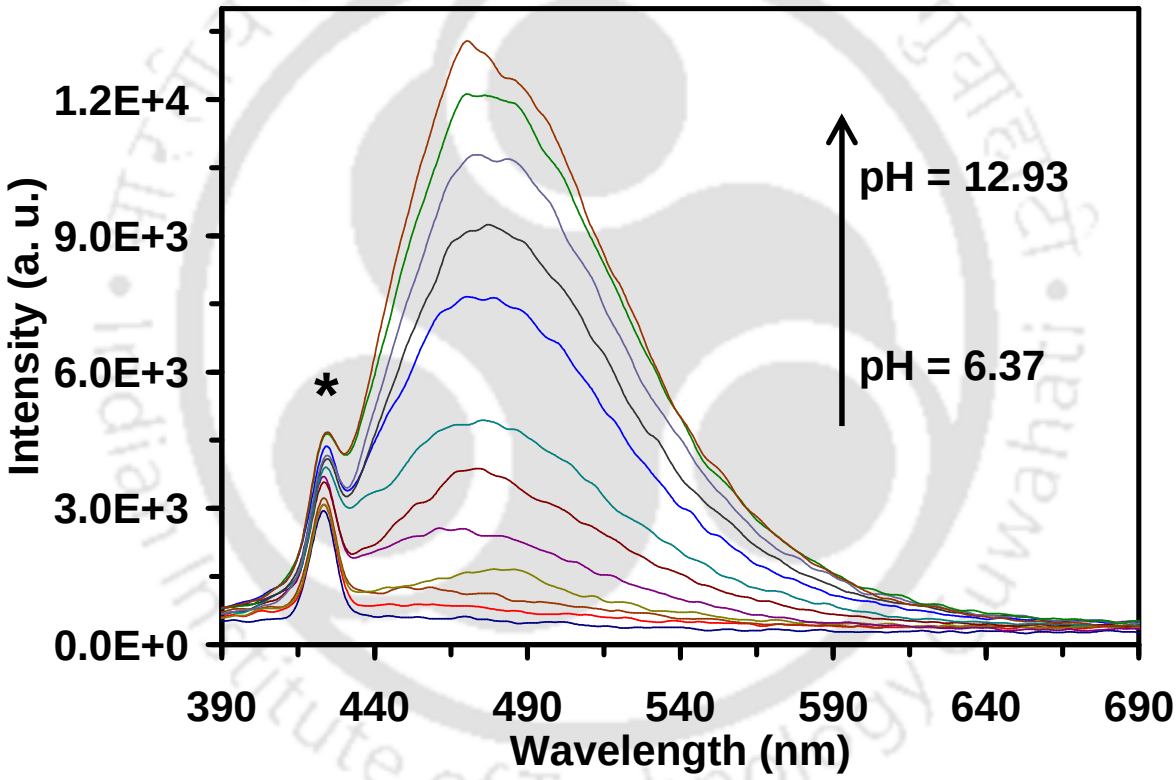

Figure 6.26. Fluorescence spectra of HPOP (λ_{ex} = 370 nm) in pH range of 6.37 to 12.93. Water Raman band is denoted by *.

Exciting at the absorption maximum of monoanion (λ_{ex} = 370 nm), the fluorescence of the monoanion at 471 nm increases with increase in pH from pH 6.37 (**Figure 6.26**). Beyond pH 12.93 no appreciable change in the fluorescence is observed. This shows that in the excited state the formation of monoanion is completed at pH 12.93. The monoanion is red shifted compared to normal emission. This indicates the increase in acidity of the molecule in the excited state.

6.4. Conclusion

The photophysical studies on a newly synthesized compound, HPOP) carried out in different solvents, pH and temperatures is reported. Solvent dependent equilibrium between the rotameric and tautomeric forms is observed in the ground state. HPOP also shows dual fluorescence viz. the normal and the tautomer bands due to emission from excited *trans*-enol and ESIPT product tautomer structures, respectively. The *cis*-enol and *trans*-enol are observed in all the solvents. Although the ground state tautomer is observed from the absorption spectrum only in DMSO, the excitation spectra monitored at the tautomer band clearly show the existence of the ground state tautomer structure in dioxane, alcohols, acetonitrile, DMF and DMSO. The study shows that nonradiative decay is more efficient in HPOP than that in HPBO and HPIP-b. Except the normal emission of HPOP in acetonitrile in all other solvents both emission decreases with increase in temperature. With rise in temperature, the *trans*-enol and *cis*-enol equilibrium shifts toward *trans*-enol and the *cis*-enol tautomer equilibrium shifts toward *cis*-enol. The pK_a for the neutral-monoanion decreases in HPOP than HPBO due to presence of pyridine nitrogen in HPOP. On the other hand, the pK_a for the neutral-monoanion increases in HPOP than HPIP-b due to less stabilization of monoanionic form of HPOP than that of HPIP-b.

Chapter 7

Conclusion and Scope for Future Work

7.1. Conclusion

A comprehensive study on the photophysical properties of ESIPT exhibiting HPBI and related molecules in different environments such as temperature, pH, homogeneous and organized microheterogeneous media was attempted. In the process of photophysical characterization, the potential implications of the fluorophores as probes and sensors are also explored.

Theoretical study on HPBI and its nitrogen substituted analogues reveals that the molecules exist in different rotameric and isomeric forms. In most cases, *cis*-enol which forms an intramolecularly hydrogen bonded ring is the most stable form. Upon photoexcitation, *cis*-enol undergoes ESIPT through the hydrogen bond to give the phototautomer keto isomer. The IPT is unfavorable in S_0 state but becomes feasible in S_1 state. After ESIPT, the phototautomer undergoes torsional rotation through the carbon-carbon double bond linking the two aromatic rings to form a twisted keto structure at 90°. The twisted keto structure is characterized by ICT from the phenolic moiety to the heterocyclic moiety and the energy of the ICT state is lower than the planar keto. This acts as a nonradiative channel from the phototautomer. When more electronegative nitrogen is substituted on the benzene ring of HPBI, the ICT is enhanced. On the other hand, nitrogen substitution on the phenolic ring of HPBI lowers the charge donating capacity of the dissociated pyridinol or pyrimidinol moiety. This reduces the ICT and thus destabilizing the twisted keto tautomer.

Experimental and theoretical study on the effect of temperature on ESIPT of HPBI and its nitrogen substituted analogues HPIP-b and HPIP-c in solvents of different polarity and hydrogen bonding capacity was also done. In solution, these molecules exist in *cis*-enol and *trans*-enol which are in equilibrium. The equilibrium shifts towards *trans*-enol with increase in temperature. The effect is more in protic solvents due to hydrogen bonding interactions between the fluorophore and solvent molecules. The excited *trans*-enol gives the normal emission while the phototautomer resulting from ESIPT gives highly Stokes' shifted emission band called the tautomer band. The increase in temperature decreases the fluorescence of both normal and tautomer emissions. The decrease is more in tautomer band and its decrease is governed by two factors: (i) the decrease in relative population of *cis*-enol, and (ii) the increase in nonradiative decay from the excited state.

The cationic sensing abilities of HPBI and its analogues were investigated. The photophysical properties of the fluorophores are significantly perturbed by the transition metal ions Ni^{2+}, Cu^{2+} and Zn^{2+}, whereas alkali and alkaline earth metal ions could produce

negligible effect. Upon binding, the ligand molecule coordinates with the metal centre through its phenolic oxygen and imidazole nitrogen which is confirmed by the single crystal structure of $[Ni(HPIP\text{-}b)_2]^{2+}$ complex. The binding breaks the intramolecular hydrogen bonded ring which is essential for ESIPT process to occur. This leads to change in normal to tautomer fluorescence intensity ratio where the changes are higher in HPBI than in its nitrogen substituted analogues. The results demonstrate that HPBI shows high selectivity towards Cu^{2+}. The normal to tautomer emission ratio of HPBI increases to as high as 143 and 10.4 fold in the presence of Cu^{2+} and Zn^{2+}, respectively. Although the increase is not as high as in HPBI, the ratio of HPIP-b increases by 2.1 and 2.8 fold in presence of Ni^{2+} and Cu^{2+}, respectively and that of HPIP-c to 1.9 fold in presence of Cu^{2+}.

In addition to the greater affinity towards transition metal ions, these fluorophores reveal susceptibility towards different microheterogenious environments. The ESIPT is favored in the β-CD nanocavity which is indicated by drastic enhancement of the tautomer emission. The effect is more in nitrogen substituted analogues HPIP-b and HPIP-c than in HPBI. All three fluorophores form 1:1 inclusion complexes with β-CD in both water and DMSO. The guest fluorophores enter the β-CD nanocavity through benzimidazole/imidazopyridine moiety. In DMSO, HPBI is present in neutral form, but the nitrogen substituted analogues are present in both neutral and monoanionic forms. However, upon encapsulation by β-CD all of the three molecules are present in both neutral and monoanionic forms in the nanocavity. The monoanion is stabilized more inside the β-CD cavity. The results reveal that the ESIPT of nitrogen substituted analogues is more susceptible to environment than HPBI and therefore are more promising probes. On the other hand, the change in the normal to tautomer emission ratio is more susceptible in AOT reverse micelle for HPBI where it increases upto 5 fold from w_0 = 0 to 30 while HPIP-b and HPIP-c depict an increase in ratio of 2.4 and 3.2 times, respectively. In addition a blue shift is observed in the tautomer band of HPBI with increasing volume of water quantity in reverse micelle while there is no shift in the tautomer bands of HPIP-b and HPIP-c. These observations show that initially these molecules preferentially reside in the interfacial region between the oil and water surface. Upon increase in w_0, the molecules drift away toward the bulk of the nanopool and the formation of solvated open enol conformer is favored. The increase in the ratio in AOT reverse micelle is ascribed to the following reasons: (i) nonradiative de-excitation of the tautomer by torsion rotation, (ii) shifting of *cis*-enol to *trans*-enol equilibrium toward *trans*-enol, and (iii) formation of solvated open enol conformer.

The photophysical properties of the fluorophores were also studied in presence of BSA. With increase in concentration of BSA, the fluorescence of both normal and tautomer bands increase and further, the intensity ratios of normal to tautomer bands of HPBI and HPIP-b decrease while that of HPIP-c increases. HPBI and HPIP-c bind in the hydrophobic site of BSA. On the other hand, HPIP-b binds at the hydrophilic site of BSA. Although both HPBI and HPIP-c bind at the hydrophobic sites, their binding pockets and interaction with BSA are different. In addition to *cis*- and *trans*-enolic forms, HPBI is present in the zwitterionic form, whereas HPIP-b and HPIP-c are present as monoanion in addition to *cis*- and *trans*-enols in the ground state.

All these results show that while HPBI shows superior chemosensing ability toward metal ions than the nitrogen substituted analogues, the substituted analogues show better promising probes in β-CD. In another scenario, all of the three fluorophores act as probes for BSA binding at different sites.

HPOP is a nitrogen substituted analogue of HPBO and structurally, resembles that of HPIP-b' which is the isomeric form of HPIP-b. The photophysical characterization of HPOP in different solvents, pH and temperatures was carried. Dual fluorescence is observed in HPOP where the large Stokes-shifted emission is due to emission from phototautomer formed by ESIPT while the less Stokes-shifted emission from excited *trans*-enol. Different equilibria between the rotameric and tautomeric forms are obtained in the ground state in different solvents. Though *cis*- and *trans*-enol are observed in all the solvents, the ground state tautomer is observed in dioxane, alcohols, acetonitrile, DMF and DMSO. At higher pH, the -OH group is deprotonated to form monoanion. The results show that nonradiative decay is more efficient in HPOP than in the corresponding benzoxazole derivative. It is observed that the increase in temperature enhances the nonradiative deactivation from the excited state and thus the quantum yield decreases with increase in temperature. Further, with rise in temperature, the *cis*-enol-*trans*-enol equilibrium shifts toward *trans*-enol and the *cis*-enol-tautomer equilibrium shifts toward *cis*-enol.

7.2. Scope for Future Work

In the solvation model followed in this work, specific interactions like hydrogen bonding are not taken into account. On the other hand, hydrogen bonding influences the *cis*-*trans* (enol) equilibrium. Therefore, calculation can be extended with explicit addition of few protic solvent molecules.

Although the photophysical properties of HPOP were studied in detail, theoretical calculations were not performed. The theoretical calculation may provide more information about ESIPT and related photophysical processes of HPOP. HPOP has one acid center and three basic centers viz. pyridine nitrogen, oxazole nitrogen and oxazole oxygen. The monoanion-neutral equilibrium is studied. Due to presence of more than one basic center, proton and metal ions may bind at more than one site to form different prototropic species/complexes. Therefore, studies may be extended to other equilibriums also. Such studies on prototropic species/complexes may lead to interesting observation. In addition knowledge on such equilibrium will help not only to understand the system, but also to understand the effect of hetero atom substitution on these equilibriums in general.

The effects of temperature, homogeneous solvents, β-cyclodextrin, reverse micelle and BSA on HPBI, HPIP-b, and HPIP-c were studied here. Docking studies can be performed to support the interaction of BSA with HPBI and its analogues. The studies can be extended in other systems such as ionic liquids and heterogeneous environments such as micelles, different albumins and allied enzymes. This may increase the application of these molecules. Such studies may be extended with HPOP also. Further, the interaction of these molecules with nanoparticles could be explored. Recent studies have shown some of the ESIPT molecules exhibit polymorphism and polymorphs have different optical properties. So the studies can be extended to explore the possible polymorphs in these molecules and investigating their optical properties.

References

1. K. S. Peters, *Acc. Chem. Res.* **2009**, *42*, 89-96.
2. Y. Lin, H. Wang, S. Gao, R. Li, and H. F. Schaefer, III, *J. Phys. Chem. B* **2012**, *116*, 8908–8915.
3. I. Belevich, M. I. Verkhovsky, and M. Wikström, *Nature* **2006**, *440*, 829-832.
4. J. Seo, S. Kim, and S. Y. Park, *J. Am. Chem. Soc.* **2004**, *126*, 11154-11155.
5. S. Ercelen, A. S. Klymchenko, and A. P. Demchenko, *Anal. Chim. Acta* **2002**, *464*, 273-287.
6. G. Krishnamoorthy, and S. K. Dogra, *J. Lumin.* **2001**, *92*, 103-114.
7. S. Santra, G. Krishnamoorthy, and S. K. Dogra, *Chem. Phys. Lett.* **2000**, *327*, 230–237.
8. F. R. Prieto, M. Mosquera, and M. Novo, *J. Phys. Chem.* **1990**, *94*, 8536-8542.
9. M. Kasha, *J. Chem. Soc., Faraday Trans. 2* **1986**, *82*, 2379-2392.
10. P. F. Barbara, and P. K. Walsh, *J. Phys. Chem.* **1989**, *93*, 29-34.
11. P. –T. Chou, S. –C. Pu, Y. –M. Cheng, W. –S. Yu, Y. –C. Yu, F. –T. Hung, and W. –P. Hu, *J. Phys. Chem. A* **2005**, *109*, 3777–3787.
12. K. –Y. Chen, C. –C. Hsieh, Y. –M. Cheng, C. –H. Lai, and P. –T. Chou, *Chem. Commun.* **2006**, *42*, 4395-4397.
13. T. Fournier, S. Pommeret, J. -C. Mialocq, A. Deflandre, and R. Rozot, *Chem. Phys. Lett*. **2000**, *325*, 171-175
14. P. K. Sengupta, and M. Kasha, *Chem. Phys. Lett.* **1979**, *68*, 382-385.
15. M. Isaks, K. Yates, and P. Kalanderopoulos, *J. Am. Chem. Soc*. **1984**, *106*, 2728–2730.
16. P. Kalanderopoulos, and K. Yates, *J. Am. Chem. Soc*. **1986**, 108, 6290-6295.
17. C. A. Taylor, M. A. El-Bayoumi, and M. Kasha, *Proc. Natl. Acad. Sci. USA* **1969**, *63*, 253-260.
18. K. C. Ingham, M. Abu-Elgheit, and M. A. El-Bayoumi, *J. Am. Chem. Soc*. **1971**, *92*, 5023-5025.
19. A. Douhal, S. K. Kim, and A. H. Zewail, *Nature* **1995**, *378*, 260-263.
20. P. –S. Song, M. Sun, A. Koziolowa, and J. Koziol, *J. Am. Chem. Soc.* **1974**, *96*, 4319–4323.
21. J. D. Choi, R. D. Fugate, and P. –S. Song, *J. Am. Chem. Soc*. **1980**, *102*, 5293-5297.
22. M. Itoh, T. Adachi, and K. Tokumura, *J. Am. Chem. Soc.* **1983**, *105*, 4828–4829.

23. R. Schipfer, O. S. Wolfbeis, and A. Knierzinger, *J. Chem. Soc., Perkin Trans. 2* **1981**, 1443-1448.

24. M. K. Nayak, and P. Wan, *Photochem. Photobiol. Sci.* **2008**, *7*, 1544-1554.

25. S. J. Formosinho, and L. G. Arnaut, *J. Photochem. Photobiol. A: Chem.* **1993**, *75*, 21-48.

26. A. Douhal, F. Lahmani, and A. H. Zewail, *Chem. Phys.* **1996**, *207*, 477-498.

27. J. E. Kwon, and S. Y. Park, *Adv. Mater.* **2011**, *23*, 3615–3642.

28. J. Zhao, S. Ji, Y. Chen, H. Guo, and P. Yang, *Phys. Chem. Chem. Phys.* **2012**, *14*, 8803–8817.

29. B. M. Uzhinov, and M. N. Khimich, *Russ. Chem. Rev.* **2011**, *80*, 553-577.

30. J. Sepiol, *Pol. J. Chem.* **2009**, *83*, 1671-1692.

31. G. Yang, S. Li, S. Wang, and Y. Li, *C. R. Chimie* **2011**, *14*, 789–798.

32. A. L. Sobolewski, and W. Domcke, in *Ultrafast Hydrogen Bonding Dynamics and Proton Transfer Processes in the Condensed Phase*; 93, T. Elsaesser, and H. J. Bakker, Eds.; Kluwer Academic Publisher, Dordrecht, The Netherlands, **2002**.

33. R. Rossetti, R. Rayford, R. C. Haddon, and L. E. Brus, *J. Am. Chem. Soc.* **1981**, *103*, 4303-4307.

34. A. Migani, L. Blancafort, M. A. Robb, and A. D. DeBellis, *J. Am. Chem. Soc.* **2008**, *130*, 6932-6933.

35. S. Lochbrunner, T. Schultz, M. Schmitt, J. P. Shaffer, M. Z. Zgierski, and A. Stolow, *J. Chem. Phys.* **2001**, *114*, 2519-2522.

36. A. L. Sobolewski, and W. Domcke, *Phys. Chem. Chem. Phys.* **1999**, *1*, 3065-3072.

37. J. Goodman, and L. E. Brus, *J. Am. Chem. Soc.* **1978**, *100*, 7472-7474.

38. K. K. Smith, and K. J. Kauman, *J. Phys. Chem.* **1978**, *82*, 2286-2291.

39. P. M. Felker, W. R. Lambert, and A. H. Zewail, *J. Chem. Phys.* **1982**, *77*, 1603-1605.

40. L. Heimbrook, J. E. Kenny, B. E. Kohler, and G. W. Scott, *J. Phys. Chem.* **1983**, *87*, 280-289.

41. T. Nishiya, S. Yamauchi, N. Hirota, M. Baba, and I. Hanazaki, *J. Phys. Chem.* **1986**, *90*, 5730-5735.

42. P. Chou, D. McMorrow, T. J. Aartsma, and M. Kasha, *J. Phys. Chem.* **1984**, *88*, 4596-4599.

43. A. J. G. Strandjord, D. E. Smith, and P. F. Barbara, *J. Phys. Chem.* **1985**, *89*, 2355-2361.

44. A. J. G. Strandjord, and P. F. Barbara, *J. Phys. Chem.* **1985**, *89*, 2362-2366.

45. A. J. G. Strandjord, and P. F. Barbara, *Chem. Phys. Lett.* **1983**, *98*, 21-26.

46. M. Itoh, Y. Tanimoto, and K. Tokumura, *J. Am. Chem. Soc.* **1983**, *105*, 3339-3340.

47. D. McMorrow, and M. Kasha, *J. Phys. Chem.* **1984**, *88*, 2235-2243.

48. B. Dick, and N. P. Ernsting, *J. Phys. Chem.* **1987**, *91*, 4261-4265.

49. D. McMorrow, T. Dzygan, and T. J. Aartsma, *Chem. Phys. Lett.* **1984**, *103*, 492-496.

50. D. L. Williams, and A. Heller, *J. Phys. Chem.* **1970**, *74*, 4473-4480.

51. P. Purkayastha, and N. Chattopadhyay, *Int. J. Mol. Sci*. **2003**, *4*, 335-361.

52. P. Purkayastha, and N. Chattopadhyay, *Phys. Chem. Chem. Phys*. **2000**, *2*, 203-210.

53. K. Ding, S. J. Courtney, A. J. Strandjord, S. Flom, D. Friedrich, and P. F. Barbara, *J. Phys. Chem. A* **1983**, *87*, 1184-1188.

54. F. R. Prieto, M. C. R. Rodríguez, M. M. González, and M. A. R. Fernandez, *J. Phys. Chem. A* **1994**, *98*, 8666-8672.

55. C. J. Fahrni, M. M. Henary, and D. G. VanDerveer, *J. Phys. Chem. A* **2002**, *106*, 7655-7663.

56. S. Lochbrunner, A. J. Wurzer, and E. Riedle, *J Phys. Chem. A* **2003**, *107*, 10580-10590.

57. R. de Vivie-Riedle, V. D. Waele, L. Kurtz, and E. Riedle, *J Phys. Chem. A* **2003**, *107*, 10591-10599.

58. J. C. del Valle, R. M. Claramunt, and J. Catalán. *J Phys. Chem. A* **2008**, *112*, 5555-5565.

59. T. Werner, *J. Phys. Chem.* **1979**, *83*, 320-325.

60. A. Huston, G. W. Scott, and A. Gupta, *J. Chem. Phys.* **1982**, *76*, 4978-4985.

61. S. R. Flom, and P. F. Barbara, *Chem. Phys. Lett.* **1983**, *94*, 488-493.

62. M. J. Paterson, M. A. Robb, Lluís Blancafort, and A. D. DeBellis, *J. Am. Chem. Soc.* **2004**, *126*, 2912-2922.

63. M. H. Van Benthem, G. D. Gillispie, and R. C. Haddon, *J. Phys. Chem.* **1982**, *86*, 4281-4283.

64. G. Smulevich, and P. Foggi, *J. Chem. Phys.* **1987**, *87*, 5657-5663.

65. S. R. Flom, and P. F. Barbara, *J. Phys. Chem.* **1985**, *89*, 4489-4494.

66. G. Zhang, H. Wang, Y. Yu, F. Xiong, G. Tang, and W. Chen, *Applied Physics B - Lasers and optics* **2003**, *76*, 677-681.

67. M. Mosquera, J. C. Penedo, M. C. R. Rodríguez, and F. Rodríguez-Prieto, *J. Phys. Chem.* **1996**, *100*, 5398-5407.

68. D. A. Yushchenko, V. V. Shvadchak, A. S. Klymchenko, G. Duportail, V. G. Pivovarenko, and Y. Mély, *J. Phys. Chem. A* **2007**, *111*, 10435–10438.

69. P. Wasserscheid, and W. Keim, *Angew. Chem. Int. Ed.* **2000**, *39*, 3772-3789.

70. S. K. Das, A. Bansal, and S. K. Dogra, *Bull. Chem. Soc. Jpn.* **1997**, *70*, 307-313.

71. S. K. Das, and S. K. Dogra, *J. Chem. Soc., Faraday Trans.* **1998**, *94*, 139-145.

72. N. Sarkar, K. Das, S. Das, A. Datta, D. Nath, and K. Bhattacharyya, *J. Phys. Chem.* **1995**, *99*, 17711-17714.

73. J. D. Coe, B. G. Levine, T. J. Martinez; *J. Phys. Chem. A* **2007**, *111*, 11302-11310.

74. Y. Wang, G. Wu; *Acta Phys. –Chim. Sin.* **2008**, *24*, 552-560.

75. S. Scheiner; *J. Phys. Chem. A* **2000**, *104*, 5898–5909.

76. S. P. De, S. Ash, D. K. Bhui, H. Bar, P. Sarkar, G. P. Sahoo, A. Misra; *Spectrochim. Acta, Part A* **2009**, *71*, 1728-1735.

77. A. L. Sobolewski, W. Domcke, and C. Hättig, *J. Phys. Chem. A* 2006, **110**, 6301-6306.

78. M. J. Paterson, M. A. Robb, L. Blancafort, and A. D. DeBellis, *J. Phys. Chem. A* **2005**, *109*, 7527-7537.

79. M. H. Van Benthem, and G. D. Gillispie, *J. Phys. Chem.* **1984**, *88*, 2954-2960.

80. D. McMorrow, and M. J. Kasha, *J. Am. Chem. Soc.* **1983**, *105*, 5133-5134.

81. A. J. G. Strandjord, and P. F. Barbara, *J. Phys. Chem.* **1985**, *89*, 2355-2361.

82. P. -T. Chou, M. L. Martinez, and J. H. Clements, *J. Phys. Chem.* **1993**, *97*, 2618-2622.

83. D. D. Pant, H. C. Josh, P. B. Bisht, and H. B. Tripathi, *Chem. Phys.* **1994**, *185*, 137-144.

84. P. B. Bisht, H. B. Tripathi, and D. D. Pant, *J. Photochem. Photobiol. A Chem.* **1995**, *90*, 103-108.

85. Y. L. Frolov, Y. M. Sapozhnikov, S. S. Barev, N. N. Pogodaeva, and N. A. Tyukavkina, *Izv. Akad. Nauk SSSR, Ser. Khim.* **1974**, *10*, 23640.

86. A. Weller, *Progr. React. Kinet.* **1961**, *1*, 188.

87. A.U. Acuña, F. Toribio, F. Amat-Guerri, and J. Catalan, *J. Photochem.* **1985**, *30*, 339-352.

88. F. Lahmani, and A. Zehnacker-Rentien, *J. Phys. Chem. A* **1997**, *101*, 6141-6147.

89. S. Nagaoka, A. Nakamura, and U. Nagashima, *J. Photochem. Photobiol. A* **2002**, *154*, 23-32.

90. M. Fores, M. Duran, and M. Sola, *Chem. Phys.* **2000**, *260*, 53-64.

91. A. S. Klymchenko, V. G. Pivovarenko, T. Ozturk, and A. P. Demchenko, *New J. Chem.* **2003**, *27*, 1336-1343.

92. A. Ito, Y. Fujiwara, and M. Itoh, *J. Chem. Phys.* **1992**, *96*, 7474-7482.

93. D. A. Parthenopoulos, D. McMorrow, and M. Kasha, *J. Phys. Chem.* **1991**, *95*, 2668-2674.

94. E. Falkovskaia, P. K. Sengupta, and M. Kasha, *Chem. Phys. Lett.* **1998**, *297*, 109–114.

95. H. K. Sinha and S. K. Dogra, *Chem. Phys.* **1986**, *102*, 337–347.

96. D. LeGourriérec, V. Kharlanov, R. G. Brown, and W. Rettig, *J. Photochem. Photobiol. A* **2000**, *130*, 101–111.

97. M. Krishnamurthy, and S. K. Dogra, *J. Photochem.* **1986**, *32*, 235–242.

98. K. Das, N. Sarkar, A. K. Ghosh, D. Majumdar, D. N. Nath, and K. Bhattacharyya, *J. Phys. Chem.* **1994**, *98*, 9126–9132.

99. A. Douhal, F. Amat-Guerrib, M. P. Lillo, and A. W. Acuna, *J. Photochem. Photobiol. A* **1994**, *78*, 127–138.

100. E. L. Roberts, J. Dey, and I. M. Warner, *J. Phys. Chem.* **1996**, *100*, 19681–19686.

101. T. Iijima, A. Momotake, Y. Shinohara, T. Sato, Y. Nishimura, and T. Arai, *J. Phys. Chem. A* **2010**, *114*, 1603-1609.

102. J. S. Stephan, and K. H. Grellmann, *J. Phys. Chem.* **1995**, *99*, 10066-10068.

103. S. Santra, and S. K. Dogra, *Chem. Phys.* **1998**, *226*, 285-296.

104. A. K. Mishra, and S. K. Dogra, *J. Photochem.* **1985**, *31*, 333-344.

105. S. Santra, G. Krishnamoorthy, and S. K. Dogra, *J. Phys. Chem. A* **2000**, *104*, 476-482.

106. S. Santra, G. Krishnamoorthy, and S. K. Dogra, *Chem. Phys. Lett.* **1999**, *311*, 55–61.

107. A. Ohshima, M. Ikegami, Y. Shinohara, A. Momotake, and T. Arai, *Bull. Chem. Soc. Jpn.* **2007**, *80*, 561-566.

108. J. Seo, S. Kim, S. Park, and S. Y. Park, *Bull. Kor. Chem. Soc.* **2005**, *26*, 1706-1710.

109. Y. H. Kim, S. –G. Roh, S. –D. Jung, M. –A. Chung, H. K. Kim, and D. W. Cho, *Photochem. Photobiol. Sci.* **2010**, *9*, 722–729.

110. C. -C. Hsieh, C. -M. Jiang, and P. -T. Chou, *Acc. Chem. Res.* **2010**, *43*, 1364-1374.

111. C. -C. Hsieh, M. -L. Ho, and P. -T. Chou, in *Advanced Fluorescence Reporters in Chemistry and Biology I*, Vol. 8, A. P. Demchenko, Eds.; Springer Berlin Heidelberg, **2010**, 225-266.

112. S. Park, S. Kim, J. Seo, and S. Y. Park, *Macromol. Res.* **2008**, *16*, 385-395.

113. P. –T. Chou, C. –H. Huang, S. –C. Pu, Y. –M. Cheng, Y. –H. Liu, Y. Wang, and C. –T. Chen, *J. Phys. Chem. A* **2004**, *108*, 6452-6454.

114. A. S. Klymchenko, V. G. Pivovarenko, and A. P. Demchenko, *J. Phys. Chem. A* **2003**, *107*, 4211-4216.

115. P. -T. Chou, S. -C. Pu, Y.-M. Cheng, W. -S. Yu, Y. -C. Yu, F. -T. Hung, and W. -P. Hu, *J. Phys. Chem. A* **2005**, *109*, 3777-3787.

116. P. -T. Chou, M. L. Martinez, and J. H. Clements, *J. Phys. Chem.* **1993**, *97*, 2618-2622.

117. P. -T. Chou, M. L. Martinez, and J. H. Clements, *Chem. Phys. Lett.* **1993**, *204*, 395-399.

118. T. C. Swinney, and D. F. Kelley, *J. Chem. Phys.* **1993**, *99*, 211-221.

119. F. Parsapour, and D. F. Kelley, *J. Phys. Chem.* **1996**, *100*, 2791-2798.

120. A. Sytnik, D. Gormin, and M. Kasha, *Proc. Natl. Acad. Sci. USA* **1994**, *91*, 11968-11972.

121. P. -T. Chou, C. -H. Huang, S. -C. Pu, Y. -M. Cheng, Y. -H. Liu, Y. Wang, and C. -T. Chen, *J. Phys. Chem. A* **2004**, *108*, 6452-6454.

122. Y. -M. Cheng, S. -C. Pu, Y. -C. Yu, P. -T. Chou, C. -H. Huang, C. -T. Chen, T. -H. Li, and W. -P. Hu, *J. Phys. Chem. A* **2005**, *109*, 11696–11706.

123. S. R. Vázquez, M. C. R. Rodríguez, and M. M. F. Rodríguez-Prieto, *J. Phys. Chem. A* **2007**, *111*, 1814-1826.

124. A. Maliakal, G. Lem, N. J. Turro, R. Ravichandran, J. C. Suhadolnik, A. D. DeBellis, M. G. Wood, and J. Lau, *J. Phys. Chem. A* **2002**, *106*, 7680-7689.

125. M. J. Paterson, M. A. Robb, L. Blancafort, and A. D. DeBellis, *J. Am. Chem. Soc.* **2004**, *126*, 2912-2922.

126. J. Catalan, P. Perez, F. Fabero, J. F. K. Wilshire, R. M. Claramunt, and J. Elguero, *J. Am. Chem. Soc.* **1992**, *114*, 964-966.

127. H. E. A. Kramer, in *Studies in Organic Chemistry, 40: Photochromism, Molecules and Systems*; H. Durr, and H. BouasLaurent, Eds.; Elsevier: Amsterdam, **1990**.

128. J. Rieker, E. Lemmert-Schmitt, G. Goeller, M. Roessler, G. J. Stueber, H. Schettler, H. E. A. Kramer, J. J. Stezowski, H. Hoier, S. Henkel, A. Schmidt, H. Port, M. Wiechmann, J. Rody, G. Rytz, M. Slongo, and J. –L. Birbaum, *J. Phys. Chem.* **1992**, *96*, 10225-10234.

129. S. Park, O. -H. Kwon, S. Kim, S. Park, M. -G. Choi, M. Cha, S. Y. Park, and D. -J. Chang, *J. Am. Chem. Soc.* **2005**, *127*, 10070-10074.

130. K. –Y. Chen, C. –C. Hsieh, Y. –M. Cheng, C. –H. Lai, and P. –T. Chou, *Chem. Commun.* **2006**, *42*, 4395-4397.

131. M. Stein, J. Keck, F. Waiblinger, A. P. Fluegge, H. E. S. Kramer, A. Hartschuh, H. Port, D. Leppard, and G. Rytz, *J. Phys. Chem. A* **2002**, *106*, 2055-2066.

132. C. M. Estévez, R. D. Bach, K. C. Hass, and W. F. Schneider, *J. Am. Chem. Soc.* **1997**, *119*, 5445-5446.

133. S. S. Maity, S. Samanta, P. S. Sardar, A. Pal, S. Dasgupta, and S. Ghosh, *Chem. Phys.* **2008**, *354*, 162-173.

134. A. S. Klymchenko, V. V. Shvadchak, D. A. Yushchenko, N. Jain, and Y. Mély, *J. Phys. Chem. B* **2008**, *112*, 12050-12055.

135. A. Sytnik, and M. Kasha, *Proc. Natl. Acad. Sci. USA* **1994**, *91*, 8627-8630.

136. P. S. Sardar, S. Samanta, S. S. Maity, S. Dasgupta, and S. Ghosh, *J. Phys. Chem. B* **2008**, *112*, 3451-3461.

137. T. Ozturk, A. S. Klymchenko, A. Capan, S. Oncul, S. Cikrikci, S. Taskiran, B. Tasan, F. B. Kaynak, S. Ozbey, and A. P. Demchenko, *Tetrahedron* **2007**, *63*, 10290-10299.

138. Y. Wu, X. Peng, J. Fan, S. Gao, M. Tian, J. Zhao, and S. Sun, *J. Org. Chem.* **2007**, *72*, 62-70.

139. N. Singh, N. Kaur, R. C. Mulrooney, and J. F. Callan, *Tetrahedron Lett.* **2008**, *49*, 6690-6692.

140. H. –Y. Luo, X. –B. Zhang, C. –L. He, G. –L. Shen, and R. –Q. Yu, *Spectrochim. Acta, Part A* **2008**, *70A*, 337-342.

141. Q. Chou, D. A. Medvetz, and Y. Pang, *Chem. Mater.* **2007**, *19*, 6421-6429.

142. D. Beer, and J. Weber, *Opt. Commun.* **1972**, *5*, 307-309.

143. A. U. Acuña, A. Costela, and J. M. Muñoz, *J. Phys. Chem.* **1986**, *90*, 2807-2808.

144. A. U. Acuña, F. Amat, J. Catalán, A. Costela, J. M. Figuera, and J. M. Muñoz, *Chem. Phys. Lett.* **1986**, *132*, 567-569.

145. K. -Y. Chen, C. -C. Hsieh, Y. -M. Cheng, C. -H. Lai, and P. -T. Chou, *Chem. Comm.* **2006**, *42*, 4395-4397.

146. S. Kim, S. Y. Park, I. Yoshida, H. Kawai, and T. Nagamura, *J. Phys. Chem. B* **2002**, *106*, 9291-9294.

147. K. -I. Sakai, T. Tsuzuki, Y. Itoh, M. Ichikawa, and Y. Taniguch, *Appl. Phys. Lett.* **2005**, *86*, 081103.

148. S. Park, S. Kim, J. Seo, and S. Y. Park, *Macromolecules* **2005**, *38*, 4557-4559.

149. S. Kim, and S. Y. Park, *Adv. Mater.* **2003**, *15*, 1341-1344.

150. S. -J. Lim, J. Seo, and S. Y. Park, *J. Am. Chem. Soc.* **2006**, *128*, 14542-14547.

151. T. Mutai, H. Tomoda, T. Ohkawa, Y. Yabe, and K. Araki, *Angew. Chem. Int. Ed.* **2008**, *47*, 9522-9524.

152. K. -I. Sakai, S. Takahashi, A. Kobayashi, T. Akutagawa, T. Nakamura, M. Dosen, M. Katoc, and U. Nagashima, *Dalton Trans.* **2010**, *39*, 1989-1995.

153. M.-K. Nah, S.-G. Rho, H. K. Kim and J.-G. Kang, J. Phys. Chem. A, 2007, 111, 11437-11443.

154. X. Li, Y. Qian, S. Wang, S. Li and G. Yang, J. Phys. Chem. C, 2009, 113, 3862-3868.

155. S. Kim, J. Seo, H. K. Jung, J. J. Kim, and S. Y. Park, *Adv. Mater.* **2005**, *17*, 2077-2082.

156. K. Szaciłowski, *Chem. Rev.* **2008**, *108*, 3481-354.

157. M. Irie, *Chem. Rev.* **2000**, *100*, 1685-1716.

158. S. Kawata, and Y. Kawata, *Chem. Rev.* **2000**, *100*, 1777-1788.

159. J. A. Delaire, and K. Nakatani, *Chem. Rev.* **2000**, *100*, 1817-1845.

160. N. Tamai, and H. Miyasaka, *Chem. Rev.* **2000**, *100*, 1875-1890.

161. V. Luxami, and S. Kumar, *New J. Chem.* **2008**, *32*, 2074-2079.

162. S. Kumar, V. Luxami, R. Saini, and D. Kaur, *Chem. Commun.* **2009**, 3044-3046.

163. J. Wu, W. Liu, J. Ge, H. Zhang, and P. Wang, *Chem. Soc. Rev.* **2011**, *40*, 3483-3495.

164. B. Pahari, S. Chakraborty, S. Chaudhuri, B. Sengupta, and P. K. Sengupta, *Chem. Phys. Lipids* **2012**, *165*, 488-496.

165. O. M. Zamotaiev, V. Y. Postupalenko, V. V. Shvadchak, V. G. Pivovarenko, A. S. Klymchenko, and Y. Mely, *Bioconjugate Chem.* **2011**, *22*, 101-107.

166. R. Das, A. S. Klymchenko,G. Duportail, and Y.Mely, *Photochem. Photobiol. Sci.* **2009**, *8*, 1583-1589.

167. K. Enander, L. Choulier, A. L. Olsson, D. A. Yushchenko, D. Kanmert, A. S. Klymchenko, A. P. Demchenko, Y. Mely, and D. Altschuh, *Bioconjugate Chem.* **2008**, *19*, 1864-1870.

168. A. S. Klymchenko, and A. P. Demchenko, *New J. Chem.* **2004**, *28*, 687-692.

169. V. V. Shynkar, A. S. Klymchenko, E. Piémont, A. P. Demchenko, Y. Mély, *J. Phys. Chem. A* **2004**, *108*, 8151-8159.

170. K. -C. Wu, Y. -S. Lin, Y. -S. Yeh, C. -Y. Chen, M. O. Ahmed, P. -T. Chou, and Y. -S. Hon, *Tetrahedron*, **2004**, *60*, 11861-11868.

171. K. -C. Wu, Y. -S. Lin, Y. -S. Yeh, C. -Y. Chen, M. O. Ahmed, P. -T. Chou, and Y.-S. Hon, *Tetrahedron* **2004**, *60*, 11861-11868.

172. A. Helal, N. T. T. Thao, S. W. Lee, and H.-S. Kim, *J. Inclusion Phenom. Macrocyclic Chem.* **2010**, *66*, 87-94.

173. W. -H. Chen, Y. Xing, and Y. Pang, *Org. Lett.* **2011**, *13*, 1362-1365.

174. G. Krishnamoorthy, and S. K. Dogra, *J. Lumin.* **2001**, *92*, 91-102.

175. M. M. Balamurali, and S. K. Dogra, *J. Photochem. Photobiol. A* **2002**, *154*, 81-92.

176. S. K. Dogra, *J. Mol. Struct.* **2005**, *734*, 51-60.

177. M. Mosquera, M. C. R. Rodríguez, and F. Rodríguez-Prieto, *J. Phys. Chem. A* **1997**, *101*, 2766-2772.

178. M. C. R. Rodríguez, M. Mosquera, and F. Rodríguez-Prieto, *J. Phys. Chem. A* **2001**, *105*, 10249-10260.

179. A. W. Hull, *Phys. Rev.* **1917**, *10*, 661-696.

180. V. I. Bakhmutov, *Chem. Rev.* **2011**, *111*, 530-562.

181. M. van Gastel, C. C. Lu, K. Wieghardt, and W. Lubitz, *Inorg. Chem.* **2009**, *48*, 2626-2632.

182. P. Serwer, and J. L. Allen, *Biochemistry* **1984**, *23*, 922-927.

183. Y. Su, C. Mu, C. Li, and Z. Jiang, *Ind. Eng. Chem. Res.* **2009**, *48*, 3136-3141.

184. W. H. Flygare, and T. D. Gierke, *Annu. Rev. Mater. Sci.* **1974**, *4*, 255-285.

185. J. D. Ingle, and S. R. Crouch, *Spectrochemical Analysis*, Englewood Cliffs, N.J., Prentice Hall, **1988**.

186. A. Romani, C. Clementi, C. Miliani, and G. Favaro, *Acc. Chem. Res.* **2010**, *43*, 837-846.

187. C. M. Orlando, J. G. Wirth, and D. R. Health, *J. Org. Chem.* **1970**, *35*, 3147-3149.

188. W. J. Coates, B. Connolly, D. Dhanak, S. T. Flynn, and A. Worby, *J. Med. Chem.* **1993**, *36*, 1387-1392.

189. R. W. Middleton, and D. G. Wibberly, *J. Heterocyclic Chem.* **1980**, *17*, 1757-1760.

190. V. Bavetsias, C. Sun, N. Bouloc, J. Reynisson, P. Workman, S. Linardopoulos, and E. McDonald, *Bioorg. Med. Chem. Lett.* **2007**, *17*, 6567-6571.

191. G. A. Crosby, and J. N. Demas, *J. Phys. Chem.* **1971**, *75*, 991-1024.

192. C. Wohlfarth, in *Permittivity (Dielectric Constant) of Liquids*; W. M. Haynes, Ed.; CRC Handbook of Chemistry and Physics; cRC Press, Taylor & Francis Group, New York, **2010**, 91 Ed.; Section 6, 186-207.

193. *Refractive Indices of Pure Liquids and Binary Liquids Mixtures (Supplement to III/38)*; Book Series: Landolt-Börnstein – Group III Condensed Matter; Springer Berlin Heidelberg, **2008**, *Vol. 47*, doi: 10.1007/978-3-540-75291-2.

194. E. Lewars, *Computational Chemistry*; Kluwer Academic, Boston **2003**.

195. C. J. Cramer, *Essentials of Computational Chemistry*; John Wiley and Sons, Chichester **2002**.

196. A. Szabo, and N. S. Ostlund, *Modern Quantum Chemistry: Introduction to Advanced Electronic Structure theory*; Dover Publication, New York **1989**.

197. Æ. Frisch, M. J. Frisch, and G. W. Trucks, *Gaussian 03 User's Reference*, 2nd Edition, Gaussian Inc. Wallingford, CT, **2005**.

198. J. B. Foresman, and Æ. Frisch, *Exploring Chemistry with Electronic Structure Methods*, 2nd Edition, Gaussian Inc. Pittsburgh, PA, **1996**.

199. J. B. Foresman, M. Head-Gordon, J. A. Pople, and M. J. Frisch, *J. Phys. Chem.* **1992**, *96*, 135-149.

200. Y. Wu, P. V. Lawson, M. M. Henary, K. Schmidt, J. -L. Brédas, and C. J. Fahrni, *J. Phys. Chem. A* **2007**, *111*, 4584-4595.

201. C. M. Gittins, E. A. Rohlfing, and C. M. Rohlfing, *J. Chem. Phys.* **1996**, *105*, 7323-7335.

202. K. B. Wiberg, Y. Wang, A. E. de Oliveira, S. A. Perera, and P. H. Vaccaro, *J. Phys. Chem. A* **2005**, *109*, 466-477.

203. A. B. J. Parusel, W. Rettig, and W. Sudholt, *J. Phys. Chem. A* **2002**, *106*, 804-815.

204. J. F. Stanton, J. Gauss, N. Ishikawa, and M. Head-Gordon, *J. Chem. Phys.* **1995**, *103*, 4160-4174.

205. V. I. Stsiapura, A. A. Maskevich, V. A. Kuzmitsky, K. K. Turoverov, and I. M. Kuznetsova, *J. Phys. Chem. A* **2007**, *111*, 4829-4835.

206. K. Luth, and S. Scheiner, *J. Phys. Chem.* **1994**, *98*, 3582-3587.

207. K. Luth, and S. Scheiner, *J. Phys. Chem.* **1995**, *99*, 7352-7359.

208. M. C. Rovira, and S. Scheiner, *J. Phys. Chem.* **1995**, *99*, 9854-9861.

209. S. Scheiner, T. Kar, and M. Čuma, *J. Phys. Chem. A* **1997**, *101*, 5901-5909.

210. V. Barone, and C. Adamo, *Int. J. Quantum Chem.* **1997**, *61*, 429-442.

211. M. J. Frisch, I. N. Ragazos, M. A. Robb, and H. B. Schlegel, *Chem. Phys. Lett.* 1992, 189, 524-528.

212. A. L. Sobolewski, and W. Domcke, *Phys. Chem. Chem. Phys.* **2006**, *8*, 3410-3417.

213. M. J. Paterson, L. Blancafort, S. Wilsey, and M. A. Robb, *J. Phys. Chem. A* **2002**, *106*, 11431-11439.

214. O. Vendrell, R. Gelabert, M. Moreno, and J. M. Lluch, *Chem. Phys. Lett.* **2004**, *396*, 202-207.

215. J. D. Coe, and T. J. Martínez, *J. Phys. Chem. A* **2006**, *110*, 618-630.

216. P. -A. Malmqvist, and B. O. Roos, *Chem. Phys. Lett.* **1989**, *155*, 189-194.

217. J. Stalring, A. Bernhardsson, and R. Lindh, *Mol. Phys.* **2001**, *99*, 103-114.

218. M. E. Casida, in *Recent Advances in Density Functional Methods, Part I*, D. P. Chong, Ed.; World Scientific, Singapore, **1995**, Chap. 5, 155-192.

219. E. K. U. Gross, J. Dobson, and M. Petersilka, *Top. Curr. Chem.* **1996**, *181*, 81-172.

220. G. J. Zhao, and K. L. Han, *J. Phys. Chem. A* **2009**, *113*, 14329-14335.

221. R. Casadesús, M. Moreno, and J. M. Lluch, *J. Photochem. Photobiol. A* **2005**, *173*, 365-374.

222. C. Jamorski, J. B. Foresman, C. Thilgen, and H. –P. Lüthi, *J. Chem. Phys.* **2002**, *116* , 8761-8771.

223. T. Pal, M. Paul, and S. Ghosh, *J. Mol. Struct. (THEOCHEM)* **2008**, *860*, 8-12.

224. H. –H. G. Tsai, H. –L. S. Sun, and C. –J. Tan, *J. Phys. Chem. A* **2010**, *114*, 4065-4079.

225. A. J. A. Aquino, H. Lischka, and C. Hättig, *J. Phys. Chem. A* **2005,** *109*, 3201-3208.

226. J. Wakita, S. Inoue, N. Kawanishi, and S. Ando, *Macromolecules* **2010**, *43*, 3594-3605.

227. C. V. Caillie, and R. D. Amos, *Chem. Phys. Lett.* **2000**, *317*, 159-164.

228. Z.Yang, S. Yang, and J. Zhang, *J. Phys. Chem. A* **2007**, *111*, 6354-6360.

229. M. K. Shukla, and J. Leszczynski, *Int. J. Quantum Chem.* **2005**, *105*, 387-395.

230. G. Gahungu, and J. Zhang, *J. Phys. Chem. B* **2005**, *109*, 17762-17767.

231. M. Belletête, N. Blouin, P. -L. T. Boudreault, M. Leclerc, and G. Durocher, *J. Phys. Chem. A* **2006**, *110*, 13696-13704.

232. F. A. S. Chipem, S. Chatterjee, and G. Krishnamoorthy, *J. Photochem. Photobiol. A* **2010**, *214*, 121-127.

233. S. Miertuš, E. Scrocco, and J. Tomasi, *Chem. Phys.* **1981**, *55*, 117-129.

234. E. Cancès, B. Mennucci, and J. Tomasi, *J. Chem. Phys.* **1997**, *107*, 3032-3041.

235. M. J. Frisch, G. W. Trucks, H. B. Schlegel, G. E. Scuseria, M. A. Robb, J. R. Cheeseman, J. A. Montgomery, T. Vreven Jr., K. N. Kudin, J. C. Burant, J. M. Millam, S. S. Iyengar, J. Tomasi, V. Barone, B. Mennucci, M. Cossi, G. Scalmani, N. Rega, G. A. Petersson, H. Nakatsuji, M. Hada, M. Ehara, K. Toyota, R. Fukuda, J. Hasegawa, M. Ishida, T. Nakajima, Y. Honda, O. Kitao, H. Nakai, M. Klene, X. Li, J. E. Knox, H. P. Hratchian, J. B. Cross, V. Bakken, C. Adamo, J. Jaramillo, R. Gomperts, R. E. Stratmann, O. Yazyev, A. J. Austin, R. Cammi, C. Pomelli, J. W. Ochterski, P. Y. Ayala, K. Morokuma, G. A. Voth, P. Salvador, J. J. Dannenberg, V. G. Zakrzewski, S. Dapprich, A. D. Daniels, M. C. Strain, O. Farkas, D. K. Malick, A. D. Rabuck, K. Raghavachari, J. B. Foresman, J. V. Ortiz, Q. Cui, A. G. Baboul, S. Clifford, J. Cioslowski, B. B. Stefanov, G. Liu, A. Liashenko, P. Piskorz, I. Komaromi, R. L. Martin, D. J. Fox,; T. Keith, M. A. Al-Laham, C. Y. Peng, A. Nanayakkara, M. Challacombe, P. M. W. Gill, B. Johnson, W. Chen, M. W. Wong, C. Gonzalez and J. A. Pople, Gaussian 03, Revision E.01, Gaussian, Inc., Wallingford CT, **2004**.

236. *GaussView 4.1*, Gaussian, Inc., Wallingford CT, **2006**.

237. W. J. Hehre, R. Ditchfield, and J. A. Pople, *J. Chem. Phys.* **1972**, *56*, 2257-2261.

238. P. Hohenberg, and W. Kohn, *Phys. Rev. B* **1964**, *136*, 864-871.

239. W. Kohn, and L. J. Sham, *Phys. Rev. A* **1965**, *140*, 1133-1138.

240. A. D. Becke, *J. Chem. Phys.* **1993**, *98*, 5648-5652.

241. C. Lee, W. Yang, and R. G. Parr, *Phys. Rev. B* **1988**, *37*, 785-789.

242. J. R. Lakowicz, *Principles of Fluorescence Spectroscopy*, 3rd ed.; Springer: New York, **2006**.

243. B. Valeur, *Molecular Fluorescence: Principles and Applications*; Wiley-VCH: Weinheim, Germany, **2002**.

244. B. Valeur, and J. -C. Brochon, *New Trends in Fluorescence Spectroscopy: Applications to Chemical and Life Science*; Springer: New York, **2001**.

245. J. A. Ross, and D. M. Jameson, *Photochem. Photobiol. Sci.* **2008**, *7*, 1301-1312.

246. M. Y. Berezin, and S. Achilefu, *Chem. Rev.* **2010,** *110*, 2641-2684.

247. W. Becker, *Advanced Time-Correlated Single Photon CountingTechniques*; Springer: Berlin, **2005**.

248. W. Becker, *The bh TCSPC Handbook*, 3rd Ed.; Becker & Hickl Gmbh: Berlin, Germany, **2008**.

249. *Fluorescence Analysis Software Technology (FAST)*, Edinburgh Intruments Ltd., 2 Bain Square, Kirkton Campus, Livingston EH54 7DQ, UK, **2007**.

250. *SMART, SAINT and XPREP*, Siemens Analytical X-ray Instruments Inc.: Madison, WI, **1995**.

251. G. M. Sheldrick, *SADABS: Software for Empirical Absorption Correction*, University of Gottingen, Institute fur Anorganische Chemieder Universitat: Tammanstrasse 4, D-3400, Gottingen, Germany, **1999-2003**.

252. G. M. Sheldrick, *SHELXS-97*, University of Gottingen: Germany, **1997**.

253. G. M. Sheldrick, *SHELXL-97: Program for Crystal Structure Refinement*, University of Gottingen, Gottingen, Germany, **1997**.

254. *Mercury 2.3*, Supplied with Cambridge Structural Database; CCDC, Cambridge, U.K., **2007**.

255. J. Waluk, in *Conformational Analysis of Molecules in Excited States*; J. Waluk, Ed.; Wiley-VCH: New York, **2000**; Chapter 2.

256. M. Itoh and Y. Fujiwara, *J. Am. Chem. Soc.* **1985**, *107*, 1561-1565.

257. F. Y. Dupradeau, D. A. Case, C. Z. Yu, R. Jimenez, and F. E. Romesberg, *J. Am. Chem. Soc.* **2005**, *127*, 15612-15617.

258. M. Rini, A. Kummrov, J. Dreyer, E. T. J. Nibbering, and T. Elsaesser, *Faraday Discuss.* **2003**, *122*, 27-40.

259. K. Das, N. Sarkar, D. Majumdar, and K. Bhattacharyya, *Chem. Phys. Lett.* **1992**, *198*, 443-448.

260. M. Forés, M. Duran, and L. Adamowicz, *J. Phys. Chem. A* **1999**, *103*, 4413-4420.

261. M. A. Ríos, and M. C. Ríos, *J. Phys. Chem. A* **1998**, *102*, 1560-1567.

262. O. Vendrell, M. Moreno and J. M. Lluch, *J. Chem. Phys*. **2002**, *117*, 7525-7533.

263. R. Casadesús, O. Vendrell, M. Moreno and J. M. Lluch, *Chem. Phys. Lett*. **2005**, *405*, 187-192.

264. S. R. Vázquez, C. R. Rodríguez, M. Mosquera, and F. R. -Prieto, *J. Phys. Chem. A* **2007**, *111*, 1814-1826.

265. V. A. Kharlanov, W. Rettig, M. I. Knyazhansky, and N. Makaraova, *J. Photochem. Photobiol. A* **1997**, *103*, 45-50.

266. A. Dreuw, J. L. Weisman, and M. Head-Gordon, *J. Chem. Phys*. **2003**, *119*, 2943-2946.

267. A. L. Sobolewski, and W. Domcke, *Chem. Phys*. **2003**, *294*, 73-83.

267b. R. Englman, and J. Jortner, *Mol. Phys.* **1970**, *18*, 145-164.

268. B. K. Paul, and N. Guchhait, *J. Lumin.* **2012**, *132*, 2194-2208.

269. S. M. Ormson, and R. G. Brown, *Prog. React. Kinet.* **1994**, 19, 45.

270. A. Mordziński, and A. Grabowska, *Chem. Phys. Lett.* **1982**, *90*, 122-127.

271. W. Al-Soufi, K. H. Grellmann, and B. Nickel, *Chem. Phys. Lett.* **1990**, *174*, 609-616.

272. R. S. Becker, C. Lenoble, and A. Zein, *J. Phys. Chem.* **1987**, *91*, 3509-3517.

273. C. A. Potter, R. G. Brown, F. Vollmer, and W. Rettig, *J. Chem. Soc., Faraday Trans.* **1994**, *90*, 59-67.

274. P. F. Barbara, L. E. Brus, and P. M. Rentzepis, *J. Am. Chem. Soc*. **1980**, *102*, 5631-5635.

275. A. Mordziński, and K. H. Grellmann, *J. Phys. Chem.* **1986**, *90*, 5503-5506.

276. W. E. Brewer, M. L. Martinez, and P. -T. Chou, *J. Phys. Chem.* **1990**, *94*, 1915-1918.

277. S. Nagaoka, A. Itoh, K. Mukai, and U. Nagashima, *J. Phys. Chem.* **1993**, *97*, 11385-11392.

278. M. Ikegami, and T. Arai, *J. Chem. Soc. Perkin Trans.* **2002**, *2*, 1296-1301.

279. H. Konoshima, S. Nagao, I. Kiyota, K. Amimoto, N. Yamamoto, M. Sekine, M. Nakata, K. Furukawa, and H. Sekiya, *Phys. Chem. Chem. Phys.* **2012**, *14*, 16448-16457.

280. A. Brenlla, M. Veiga, M. C. R. Rodríguez, M. Mosquera, and F. Rodríguez-Prieto, *Photochem. Photobiol. Sci.*, **2011**, *10*, 1622-1636.

281. E. L. Roberts, J. Dey, and I. M. Warner, *J. Phys. Chem. A* **1997**, *101*, 5296-5301.

282. D. R. James, and W. R. Ware, *Chem. Phys. Lett.* **1985**, *120*, 455-459.

283. A. P. de Silva, H. Q. N. Gunaratne, T. Gunnlaugsson, A. J. M. Huxley, C. P. McCoy, J. T. Rademacher, and T. E. Rice, *Chem. Rev.* **1997**, *97*, 1515-1566.

284. D. T. McQuade, A. E. Pullen, and T. M. Swager, *Chem. Rev.* **2000**, *100*, 2537-2574.

285. J. Yuasa, and S. Fukuzumi, *J. Am. Chem. Soc.* **2006**, *128*, 15976-15977.

286. X. Chen, M. J. Jou, and J. Yoon, *Org. Lett.* **2009**, *11*, 2181-2184.

287. Z. C. Wen, J. A. B. Ferreira, S. M. B. Costa, *J. Photochem. Photobiol. A Chem.* **2008**, *199*, 98-104.

288. A. Afkhami, M. Abbasi-Tarighat, and H. Khanmohammadi, *Talanta* **2009**, *77*, 995-1001.

289. Q. -S. Lu, L. Dong, J. Zhang, J. Li, L. Jiang, Y. Huang, S. Qin, C. -W. Hu, and X. -Q. Yu, *Org. Lett.* **2009**, *11*, 669-672.

290. M. R. Loken, J. W. Mayer, J. Gohlke, and C. Brand, *Biochemistry* **1972**, *11*, 4779-4786.

291. J. Seo, S. Kim, S. Y. Park; *J. Am. Chem. Soc.* **2004**, *126*, 11154-11155.

292. A. Ajayaghosh, P. Carol, and S. Sreejith, *J. Am. Chem. Soc.* **2005**, *127*, 14962-14963.

293. L. Xue, C. Liu, and H. Jiang, *Chem. Commun.* **2009**, 1061-1063.

294. L. Xue, Q. Liu, and H. Jiang, *Org. Lett.* **2009**, *11*, 3254-3457.

295. C. Hou, Y. Xiong, N. Fu, C. C. Jacquot, T. C. Squier, H. Cao, *Tet. Lett.* **2011**, *52*, 2692-2696.

296. H. Yang, Z. -Q. Liu, Z. -G. Zhou, E. -X. Shi, F. -Y. Li, Y. -K. Du, T. Yi, and C. -H. Huang, *Tet. Lett.* **2006**, *47*, 2911-2914.

297. G. Grynkiewicz, M. Poenie, and R. Y. Tsien, *J. Biol. Chem.* **1985**, *260*, 3440-3450.

298. M. M. Henary, and C. J. Fahrni, *J. Phys. Chem. A* **2002**, *106*, 5210-5220.

299. S. Ercelen, A. S. Klymchenko, and A. P. Demchenko, *Anal. Chim. Acta* **2002**, *464*, 273-287.

300. A. S. Klymchenko, and A. P. Demchenko, *Phys. Chem. Chem. Phys.* **2003**, *5*, 461-468.

301. D. A. Yushchenko, V. V. Shvadchak, A. S. Klymchenko, G. Duportail, V G. Pivovarenko, and Y. Mely, *J. Phys. Chem. A* **2007**, *111*, 10435-10438.

302. H. Tong, G. Zhou, L. X. Wang, X. Jing, F. S. Wang, and J. P. Zhang, *Tetrahedron Lett.* **2003**, *44*, 131-134.

303. X. Peng, Y. Wu, J. Fan, M. Tian, K. and Han, *J. Org. Chem.* **2005**, *70*, 10524-10531.

304. M. K. Nayak, J. Seo, S. Park, and S. Y. Park, *J. Photochem. Photobiol. A: Chem.* **2007**, 191, 228-232.

305. R. Hu, J. Feng, D. Hu, S. Wang, S. Li, Y. Li, G. Yang, *Angew. Chem. Int. Ed.* **2010**, *49*, 4915-4918.

306. X. -F. Yang, H. Qi, L. Wang, Z. Su, G. Wang, *Talanta* **2009**, *80*, 92-97.

307. S. O. Obare, and C. J. Murphy, *New J. Chem.* **2001**, *25*, 1600-1604.

308. M. M. Henary, Y. Wu, and C. J. Fahrni, *Chem. Eur. J.* **2004**, *10*, 3015-3025.

309. M. Taki, J. L. Wolford, and T. V. O'Halloran, *J. Am. Chem. Soc.* **2004**, *126*, 712-713.

310. X. -B. Zhang, G. Cheng, W. -J. Zhang, G. -L. Shen, R. -Q. Yu, *Talanta* **2007**, *71*, 171-177.

311. Y. Tian, C. -Y. Chen, C. -C. Yang, A. C. Young, S. -H. Jang, W. -C. Chen, A. K. -Y. Jen, *Chem. Mater.* **2008**, *20*, 1977-1987.

312. X. Yongqian, and P. Yi, *Dalton Trans.* **2011**, *40*, 1503-1509.

313. N. C. Lim, H. C. Freake, and C. Brückner, *Chem. -Eur. J.* **2005**, *11*, 38-49.

314. G. Krishnamoorthy, and S. K. Dogra, *J. Org. Chem.* **1999**, *64*, 6566-6574.

315. N. Dash, and G. Krishnamoorthy, *J. Fluoresc.* **2010**, *20*, 135-142.

316. M. V. Rekharsky, and Y. Inoue, *Chem. Rev.* **1998**, *98*, 1875-1918.

317. R. Villalonga, R. Cao, and A. Fragoso, *Chem. Rev.* **2007**, *107*, 3088-3116.

318. K. Ukeama, F. Hirayama, and T. Irie, *Chem. Rev.* **1998**, *98*, 2045-2076.

319. W. Saenger, *Angew. Chem., Int. Ed. Engl.* **1980**, *19*, 344-362.

320. A. Harada, *Acc. Chem. Res.* **2001**, *34*, 456-464.

321. S. Hashimoto, and J. K. Thomas, *J. Am. Chem. Soc.* **1985**, *107*, 4655-4662.

322. W. Saenger, J. Jacob, K. Gessler, T. Steiner, D. Hoffman, H. Sanbe, K. Koizumi, S. M. Smith, and T. Tahaka, *Chem. Rev.* **1998**, *98*, 1787-1802.

323. S. Li, and W. C. Purdy, *Chem. Rev.* **1992**, *92*, 1457-1490.

324. C. L. Jeang, D. G. Lin, and S. H. Hsieh, *J. Agric. Food Chem.* **2005**, 53, 6301-6304.

325. V. Rimphanitchayakit, T. Tonuzuka, and Y. Sakano, *Carbohydr. Res.* **2005**, *340*, 2279-2289.

326. J. Szejtli, *Chem. Rev.* **1998**, *98*, 1743-1754.

327. K. L. Mittal, and B. Landman, Eds.; *Surfactants in Solutions*, Plenum Press, New York, **1984**.

328. D. Langevin, *Acc. Chem. Res.* **1988**, *21*, 255-260.

329. W. M. Gelbart, A. Ben-Shaul, and D. Roux, *Micelles, Membranes, Microemulsions and Monolayers*; Springer-Verlag: New York, **1994**.

330. J. Eastoe, W. K. Young, B. H. Robinson, and D. C. Steytler, *J. Chem. Soc. Faraday Trans.* **1990**, *86*, 2883-2889.

331. T. K. Jain, M. Varshney, and A. J. Maitra, *J. Phys. Chem.* **1989**, *93*, 7409-7416.

332. J. H. Fendler, in *Membrane Mimetic Chemistry*, Wiley, New York, **1982,** 48.

333. D. L. Sacket, J. R. Knutson, and J. Wolff, *J. Biol. Chem.* **1990**, *265*, 14899-14906.

334. K. B. Einsenthal, *Chem. Rev.* **1996**, *96*, 1343-1360.

335. S. B. Zhu, S. Singh, and G. W. Robinson, *Adv. Chem. Phys.* **1994**, *85*, 627.

336. P. L. Luisi, M. Giomini, M. P. Pileni, and R. H. Robinson, *Biochim. Biophys. Acta* **1988**, *947*, 209-246.

337. D. L. Nelson, and M. M. Cox, in *Lehninger Principles of Biochemistry*, 4th Edition, W.H. Freeman, New York, **2005**.

338. C. K. Mathews, K. E. van Holde, and K. G. Ahern, in *Biochemistry*, 3rd Edition, Prentice Hall, **2000**.

339. J. P. Nicholson, M. R. Wolmarans, and G. R. Park, *Brit. J. Anaesth.* **2000**, *85*, 599-610.

340. A. D. McLachlan, and J. E. Walker, *J. Mol. Biol.* **1977**, *112*, 543-558.

341. N. Sarkar, A. Datta, S. Das, K. Das, and K. Bhattacharyya, *J. Photochem. Photobiol. A* **1997**, *109*, 259-265.

342. N. Chattopadhyay, *J. Photochem. Photobiol. A* **1991**, *58*, 31-36.

343. P. T. Chou, W. C. Cooper, J. H. Clements, S. L. Studer, and C. P. Cheng, *Chem. Phys. Lett.* **1993**, *216*, 300-304.

344. S. Banthia, and A. Samanta, *J. Phys. Chem. B* **2006**, *110*, 6437-6440.

345. L. A. Blyshak, T. M. Rossi, G. Patonay, and I. M. Warner, *Anal. Chem.* **1988**, *60*, 2127-2131.

346. E. Iglesias, *J. Org. Chem.* **2006**, *71*, 4383-4392.

347. A. Banerjee, K. Basu, and P. K. Sengupta, *J. Photochem. Photobiol. B* **2007**, *89*, 88-97.

348. M. Sanz, J. A. Organero, and A. Douhal, *Chem. Phys.* **2007**, *338*, 135-142.

349. N. Dash, F. A. S. Chipem, and G. Krishnamoorthy, *Photochem. Photobiol. Sci.* **2009**, *8*, 1708-1715.

350. P. Das, A. Chakrabarty, B. Haldar, A. Mallick, and N. Chattopadhyay, *J. Phys. Chem. B* **2007**, *111*, 7401-7408.

351. Y. Matsushita, T. Suzuki, T. Ichimura, and T. Hikida, *J. Phys. Chem. A* **2004,** *108*, 7490-7496.

352. S. Ralkshit, and S. Vasudevan, *ACS Nano* **2008**, *2*, 1473-1479.

353. J. A. Faiz, L. E. P. Kyllonen, P. Contreras-Carballada, R. M. Williams, L. De Cola, and Z. Pikramenou, *Dalton Trans.* **2009**, 3980-3987.

354. A. Douhal, *Chem. Rev.* **2004**, *104*, 1955-1976.

355. C. Martín, M. Gil, B. Cohen, and A. Douhal, *Langmuir* **2012**, *28*, 6746-6759.

356. R. N. DSouza, U. Pischel, and W. M. Nau, *Chem. Rev*. **2011**, *111*, 7941-7980.

357. B. D. Wagner, *Phys. Chem. Chem. Phys.* **2012**, *14*, 8825-8835.

358. E. L. Roberts, P. T. Chou, T. A. Alexander, R. A. Agbaris, and I. M. Warner, *J. Phys. Chem.* **1995**, *99*, 5431-5437.

359. B. K. Paul, A. Samanta, and N. Guchhait, *Langmuir* **2010**, *26*, 3214-3224.

360. Y. -B. Jiang, *J. Photochem. Photobiol. A* **1995**, *88*, 109-116.

361. S. Panja, P. Chowdhury, and S. Chakravorti, *Chem. Phys. Lett.* **2004**, *393*, 409-415.

362. A. Douhal, T. Fiebig, M. Chachisvilis, and A. H. Zewail, *J. Phys. Chem. A* **1998**, *102*, 1657-1660.

363. N. Dash, F. A. S. Chipem, R. Swaminathan, and G. Krishnamoorthy, *Chem. Phys. Lett.* **2008**, *460*, 119-124.

364. G. Krishnamoorthy, in *Hydrogen Bonding and Transfer in the Excited State*, Han, K.-L.; Zhao, G. J. (Eds.), John Wiley & Sons Ltd., **2011**, Vol. 1, pp. 313-327.

365. M. Mukhopadhyay, D. Banerjee, and S. Mukherjee, *J. Phys. Chem. A*, **2006**, *110*, 12743-12751.

366. M. L. Benesi, and J. H. Hildebrand, *J. Am. Chem. Soc.* **1949**, *71*, 2703-2707.

367. S. Hamai, *J. Phys. Chem.* **1989**, *93*, 2074-2078.

368. M. K. Singh, H. Pal, A. S. R. Koti, and A. V. Sapre, *J. Phys. Chem. A* **2004**, *108*, 1465-1474.

369. M. A. Voinov, I. A. Kirilyuk, and A. I. Smirnov, *J. Phys. Chem. B* **2009**, *113*, 3453-3460.

370. J. Szejtli, in *Cyclodextrins and Their Inclusion Complexes*; Akademiai Kiado: Budepest, **1982**.

371. G. Krishnamoorthy, and S. K. Dogra, *J. Photochem. Photobiol. A* **1999**, *123*, 109-119.

372. G. Krishnamoorthy, and S. K. Dogra, *J. Phys. Chem. A* **2000**, *104*, 2542-2551.

373. M. El-Kemary, J. A. Organero, L. Santos, and A. Douhal, *J. Phys. Chem. B* **2006**, *110*, 14128-14134.

374. S. K. Pal, and A. H. Zewail, *Chem. Rev.* **2004**, *104*, 2099-2123.

375. N. Nandi, K. Bhattacharyya, and B. Bagchi, *Chem. Rev.* **2000**, *100*, 2013-2045.

376. N. Prabhu, and K. Sharp, *Chem. Rev.* **2006**, *106*, 1616-1623.

377. B. Bagchi, *Chem. Rev.* **2005**, *105*, 3197-3219.

378. A. S. Klymchenko, and A. P. Demchenko, *Langmuir* **2002**, *18*, 5637-5639.

379. A. Douhal, G. Angulo, M. Gil, J. A. Organero, M. Sanz, and L. Tormo, *J. Phys. Chem. B* **2007**, *111*, 5487-5493.

380. E. Levinger, *Science* **2002**, *298*, 1722-1723.

381. I. A. Heisler, M. Kondo, and S. R. Meech, *J. Phys. Chem. B* **2009**, *113*, 1623-1631.

382. K. M. Manoj, R. Jayakumar, and S. K. Rakshit, *Langmuir* **1996**, *12*, 4068-4072.

383. M. Hof, P. Lianos, and A. Laschewsky, *Langmuir* **1997**, *13*, 2181-2183.

384. J. Kim, and M. Lee, *J. Phys. Chem. A* **1999**, *103*, 3378-3382.

385. A. Datta, D. Mandal, S. K. Pal, and K. Bhattacharyya, *J. Phys. Chem. B* **1997**, *101*, 10221-10225.

386. S. D. Choudhury, S. Nath, and H. Pal, *J. Phys. Chem. B* **2008**, *112*, 7748-7753.

387. S. D. Choudhury, and H. Pal, *J. Phys. Chem. B* **2009**, *113*, 6736-6744.

388. M. Hasegawa, *Langmuir* **2001**, *17*, 1426-1431.

389. B. Cohen, D. Huppert, K. M. Solntsev, Y. Tsfadia, E. Nachliel, and M. Gutman, *J. Am. Chem. Soc.* **2002**, *124*, 7539-7547.

390. G. Angulo, J. A. Organero, M. A. Carranza, and A. Douhal, *J. Phys. Chem. B* **2006**, *110*, 24231-24237.

391. E. Bardez, B. -T. Goguillon, E. Keh, and B. Valeur, *J. Phys. Chem.* **1984**, *88*, 1909-1913.

392. E. Bardez, E. Monnier, and B. Valeur, *J. Phys. Chem.* **1985**, *89*, 5031-5036.

393. S. M. Andrade, S. M. B. Costa, and R. Pansu, *Photochem. Photobiol.* **2000**, *71*, 405-412.

394. J. G. Ray, and P. K. Sengupta, *Chem. Phys. Lett.* **1994**, *230*, 75-81.

395. D. E. Moilanen, N. E. Levinger, D. B. Spry, and M. D. Fayer, *J. Am. Chem. Soc.* **2007**, *129*, 14311-14318.

396. I. R. Piletic, D. E. Moilanen, D. B. Spry, N. E. Levinger, and M. D. Fayer, *J. Phys. Chem. A* **2006**, *110*, 4985-4999.

397. P. L. Luisi, and B. E. Straub, Eds.; *Reverse Micelles: Biological and Technological Relevance of Amphiphilic Structures in Apolar Media*; Plenum Press, New York, **1984**.

398. K. Kalyanasundaram, in *Photochemistry in Microheterogeneous Systems*; Academic Press, London, **1987**.

399. G. Krishnamoorthy, and S. K. Dogra, *J. Colloid Interface. Sci.* **1999**, *213*, 53-61.

400. C. Kumar, and D. Balasubramanian, *J. Colloid Interface Sci.* **1980**, *74*, 64-70.

401. G. B. Dutt, *J. Phys. Chem. B* **2004**, *108*, 7944-7949.

402. S. D. Choudhury, M. Kumbhakar, S. Nath, S. K. Sarkar, T. Mukherjee, and H. Pal, *J. Phys. Chem. B* **2007**, *111*, 8842-8853.

403. D. A. Kelkar, and A. Chattopadhyay, *J. Phys. Chem. B* **2004**, *108*, 2004, 12151-12158.

404. P. K. Singh, M. Kumbhakar, H. Pal, and S. Nath, *J. Phys. Chem. B* **2009**, *113*, 1353-1359.

405. A. A. Waheed, R. K. Sridhar, and P. D. Gupta, *Anal. Biochem.* **2000**, *287*, 73-79.

406. X. M. He, and D. C. Carter, *Nature* **1992**, *358*, 209-216.

407. U. Kragh-Hansen, *Pharmacological Review* **1981**, *33*, 17-53.

408. F. Karush, *J. Am. Chem. Soc.* **1950**, *72*, 7205-2713.

409. P. Bourassa, C. D. Kanakis, P. Tarantilis, M. G. Pollissiou, and H. A. Tajmir-Riahi, *J. Phys. Chem. B* **2010**, *114*, 3348-3354.

410. F. -L. Cui, J. Fan, J. -P. Lib, and Z. -D. Hua, *Bioorg. Med. Chem.* **2004**, *12*, 151-157.

411. V. S. Jisha, K. T. Arun, M. Hariharan, and D. Ramaiah, *J. Am. Chem. Soc.* **2006**, *128*, 6024-6025.

412. G. Sudlow, D. J. Birkett, and D. N. Wade, *Mol. Pharmacl.* **1976**, *12*, 1052-1061.

413. A. J. Ozinskas, *Principles of Fluorescence Immunoassay*, in *Topics in Fluorescence Spectroscopy*, Volume 4 – *Probe Design and Chemical Sensing*, J. R. Lakowicz, Ed.; Plenum Press, New York and London, **1994**, Vol. 4, 449-496.

414. H. Dodiuk, H. Kanety, and E. M. Kosower, *J. Phys. Chem.* **1979,** *83*, 515-521.

415. B. K. Paul, A. Samanta, and N. Guchhait, *J. Phys. Chem. B* **2010**, *114*, 6183-6196.

416. B. K. Paul, D. Ray, and N. Guchhait, *Phys. Chem. Chem. Phys.* **2012**, *14*, 8892-8902.

417. L. Fabrizzi, and A. Poggi, *Chem. Soc. Rev.* **1995**, *24*, 197-202.

418. B. Bhattacharya, S. Nakka, L. Guruprasad, and A. Samanta, *J. Phys. Chem. B* **2009,** *113*, 2143-2150.

419. B. K. Paul, and N. Guchhait, *J. Phys. Chem. B* **2011**, *115*, 10322-10334.

420. J. C. Penedo, M. Mosquera, and F. Rodríguez-Prieto, *J. Phys. Chem. A* **2000**, *104*, 7429-7441.

421. N. Kungwan, F. Plasser, A. J. A. Aquino, M. Barbatti, P. Wolschann, and H, Lischka, *Phys. Chem. Chem. Phys.* **2012**, *14*, 9016-9025.

422. W. Al-Soufi, K. H. Grellmann, and B. Nickel, *J. Phys. Chem.* **1991**, *95*, 10503-10509.

423. H. Eisenberger, B. Nickel, A. A. Ruth, W. Al-Soufi, K. H. Grellmann, and M. Novo, *J. Phys. Chem.* **1991**, *95*, 10509-10518.

424. M. F. Rodríguez-Prieto, B. Nickel, K. H. Grellmann, and A. Mordziński, *Chem. Phys. Lett.* **1988**, *146*, 387-392.

425. B. Nickel, and M. F. Rodríguez-Prieto, *Chem. Phys. Lett.* **1988**, *146*, 393-398.

426. A. Ohshima, A. Momotake, R. Nagahata, and T. Arai, *J. Phys. Chem. A* **2005**, *109*, 9731-9736.

427. A. K. Ogawa, O. K. Abou-Zied, V. Tsui, R. Jimenez, D. A. Case, and F. E. Romesberg, *J. Am. Chem. Soc.* **2000**, *122*, 9917-9920.

428. O. K. Abou-Zied, R. Jimenez, and F. E. Romesberg, *J. Am. Chem. Soc.* **2001**, *123*, 4613-4614.

429. H. Wang, H. Zhang, O. K. Abou-Zied, C. Yu, F. E. Romesberg, and M. Glasbeek, *Chem. Phys. Lett.* **2003**, *367*, 599-608.

430. O. K. Abou-Zied, R. Jimenez, E. H. Z. Thompson, D. P. Millar, and F. E. Romesberg, *J. Phys. Chem. A* **2002**, *106*, 3665-3672.

431. Th. Arten-Engeland, T. Bultmann, N. P. Ernsting, M. A. Rodríguez, and W. Thiel, *Chem. Phys.* **1992**, *163*, 43-54.

432. G. J. Woolfe, M. Melzig, S. Schneider, and F. Dorr, *Chem. Phys.*, **1983**, *77*, 213-221.

433. M. A. Ríos, and M. C. Ríos, *J. Phys. Chem.* **1995**, *99*, 12456-12460.

434. A. Fernández-Ramos, J. Rodríguez-Otero, M. A. Ríos, and J. Soto, *J. Mol. Struct. Theochem.* **1999**, *489*, 255-262.

435. S. Lochbrunner, K. Stock, and E. Riedle, *J. Mol. Struct.* **2004**, *700*, 13-18.

436. P. -T. Chou, S. L. Studer, and M. L. Martinez, *Chem. Phys. Lett.* **1991**, *178*, 393-398.

437. P. -T. Chou, M. L. Martinez, and S. L. Studer, *Chem. Phys. Lett.* **1992**, *195*, 586-590.

438. P. F. Barbara, P. K. Walsh, and L. E. Brus, *J. Phys. Chem.* **1989**, *93*, 29-34.

439. T. Elsaesser, B. Schmetzer, M. Lipp, and R. J. Bäuerle, *Chem. Phys. Lett.* **1988**, *148*, 112-118.

440. F. Laermer, T. Elsaesser, and W. Kaiser, *Chem. Phys. Lett.* **1988**, *148*, 119-124.

441. W. Frey, F. Laermer, and T. Elsaesser, *J. Phys. Chem.* **1991**, *95*, 10391-10395.

442. S. Lochbrunner, A. J. Wurzer, and E. Riedle, *J. Chem. Phys.*, **2000**, *112*, 10699-10702.

443. S. Mintova, V. De Waele, M. Ho1lzl, U. Schmidhammer, B. Mihailova, E. Riedle, and T. Bein, *J. Phys. Chem. A* **2004**, *108*, 10640-10648.

444. D. Xiao, G. Zhang, H. Wang, G. Tang, and W. Chen, *J. Nonlinear Opt. Phys. Mater.* **2000**, *9*, 309-314.

445. S. Hillebrand, M. Segala, T. Buckup, R. R. B. Correia, F. Horowitz, and V. Stefani, *Chem. Phys.* **2001**, *273*, 1-10.

446. S. M. Chang, K. L. Hsueh, B. K. Huang, J. H. Wu, C. C. Liao, and K. C. Lin, *Surf. Coat. Technol.* **2006**, *200*, 3278-3282.

447. M. Krishnamoorthy, P. Phaniraj, and S. K. Dogra, *J. Chem. Soc., Perkin Trans. II* **1986**, 1917-1925.

448. H. K. Sinha, and S. K. Dogra, *J. Chem. Soc., Perkin Trans. II* **1987**, 1165-1472.

449. A. K. Mishra, and S. K. Dogra, *Spectrochim. Acta A* **1983**, *39*, 609-611.

450. M. Krishnamurthy, and S. K. Dogra, *J. Photochem.* **1986**, *32*, 235-242.

451. S. R. Vázquez, M. C. R. Rodríguez, M. Mosquera, and F. Rodríguez-Prieto, *J. Phys. Chem. A* **2008**, *112*, 376-387.

452. A. Brenlla, F. Rodríguez-Prieto, M. Mosquera, M. A. Ríos, and M. C. R. Rodríguez, *J. Phys. Chem. A* **2009**, *113*, 56-67.

A1. Assignment of Protons in NMR Spectrum of HPIP-c

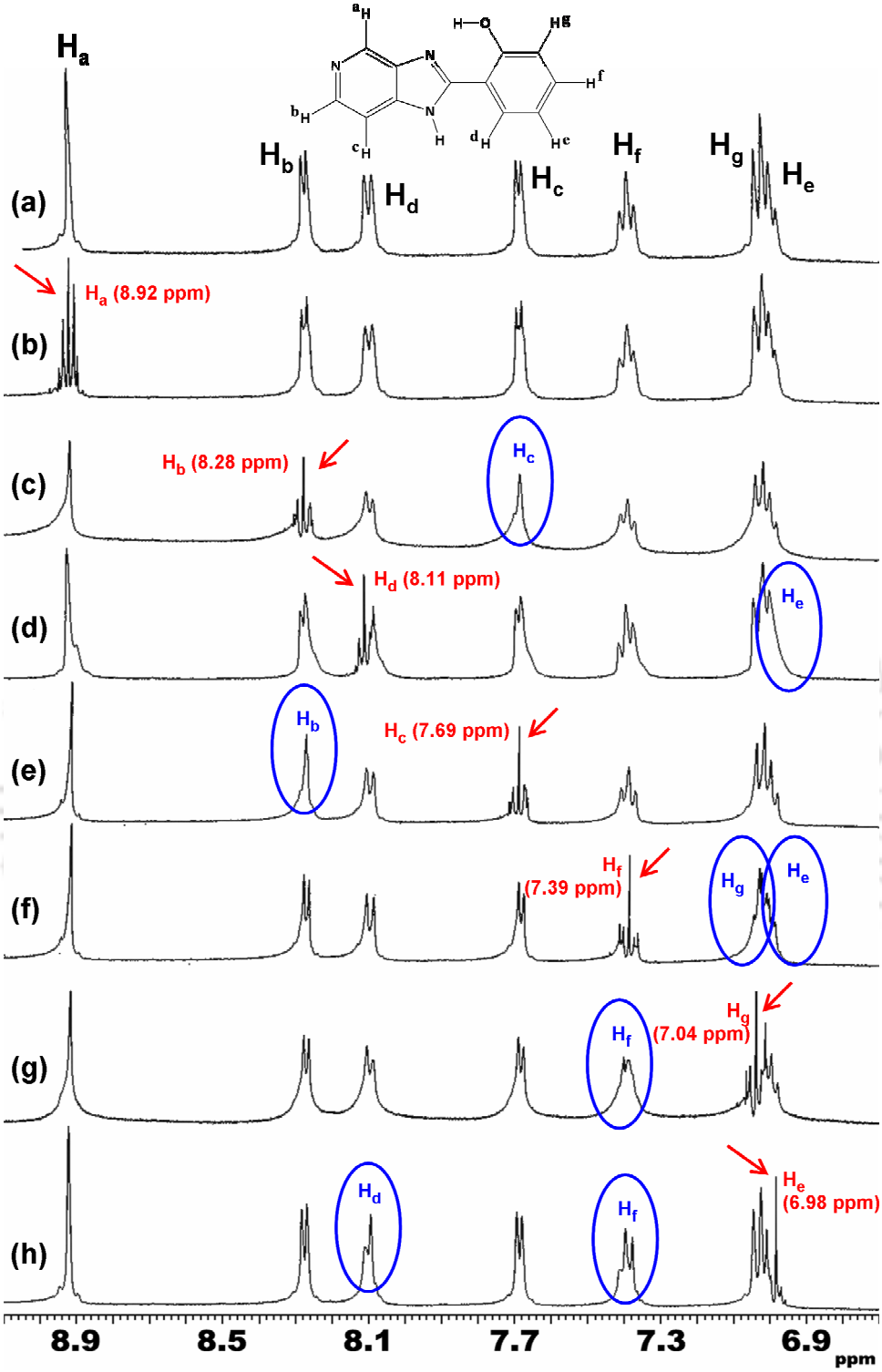

Figure A1. Normal and decoupled ^{1}H NMR spectra of HPIP-c. The arrows indicate the position of decoupler and circles denote the proton(s) that/those is/are affected.

Proton H_a (**Figure A1**) is expected to give a singlet and be found in down field region due to the presence of a neighboring nitrogen atom. Accordingly, the peak at δ = 8.92 ppm (1H, s) can be assigned to H_a proton.

H_b and H_c protons are expected to give doublet peaks. Placing the decoupler at 8.28 ppm (**Figure A1c**), the doublet at 7.69 ppm merges to give a singlet. Similarly, placing the decoupler at 7.69 ppm (**Figure A1e**), the doublet peak at 8.28 ppm becomes singlet. This shows these two protons are coupled and no other protons are involved in coupling. Besides, H_b proton is expected to be down field due to presence of neighboring nitrogen atom. Hence, the peaks at 8.28 ppm (1H, d, J = 6.0 Hz) and 7.69 ppm (1H, d, J = 5.6 Hz) are assigned to H_b and H_c protons, respectively.

Protons H_d and H_g have one neighboring proton H_e and H_f, respectively. Therefore, they are also expected to give doublet. It is reported for similar compounds[1] the H_d type proton appears at down field than the H_g type proton, due to the proximity to heterocyclic ring. Therefore the doublet peak at 8.11 ppm (1H, d, J = 7.6 Hz) may be assigned to H_d proton.

Both H_e and H_f have two different surrounding protons viz. H_d and H_f for H_e proton and H_e and H_g for H_f proton. Hence, doublet of doublet peaks are expected for H_e and H_f protons. The pseudo triplet peak at 7.39 ppm which is because of merging of doublet of doublet peak is due to either H_e or H_f. The quadruplet peak at 6.98 – 7.04 ppm which is composed of two protons is either due to H_g and H_e or H_f protons.

When the decoupler is placed at 8.11 ppm (H_d proton, **Figure A1d**), the peak at 6.98 ppm is affected. Similarly, placing the decoupler at 6.98 ppm (**Figure A1h**), the doublet peak at 8.11 ppm becomes singlet and the pseudo triplet peak at 7.39 ppm is also affected. This shows the peak at 6.98 ppm is due to H_e proton and the pseudo triplet peak at 7.39 ppm (1H, t, J = 8.0 Hz, 7.6 Hz) is due to H_f proton. Further, this confirms the peak at 8.11 ppm is due to H_d proton.

When the decoupler is placed at 7.39 ppm (**Figure A1f**), the peaks at 6.98 ppm and 7.04 ppm (which constitute the quadruplet) are affected. This implies the 7.04 ppm peak is due to H_g proton. This also confirms the peak at 6.98 ppm is due to H_e proton.

References

1. N. Dash, F. A. S. Chipem, and G. Krishnamoorthy, *Photochem. Photobiol. Sci.* **2009**, *8*, 1708–1715.

A2. Assignment of Protons in NMR Spectrum of HPIP-b

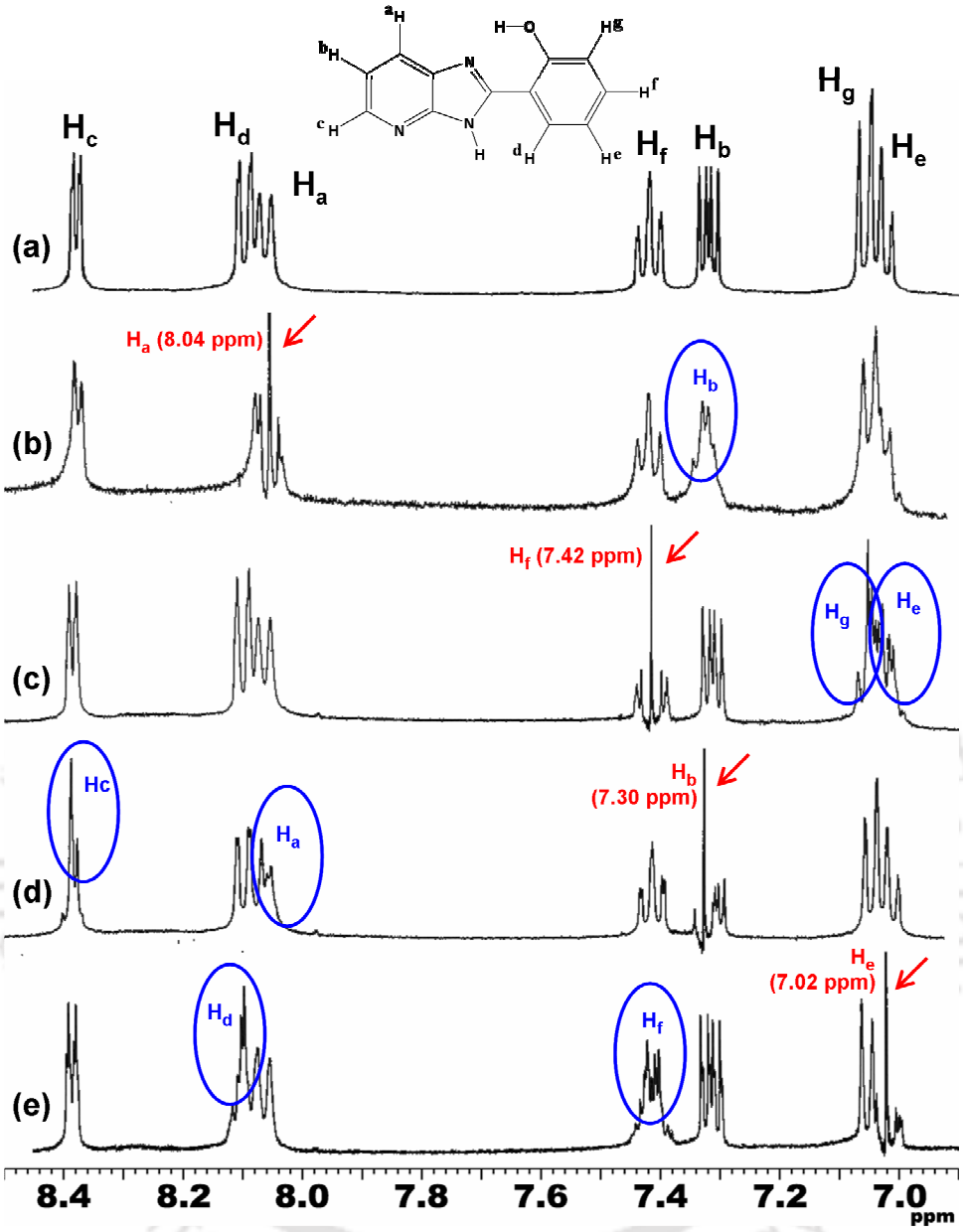

Figure A2. Normal and decoupled ^{1}H NMR spectra of HPIP-b. The arrows indicate the position of decoupler and circles denote the proton(s) that/those is/are affected.

Protons H_a and H_c (**Figure A2**) are expected to give doublet while the H_b proton is expected to give doublet of doublet. When the decoupler is placed at 8.04 ppm (**Figure A2b**), the quadruplet at 7.30 ppm is affected. In turn, when the decoupler is placed at 7.30 ppm (**Figure A2d**), the douplet peaks at 8.39 ppm and 8.04 ppm are affected. These results indicate that the doublet of doublet at 7.30 - 7.33 ppm (1H, dd, J = 4.8, 3.2, and 4.8 Hz) is due to H_b proton. Since H_c type proton is expected to be at down field due to presence of neighboring nitrogen atom, the doublet peaks at 8.39 ppm (1H, d, J = 4.8 Hz) and 8.04 ppm (1H, d, J = 8.0 Hz) are assigned to H_c and H_a protons, respectively.

The environment for H_d, H_e, H_f and H_g protons of HPIP-b are similar to those of HPIP-c. Therefore, H_d and H_g protons are expected to give doublets while the H_e and H_f protons are expected to give doublet of doublet peaks or pseudo triplet by merging of doublet of doublet peak. Therefore, the doublet at 8.11 ppm is due to H_d or H_g proton and the pseudo triplet at 7.42 ppm is due to H_e or H_f proton.

Since the H_d type proton is expected to have a higher chemical shift than H_g type proton (as is also seen in HPIP-c), the doublet at 8.11 ppm (1H, d, J = 8.0 Hz) is assigned to H_d proton. When the decoupler is placed at 7.02 ppm (**Figure A2e**), the doublet peak at 8.11 ppm and the pseudo triplet peak at 7.42 ppm are affected. This shows the peak at 7.02 ppm (1H, d, J = 7.2 Hz) is due to H_e proton and the peak at 7.42 ppm (1H, t, J = 8.4, 8.4 Hz) is due to H_f proton. By placing the decoupler at 7.42 ppm (**Figure A2c**), the peaks at 7.02 ppm and 7.06 ppm are affected. This shows the peak at 7.06 ppm (1H, d, 8.0 Hz) is due to H_g proton.

A3. Assignment of Protons in NMR Spectrum of HPBI

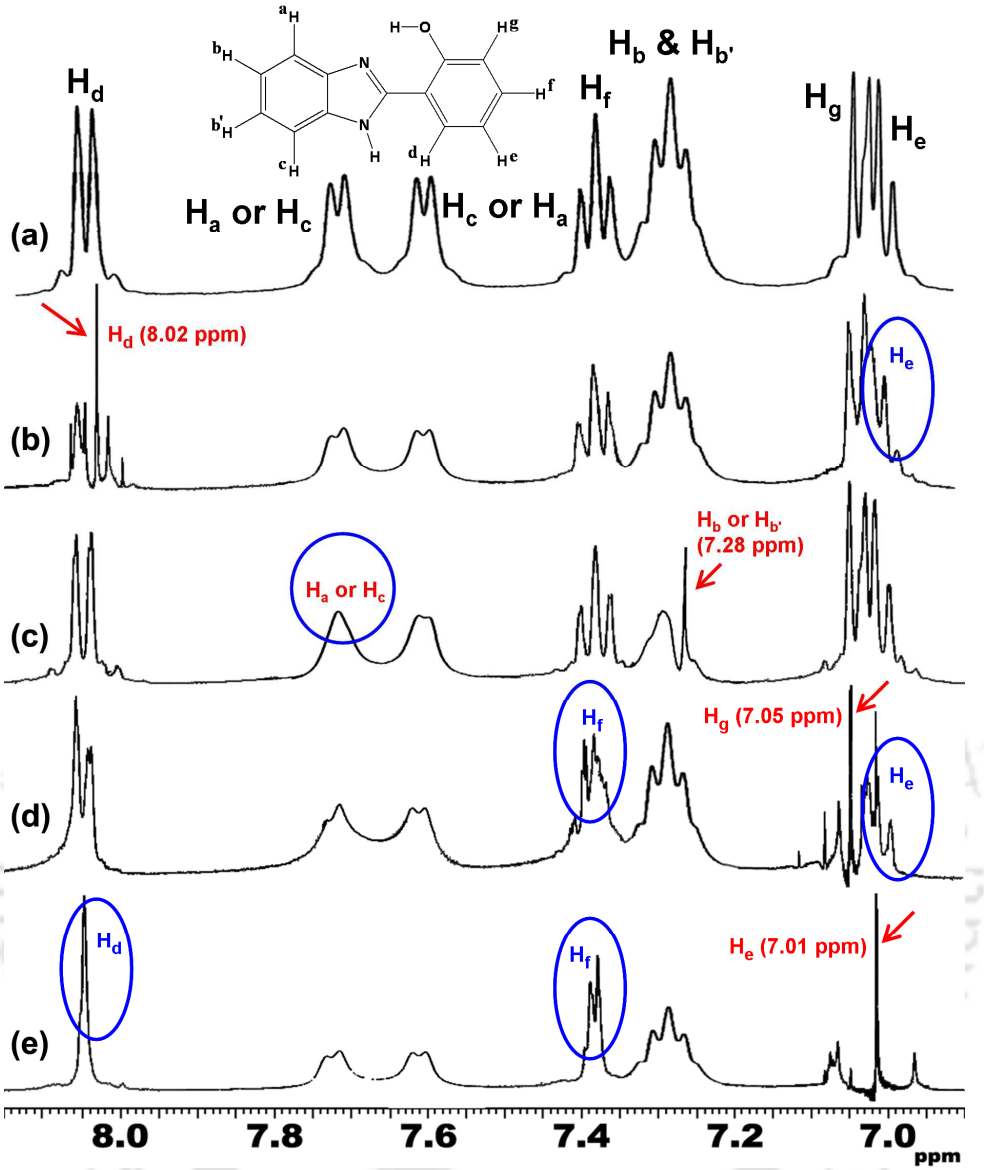

Figure A3: Normal and decoupled ^{1}H NMR spectra of HPBI. The arrows indicate the position of decoupler and circles denote the proton(s) that/those is/are affected.

Protons H_a and H_c are expected to give doublet (**Figure A3**) while H_b and $H_{b'}$ protons are expected to give quadruplet/multiplet. Two doublet peaks each of one proton count are observed at 7.61 ppm and 7.70 ppm. Another triplet like peak of two proton counts is observed at 7.28 ppm. When the decoupler is placed at 7.28 ppm (**Figure A3c**), the doublet at 7.70 ppm merged to appear as singlet. Since H_b and $H_{b'}$ protons are expected to be upfield relative to H_a and H_c protons, from these results, the peak at 7.28 ppm (2H, pseudo triplet) is assigned to H_b and $H_{b'}$ protons. The peaks at 7.61 ppm (1H, d) and 7.70 ppm (1H, d) are assigned to either H_a/H_c or H_c/H_a protons.

Similar to HPIP-b and HPIP-c, H_d and H_g protons of HPBI are expected to give doublets while the H_e and H_f protons are expected to exhibit doublet of doublet peaks or mutiplet by merging of doublet of doublet peak. H_d type proton appears at ~ 8.1 ppm region (as is seen in HPIP-b and HPIP-c).

When the decoupler is placed at 8.02 ppm (**Figure A3b**), the peak at 7.01 ppm only is affected. This shows the doublet peak at 8.02 ppm (1H, d, J = 8.0 Hz) is due to H_d proton and the peak at 7.01 ppm (1H, d, J = 8.0 Hz) is assigned to H_e proton.

When the decoupler is placed at 7.01 ppm (**Figure A3e**), the doublet peak at 8.02 ppm and the peak at 7.38 ppm are affected. This further confirms the peak at 7.01 ppm is due to H_e proton and the peak at 7.38 ppm (1H, t, J = 7.2, 7.2 Hz) is due to H_f proton.

By placing the decoupler at 7.05 ppm (**Figure A3d**), mainly the peak at 7.38 ppm is mainly affected. This implies the peak 7.05 ppm (1H, d, J = 9.6 Hz) is due to H_g proton.

A4. Parameters for Single Crystal of $Ni(HPIP\text{-}b)_2^{2+}$ Complex

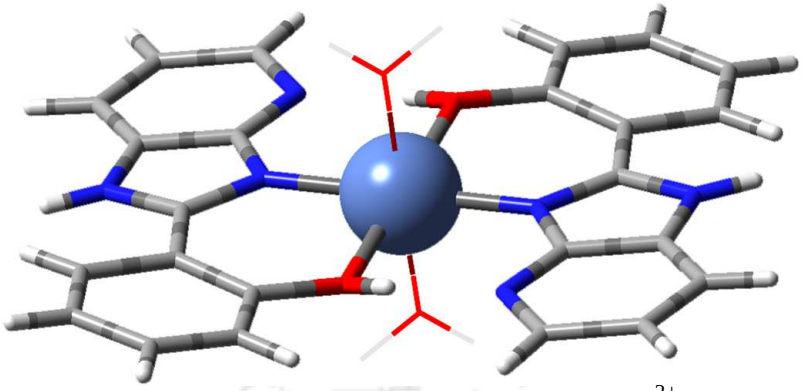

Figure A4. 3D molecular structures of $Ni(HPIP\text{-}b)_2^{2+}$ Complex.

Chemical Formula:	$C_{14}\ H_{12}\ Cl\ N_4\ Ni\ O$
Formula Weight	346.44
Temperature (K)	296(2)
Crystal system	Monoclinic
Space Group	P 21/n
a (Å)	9.5392(19)
b (Å)	11.270(2)
c (Å)	13.306(2)
α (º)	90.00
β (º)	95.357(12)
γ (º)	90.00
Cell Volume ($Å^3$)	1424.1(5)
Formula Units Z	4
Density, ρ ($g\ cm^{-3}$)	1.616
F(000)	708
Absorption Coefficient, μ (mm^{-1})	1.552
Diffractometer	SMART APEX-II CCD (Brucker)
Radiation Wavelength (Å)	0.71073
Radiation Type	Mo-K_α
θ Range for Data Collection (º)	4.01-28.39
Measured Reflections	16136
Unique Reflections	3526
Index Ranges (º)	$-12 \le h \le 12$, $-14 \le k \le 13$, $-17 \le l \le 17$
Unique Reflections [$F^2>2\sigma(F^2)$]	3526
Weighting Scheme	$w = [S^2(F_o^2) + (0.1985P)^2 + 0.0000P]^{-1}$, where $P = (F_o^2 + 2F_c^2)/3$
Data/Parameters	
R [$F^2>2\sigma(F^2)$]	R [a] = 0.0893, wR [b] = 0.2613
R (all data)	R [a] = 0.1180, wR [b] = 0.2978
Goodness-of-fit	0.961

[a] $R = \Sigma||F_o|-|F_c||/\Sigma|F_o|$

[b] $wR = \Sigma\{w(F_o^2-F_c^2)^2/\Sigma w(F_o^2)^2\}^{1/2}$

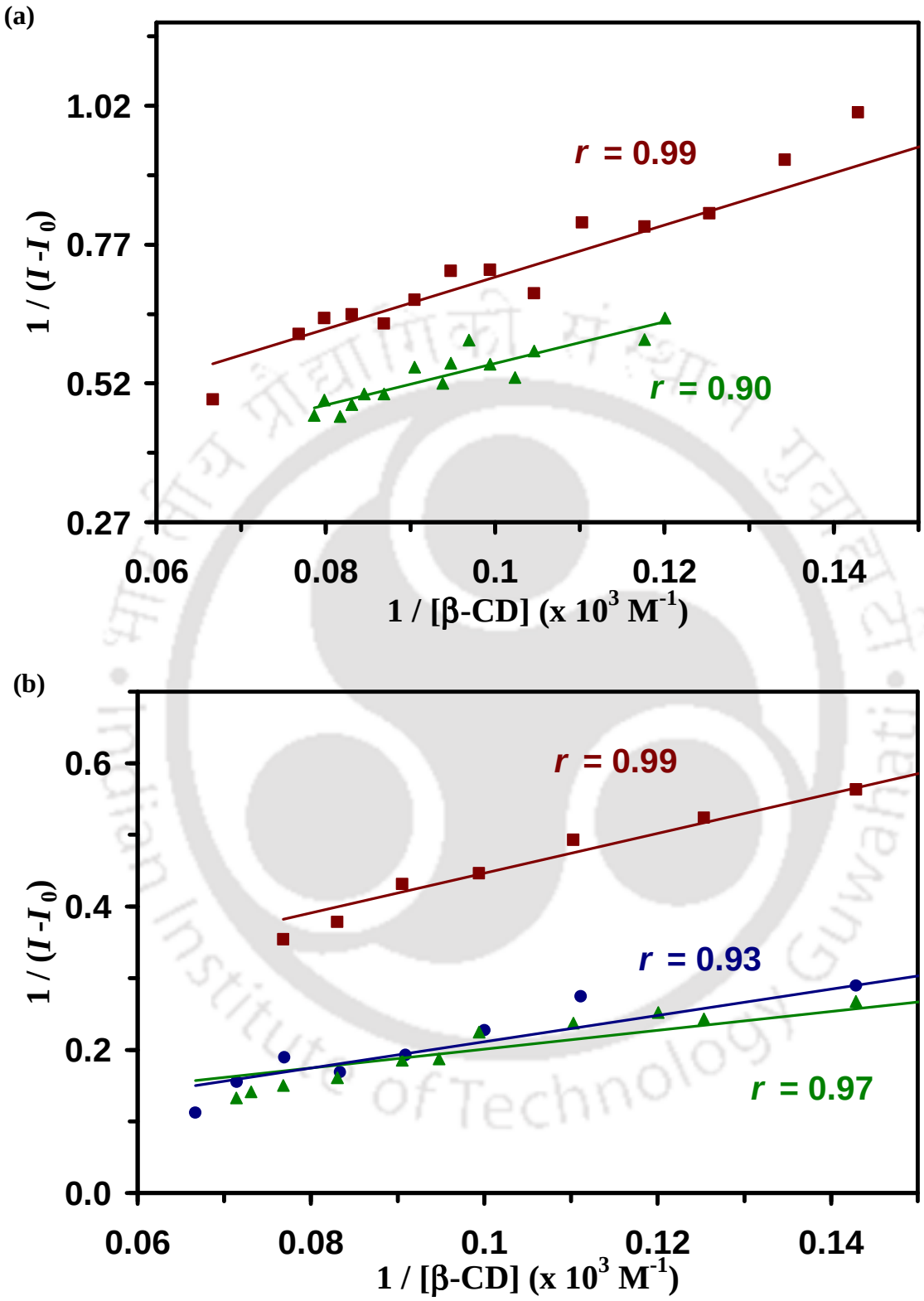

Figure A5. Benesi-Hildebrand plot for the tautomer band of (a) HPIP-b (■), and HPIP-c (▲) in water, (b) HPBI (●), HPIP-b (■), and HPIP-c (▲) in DMSO as a function of [β-CD].

Journal Publications:

1. Nihar Dash, **Francis A. S. Chipem**, R. Swaminathan, and G. Krishnamoorthy
"**Hydrogen Bond Induced Twisted Intramolecular Charge Transfer in 2-(4'-*N*,*N*-Dimethylaminophenyl)imidazo[4,5-*b*]pyridine**"
Chem. Phys. Lett. **2008**, *460*(1-3), 119-124.

2. Nihar Dash, **Francis A. S. Chipem**, and G. Krishnamoorthy
"**Encapsulation of 2-(4'-*N*,*N*-Dimethylamino)phenylimidazo[4,5-*b*]pyridine in β-Cyclodextrin: effect on H-Bond Induced Intramolecular Charge Transfer emission**"
Photochem. Photobiol. Sci. **2009**, *8*(12), 1708-1715.

3. **Francis A. S. Chipem**, and G. Krishnamoorthy
"**Comparative Theoretical Study of Rotamerism and Excited State Intramolecular Proton Transfer of 2-(2'-Hydroxyphenyl)benzimidazole, 2-(2'-Hydroxyphenyl)imidazo[4,5-*b*]pyridine, 2-(2'-Hydroxyphenyl)imidazo[4,5-*c*]pyridine and 8-(2'-Hydroxyphenyl)purine**"†
J. Phys. Chem. A. **2009**, *113*(44), 12063-12070.

4. **Francis A. S. Chipem**, Soumya Chatterjee, and G. Krishnamoorthy
"**Theoretical Study on Photochemical Behavior of *trans*-2-[4'-(Dimethylamino)styryl]benzothiazole**"
J. Photochem. Photobiol. A: Chem. **2010**, *214*(2-3), 121-127.

5. **Francis A. S. Chipem**, Nihar Dash, and G. Krishnamoorthy
"**Role of Nitrogen Substitution in Phenyl Ring on Excited State Intramolecular Proton Transfer and Rotamerism of 2-(2‘Hydroxyphenyl)benzimidazole: a Theoretical Study**"†
J. Chem. Phys. **2011**, *134*(10), 104308.

6. **Francis A. S. Chipem**, Anasuya Mishra, and G. Krishnamoorthy
"**The Role of Hydrogen Bonding in Excited State Intramolecular Charge Transfer**"†
Phys. Chem. Chem. Phys., **2012**, *14*(25), 8775-8790. (**Coverpage and Perspective article**)
Top 10 most read article in PCCP in June, 2012.

7. Anasuya Mishra, A. Thangamani, Soumya Chatterjee, **Francis A. S. Chipem**, and G. Krishnamoorthy
"**Photoisomerization of *trans*-2-[4'-(Dimethylamino)styryl]benzothiazole**"
Photochem. Photobiol. **2013**, *89*(1), 247-252. doi: 10.1111/j.1751-1097.2012.01227.x

8. **Francis A. S. Chipem**, Santosh K. Behera, and G. Krishnamoorthy
"**Enhancing excited state intramolecular proton transfer in 2-(2'-hydroxyphenyl)benzimidazole and its nitrogen substituted analogues by β-cyclodextrin: the effect of nitrogen substitution**"†
J. Phys. Chem. A **2013** (in press). doi: 10.1021/jp311438s

9. **Francis A. S. Chipem**, and G. Krishnamoorthy

"**Role of Temperature on the Dual Fluorescence of 2-(2'-Hydroxyphenyl)benzimidazole and its Nitrogen Substituted Analogues due to Excited-State Intramolecular Proton Transfer and Rotamerism**"†
(manuscript under preparation).

10. **Francis A. S. Chipem**, Santosh K. Behera, and G. Krishnamoorthy
"**Study of Fluorescence Sensing Ability of 2-(2'-Hydroxyphenyl)benzimidazole and its Nitrogen Substituted Analogues Toward Metal Ions Based on Ratiometric Measurments**"†
(manuscript under preparation).

11. **Francis A. S. Chipem**, and G. Krishnamoorthy
"**Excited State Intramolecular Proton Transfer Behavior of 2-(2'-Hydroxyphenyl)benzimidazole and its Nitrogen Substituted Analogues in Aerosol-OT Reverse Micelle**"†
(manuscript under preparation).

12. **Francis A. S. Chipem**, Santosh K. Behera, and G. Krishnamoorthy
"**Interaction of Bovine Serum Albumin with 2-(2'-Hydroxyphenyl)benzimidazole and its Nitrogen Substituted Analogues**"†
(manuscript under preparation).

13. **Francis A. S. Chipem**, and G. Krishnamoorthy
"**Excited State Intramolecular Proton Transfer and Rotamerism of 2-(2'-Hydroxyphenyl)-3*H*-oxazo[4,5-*b*]pyridine**"†
(manuscript under preparation).

Conference Proceedings:

International Conference

1. **Francis A. S. Chipem**, and G. Krishnamoorthy
"**2-(2'-Hydroxyphenyl)-3*H*-imidazo[4,5-*b*]pyridine a Fluorescence Sensor for Metal Ions**"†
Fluorescence 2009 (*An International Conference of Fluorescence in Biology*), Mumbai, India, March **2009**.

2. **Francis A. S. Chipem**, Nihar Dash, and G. Krishnamoorthy
"**Temperature Effects on Excited-State Intramolecular Proton Transfer in 2-(2'-Hydroxyphenyl)benzimidazole and its Nitrogen Substituted Analogues**"†
Third Asia Pacific Symposium on Radiation Chemistry and DAE-BRNS Tenth Biennial Trombay Symposium on Radiation & Photochemistry (APSRC/TSRP-2010), Lonavala, India, September **2010**.

3. Anasuya Mishra, **Francis A. S. Chipem**, A. Thangamani, Soumya Chatterjee, and G. Krishnamoorthy
"**Spectral Characteristic and Photochemistry of *trans*-2-[4'-(Dimethylamino) styryl]benzothiazole: A Combined Theoretical and Experimental Study**"
I*nternational Conference on Recent Frontiers in Applied Spectroscopy (ICORFAS-2010)*, Annamalai, India, September **2010**.

4. Ashim Malakar, **Francis A. S. Chipem**, G. Krishnamoorthy
"**Interaction of 2-(2'-Hydroxyphenyl)benzimidazole, 2-(2'-Hydroxyphenyl)-3*H*-imidazo[4,5-*b*]pyridine, 2-(2'-Hydroxyphenyl)-3*H*-imidazo [4,5-*c*]pyridine with Silver Nanoparticle: A Photophysical Study**"
International Symposium on Advances in Chemical Sciences – 2012, Guwahati, India, March **2012**.

National Conference

1. Nihar Dash, Mrinmoy Saha, **Francis A. S. Chipem,** and G. Krishnamoorthy
"**Experimental and Computation Study of the Spectral Properties of 2-(4-*N*,*N*-Dimethylaminophenyl)pyrido[2,3-*d*]imidazole**"
National Conference on Theoretical and Chemical Sciences, Chidambaram (Tamil Nadu), February **2008**.

2. Nihar Dash, Mrinmoy Saha, **Francis A. S. Chipem** and G. Krishnamoorthy
"**Dual Fluorescence of 2-(4'-*N*,*N*-Dimethylaminophenyl)pyrido[2,3-*d*]imidazole: Effects of Solvents**"
National Symposium on Emerging Trends in Advanced Chemistry, Jaipur (Rajasthan), March **2008**.

3. Nihar Dash, **Francis A. S. Chipem,** and G. Krishnamoorthy
"**Effect of Micelles on Prototropic equilibria of 2-(4'-*N*,*N*-Dimethylaminophenyl)imidazo[4,5-*b*]pyridine**"
National Conference on Frontiers of Colloids, Surfaces and Nanostructured Systems, Imphal (Manipur), February **2009**.

4. **Francis A. S. Chipem**, N. Dash, and G. Krishnamoorthy
"**Excited-State Intramolecular Proton Transfer in 2-(2'-Hydroxyphenyl)benzimidazole and its Nitrogen Substituted Analogues**"†
National Seminar on New Frontiers in Chemistry, Annamalainagar, India, March **2010**.

5. Rameswar Bhattacharjee, **Francis A. S. Chipem**, and G. Krishnamoorthy
"**Effect of Solvents on Excited State Intramolecular Proton Transfer in 2-(2'-Hydroxyphenyl)-3*H*-oxazo[4,5-*b*]pyridine**"†
Conference on Photochemistry and Luminescence, Guwahati (Assam), March **2012**.

6. Saugata Sahu, **Francis A. S. Chipem**, and G. Krishnamoorthy
"**Effects of β-Cyclodextrin on Dual Fluorescence of 2-(2'-Hydroxyphenyl)-3*H*-imidazo[4,5-*b*]pyridine and 2-(2'-Hydroxyphenyl)-3*H*-imidazo[4,5-*c*]pyridine**"†
Conference on Photochemistry and Luminescence, Guwahati (Assam), March **2012**.

7. **Francis A. S. Chipem**, and G. Krishnamoorthy
"**Torsion Induced Nonradiative Decay of Phototautomer of 2-(2'-Hydroxyphenyl)benzimidazole and its Nitrogen Substituted Analogues**"†
Conference on Photochemistry and Luminescence, Guwahati (Assam), March **2012**.

†Part of this thesis.